PKD2-DEPENDENT SENSING MECHANISM IN KUPFFER'S VESICLE: HOW IT AFFECTS THE LEFT-RIGHT AXIS ESTABLISHMENT IN ZEBRAFISH

ANA RAQUEL MARQUES JACINTO

Tese para obtenção do grau de Doutor em Mecanismos de Doença e Medicina Regenerativa

na NOVA Medical School | Faculdade de Ciências Médicas

Janeiro, 2018

PKD2-DEPENDENT SENSING MECHANISM IN KUPFFER'S VESICLE: HOW IT AFFECTS THE LEFT-RIGHT AXIS ESTABLISHMENT IN ZEBRAFISH

Ana Raquel Marques Jacinto

Orientador: Susana Santos Lopes, PhD

Tese para obtenção do grau de Doutor em Mecanismos de Doença e Medicina Regenerativa

Janeiro, 2018

Contents

To my family and friends!

“Serpenteio, mas não me desvio”

Carvalho Monteiro, idealizador da Quinta da Regaleira

Agradecimentos

Em primeiro lugar, gostaria de agradecer à Susana pela oportunidade que me deu. Tu aceitaste-me no teu laboratório numa altura crítica da minha vida em que provavelmente muitos outros PIs talvez não o fizessem. Espero ter estado à altura das expectativas e dos desafios que tu tinhas para mim e espero que saibas que sempre dei o meu melhor em tudo o que fiz. Quero que saibas que estarei sempre grata pela tua aposta e desejo-te continuado sucesso em tudo o que faças! Obrigado por tudo!

De seguida, gostaria de agradecer a todos os membros do grupo que nestes 4 anos me acompanharam. Quero começar com as duas posdocs, pois se houve alguma coisa que estes 4 anos me ensinaram é que um laboratório sem posdocs é um laboratório mais pobre. Bárbara, tu és uma fonte de inspiração e boa disposição. A tua visão da vida e do mundo e a tua atitude definem-te como uma pessoa com uma forte conduta moral e grande código de trabalho. Posso dizer à vontade que aprendi contigo uma metodologia e disciplina de trabalho que realmente funciona e dá frutos. Adorei trabalhar e conviver contigo, fosse a discutir ciência ou a contar cílios imóveis em 3D ou a discutir a atualidade política. Obrigada por tudo. Mónica, a tua boa disposição e visão clara das coisas iluminou-me o caminho em várias ocasiões. Vou para sempre guardar as nossas conversas e as tuas palavras sábias e de conselho. Sim, foste tu que sempre me disseste que tudo ia correr bem e que eu ia terminar com algo do qual me ia orgulhar. E não é que tinhas mesmo razão? O teu percurso científico e de vida é algo que vou guardar como uma inspiração para os dias difíceis. E nessas ocasiões quero parar e pensar: o que será que a Mónica faria nesta situação? Obrigada por todas as discussões científicas, por me obrigares a parar e a ver melhor as coisas, por todos os puxões de orelhas e por todos os sorrisos e gargalhadas! Não podia deixar de agradecer à pessoa que primeiro me mostrou onde estava tudo no laboratório quando cheguei. A estudante de doutoramento que já lá estava quando comecei: Petra. A nossa relação cresceu e ultrapassou as barreiras do laboratório. Eu vi-te crescer de estudante de doutoramento com dúvidas e incertezas, para doutorada com uma confiança redobrada nas suas capacidades, para mulher feliz e realizada em vários aspetos da vida. Poder ver isto tudo foi uma bênção e algo que sempre me deixou feliz. Poder ajudar neste processo deixou-me também realizada. És uma grande e boa amiga que vou estimar para a vida! Obrigada por todas as confidências no telhado do IGC. Quero também agradecer ao meu parceiro de flow: Pedro. A tua energia calma e racional, o teu sentido de humor e os teus comentários certeiros tornam-te alguém com quem é

extremamente agradável de trabalhar e conviver. Conto contigo para sempre me relembrar de que está na hora de ir lá abaixo matar a sede. Obrigada pelo apoio continuado, pelo chocolate, pela piada na altura certa e pelo comentário científico certeiro. No tempo em que tive no laboratório da Susana, tive a oportunidade de ajudar a formar novas gerações de cientistas. De todos, gostaria de primeiramente destacar aquela com quem acabei por ter uma convivência que ultrapassou o iniciar de alguém num laboratório: Sara. É difícil para mim descrever o orgulho que senti quando te vi a defender a tua tese. Tu és uma pessoa especial, que me ensinou muita coisa e com quem tenho um prazer imenso de conviver e chamar amiga. Quero que nunca te esqueças do teu valor como pessoa e como cientista. Tens capacidade para ir longe mas, mais que tudo, tens coragem para isso também! Pedro e Sara, obrigada pela ajuda, apoio e camaradagem e nunca se esqueçam: cuidado com as leguminosas ácidas! Finalmente, quero agradecer a todos os outros estudantes que partilharam a vida do 'lab' comigo: Diana, Hanna, Rita, Inês, Catarina Bota, Margarida Rasteiro e Filipe Tiago. Espero não vos ter aborrecido com as conversas "de velha" e que vos tenha conseguido ajudar. Quero agradecer a todos os técnicos de Fish Facility com quem tive o privilégio de trabalhar, particularmente ao mais recente: Fábio Valério. Obrigada pela animação, pela ajuda e camaradagem.

Gostava de deixar um agradecimento especial às pessoas do CEDOC que sempre se disponibilizaram para me ajudar e encorajar, particularmente à Ana Roberto, Sílvia Costa, Marta Santos e Rita Teodoro, mas também a toda a comunidade científica que está em franco crescimento. Quero também agradecer aos membros do Programa Doutoral ProRegeM, pela oportunidade e pela convivência.

Sou uma sortuda, pois tenho uma lista de bons amigos a quem devo a manutenção da sanidade mental. Quero agradecer a: Patrícia Gomes, Lucas Coito, Diana Espadinha, Andreia Nunes, Raquel Silva, Tiago Marinho, Inês Fragata, Carlos Almeida, Bruno Franco, Mariana Liberato, Joana Silva, Sofia Carvalho, Margarida Bárbaro, Alexandra Santos, Inês Albuquerque, Catarina Nabais, Eduardo Marabuto, Inês Pereira, Sofia Henriques, Tiago Mendes e Daniela Grácio. Inês, Sofia e Daniela, as originais do Team Banana, e Tiago, Banana Honorário: a vida tratou de nos afastar a todos e é difícil combater isso ao ritmo em que vivemos. No entanto, a minha dívida para convosco é grande e por isso quero agradecer-vos. Gosto de saber que sempre que conseguimos nos encontrar todos, é como se o tempo não tivesse passado. Joana, Sofia, Margarida, Alexandra, Inês, Catarina e Eduardo: os nossos encontros são sempre mais divertidos quando estamos todos juntos. São momentos como

esses que nos renovam as forças e fazem o resto valer a pena. Obrigada pelas palavras de apoio e preocupação! Inês e Carlos: os meus Game Masters favoritos. Adoro conversar com vocês – sinto que saio sempre uma pessoa mais rica e feliz ao fim de cada encontro nosso. Obrigada por me fazerem sentir sempre incluída! Bruno e Mariana: a vossa adição aos nossos convívios tornam-nos imensamente mais ricos. Vocês são impecáveis e agradeço-vos a amizade e o carinho com que sempre me trataram. Tiago: o meu informático favorito. Relativamente à tese, obrigada pela ajuda quando o meu PC decidiu apagar todas as fontes no dia 2 da escrita da tese. Nunca me tinha posto na Malveira tão depressa. Sem ser relativamente à tese, obrigada por me relembrares sempre que mão direita é penalti e pela diversão que é sempre garantida. A forma como vês a vida é uma inspiração. Raquel Silva: adoro o facto de seres um doce e uma fonte de conforto. As nossas parelhas para o jantar têm sido fantásticas e creio que temos o dever moral de as continuar. A tua presença e energia calma faz tudo parecer naturalmente melhor! Andreia Nunes: oh well…. Tu és a minha definição de cientista. Persistente, inteligente, trabalhadora e focada; és uma força da natureza e nada te consegue parar! Por todas as vezes que disseste que conseguia e que ia dar, o meu muito obrigado! O teu entusiasmo é sempre contagiante e apenas desejo que sejas sempre feliz! Di: amiga desde os primeiros dias da licenciatura, ainda não nos tornamos jardineiras nos jardins da Gulbenkian! Mas ainda vamos a tempo! És o meu mori e quero manter-te na minha vida para sempre. Espero que nunca nada se ponha entre a nossa amizade! Obrigada pelo apoio sempre e pelas palavras de conforto. Lucas: és impecável. Adoro conversar contigo, os teus conselhos são sempre bem-vindos, e a tua fantástica “sorte” em SW é algo digno de nota! Obrigada por tudo! Patrícia: simplesmente, obrigada! Tu estás sempre presente, mesmo quando o que mais precisas é de não estar. Tu preocupas-te sempre e dás sempre mais, mesmo quando o esforço já é inumano. É algo que aprecio em ti e agradeço imensamente que me aches digna de tal. Obrigada!

Finalmente, quero agradecer à minha família. Aos meus pais, Modesto e Olga Jacinto. Por terem apoiado a decisão da filha deles que sempre disse que queria ser médica e um dia decidiu que afinal queria ser cientista. Por continuarem a apoiar quando essa decisão levou a filha deles para longe e que tem sempre o potencial de continuar a levar. A nossa amizade é tão forte que não há distância que a desfaça. Eu amo-vos e agradeço-vos e espero ter sido sempre digna do vosso orgulho. Aos meus tios, Ana e Victor Jacinto, por estarem sempre por perto e positivos, pelas sobremesas e pelos filmes ao sábado à tarde e pelas gargalhadas. Aos meus avós, Mário e Irene Jacinto. Porque nem sempre perceberam o que a neta deles estava a fazer, mas que mesmo assim sempre manifestaram apoio, à maneira deles. Á minha

prima que podia bem ser minha irmã: Filipa. Eu adoro-te mais que tudo e quero ver-te vencer na vida! É o que mais mereces. Aos meus primos de Coimbra: Anabela, Tomané, Vanessa e Hugo Murta (e respectivos!). A vossa boa disposição é contagiante e as idas a Coimbra são sempre entusiasmantes! Á minha nova família, que sempre demonstra interesse no que faço. Ao meu primogénito: Luke. Por sempre me lembrar que qualquer hora do dia é hora de parar e dar festas ao gatinho. Ao meu adotado: Sora. Porque o adoro como se fosse meu e é claramente o mais fotogénico! Ao meu mais novo: Rocky. Por me lembrar que a paciência é uma virtude e que o amor está nas pequenas coisas. E a ti, Nelson, o meu companheiro de luta, que tornas tudo isto mais fácil a cada gargalhada dada e momento partilhado. Porque tens estado incansável na linha da frente e na linha de trás, a segurar as pontas e a fazer com que eu ultrapassasse a reta final com sucesso. Por tudo isso e muito mais, muito Obrigado!

Abstract

Left-Right (LR) axis establishment is a complex process that happens early in development. It requires the interplay of several genetic pathways like TGF-β, Notch, Wnt and Calcium signalling. It also involves the integration of fluid dynamics, morphogen diffusion and cilium biosynthesis to correctly position the internal organs in their final destinations. Problems in LR axis establishment are often associated with chronic diseases. The first asymmetric decision commonly happens in a small transient structure, the Left-Right Organizer (LRO), a ciliated structure present in many vertebrates. Motile cilia generate an asymmetric fluid flow that is perceived differently between the left and the right side, which generates a calcium response and asymmetric gene expression. These signals are then transferred to the Lateral Plate Mesoderm, the tissue that will later give rise to the heart and influence the endoderm derived organs such as the liver and pancreas.

In Chapter 2, we focused in understand the pathways behind deciding between being a motile vs immotile cilium in the LRO. Although all cilia are made motile in terms of ultrastructure due to Foxj1a expression, the decision to move or not is dependent on Notch signalling alone. Then, we focused on further characterization of an important calcium channel, Pkd2, in the LR. This channel is thought to partner with Pkd1l1 and sense flow, an important feature in LR. In Chapter 3, we asked if having no flow had the same impact as having no Pkd2-mediated sensing. The only manipulation that did not affect the LRO architecture was to target Pkd2 on the LRO cells only, which still left visible Pkd2 protein and a slower flow. Still, all our manipulations had the same phenotype: randomization of organ *situs*. In Chapter 4, we performed a LRO-specific microarray between WT and pkd2 morphant embryos in order to find other asymmetric genes present in the LRO. Although we did not find any gene expressed asymmetrically between left and right side, we indeed find four new genes with minor roles in LR: *cacybp, frzb, pvalb6* and *ncl1*. In Chapter 5, we further focused in manipulating *ncl1*, a new

gene in LR that is known to act as a TGF-β antagonist by facilitating Lefty secretion and impacting on mesendoderm patterning. Indeed, we found that it has an impact on LR, probably by influencing the secretion of some TGF- β signalling player. In Chapter 6, we set to establish zebrafish as a good model to study kidney toxicity when metabolizing drugs.

Together, the results presented in this thesis provide new clues for LR axis establishment, from cilia motility to new downstream genes of Pkd2 and calcium. It also highlights the zebrafish as a good model to study human disease.

Key-words: Left-Right axis establishment, Pkd2, Cilia motility, TGF- β signalling, Notch signalling

Resumo

Estabelecimento do eixo Esquerda-Direita (ED) é um processo complexo que ocorre cedo durante o desenvolvimento. Exige a integração de várias vias de sinalização, tais como TGF-β, Notch, Wnt e Cálcio. Também envolve a coordenação de dinâmica de fluídos, difusão de morfogénios e movimento ciliar. Tudo junto e coordenado no tempo leva à correta localização dos órgãos internos. Problemas no estabelecimento deste eixo estão normalmente associados a doenças crónicas. As primeiras decisões assimétricas acontecem numa pequena e transiente estrutura chamada o Organizador Esquerda Direita, uma estrutura ciliar que existe em vários vertebrados. Cílios móveis geram um fluxo de fluido assimétrico que se traduz numa expressão génica assimétrica entre o lado esquerdo e o lado direito. Estes sinais são depois transferidos à Mesoderme Lateral, o tecido que mais tarde dá origem ao coração e influencia a endoderme que dá origem a órgãos como o fígado e o pâncreas.

No Capítulo 2, focámo-nos em tentar compreender como é que as vias de sinalização se coordenavam para decidir entre um cílio móvel e imóvel no Organizador. Embora a expressão de Foxj1a em todas as células do Organizador produza cílios com ultra-estrutura compatível com motilidade, a decisão entre mover ou não é exclusiva da via de sinalização Notch. A seguir, focámo-nos em caracterizar Pkd2, um canal de cálcio importante no estabelecimento do eixo ED. Este canal está associado ao Pkd1l1, uma molécula com domínios capazes de sentir fluido e responder com entrada de cálcio na célula. No Capítulo 3, questionámos se não ter fluxo no Organizador tinha o mesmo impacto que não ter um mecanismo para sentir esse fluxo através da ausência do Pkd2. A única manipulação que não afetou a arquitetura do Organizador foi remover o Pkd2 apenas nas células do Organizador, o que não é muito eficiente e tem impacto na velocidade do fluxo dentro do Organizador. Ainda assim, todas as manipulações efetuadas deram o mesmo fenótipo: randomização da posição dos órgãos. No Capítulo 4, fizemos um estudo de transcritómica usando apenas as células do Organizador

em embriões normais ou injetados com morpholino contra o Pkd2. Embora não tenhamos encontrado genes com expressão assimétrica à volta do Organizador, encontramos quatro novos genes que influenciam o estabelecimento do eixo: *cacybp, frzb, pvalb6* e *ncl1*. No Capítulo 5, focámo-nos na *ncl1*, um gene nunca antes associado ao estabelecimento do eixo e que atua como antagonista da via de sinalização TGF-β ao influenciar a secreção de Lefty e influenciando a padronização da mesoderme-endoderme. Nós descobrimos que este gene impactua no estabelecimento do eixo, provavelmente ao influenciar a secreção de algum elemento da via de sinalização TGF-β. No Capítulo 6, focámo-nos em estabelecer o peixe-zebra como um bom modelo para estudar toxicidade no rim em resposta a fármacos.

Em suma, os resultados apresentados nesta tese providenciam novas pistas para o estabelecimento do eixo ED, desde o movimento do cílio a novos genes a jusante do Pkd2 e do cálcio. Também reforçámos a ideia de que o peixe-zebra pode ser um bom modelo para estudar doenças humanas.

Palavras-Chave: Estabelecimento do eixo Esquerda-Direita, Pkd2, Motilidade ciliar, Via de sinalização TGF-β e Notch

Resumo Alargado

O correto estabelecimento dos órgãos internos no seu devido lugar dentro do organismo é importante para o correto funcionamento dos mesmos. É um processo comum a vertebrados e invertebrados, embora a forma como o atingem nem sempre é a mesma. Algo em comum é a expressão assimétrica de genes da via de sinalização TGF-β nos tecidos embrionários que vão dar origem a estes órgãos mais tarde durante o desenvolvimento. Em alguns vertebrados, incluindo nós seres humanos, as primeiras decisões assimétricas ocorrem numa pequena e transiente estrutura denominada Organizador Esquerda Direita (ED). Esta estrutura é composta por células que têm à sua superfície um cílio inclinado. Este tem a capacidade de mexer e a combinação de vários cílios móveis faz com que se gere um fluxo de líquido assimétrico da direita para a esquerda. Este fluxo gera uma resposta assimétrica nas células do Organizador: as células da esquerda têm uma subida da concentração de cálcio intracelular e expressão de *nodal* enquanto as células do lado direito expressam *cerl2*/*dand5*, o primeiro sendo um ativador e o segundo um inibidor da família TFG-β. Esta primeira assimetria é propagada pelos tecidos até chegar à Mesoderme Lateral, o tecido que origina o coração e influencia a endoderme, que dá origem aos órgãos viscerais.

Muitas questões permanecem em aberto neste processo, particularmente como é que o fluxo é interpretado pelas células do Organizador. Tipicamente, o Organizador é composto por células com cílios móveis, responsáveis por gerar o fluxo, e células com cílios imóveis, potenciais sensores desse mesmo fluxo. Há duas grandes teorias sobre isto: o fluxo transposta um morfogénio em vesículas que embatem do lado esquerdo do Organizador e libertam aí o seu conteúdo, dando assim origem à expressão assimétrica de genes; ou a força e direção do fluxo são de alguma forma percebidos pelos cílios imóveis. A descoberta de um complexo proteico composto por polycysteins (Pkd2, um canal de cálcio e Pkd1l1, um recetor) nos cílios do Organizador deu força redobrada a esta segunda hipótese. Este complexo

proteico é conhecido por ser expresso nos cílios dos rins e ser capaz de responder à força mecânica do fluxo de urina, respondendo com uma entrada de cálcio nas células. A ausência deste complexo dá origem à doença dos rins policísticos e em ratinho original também problemas de lateralidade – perde-se a expressão assimétrica de genes da família TFG-β na proximidade do Organizador e na mesoderme lateral e tem impacto na posição dos órgãos.

Com esta tese, começámos por tentar compreender melhor a base molecular por detrás da decisão entre ser um cílio móvel ou imóvel no Organizador. Depois, tentámos averiguar se há diferenças entre abolir completamente o fluxo ou não ter uma forma de sentir esse fluxo atrás do knockdown do Pkd2 em termos de fenótipos ao nível da expressão génica e da posição final dos órgãos. Através de um estudo de transcritómica, averiguamos quais os genes que estão a jusante do Pkd2 e debruçámo-nos sobre 4 em particular: *parvalbumin6, calcyclin binding protein*, *frizzled-related protein* e *nicalin1.* Por fim, fizemos uma comparação mais exaustiva entre dois inibidores pertencentes à via de sinalização TFG-β: Dand5, que já era conhecido por influenciar o estabelecimento ED, e Nicalin1, que nunca tinha sido descrito neste processo. Todos estes trabalhos usaram o peixe-zebra como animal modelo. É possível encontrar 70% de genes humanos neste vertebrado, o que o torna bastante atrativo para investigar processos que ocorram de forma semelhante em humanos. O facto de os embriões terem propriedades óticas que os tornam atrativos para microscopia e gerar um grande número de embriões são algumas das características mais apreciadas pelos cientistas. Por isso, terminámos com uma avaliação do peixe-zebra como um bom modelo para testar toxicidade renal à exposição de fármacos.

Todas as células do Organizador expressam *foxj1a*, um gene necessário e suficiente para especificar cílios móveis. No entanto, os resultados apresentados no segundo capítulo desta tese mostraram que a via de sinalização Notch é responsável pela decisão móvel vs imóvel. Recorrendo a estudos transcricionais, microscopia eletrónica com amostragem exaustiva do

Organizador e microscopia de multifotão de aquisição lenta, percebemos que a despeito de todos os cílios expressarem *foxj1a* e os axonemas ciliares terem dynein arms e radial spokes responsáveis pela motilidade, alguns cílios se mantém imóveis durante todo o processo. Esta decisão é tomada cedo e parece ser a jusante da transcrição de *her12*, um elemento da via de sinalização Notch. A sobrexpressão de *her12* aumenta o número de cílios imóveis em troca de cílios móveis, o que leva à perturbação do fluxo normal dentro do Organizador e tem impacto na posição dos órgãos.

A importância do canal de cálcio Pkd2 no estabelecimento do eixo ED está bem fundamentada no número de trabalhos feitos com este gene em vários animais modelo. Há várias evidencias que apontam para esta proteína fazer parte do mecanismo capaz de sentir o fluxo e iniciar a onda de cálcio observada no lado esquerdo. No terceiro capítulo desta tese perguntámos se abolir o fluxo, que se sabe estar a montante da expressão assimétrica de *dand5*, originava defeitos tão graves como abolir a forma de sentir este fluxo. Através deste trabalho percebemos que tirar diferentes níveis de Pkd2 em todo o peixe-zebra levam a diferentes respostas em termos de volume e arquitetura do Organizador. A única abordagem que minimiza a interferência com a arquitetura do Organizador é quando se tira o Pkd2 exclusivamente das células do Organizador. No entanto, esta abordagem não remove completamente o Pkd2 e resulta numa velocidade de fluxo mais baixa. De qualquer forma, todas as manipulações deram o mesmo resultado em termos de *dand5* (maioritariamente simétrico) e randomização da posição dos órgãos.

Embora haja evidencias que suportam a importância da onda de cálcio observada à esquerda do Organizador, pouco se sabe sobre o que é ativado a jusante da mesma. Por isso, no Capítulo 4, fizemos um estudo de transcritómica usando apenas as células do Organizador de embriões normais e embriões sem Pkd2. Da lista de genes obtida, escolhemos 4 para manipular individualmente e perceber o seu impacto no eixo ED. Primeiro avaliou-se o padrão

de expressão, onde nenhum mostrou um padrão assimétrico semelhante ao observado para *dand5,* o primeiro gene que se sabe ser assimétrico no Organizador do peixe-zebra. A seguir avaliámos o impacto da sua manipulação na assimetria de *dand5* e na posição dos órgãos. Nenhum revelou ter impacto tão forte como manipular Pkd2, mas todos parecem ter algum papel no estabelecimento do eixo ED. Em suma e para futura verificação, *parvalbumin6* pode estar a controlar a cálcio do lado esquerdo, *frizzled-related protein* pode afetar o tamanho ciliar, *calcycling binding protein* pode influenciar a degradação de *dand5* através de β-catenin e *nicalin1* pode influenciar a secreção de outros elementos da via TGF-β como Dand5 ou Lefty.

Uma vez que Ncl1 está descrito na literatura como inibidor de TGF-β e nunca foi associado ao estabelecimento do eixo ED, no Capítulo 5 decidimos explorar o impacto deste gene. Knockdown deste gene leva a um aumento de defeitos de posição dos órgãos com um efeito dependente da dose de morfolino usado. Afeta a expressão de *dand5* e *spaw*, randomizando o padrão e levando a uma menor expressão dos mesmos. Experiências onde se fez o knockdown de ambos *dand5* e *ncl1* mostraram mais defeitos em termos de posição de órgãos, apontando para uma potencial epistasia dos dois genes. Sobrexpressar *dand5* em embriões com knockdown de *ncl1* não consegue melhorar os efeitos da ausência de *ncl1*, o que aponta para potenciais vias separadas. Dados preliminares do mutante de *ncl1* suportam os fenótipos observados com o morfolino.

Finalmente, no Capítulo 6, confirmámos que o peixe-zebra pode ser um bom modelo para testar a metabolização de fármacos como anti-retrovirais usados no tratamento da SIDA. Os prónefros presentes nas larvas do peixe-zebra apresenta elevada homologia com o que se encontra no rim humano. Neste estudo, através de várias técnicas como espectrometria de massa para avaliar metabolismo, estudos de filtração de inolina para testar a função renal, microscopia com multifotão e eletrónica de transmissão, avaliámos os danos que a exposição

a certos fármacos provocam nos prónefros do peixe-zebra. Todos os defeitos encontrados estão em concordância com o tipicamente se observa nos rins humanos expostos aos mesmos fármacos, confirmando o peixe-zebra um animal modelo bastante atrativo para este tipo de estudos.

Os capítulos desta tese ilustram a versatilidade do peixe-zebra para testar o estabelecimento do eixo ED nos vários níveis que influenciam este processo. Podemos estudar a formação dos cílios no Organizador e podemos estudar em detalhe a expressão génica dos vários intervenientes das diferentes vias de sinalização ao nível do Organizador e ao nível dos tecidos que vão dar origem aos órgãos. Descobrimos novos interveniente nunca antes descritos neste processo, adicionando novos níveis de complexidade a um processo já de si fascinante.

List of abbreviations

BMP – Bone Morphogenetic Protein

Cacybp – Calcyclin Binding Protein

Cerl2 – Cerberus-like 2

Dand5 – DAN family member 5

DFCs – Dorsal Forerunner Cells

DNA – Deoxyribonucleic Acid

Dnah – Dynein axonemal heavy chain

ECM – Extracellular Matrix

ER – Endoplasmic Reticulum

Fgf – Fibroblast Growth Factor

Foxj1a – Forkhead box J1a

Frzb – Frizzled related protein

ICOs – Intracilliary calcium oscillations

Her12 – Hairy-related 12

HPF – Hours Post Fertilization

KV – Kupffer's Vesicle

LPM – Lateral Plate Mesoderm

LR – Left-Right

LRO – Left-Right Organizer

mRNA – Messenger Ribonucleic Acid

Ncl1 – Nicalin1

NICD – Notch Intracellular Domain

PCP – Planar Cell Polarity

Pkd – Polycystin kidney disease

PSM – Presomitic Mesoderm

Pvalb6 – Parvalbumin 6

SHH – Sonic Hedgehog

SS – Somite Stage

TGFβ – Transforming Growth Factor Beta

Wnt – Wingless/Integrated Family Members

CHAPTER 1

Introduction

“It always seems impossible until it’s done”

Nelson Mandela

1. INTRODUCTION

Correct Left-Right (LR) axis establishment comes from a combination of cell morphology, ciliogenesis, fluid flow physical dynamics, several signalling pathways (calcium, Nodal, Notch and Wnt), signal transduction and organogenesis. Although a lot has been done do address all these steps and we already have a good idea how these steps coordinate to give rise to correct organ position, still a lot is missing. One of the biggest questions that remains highly debated in the field is how the biophysical properties of fluid flow are interpreted from the Left-Right Organizer (LRO) cells. Is there a morphogen being released in the LRO space or is it the mechanical force that is being somehow interpreted? Other related question regards the two cilia types present in the LRO; what are the relevant differences between motile and immotile cilia and whether these immotile cilia are the predicted sensors by McGrath et al. in 2003. What is also still unknown is what are the downstream targets of the asymmetric calcium signalling on the left, and its relationship to the complementary asymmetry observed for *dand5.* This thesis aims to answer to some of these questions and add more knowledge to the field.

1.1 WHAT WE NEED TO KNOW ABOUT CILIA (for this study)

For many vertebrates, LR is decided downstream of the beating motion of cilia. So, in order to understand LR, one needs to acquire some notions about this organelle. Cilia are hair-like structures that occur on the surface of most cells. There are several subtypes of cilia but, typically, cells have a primary, sensory cilium. These tend to be very dynamic in terms of morphology and molecular composition, so they can sense fluid flow, light, odorants or signalling molecules. Primary cilia are seen like a hub for signalling pathways like sonic hedgehog (Huangfu et al., 2003), Wnt signalling (Corbit et al., 2008), Notch signalling

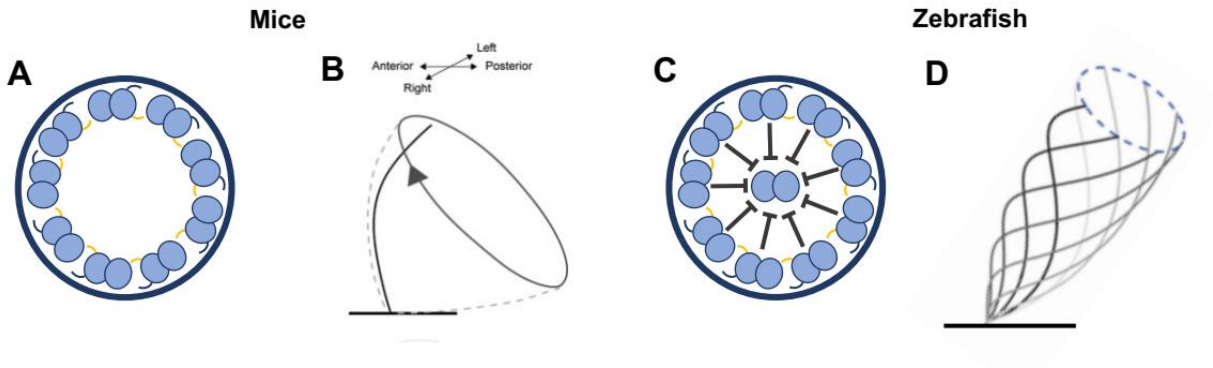

Figure 1 – Cilia in Left-Right axis establishment

(A) Motile cilium 9+0 typically found in the mice LRO. It has 9 pairs of microtubule doublets, with inner (yellow) and outer (blue) dynein arms. (B) Rotational movement of a 9+0 cilium. Scheme from (Huang et al., 2009). (C) Motile cilium 9+2 typically found in the zebrafish LRO. It has 9 pairs of microtubule doublets plus a central pair, with inner (yellow) and outer (blue) dynein arms and radial spokes (black). (D) Typical movement of a 9+2 cilium. Scheme from Pintado et al. (2017)

(Ezratty et al., 2011; Leitch et al., 2014) and others further reviewed in Pala et al., (2017). The ultrastructure of a primary cilium is typically 9+0, which means that it has only 9 doublets of microtubules and lacks motility components. Conventional motile cilia on the other hand have a 9+2 organization, presenting an extra central pair of microtubules connected to the 9 outer doublets by radial spokes (Figure 1C). They also present dynein motors arranged in outer and inner arms that allow for movement (as reviewed in Choksi et al., 2014). This kind of cilia generally beat in a wavelike or corkscrew fashion to generate fluid movement or to allow cells to move through fluid (Kramer-Zucker et al., 2005a) (Figure 1D). These 9+2 motile cilia are what is typically observed in the LRO of zebrafish and Xenopus. The mouse LRO presents motile cilia with a 9+0 configuration, with dynein arms but without central pair (Hirokawa et al., 2006; Nonaka et al., 1998; Takeda et al., 1999) (Figure 1A). Odate et al. (2016) observed very few 9+2 cilia in the mouse LRO, these being randomly distributed (Odate et al., 2016). The absence of central pair and radial spokes makes the cilia ultrastructurally more fragile than 9+2 cilia, but allows stable unidirectional rotation of node cilia (Shinohara et al., 2015) (Figure 1B). In the mouse model, the direction of the flow is

determined by two features: posterior tilt and clockwise rotation. Due to these two features, mice cilia can generate a leftward effective stroke and a rightward recovery stroke on the cell surface (Cartwright et al., 2004; Nonaka et al., 2005; Okada et al., 2005). Cilia tilt is given by the basal body position in the cell. The basal body is initially positioned centrally but then gradually shifts toward the posterior side of the node cells. Positioning of the basal body and unidirectional flow were found to be impaired in mice lacking Dishevelled (Hashimoto et al., 2010), Prickle (Antic et al., 2010) or Vangl (Antic et al., 2010; Song et al., 2010). All these are components of the noncanonical Wnt signalling planar cell polarity (PCP) pathway. While Dishevelled protein is localized to the posterior side of the apical membrane of mice LRO cells (Hashimoto et al., 2010), Vangl and Prickle localized to the anterior side (Antic et al., 2010). Vangl is also critical for LR determination in zebrafish and Xenopus (Antic et al., 2010; Borovina et al., 2010). Also at play are opposing gradients of Wnt5a/b posteriorly and secreted Frizzled-related proteins (Sfrp) inhibitors anteriorly that help polarize node cells along the anterior-posterior axis (Minegishi et al., 2017).

The transcription factor Forkhead box J1 (Foxj1) is important to regulate the motile ciliogenesis. Loss of Foxj1 in mice disrupts 9+2 motile cilia, leading to defective ciliogenesis in airway epithelial cells and Left-Right axis establishment defects due to abnormal centriole migration and/or apical membrane docking (Brody et al., 2000). Foxj1 is also important to make motile monocila, including the 9+0 subtype found in the mice LRO (Alten et al., 2012; Chen et al., 1998). Knockdown of Foxj1 in both Xenopus and zebrafish can cause loss of all motile cilia (Stubbs et al., 2008; Yu et al., 2008) revealing that Foxj1a has a larger role than motility per se. Foxj1 is considered a master regulator of motile cilia since it is responsible for the regulation of a cohort of ciliary genes required for different structural and functional aspects of motile cilia, such as the ones used to make, assemble, transport and dock the inner and outer dynein arms, radial spokes and central pair (Didon et al., 2013; Jacquet et

al., 2009; Newton et al., 2012; Stubbs et al., 2008; Yu et al., 2008). In zebrafish, fibroblast growth factor (FGF) signalling induces *foxj1* expression in LRO (Neugebauer et al., 2009) and Wnt signalling seems to act downstream of FGF to directly control *foxj1* expression through TCF/LEF transcription factor-binding sites within the *foxj1* promoter (Caron et al., 2012). This relationship between Wnt signalling and *foxj1* expression is conserved in Xenopus GRP (Walentek et al., 2012). Notch signalling has also been linked to motile cilia through length and motility control. In zebrafish LRO, Notch signalling is required for proper *foxj1* expression, *deltaD* homozygous mutants showed significantly shorter cilia and abnormal motile/immotile ratio, making more motile cilia at the expense of the immotile. Overactivation of Notch signalling through Notch Intracellular Domain (NICD) lead to longer and more immotile cilia in the zebrafish LRO (Lopes et al., 2010; Tavares et al., 2017). In terms of length, two other studies reported opposing results. While, overactivation of Notch signalling led to shorter cilia in CL4 cells (Jurisch-Yaksi et al., 2013), it led to neural tube longer primary cilia *in vitro* and *in vivo.* In terms of motility, data from Xenopus LRO had suggested a similar role for Notch signalling, through Galnt11 and NICD manipulation, regarding motile/immotile cilia ratio (Boskovski et al., 2013). Although decreasing cilia length has a high impact on left-right axis establishment, increasing length seems to cause milder left-right defects in zebrafish. *Arl13b* overexpression, which increases cilium length without affecting cilia beat frequency, results in reduced beat amplitude and similar flow strengths as control embryos (Pintado et al., 2017).

1.2 WHAT WE NEED TO KNOW ABOUT NODAL SIGNALING (for this study)

LR axis establishment requires TGF-β family ligands to function at many different levels: from LRO establishment, to interpretation of symmetry breaking fluid flow, to transducing and propagating this asymmetric information into the presumptive tissues that will give rise to

organ positioning, the lateral plate mesoderm and the endoderm. The main players so far studied in LR development of mouse, xenopus and fish are Nodal/Southspaw (Spaw) and its auto-induction capabilities (Long et al., 2003; Ohi and Wright, 2007; Oki et al., 2007; Osada et al., 2000; Saijoh et al., 2000; Wang and Yost, 2008), the inhibitors Cerberus/Dan and Lefty (Branford et al., 2000; Hashimoto et al., 2004; Katsu et al., 2012; Marques et al., 2004; Meno et al., 1996; Schweickert et al., 2010; Vonica and Brivanlou, 2007; Wang and Yost, 2008; Yokouchi et al., 1999) and the transcription factor Pitx2 (St. Amand et al., 1998; Campione et al., 1999; Essner et al., 2000; Logan et al., 1998; Piedra et al., 1998; Yoshioka et al., 1998).

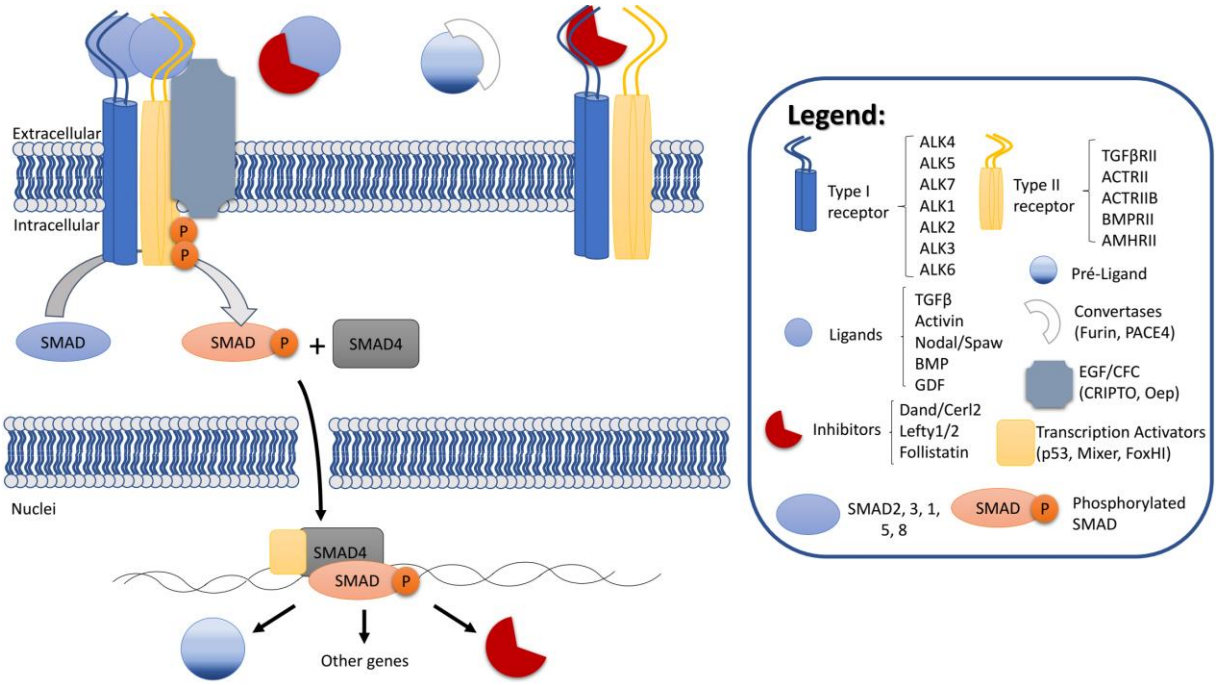

Figure 2 – TGF-β signalling pathway overview

There are many ligands in TGF-β signalling. Focusing on Nodal protein, it has to be processed in the extracellular space by Convertases to become fully mature. Mature Nodal binds to Type I and Type II receptors and the co-receptor from the EGF/CFC family. When activated, the receptors phosphorylate SMAD, which can bind to SMAD4. This complex can enter the nucleus and activate transcription by binding to transcription factors like FoxHI. The ligand Nodal and its repressor Lefty are both expressed in response to Nodal signalling. The interaction of Nodal with inhibitors like Lefty or Cerl2 in the outside of the cells affects its ability to bind to the receptors and activate the pathway. Scheme adapted from Schmierer and Hill, (2007).

Nodals are synthesized as proproteins that are proteolytically processed extracellularly by conversates (subtilisin-like proprotein 1 and 4, also known as Furin and Pace4) (Beck et al., 2002; Le Good et al., 2005). Several experiments led to the understanding that Nodal acts via activin receptors, Smad transcription factors and associated transcription factors such as FoxH1 (as reviewed in Shen and Schier, 2000; Whitman, 2001). Nodal/Spaw bind to a receptor complex composed of type I and type II receptors that can function as serine/threonine kinases (Attisano and Wrana, 2002; Shi and Massague, 2003). Ligand/receptor assembly results in phosphorylation and activation of type I receptor through the type II receptor, which in turn starts the phosphorylation of a downstream Smad cascade. Nodal signalling acts by regulating the phosphorylation of Smad2 (Kumar et al., 2001; Lee et al., 2001; Yeo and Whitman, 2001), which forms a complex with Smad4 and enter the nucleus. Then, it binds to transcription factors like FoxH1 (previously known as Fast2) and activates transcription of *lefty1/2*, *nodal* itself and *pitx2*, as well as other genes (reviewed in Whitman, 2001). Multiple receptors/ligands can diversify the output of Nodal signalling. Members of the epidermal growth factor (EGF-CFC) family are extracellular and GPI-linked proteins that include zebrafish one-eyed pinhead (Oep), frog FRL-1, chick CFC and mouse/human Cripto/Cryptic (reviewed in Shen and Schier, 2000). These are important components of the Nodal signalling pathway by acting as coreceptors for Nodal ligands. Its absence leads to defects in germ layer formation, organizer development and positioning of the anterior-posterior axis (Gritsman et al., 1999). Lefty action is also EGF-CFC-dependent, by interacting with EGF-CFC proteins and competing with Nodal for binding to these coreceptors (Cheng et al., 2004). In the LR context, EGF-CFC is expressed at both right and left Lateral Plate Mesoderm (LPM), where it is thought to interact with Nodal and induce Nodal signalling, and at the notochord, where it physically binds to Lefty1 to antagonize Nodal signalling (Shen et al., 1997; Yan et al., 1999). LR nodal antagonists Lefty proteins are secreted and can compete with Nodals by binding to common receptors and by

physically binding to Nodal (Chen and Schier, 2002; Cheng et al., 2004). Nodal signalling induces the expression of both *nodal* and of its antagonists (Hamada et al., 2002). In zebrafish, *lefty1* is expressed first in the posterior notochord, prior to asymmetric gene expression, where it might be inhibiting Nodal signalling from happening before the asymmetric cues from the LRO. An *oep*-dependent signalling event in the midline weakens the midline *lefty1*, alleviating the repression and allowing for the asymmetric left cue from the LRO to start Nodal signalling in the left LPM (Burdine and Grimes, 2016). Another important inhibitor is Dand5, a member of the differential screening-selected gene in neuroblastoma (DAN) family of predicted secreted proteins, that exhibits a finger-wrist-finger architecture with the cystine-knot motif, which makes the overall architecture similar to other cystine-knot containing proteins including BMP and Noggin (further reviewed in Nolan and Thompson, 2014). Cerberus2 in mouse, Coco in xenopus and Charon in zebrafish were all renamed as Dand5 and are potent secreted inhibitors of Nodals, impacting on mesendoderm patterning and left-right establishment (Bell et al., 2003; Belo et al., 2000; Hashimoto et al., 2004; Pearce et al., 1999; Piccolo et al., 1999). Most of TGF-β signalling interactions are illustrated in Figure 2.

Since Nodal act as a morphogen, it is important to understand how gradients are formed. Alan Turing, in his paper entitled “The Chemical Basis of Morphogenesis” in 1952 predicted a chemical mechanism for biological gradient pattern formation (Turing, 1952). He suggested a reaction-diffusion system where chemicals react to each other and diffuse across the space. This concept was redefined by Lewis Wolpert in his “French Flag Model” (Wolpert, 1969), where morphogens affect a field of cells in a concentration-dependent fashion – more morphogen activate certain genes while less morphogen activates other genes. Only decades later, it was formally demonstrated by Christiane Nüsslein-Volhard in Drosophila, with the identification of *bicoid* as a morphogen (Berleth et al., 1988). There are many models

for morphogen gradient formation based in complex mathematical equations, it can be put in simplified terms (thoroughly reviewed in Müller et al., 2013). It is possible to describe five major models: free diffusion, tortuosity and binding-mediated hindered diffusion, facilitated diffusion, transcytosis and directed transport via filopodial extensions known as cytonemes (Figure 3). Free diffusion is the simplest case, where molecules move freely from the source to the target tissue. However, this would not produce a gradient since this would result in uniform distribution of morphogen in the target tissue. Gradient formation happens when either the morphogen is degraded or is permanently trapped by a cell, producing a graded distribution of morphogens on the target tissue. Hindered diffusion assumes that the target tissue is densely packed with cells, which can cause hindrance by making the morphogens going around them (tortuosity-mediated hindrance), and/or by transiently binding morphogens through receptors or extracellular matrix components (binding-mediated

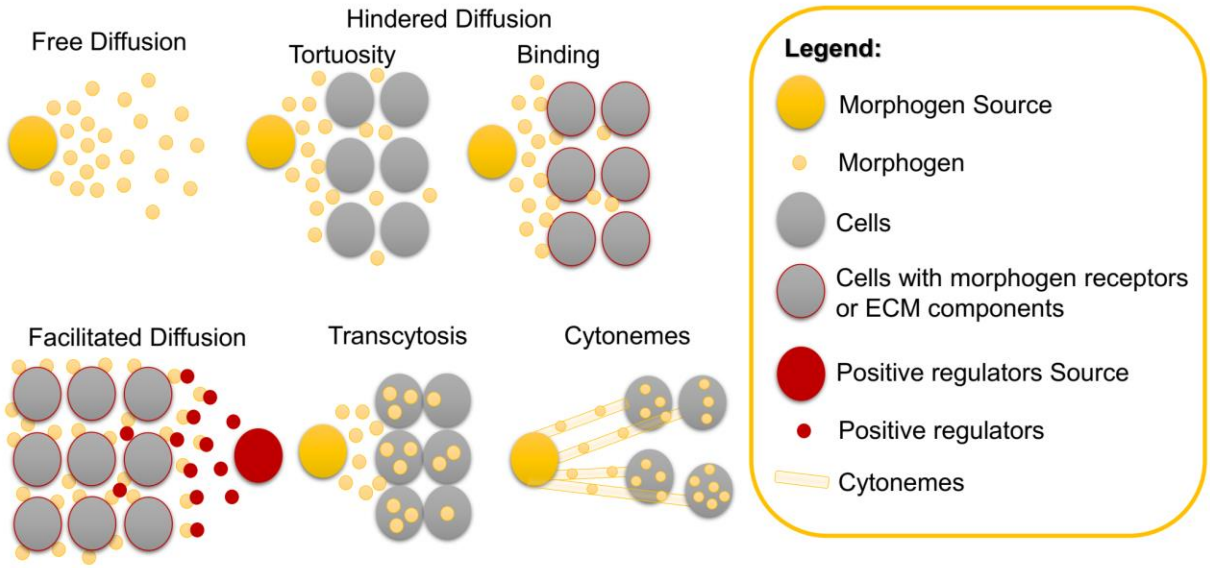

Figure 3 - Theories of Morphogen Transport

There are 5 major models to explain gradient formation of a morphogen: free diffusion, hindered diffusion by tortuosity or binding, facilitated diffusion, transcytosis and cytonemes. Scheme adapted from Müller et al. (2013).

hindrance). This would allow a faster gradient formation. Facilitated diffusion and shuttling assumes that a morphogen is largely immobile until a “positive” diffusion regulator comes and release the hindrance exerted by the “negative” diffusion regulators. In this scenario, morphogens and “negative” diffusion regulators are uniformly distributed while the “positive” diffusion regulators have a localized source and help to generate the morphogen gradient. These diffusion-based models have four potential weaknesses: length of patterning fields, solubility of morphogens, reliability of patterning and geometry of patterning fields. Because of that, two additional models were proposed. Transcytosis, where morphogens bind to cell surface and are endocytosed, only to be exocytosed again and endocytosed by other cells. This process leads to a slow shaped gradient over time. The final model is through cytonemes, where long dynamic filopodia-like structures project from target cells and contact morphogen-producing cells. Therefore, morphogens are ‘handed over’ to and transporter along cytonemes, forming a concentration gradient (reviewed by Müller et al., 2013).

Nodal and Lefty have signal peptide sequences required for secretion (Beck et al., 2002; Blanchet et al., 2008; Le Good et al., 2005; Jing et al., 2006; Marjoram and Wright, 2011; Meno et al., 1996; Müller et al., 2012; Sakuma et al., 2002; Tian et al., 2008; Zhou et al., 1993) and experiments with fused GFP support an extracellular localization (Müller et al., 2012). This supports the idea that these two proteins move through tortuosity-mediated diffusion, where cells increase the path length of molecules diffusion in the extracellular space. Therefore, global effective diffusion coefficient of molecules moving through a tissue should be lower than the local diffusivity. Lefty and Nodal have similar local diffusivity (which could explain by having similar molecular weight) (Müller et al., 2013). However, while Lefty showed a local diffusivity double of its effective diffusivity, Nodal had a local diffusivity 90% higher than its effective diffusivity. This suggests that Lefty is mostly hindered by cell packing, while Nodal is hindered by cell packing and extracellular diffusion regulators (Müller et al.,

2013), explaining why Lefty is long range while Nodal is short range (Chen and Schier, 2002; further reviewed in Schier, 2003). Diffusional movement can be altered by transient binding to other molecules such as receptors or components of the extracellular matrix (Baeg et al., 2004; Belenkaya et al., 2004; Wang and Yost, 2008). Also, different affinities for receptors might account for different ranges of distribution (Müller et al., 2012). Another mechanism might be rapid clearance of molecules during diffusion (Kicheva et al., 2007). All data seems to indicate that Nodal gradient is dependent of diffusion, binding and degradation of the morphogen (Wang et al., 2016).

1.3 LEFT-RIGHT AXIS ESTABLISHMENT

1.3.1 MICE

Left-Right Hypothesis

Immotile cilia syndromes in Humans, such as Kartagener syndrome, are typically accompanied with LR axis abnormalities of organ *situs* which were thought to be associated with ciliary dysfunction (Afzelius, 1976; Kosaki and Casey, 1998). Finding asymmetric gene expression like *lefty* (Meno et al., 1996) and *nodal* (Collignon et al., 1996; Lowe et al., 1996) and motile cilia (Nonaka et al., 1998) in the embryonic node linked both fluid flow dynamics and gene expression. Two mice models were extremely important for the progress of LR studies: *situs inversus viscerum (iv)* and *inversion of embryonic turning (inv).* While the first was a mouse with a spontaneous mutation in the axonemal dynein heavy-chain 11 gene (also known as left/right-dynein) that led to random organ *situs* (Hummel and Chapman, 1959; Supp et al., 1997), the second was an insertion mutation that affected *inversin* gene and always resulted in *situs inversus* (Mochizuki et al., 2002; Morgan et al., 2002; Yokoyama et al., 1993). These mutants presented problems in *nodal* expression around the node and in

the Lateral Plate Mesoderm (LPM), becoming bilateral or reversed (Lowe et al., 1996). Both *iv* and *inv* mutants had flow abnormalities, but while *iv* had all cilia immotile and no flow, *inv* mutant had motile cilia that produced a very weak and disorganized leftward flow. Besides, *inv* mutants had a misshaped node (Okada et al., 1999) which confirmed the shape of node was also important for proper flow. A third mutant, a KIF3B knockout mice, was done around the same time and also showed LR randomization problems. Disruption of KIF3B, a microtubule-dependent motor, was shown to be important for cilia assembly and maintenance. Without it, the node lacked cilia and therefore showed randomization of organ position and randomization of *lefty2*, a nodal antagonist (Nonaka et al., 1998). Mutations in KIF3A, that heterotrimers with KIF3B (Kondo et al., 1994; Yamazaki et al., 1995), showed similar phenotypes (Takeda et al., 1999). In fact, Nonaka et al. (1998) proposed the first morphogen model for LR axis establishment, where a secreted factor X would be transported by the fluid flow. Moreover, this model can explain why cultured embryos frequently reverse their body *situs*. A mature node comprises approximately 250 cells, with 50-60um wide and 70-90um long, and up to 50um deep (Sulik et al., 1994; Bellomo et al., 1996; Yamanaka et al., 2007). It is a concave, tear-drop-shaped epithelial field of cells located distally on the ventral surface of the embryo, covered by the Reichert's membrane (Figure 4A). The removal of this membrane during the culture procedure exposes the node to the outer environment, increasing the external turbulence and allowing diffusion of the factor X.

Further confirmation that motile cilia were crucial in LR came from targeted deletion of the ATP binding domain of *lrd*, which also resulted in randomization of laterality due to immotility of node cilia (Supp et al., 1999). All this body of information indicates that flow occupies an upstream position in this process, elegantly backed up by the manipulative flow experiments done by Nonaka et al. (2002). This work showed that artificially provided strong or weak leftward flow did not affect *pitx2* or heart looping, while strong (but not weak) rightward flow

could reverse organ *situs* in cultures of WT mice submitted to a fluid peristaltic chamber. The same experiments were repeated with *iv* mutant embryos, that lack fluid flow due to immotile cilia. When iv mutant embryos were submitted to strong or weak leftward flow, they showed left sided *pitx2* and normal heart looping, while strong or weak rightward flow induced reversal LR *situs* (Nonaka et al., 2002).

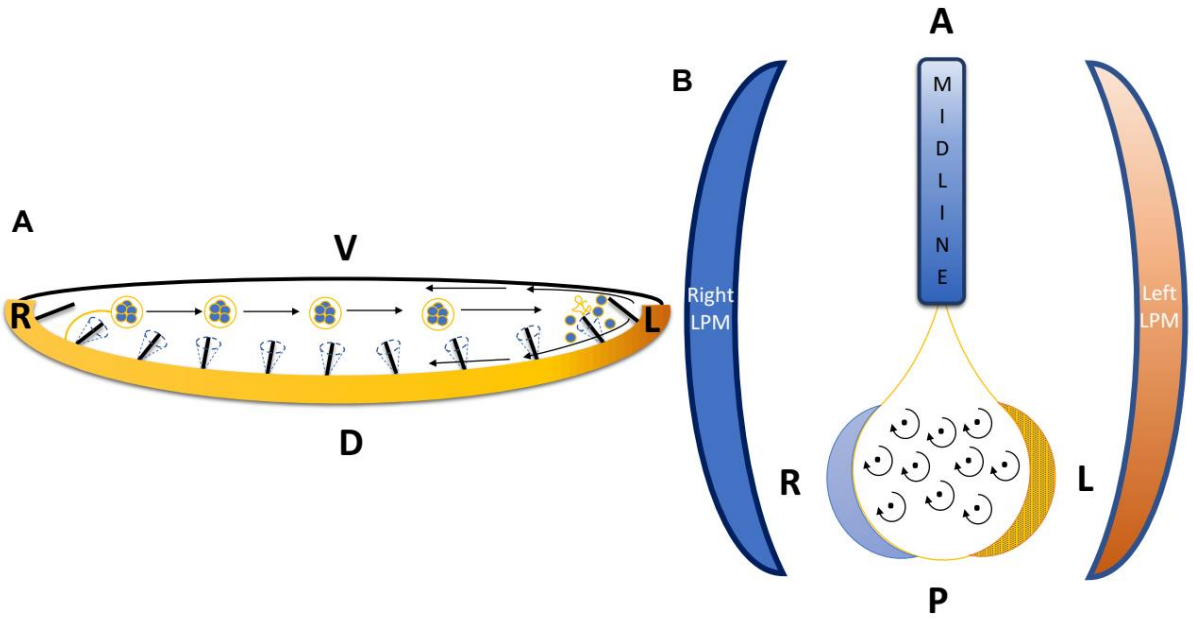

Figure 4 – Left-Right axis establishment in Mice

(A) Schematic of a mice LRO, with immotile cilia in the periphery and motile cilia in the pit. The flow generated has two main directions: from right to left in the middle plane and from left to right ventrally, near the Reichert's membrane and dorsally on the LRO cell surface. NVPs are depicted in yellow spheres with blue content, that are released on the right side by microvilli (in yellow) and break on the left side, releasing there the content and leading to an intracellular calcium rise (orange end). Scheme adapted from Tanaka et al. (2005). (B) Schematics of Nodal signalling pathway in LR. The node has a tear-drop shape with motile cilia (black dots). Nodal is expressed on the left side of the LRO (yellow crescent moon) where is also observed an intracellular calcium rise (black dots on the yellow crescent moon). The antagonist *cerl2* is expressed on the right side (light blue crescent moon). Another antagonist, *lefty* is expressed in the midline. Since there is stronger Nodal signalling on the left side versus the right side, Nodal protein can travel to the left Lateral Plate Mesoderm (LPM) and start Nodal signalling there (big crescent moon in orange). Blue contours around the LPM and midline means EGF/CFC expression. A – Anterior, P – Posterior, D – Dorsal, V – Ventral, L – Left, R - Right

A few years later, work from Tanaka et al., 2005 shed some light on the identity of the potential morphogens working on LR axis establishment: FGF-dependent release of small membrane-bound vesicles called nodal vesicular parcels (NVPs) carrying Sonic Hedgehog and Retinoic Acid. Node cells and cilia expressed receptors for Fibroblast Growth Factors (FGFR) and when FGF signalling was antagonized, the typical intracellular calcium elevation was suppressed. Giving SHH or RA to mice embryos in culture could restore Ca^{2+} elevation on the left margin of the node. Confocal microscopy time-lapse showed that these NVPs labelled with lipophilic fluorescent dye DiI were released every 5-15 seconds from the protruding microvilli on floor of the node and were transported towards the left side of the node where they were fragmented by the ciliated surface into several smaller particles. Scanning and transmission electron microscopy detected several NVPs in the cell surface and, when FGF signalling was inhibited, showed an accumulation of unsheathed particles, potentially reflecting a failure in launching. Live imaging showed that in immotile cilia mutants, NVPs were still released but were slowly being carried in every direction by Brownian motion. In cilia-free mutants, NVPs still formed but took longer to break, which suggested that cilia are important for breaking these vesicles (Tanaka et al., 2005). All this data together gave a new look into the morphogen hypothesis first laid down by Nonaka et al. (1998). The reformed morphogen hypothesis claimed that NVPs (instead of free morphogens) would be transported by the flow towards the left side of the node, delivering SHH and RA and inducing the calcium wave, culminating with differential *nodal* expression on the cells lining the node (Figure 4A). Nevertheless, these experiments were never confirmed by other labs and the role of SHH and RA is controversial in LR because these molecules have other functions in important organs such as the midline (Tsukui et al., 1999).

Concomitantly with this body of work, other evidence started to appear. The knockout of Polycystin 2 (Pkd2), a calcium channel that when mutated causes autosomal dominant

polycystic kidney disease, led to randomization of organ *situs* and defects in asymmetric gene expression like loss of expression of *lefty2* and *nodal* on the lateral plate mesoderm and symmetric expression of *pitx2* (Pennekamp et al., 2002). This calcium channel is known to partner with a sensing molecule called polycystin 1 (Pkd1) and together sense the urine flow in the primary cilia of kidney epithelium and respond with a calcium intake. Lack of any of the polycystins makes cells unable to respond mechanically to flow (Nauli et al., 2003, 2006). In the node, all cilia express Pkd2 and can be divided in two categories: motile and expressing Dnah9, centrally localized in the pit region, and immotile, peripherally localized in the crown cells (McGrath et al., 2003). Besides, a wave of calcium signalling was observed at the left margin of the node, coinciding with directional flow. In the absence of Pkd2, this calcium wave was not observed (McGrath et al., 2003). Moreover, it was shown that specific localization of Pkd2 in the cilium of perinodal crown cells was important for correct LR axis establishment. Only when using Pkd2 constructs that were able to localize in the crown cells cilia of $Pkd2^{-/-}$ embryos, these were able to rescue LR (Yoshiba et al., 2012). Importantly, Pkd2 mutants still show normal leftward flow and normal beating cilia in mice (Yoshiba et al., 2012). By using a flow responsive enhancer ANE (Kawasumi et al., 2011), Yoshiba et al. (2012) showed that, in normal flow conditions ANE gave more expression on the left side while with artificially reversed flow ANE gave more expression on the right side. In Pkd2 mutant embryos, ANE activity was equal on both sides, which would suggest that the lack of Pkd2 in the crown cells makes embryos fail to sense the flow. Calcium signalling was still detected in crown cells of Pkd2 mutants, but it was present bilaterally and not asymmetric to the left as in WT (which is in contrast to the absence of signal found by McGrath et al., 2003). Restoration of Pkd2-positive primary cilia on crown cells of Kif3a mutant embryos that lack beating cilia conferred capacity to respond to artificial flow, reinforcing that immotile cilia in the crown cells were indeed fundamental to elicit a flow response (Yoshiba et al., 2012). All together these data strengthened the mechanosensation hypothesis first laid down by

McGrath et al. (2003), where one population of cilia would create the flow and the immotile population would have the ability to sense the flow and respond accordingly.

Nodal – the left-side determinant

It was shown by Collignon et al. (1996) and Lowe et al. (1996) that in mice *nodal* has two asymmetric (stronger on the left) expression domains: one around the node and another in the lateral plate mesoderm (LPM). They also showed that these expressions were strongly affected in the *inv/inv* and *iv/iv* mutants and these correlated with heart looping and embryonic turning defects (Collignon et al., 1996; Lowe et al., 1996). The nodal expression around the node at early head-fold stage (embryonic day 7.0) is first symmetric between left and right, only becoming asymmetric (strong on the left) between late head-fold stage and early somitogenesis (embryonic day 7.5-8.0) (Collignon et al., 1996; Lowe et al., 1996). Another asymmetric gene observed around the node was the nodal antagonist *cerl2* (Marques et al., 2004). Similar to *nodal*, expression of *cerl2* is initially symmetric at early headfold stage but, in contrast to nodal, becomes strongly expressed on the right side at late headfold stage, earlier than the observed asymmetry for *nodal* (Marques et al., 2004). Experiments with Xenopus and mouse *nodal* and *cerl2* mRNA injections suggested that Cerl2 might antagonize Nodal in the extracellular space by physical interaction (Marques et al., 2004). *cerl2* knockout leads to 50% bilateral nodal expression in the LPM and 10% asymmetric expression of the right LPM. It also affects *lefty2* expression, while *lefty1* in the midline remains normal. In terms of organs, 54% of *cerl2*$^{-/-}$ mutant embryos show leftward or ventral loop instead of the WT rightward heart loop. Embryos also showed left isomerism of the lungs or *situs inversus* (Marques et al., 2004). In the absence of Pkd2, *cerl2* never becomes asymmetric and *nodal* expression in LPM is absent (Yoshiba et al., 2012). In the double mutant Pkd2$^{-/-}$;Cerl2$^{-/-}$, *nodal* loses its direct repressor and becomes randomized, just like in the Cerl2$^{-/-}$ mutant alone, making Cerl2 the major target of Pkd2 (Yoshiba et al., 2012).

This *cerl2* mRNA asymmetry was found to occur post-transcriptionally and via its 3'UTR. Careful analysis of the subcellular localization of *cerl2* mRNA revealed a preference for the apical side of the crown cells on the right side of the node that was dependent on the integrity of the 3'UTR. In sum, it was suggested that asymmetric fluid flow induces the degradation of *cerl2* mRNA in the apical side of the crown cells through the 3'UTR, a degradation that then is further enhanced through a feedback loop involving Wnt3, that in turn becomes strongly expressed on the left. The stronger the *wnt3* expression, more *cerl2* becomes degraded on the left side (Kitajima et al., 2013; Nakamura et al., 2012). The fact that *cerl2* becomes symmetric in the absence of Pkd2 puts *cerl2* degradation downstream of calcium signaling (Nakamura et al., 2012; Yoshiba et al., 2012). Furthermore, Cerl2 mRNA 3'UTR is rich for AU-rich elements which confer instability to mRNA (Schoenberg and Maquat, 2012). Interestingly, Cerl2 protein starts by localizing and prevent Nodal activation on the right side, but from 3 somite stage onwards seems to translocate from right to left in a flow-dependent manner and help to shut down Nodal activity on the left side of the node, in a time where *cerl2* mRNA is no longer observed on the left (Inácio et al., 2013). In sum, this fine balance between *nodal* and *cerl2* at the node seems to influence Cerl2 protein dynamics by the presence of flow and greatly impacts on peri-nodal phosphorylated Smad (Nodal signalling activity readout) which is markedly stronger on the left side (Kawasumi et al., 2011; Nakamura et al., 2012) and at the LPM (Oki et al., 2009). Many of the Nodal signalling pathway elements in LR are illustrated in Figure 4B.

Other players help fine-tune this process. One is GDF1, which is required as a binding partner of Nodal and is necessary for Nodal full activity (Tanaka et al., 2007). It is expressed in crown cells and LPM (Rankin et al., 2000). Also, the enhancer regulating node-specific Nodal expression (NDE), which is indispensable for peri-node expression, showed the presence of binding sites for RBP-J protein, the primary transcriptional mediator for Notch

signalling. Without this sites, the enhancer loosed the ability to regulate *nodal* expression in the node (Krebs et al., 2003; Raya et al., 2003). *Tbx6*, a T-box transcription factor, is upstream of Delta-like 1 (Dll1) and is important for Nodal signalling in the node. Tbx6 mutant show shorter and thicker cilia in the node, with erratic motion and higher proportion of immotile cilia in the pit region compared with WT embryos, which impacted on intracellular calcium at the node periphery (Hadjantonakis et al., 2008). Finally, Wnt3a expressed in the primitive streak and dorsal posterior node can act as a long-range signalling molecule and directly activate Notch signalling pathway to regulate the left perinodal expression of *nodal* (Nakaya et al., 2005). Important to restrict Nodal expression only on the left LPM is the presence of the embryonic midline – notochord and/or floorplate of the neural tube (Danos and Yost, 1996). Expression of *lefty1* in the midline has been shown to be important to prevent the passage of Nodal to the right side and this *lefty1* expression is induced by Nodal itself (Meno et al., 1998; Yamamoto et al., 2003).

Since Nodal can induce its own transcription and the transcription of its antagonists, it has the necessary features to constitute a SELI (Self-Enhanced and Lateral-Inhibition) system (Nakamura et al., 2006; Saijoh et al., 1999, 2000; Yashiro et al., 2000). According to this system, nodal flow generates an initial small difference in signal strength between left and right peri-nodal cells. Although the signal is transmitted to left and right LPM, the fact that the signal is stronger on the left leads to an asymmetric induction of the initial burst of nodal transcription on the left vs the right LPM. Concomitantly, Nodal induces *lefty1* and *lefty2* in the midline and LPM. Mathematical modelling shows that this set of starting conditions can resolve itself in a robust amplification into the stable pattern of left LPM nodal expression observed *in vivo* (Nakamura et al., 2006). This model can provide explanations for the LR phenotypes of various mouse mutants and is very consistent with the observed dynamics of *nodal* and *lefty* mRNA expression dynamics. It has been suggested that the initial signal

strength might be the perinode Nodal activity and this is consistent with the fact that perinode expression is necessary for the expression of nodal LPM expression (although the establishment of a left asymmetry is not) (Brennan et al., 2002; Saijoh et al., 2003). This would indicate that Nodal protein produced at the node can travel to the left LPM, perhaps through the interaction with sulphated glycosaminoglycans that are specifically localized to the basement membrane-like structure between the node and LPM and therefore starting nodal expression on the LPM (crypto, nodal co-receptor, is only expressed on the LPM) (Kawasumi et al., 2011; Oki et al., 2007). Another possibility is that it could be travelling through gap junctions on the endoderm cells that are just opposed to the node (Saund et al., 2012; Viotti et al., 2012). Either way, when Nodal reaches the LPM it can activate its own expression via a Nodal-responsive transcriptional enhancer (ASE) (Saijoh et al., 2000). However, another more recent report stated that Man1, an inner nuclear membrane protein that regulates TGF-β, is sufficient to induce Nodal in the LPM even in the absence of peri-node Nodal (Ishimura et al., 2008). So, there might still be another molecule around the node, symmetric or not, that influences the travelling of nodal to the LPM.

1.3.2 ZEBRAFISH

Left-Right establishment

Left-right in zebrafish starts in a vesicular organ called Kupffer's Vesicle (KV). The KV derives from the dorsal "forerunner" cells (DFCs). Cooper and D'Amico (1996) used BODIPY and live confocal microscopy time-lapses to visualize how deep cells within the non-involuting endocytic marginal cell cluster rearrange and move to the distal edge of the blastoderm between 50 and 60% epiboly. Here they contribute to the formation of the dorsal "forerunner" cells (DFCs) and between 60 and 80% epiboly they coalesce into a cell cluster that will later give rise to the KV (Cooper and D'Amico, 1996). Another study by Oteíza et al. (2008) used 2-Photon microscopy and the transgenic line Tg(β-actin:HRAS-EGFP)

expressing a membrane marker and observed a subset of marginal and submarginal dorsal surface epithelial cells internalize beneath the surface epithelium in a Nodal signaling-dependent way at the dorsal germ ring margin prior to gastrulation. They then migrate ahead of the shield region attached to the overlying surface epithelium and rearrange into rosette-like epithelial structures at the end of gastrulation (Oteíza et al., 2008). Oteíza et al. (2008) claimed that the differences observed between this work and Cooper and D'Amico (1996) work could be due to different labeling and imaging methods to identify DFCs. Despite this, DFCs migration is dependent on endogenous calcium release that inactivates β-catenin nuclear translocation through naked cuticle (Nkd) binding to Disheveled. Affecting this initial calcium release or knocking down Nkd resulted in nuclear localization of β-catenin, disrupting DFCs migration and impairing the KV formation (Lin and Xu, 2009; Schneider et al., 2008, 2010). In addition, it was demonstrated that suppression of the sarco/endoplasmic reticulum calcium ATPase with thapsigargin elevates cytosolic Ca^{2+} and impairs KV formation (Kreiling et al., 2008). At early somitogenesis, the epithelial rosettes coalesce into a single rosette, open a lumen and each cell starts to generate a cilium on its apical surface (Kramer-Zucker et al., 2005a; Oteíza et al., 2008). DFCs express motility genes like left-right dynein and videomicroscopy confirmed that most cilia are motile and are capable of creating a directional fluid flow prior to asymmetric gene expression (Essner et al., 2005). *spadetail* and *notail* are both required for formation of a functional KV (Bisgrove et al., 2005; Essner et al., 2005). As development proceeds, this first radially symmetric structure starts to get asymmetric along the AP axis, with more ciliated cells packed into the anterior region creating a dorsal anterior cluster of cilia (Wang et al., 2012). This coordinated cell movement is dependent on Rho kinase gene rock2b and non-muscle myosin II (Wang et al., 2012) and it is important for the generation of the anterior dorsal cluster of motile cilia that generates stronger leftward flow on the anterior side and weaker rightward flow on the posterior side (Wang et al., 2011, 2012), also confirmed by the flow studies that followed by Sampaio et al., (2014). Affecting

Rock2b or Myosin II affected this AP position of cells without affecting the number or length of cilia. This was enough to homogenize the anterior and posterior flow velocities and to lose directionality (Wang et al., 2011, 2012). One factor that contributes to these cell reshaping is the increase in KV volume that occurs during normal development of the LRO, through a process involving CFTR (Navis et al., 2013), later demonstrated to be involved in a crosstalk between Pkd2 (Roxo-Rosa et al., 2015). This anterior dorsal cluster was also reported to be induced and maintained by the extracellular matrix (ECM) accumulation that the notochord produces and assembles in the anterior-dorsal region. In fact, affecting the function of laminin-γ1 with a morpholino or using a truncated version of fibronectin abrogated the dorsal anterior cluster (Compagnon et al., 2014). This ECM accumulation restricts the apical expansion of cells in the anterior dorsal region so, as the lumen inflates, only cells in the posterior ventral side undergo apical expansion. These differences in apical expansion are accompanied by Rock2b-dependent actin cytoskeleton reshaping and lead to an accumulation of cilia in the anterior dorsal region, compared with the posterior ventral region (Compagnon et al., 2014; Wang et al., 2011).

Sampaio et al. (2014) showed that the flow speed pattern inside the KV has a biological relevance that correlates with organ *situs*. They showed that whenever the flow pattern changed from stronger on the anterior dorsal pole to other patterns the organ *situs* became abnormal. Then, through mathematical simulations, Sampaio et al. (2014) showed that a minimum number of 30 motile cilia was necessary for robust fluid flow and consistent correct organ *situs* (Sampaio et al., 2014). It is known that KV size and cilia number are variable among WT fish, but cilia length is not so variable (Gokey et al., 2015). Notch signaling seems to play a role for cilia length control in the KV (Lopes et al., 2010). While increased cilia length through Arl13b overexpression does not seem to strongly impact on flow pattern and intensity (Pintado et al., 2017), decreased cilia length through inactivating Notch signaling

(*dld*$^{-/-}$ mutant) slows down fluid flow velocity and compromises the asymmetric gene expression and organ *situs* (Lopes et al., 2010; Sampaio et al., 2014). The shorter cilia phenotype found in *dld*$^{-/-}$ mutants could be rescued by overexpression of the transcription factor *foxj1a*, a motile ciliogenic factor (Lopes et al., 2010). Like in other models, Foxj1 is upstream of cilia formation and is expressed in DFCs, KV and other ciliated structures (Aamar and Dawid, 2008). Besides length, Notch signaling also impacts on motile/immotile cilia ratio (Sampaio et al., 2014; Tavares et al., 2017). Through a thorough electron microscopy protocol, Tavares et al., (2017) were able to show that all cilia present in the KV have the necessary ultrastructure to move. Despite that, there are 20% of immotile cilia that never beat in the KV of WT embryos. This was confirmed by time-lapse 2-Photon microscopy and by using a mild *arl13b-GFP* mRNA overexpression that allowed following individual cilia and tracking their behaviors during KV inflation. Again, less Notch signaling led to more motile cilia, while having more Notch signaling led to less motile cilia (Tavares et al., 2017). This feature is common to the *Xenopus* LRO, where motile/immotile cilia ratio was affected by Galnt11 - an enzyme needed for the proper cleavage of the Notch receptor. So, mediated Notch1 signaling modulates the spatial distribution and motile/immotile ratio: galnt11 or notch1 knockdown increases the motile cilia ratio while overexpression decreases it (Boskovski et al., 2013). In zebrafish, this motile/immotile ratio could not be rescued by *foxj1a* overexpression; in fact, it seemed to be regulated by the transcription factor Her12 (Tavares et al., 2017). An interesting observation was that more immotile cilia at the expense of motile slowed down fluid flow velocity and thereby affected organ *situs*, as it approached the 30 minimum motile cilia number modeled by Sampaio et al. (2014).

Another molecule that seems to regulate cilia length and motility comes from the heparan sulfate O-sulfotransferase (OST) family. 3-OST-5 seems to control Foxj1 to regulate cilia length, while 3-OST-6 regulates cilia motility through kinesin motor molecule (Kif3b)

expression and cilia arm dynein assembly (Neugebauer et al., 2013). Wnt signaling also affects ciliogenesis by regulating *foxj1a*, since Foxj1a promotor has binding sites for Lef1/Tcf that are indispensable for *foxj1a* expression in the KV (Caron et al., 2012). Indeed, overexpression of wnt8a in a single cell in a 128-cell stage embryo is sufficient to induce the formation of an ectopic protrusion with ectopic *foxj1a* expression and ectopic cilia-like structures (Zhu et al., 2015). Disruption of Lef1 or Tcf7 or both lead to downregulation of *foxj1a* in the DFCs and affect ciliogenesis in the KV, leading to shorter and fewer cilia (Zhu et al., 2015). Finally, cilia are positioned with a posterior tilt and Vangl2, a core component of PCP signaling pathway, is required for this (Borovina et al., 2010), similar to what has been shown in mice (Hashimoto et al., 2010; Song et al., 2010).

The global flow in the KV is circular having a counterclockwise direction (Figure 5A). This means that in the anterior part of the KV flow goes towards the left, while it moves towards the right in the posterior part. This is generated by the dorsal anterior cluster, but the local flow differs in direction dependent on the location within the KV (Okabe et al., 2008). “Useful” cilia are mainly present in the KV’s dorsal side and in the equatorial line with a dorsal tilt and these are important to give the leftward direction that breaks the symmetry, while the dorsal anterior cluster is important only to strengthen the flow in the anterior region vs the posterior (Montenegro-Johnson et al., 2016; Smith et al., 2014).

According to mathematical simulations, assuming the dorsal anterior cluster was eliminated, if the dorsal side still had more cilia than the ventral this would still generate a counterclockwise flow that would be homogeneous in strength in all KV (Figure 5A). This should still be enough to break symmetry if it was done by morphogens or vesicles carrying molecules, because the transport by the flow would still be available, but would not be heterogeneous enough to break symmetry by a mechanosensor system. To reverse the flow, one would need to have more cilia beating in the ventral side of the KV, since these generate

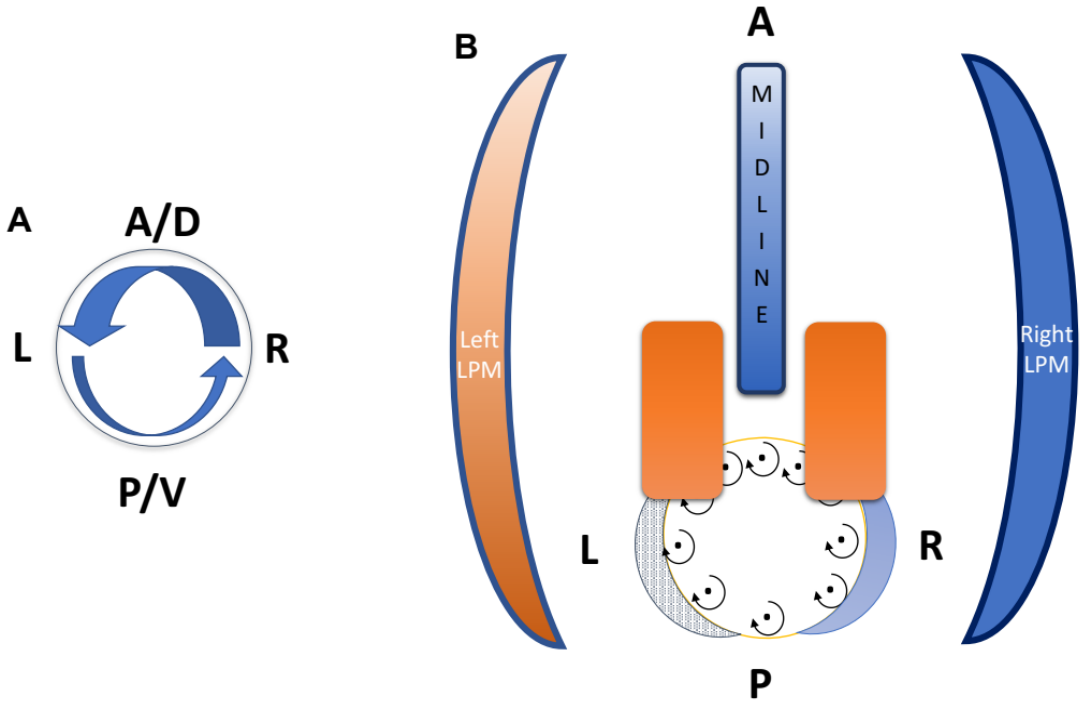

Figure 5 – Left-Right axis establishment in Zebrafish

(A) Schematic of a zebrafish LRO, with arrows depicting stronger leftward flow on the anterior dorsal region and weaker rightward flow on the posterior ventral region (B) Schematics of Nodal signalling pathway in LR. The Kupffer's Vesicle has a sphere-like shape, with motile cilia showing an anterior bias (black dots) and the immotile cilia evenly distributed. *spaw* is expressed on two domains dorsally localized in relation to the KV (orange rectangles). The antagonist *dand5* is expressed on the right side (light blue crescent moon), while on the right side of the LRO it is possible to observe a calcium wave (black dots in the left-sided crescent near the KV). Another antagonist, *lefty* is expressed in the midline. Since there is stronger Nodal signalling on the left side versus the right side, Nodal protein can travel to the left Lateral Plate Mesoderm (LPM) and start Nodal signalling there (big crescent moon in orange). Blue contours around the LPM and midline means EGF/CFC expression. A – Anterior, P – Posterior, D – Dorsal, V – Ventral, L – Left, R – Right.

an antagonistic flow (Montenegro-Johnson et al., 2016). This theoretically would produce similar results to the experiments of flow reversal in mice (Nonaka et al., 2002). All these predictions remain to be experimentally demonstrated. Another striking difference between zebrafish and mice is the fact that the locally generated flow seems to be extremely important for the zebrafish and not to the mouse. Accordingly, zebrafish with motile cilia on the left or

right side of the KV showed consistent normal *situs* or reversal of organ position, respectively (Sampaio et al., 2014). On the other hand, mice with as few as 2 cilia beating, irrespectively of their position, would show normal organ *situs* (Shinohara et al., 2012). This is explained by their LRO shapes being so different. While all cilia in the mouse LRO are “useful”, meaning that they are all located in the pit region and therefore contributing to the leftward flow, in zebrafish there are productive flow regions and unproductive flow regions. Therefore, while two beating cilia in the mouse are enough to originate productive flow, in zebrafish there is need of a certain number and localization. In a normal embryo, this corresponds to the equatorial line for flow direction and anterior dorsal region for flow strength (Pintado et al., 2017).

Pkd2-mediated sensing and Nodal pathway

Pkd2 is also expressed in Zebrafish DFCs from gastrulation to early somite stages. Knockdown of Pkd2 also leads to LR problems in zebrafish. However these are different from the phenotypes seen in the mouse $PKD2^{-/-}$ mutant by Pennekamp et al. (2002), despite the similar loss of asymmetric *dand5* gene expression and the clear randomization of organ *situs* (Bisgrove et al., 2005; Schottenfeld et al., 2007) in zebrafish there is also a randomization of LPM markers, different when compared to the loss of expression of *lefty2* and *nodal* on the LPM and symmetric expression of *pitx2* reported in the mouse model.

The precursors of the Kupffer’s vesicle, the DFCs, have an interesting and advantageous feature that allows for unique and specific manipulations in the fish LRO. Since DFCs are the last cluster of cells to close their bridges with the yolk (Cooper and D’Amico, 1996), they can be exclusively targeted by injecting substances, such as antisense oligos, at 500-1000 cell stage instead at 1 cell stage (Amack and Yost, 2004). This approach allows for genetic manipulations in the KV only, making possible to distinguish between KV cell autonomous processes from other contributions. Knocking down Pkd2 in the DFCs alone produced milder

results in terms of organ *situs* and asymmetric gene expression in the LPM than knocking it down at 1 cell stage (Bisgrove et al., 2005). This suggests that the Pkd2 contribution to LR is not exclusively coming from the DFC cells but may be coming from other tissues as well. This is not surprising since that expression of *pkd2* is very broad in the developmental stages important for LR (Bisgrove et al., 2005; England et al., 2017). Overexpression of full-length zebrafish *pkd2* mRNA at 1 cell stage can rescue the organ *situs* of *pkd2* morphants to some extent (Bisgrove et al., 2005) but a DFC rescue was not tried. Interestingly, a human Pkd2 construct that had an important Serine in the position 812 substituted to an Aspartic Acid and therefore resulted in a protein that was predicted to be trapped in the endoplasmic reticulum via a strong interaction with PACs molecules was more effective at rescuing zebrafish abnormalities of LR asymmetry than the human Pkd2 WT version in *pkd2* morphant zebrafish embryos (Fu et al., 2008).

Yuan et al. (2015) used genetically encoded calcium indicators targeted to zebrafish LRO cilia and was able to observe intraciliary calcium oscillations (ICOs). These were observed in KV midplane of some cilia on the left side of the KV, which preceded a leftward calcium wave that extended through the mesendodermal cells beyond the LRO. These calcium oscillations were abolished in the absence of Pkd2 by morpholino knockdown or when targeting calcium chelators into the cilium (by using arl13b-parvalbumin construct), having significant impact on left right outcomes (Yuan et al., 2015). Temporally speaking, these ICOs happened at the onset of flow, just when cilia start to beat, and peak earlier than the cytosolic waves, which suggests that cumulative ICOs are necessary for a robust cytosolic calcium signal to occur and spread (Yuan et al., 2015). Although still unreported in zebrafish, in mouse and in medaka it has been found that the sensory partner of Pkd2 in the LRO is Pkd1l1 (Field et al., 2011; Kamura et al., 2011). In medaka it seems to be present in all KV cilia along with Pkd2 (Kamura et al., 2011). Together these results explained the lack of laterality defects observed

when Pkd1 was absent (Karcher et al., 2005) and suggest a dual role for cilia: generate flow and sensing it through a pkd2-pkd1l1 mediated sensing mechanism.

Associated with the calcium wave now observed by Yuan et al., (2015) there was a previous study reporting a transient activation of Ca^{2+}/Calmodulin-dependent protein kinase (CaMK-II) in the four interconnected cell layers along the anterior left wall of the KV (Francescatto et al., 2010). These studies showed that knocking down CaMKII leads to randomization of organ *situs* and disturbed expression of asymmetric genes. Indeed, the phosphorylated form of CaMKII was the first identified left-sided calcium sensitive target in LR asymmetry, which could be transducing the Pkd2-dependent calcium signals from the KV to the LPM (Francescatto et al., 2010; Rothschild et al., 2011). Embryos injected with CaMKII morpholino showed around 60% of abnormal heart *situs* and around 70% of abnormal gut *situs* (Francescatto et al., 2010), while embryos injected with *pkd2* morpholino showed only around 30% of abnormal hearts and guts (Bisgrove et al., 2005) or around 46% of combined *situs inversus* and heterotaxia (Schottenfeld et al., 2007). On the other hand, *pkd2/cup*$^{-/-}$ mutants have a much stronger phenotype for organ *situs*, with only 35% of *situs solitus* (Schottenfeld et al., 2007). In sum, if we compare Pkd2 and CaMKII morphants, there are still space for something else besides Pkd2 to affect the calcium signalling on the left side, while if we compare it with the *pkd2/cup*$^{-/-}$ mutant, then the levels of organ *situs* defects observed are similar. More work with mutants needs to be done on this level to further clarify the mechanism.

Zebrafish homologue for *nodal, (southpaw* or *spaw*) is first expressed in two symmetric domains flanking the KV and then on the left lateral plate mesoderm (Figure 4D). *Spaw* knockdown leads to severe organ *situs* defects and downregulation of other LR genes like *pitx2*, *lefty1* and *lefty2* (Long et al., 2003; Soroldoni et al., 2007). *Spadetail* and *notail* overlap in the region around the KV and are known to trans-activate peri-KV *spaw* expression

(Gourronc et al., 2007). *dand5* is expressed exclusively in KV cells in zebrafish and medaka. Dand5 is a homologue for Cerl2, which acts as a secreted antagonist for Nodal proteins (Hashimoto et al., 2004; Hojo et al., 2007; Pearce et al., 1999). Overexpression of *dand5* in the whole embryo counteracted the action of all the three zebrafish nodals: *cyclops*, *squint* and *spaw*, important genes for dorsal-ventral patterning of the embryo. On the other hand, knockdown of *dand5* led to specific laterality defects such as bilateral expression of *spaw*, *lefty1*, *lefty2* and *pitx2* and associated organ *situs* problems (Hashimoto et al., 2004). Loss of *notail* has a stricking impact on *dand5* production due to a direct role of *notail* in *dand5* transcriptional regulation (Gourronc et al., 2007). Also, Notch signaling seems to have a role in restricting *dand5* expression (Gourronc et al., 2007). Curiously, *foxj1a* seems to be important for *dand5* initial expression because ectopic expression of *foxj1a* in *ntla* mutants recovered *dand5* expression (Zhu et al., 2015). Many of the Nodal signaling pathway elements in LR are illustrated in Figure 5B.

From mouse studies we know that Nodal is a potent activator of its own transcription, as well as of its two antagonists *lefty1* and *lefty2* (Saijoh et al., 1999, 2000; Yashiro et al., 2000). Due to that, a midline barrier of *lefty1*, which codes for a Spaw inhibitor, is a conserved mechanism that restricts Spaw protein to the left side of the midline (Bisgrove et al., 1999). Regarding the midline barrier, in left-right development the midline is extremely important because it separates the two sides of the embryo physically and molecularly. β-catenin2 is essential for establishing a physical midline (when β-catenin2 is absent, the notochord and floorplate are lost) and β-catenin1 is important only for *lefty1* expression (Zhang et al., 2012). An extra anterior and posterior midline barriers were also described in zebrafish: posterior barrier mediated by BMP signaling that represses Spaw and prevents its passage from the posterior left side towards the right posterior side; and an anterior barrier mediated by *lefty2* expression in the cardiac left field, that helps prevent the passage of Spaw from left anterior

PSM to right anterior and posterior PSM (Lenhart et al., 2011; Long et al., 2003). The initiation of both *pitx2* in LPM and *lefty1* in the midline depends on Spaw. On the other hand, embryos lacking *lefty1* have premature *spaw* expression on the left LPM, meaning that *lefty1* expression in the midline helps timing the beginning of *spaw* expression in the LPM. Physical interaction of Lefty1 with one-eyed pinhead (oep), the zebrafish EGF-CFC receptor, in the midline leads to a reduction of the free Lefty1, alleviating its repression on LPM Nodal signaling and allowing it to happen. Absence of *dand5* also leads to premature *spaw* initiation in the LPM but without a left bias (Burdine and Grimes, 2016; Wang and Yost, 2008). Interestingly, recent *pitx2* mutants made in zebrafish have shown that this gene, despite being asymmetrically expressed in the LPM, is not required for LR establishment. Instead, a gene adjacent to *pitx2* that encodes a fatty acid elongase, *elovl6*, was showed to contribute to LR, by being asymmetrically expressed in the left LPM and dependent on Nodal activity (Ji et al., 2016). Zebrafish *spaw* mutants show randomization of both heart and gut laterality, although hearts exhibit a preferential dextral loop direction, which is independent of Nodal activity. This study also suggested that Nodal signaling might act by regulating actin gene expression and that asymmetric Nodal signaling may enhance cytoskeleton-based tissue-intrinsic mechanisms of heart looping (Noël et al., 2013). A very recent work by Ocaña et al. (2017) showed that BMP can mediate the activation of an epithelial-to-mesenchymal transition (EMT) inducer Prrx1a, a snail related gene, on the LPM. This new pathway is stronger on the right than on the left LPM. Through an actomyosin-dependent mechanism, Prrx1a-positive cells undergo EMT and lead to a leftward displacement of the cardiac posterior pole. The authors showed that when *prrx1a* was downregulated, embryos developed central hearts (Ocaña et al., 2017).

1.4 CILIA, FLOW AND LRO ARCHITECTURE – MECHANOSENSORY VS CHEMOSENSORY

Flow direction at the LRO is fundamentally asymmetric. The first asymmetry that must be considered is the clockwise rotation of the cilium itself, which is determined by the motor proteins that power its movement. These are made up of chiral amino acids in just one of their two possible forms: laevo. An equivalent molecular motor using the same amino acids in their opposite (dextro) configuration would be predicted to rotate in the reverse direction. Cartwright et al. (2004) discusses that, ultimately, LR symmetry breaking is determined by the chirality of natural amino acids that compose cilia which, by being in laevo conformation, impose a leftward direction to the flow (Cartwright et al., 2004). The second asymmetry to consider is the posterior tilt found in these cilia. Mathematical modelling predicted cilia tilting to be important for further establishment of a directional flow (Cartwright et al., 2004; Smith et al., 2007). This was later experimentally verified by Okada et al. (2005), further followed by Hashimoto et al. (2010) and Song et al. (2010) in mice and by Borovina et al. (2010) in zebrafish, and happens due to a process that is dependent on Planar Cell Polarity (Borovina et al., 2010; Hashimoto et al., 2010; Song et al., 2010).

With that established, one must think about the flow itself and how it is conveying the asymmetric message. In the mice LRO, the flow is extremely slow, with a low Reynolds number. In the reformed morphogen model with NVPs (Tanaka et al., 2005), the authors saw by time-lapse confocal microscopy that the NVPs were fragmented by the cilia or cell wall into smaller particles on the left side after being transported across the node. The majority of NVPs are indeed transported in the leftward flow, while some stay around each cilium and collide at other points of the node (Cartwright et al., 2007). However, physics states that the observed flow is not enough to just mechanically break the vesicles. This suggests that there must exist an active rupture mechanism that acts when the vesicle collides with a particular

region of the node or cilium, which would destabilize the membrane in a chemical way (Cartwright et al., 2007). A piece of data that seems to support this idea is the fact that mutant mice embryos in which NVPs are released but cilia are immotile, still seem to have NVP rupture (Tanaka et al., 2005). It was suggested that it might even be possible that this rupture mechanism is associated with the immotile cilia present around the mice node (Cartwright et al., 2007).

Interestingly, mice leftward fluid flow starts to be locally generated at early headfold stage and is fully developed at two-somite stage, increasing from 1 to 3ums^{-1} (Shinohara et al., 2012). However, gene asymmetry is established around the node at late headfold stage, soon after the local flow is generated but before global flow becomes maximal, suggesting that the system does not need strong flow to properly establish LR (Shinohara et al., 2012). Shinohara et al. (2012) confirmed this by methylcellulose experiments, where ciliary motion and fluid flow were abolished when using a medium containing 1% (w/v) methylcellulose, but using half the concentration impacted mildly on average rotating speed and established a weak flow of less than 2ums^{-1}. Treating with 1% of methylcellulose made asymmetric gene expression randomized, but embryos where weak flow was present (treated with 0.5%) had normal LR asymmetric gene expression (Shinohara et al., 2012). In addition, mutants with variable number of motile cilia (*Dpcd* and *Rfx3* mutants) were shown to have severe phenotypes with only zero to one motile cilia, and mild phenotypes with more than four motile cilia (Shinohara et al., 2012). The severely affected embryos (zero to one cilia beating) showed bilateral *cerl2* expression in the node and *nodal* expression in LPM was lost. The mildly affected embryos had normal asymmetric expression of *cerl2* and *pitx2*, despite losing the global flow and only showing weak leftward flow similar to embryos at early headfold stage (Shinohara et al., 2012). The weak local flow that remained in the embryos with only two rotating cilia was 1ums^{-1} in the area close to the cilia, which would decrease steeply with

distance, making the flow at the edge of the node too low for detection (Shinohara et al., 2012). When these mildly affected mutants were treated with 0.5% methylcellulose, which in WT embryos do not affect LR, they started to exhibit LR defects, suggesting that the LR decision indeed depends on the flow generated by these few rotating cilia. Also, these mildly affected mutants exhibited normal LR irrespective of the positions of the cilia regarding the node cavity. The authors argue that their data support mechanosensation since this weak leftward flow would take a very long time to transport morphogens and their data indicated that 2h of flow was enough to establish LR (Shinohara et al., 2012).

Curiously, in zebrafish the flow also starts slow (Tavares et al., 2017) and the intraciliary calcium oscillations described in Yuan et al. (2015) also happen prior to the strong flow is established (Yuan et al., 2015). By using experimental data and modelling, Ferreira et al. (2017) tried to test in zebrafish if the system was sensitive enough for mechanosensation to happen. They analysed the system from individual cilia to the entire LRO and showed that the local variability of flow velocities is too high to be well interpreted by such a small percentage of immotile cilia (less than 5% at 8 somite-stage), stating that chemosensation would be more likely to happen in zebrafish LRO (Ferreira et al., 2017). However, our own data showed that, at the same time-point as studied by Ferreira et al. (2017), there are not 5% but 20% of immotile cilia. If we consider that Yuan et al. (2015) showed calcium signalling is happening even earlier, when flow is slower, then the number of immotile cilia would be even higher (Tavares et al., 2017). Therefore, more should be done to proper understand if slow flow and higher number of immotile cilia are indeed sufficient for supporting mechanosensation and/or chemosensation.

Mechanosensation has been the latest fashion since the discovery that Pkd2 is key for LR patterning, with several reports showing that embryos lacking Pkd2 had numerous LR defects, in terms of organs and asymmetric gene expression (Bisgrove et al., 2005; Kamura

et al., 2011; Schottenfeld et al., 2007; Yoshiba et al., 2012). The general concept behind the role of Pkd2 was that the flow would bend the immotile cilia in the mice LRO crown cells or, in case of the zebrafish, the immotile cilia distributed throughout the LRO, and that this cilium bending would be sensed by the complex Pkd1l1 – Pkd2 so that a calcium influx of extracellular calcium would enter through the ciliary compartment and start a calcium-induced calcium release mechanism specifically on the left sided cells. However, it was reported that despite primary cilia are indeed unique calcium compartments with calcium concentration in the cilium ~7 times higher than the cytoplasmic concentration, calcium changes in the cilium rapidly dilute in the large cytoplasmic volume without initiating a measurable calcium-induced calcium release wave in the cytoplasm (Delling et al., 2013). Also, it was recently shown, using a calcium genetically encoded probe, that intraciliary calcium increase was not observed in the mouse LRO in response to physiological and supra-physiological flow forces, suggesting that indeed the primary cilia is not a good calcium-responsive mechanosensor (Delling et al., 2016). At the moment, the field needs to be clarified if the appropriate calcium sensors are being used as they differ across studies according to several properties such as the correct dissociation constant for observing small and fast variances in calcium concentrations. Nevertheless, there are alternative explanations. For instance, Pkd1 proteins have been described to be activated by signalling molecules, such as Wnt ligands (Kim et al., 2016), and still respond with an intracellular calcium signalling, therefore chemosensation poses as a possible alternative for mechanosensation. In sum, this is still a very hot topic in the field, with many labs continuously working to comprehend the full picture.

1.5 ZEBRAFISH AS A DISEASE MODEL

The potential of Zebrafish as a disease model is reflected by the increasing number of publications and meetings, such as the Zebrafish Disease Models. Genetically speaking, it is

possible to find 70% of human genes in zebrafish (Howe et al., 2013). Many of the genes and genetic pathways involved in organ formation are shared between humans and zebrafish and the genetic base of many human diseases can be mimicked in zebrafish. Only in 2017, zebrafish has been used to model myeloid malignancy (Potts and Bowman, 2017), liver diseases (reviewed in Pham et al., 2017), vascular development and disease (reviewed in Hogan and Schulte-Merker, 2017), infection (Madigan et al., 2017), diabetes (Heckler and Kroll, 2017) and other metabolic diseases (Kamel and Ninov, 2017), just to name a few examples.

Roxo-Rosa et al. (2015) as shown that the Kupffer's vesicle in the zebrafish embryo model can work as a simplified kidney cyst model (Roxo-Rosa et al., 2015). It is a fluid-filled vesicular structure that resembles an ADPKD kidney cyst, in which cells facing the lumen bear a cilium (Roxo-Rosa et al., 2015). These cells both express Pkd2 (Bisgrove et al., 2005; Schottenfeld et al., 2007) and CFTR (Navis et al., 2013; Roxo-Rosa et al., 2015;), which can be manipulated through morpholinos and drugs (Compagnon et al., 2014; Navis et al., 2013; Schottenfeld et al., 2007). KV lumen inflation is mediated by CFTR (Navis et al., 2013) and it has been shown that by manipulating Pkd2 and CFTR levels, it is possible to manipulate the KV volume. Knockdown of Pkd2 leads to an increase of volume that is mediated by an overactivation of CFTR. This was shown by using drugs that inhibit CFTR like the CFTRinh-172 (Li et al., 2004). All this together makes the zebrafish a good model system to study the molecular mechanisms involved in ADPKD and even to test new compounds that may prevent cyst enlargement, since KV volume can be a direct readout for treatment effectiveness (Roxo-Rosa e tal., 2015).

Despite the kidney cysts in zebrafish are not real cysts and look more like dilations of the pronephros (Schottenfeld et al., 2007), zebrafish is a very good model to test compound toxicity in the kidney. It is easy to obtain hundreds of zebrafish larvae to allow high

throughput screenings but the larvae are still small enough to fit in 96-well plates, allowing easy and fast drug administration in small amounts. Besides, zebrafish shares several features with mammals regarding genetics, metabolism and physiology (Peterson and MacRae, 2012). The larval pronephros is fully mature at 4 days post-fertilization and consists of two nephrons with a glomerulus fused at the embryo midline. Although much more simplified, the structures maintain several features that are similar to those found in mammal nephron tubules (Kramer-Zucker et al., 2005b; Wingert et al., 2007). Many studies have addressed acute toxicity response in zebrafish larvae to drugs known to cause tubular damage in humans: paracetamol, gentamicin and tenofovir (Gorgulho et al., 2017; Hentschel et al., 2005; Peng et al., 2010; Rider et al., 2012; Westhoff et al., 2013). A recent analysis of the drug-induced morphological and functional tubular alterations showed high homology between zebrafish and mammals in terms of drug metabolism and demonstrated in detail proximal tubule morphological defects in 3D by optical microscopy and detailed mitochondrial defects by Electron Microscopy (Gorgulho et al., 2017). All these papers together strongly support further use of zebrafish as a disease model.

Coming back to the left right field, zebrafish offers huge advantages as a disease model for laterality disorders because it allows researchers to manipulate the LRO mechanically or genetically and then observe the results along the development of the LPM and organs. Our own work can attest to these advantages (Sampaio et al., 2014; Tavares et al., 2017).

2. AIMS

In this study I intended to investigate several events that occur upstream and downstream of the Pkd2-dependent calcium mediated signalling in zebrafish left-right development.

This first chapter reviewed and highlighted the many similarities and differences between two animal models (mouse and zebrafish) in terms of Left-Right axis establishment, from LRO

formation to ciliogenesis, passing through Calcium signalling and Nodal signalling pathways. We reviewed the main findings in fluid flow mathematical simulations and how different experiments support different views for early LR establishment: chemosensory versus mechanosensory hypotheses are explained and debated. We finish presenting some studies that indicate how zebrafish is becoming more and more interesting to study human diseases and help finding therapeutic approaches.

In Chapter 2, we assessed the role of Notch signalling on the fate decision between a motile and an immotile cilium in the Kupffer's vesicle of the zebrafish embryo. In order to do that, we manipulated Notch component levels by using mutants and overexpression studies and assess their impact on *foxj1a* and *dnah*7 mRNA levels by qRT-PCR and in motile/immotile cilia ratio through microscopy. We uncovered by Electron Microscopy that all KV cilia have dynein arms and that Notch, through its effector Her12, is making some cilia stay immotile while others move. The study presented in this chapter was published in eLife 6:e25165

In Chapter 3, we tried to isolate the impact of absence of flow from the impact of the absence of Pkd2-mediated signalling on asymmetric gene expression and organ *situs*. Conceptually, if Pkd2 channel is the sole calcium channel responsible for the flow sensory pathway then the output results should be the same. By knocking down Pkd2 in whole embryo or only on KV precursor cells, we assessed the impact of these manipulations versus abrogating flow via *dnah7* knock down. We assessed the expression pattern and levels of the first asymmetric gene *dand5* by in situ hybridization and qRT-PCR, respectively, and the impact on organ *situs* by scoring heart and liver positions in the same embryos. The work presented in this chapter was done in collaboration with Pedro Sampaio and will be part of a manuscript, which is in preparation.

In Chapter 4, we assessed the impact of Pkd2 in the KV ciliated cells by looking to the downstream targets of this calcium signalling pathway and trying to understand how they influence the early left-right (LR) axis specification. In order to achieve these goals, a tissue-specific mRNA profiling of the Zebrafish KV cells was performed. The results were analysed, clustered and candidate genes were chosen and validated by qPCR for further testing. I then studied the localization of four candidate genes in the KV at the correct time through *in situ* hybridization: *parvalbumin6, calcyclin binding protein, frizzled related protein* and *nicalin1*. None of these four genes had an asymmetric expression pattern around the KV in WT embryos. I used morpholinos to knockdown their function and cloned the four genes to perform mRNA overexpression and explored if they generated any laterality phenotypes. This study was done in collaboration with Dr Mónica Roxo-Rosa who performed the microarrays and data analysis of transcript list. Follow up studies of some of these genes will be performed in the future.

In Chapter 5, we investigated the role of the Nodal antagonist Nicalin1 (Ncl1) in Left-right axis establishment, a protein which has never been described in this process. Ncl1 is known to inhibit Nodal signalling at the endoplasmic reticulum level, by impairing the trafficking of Lefty and affecting mesendoderm patterning. We show here that absence of *ncl1* affects LR in a dose-dependent manner. Knockdown of *ncl1* does not produce as severe LR defects as knockdown of *dand5*, but abrogating both leads to a stronger phenotype. The work presented in this chapter will be part of a manuscript that is in preparation.

The study presented in Chapter 6 was done in collaboration with Rita Gorgulho where we validated zebrafish as a useful animal model to study drug toxicity and its impact on kidney function and morphology. We treated zebrafish larvae with gentamicin, paracetamol and tenofovir and observed the effects on metabolites profile, urine production, macro and micro morphological defects. The metabolites profile showed striking similarities between zebrafish

and human drug metabolism. In terms of morphological defects, my contribution to this work provided for the first time detailed imaging of zebrafish pronephros that allowed 3D reconstructions of the structure for volume measurements. We saw defects typically found in acute tubular injury like tubular dilations and epithelium disorganization. This study was published in Archives of Toxicology (DOI 10.1007/s00204-017-2063-1).

Finally, in the Chapter 7, we discuss the main findings described in the previous chapters with an integrative perspective regarding the existing literature. We also highlight the contribution of this work towards understanding the role of Pkd2 and Nicalin1 in left-right axis establishment.

REFERENCES

Aamar, E., and Dawid, I.B. (2008). Isolation and expression analysis of foxj1 and foxj1.2 in zebrafish embryos. Int J Dev Biol. *52*, 985–991.

Afzelius, B.A. (1976). A human syndrome caused by immotile cilia. Science (80-.). *193*, 317–319.

Alten, L., Schuster-Gossler, K., Beckers, A., Groos, S., Ulmer, B., Hegermann, J., Ochs, M., and Gossler, A. (2012). Differential regulation of node formation, nodal ciliogenesis and cilia positioning by Noto and Foxj1. J. Cell Sci. *125*, 1276–1284.

Amack, J.D., and Yost, H.J. (2004). The T box transcription factor no tail in ciliated cells controls zebrafish left-right asymmetry. Curr. Biol. *14*, 685–690.

St. Amand, T.R., Ra, J., Zhang, Y., Hu, Y., Baber, S.I., and Chen, Y.-P. (1998). Cloning and Expression Pattern of Chicken Pitx2: A New Component in the SHH Signaling Pathway Controlling Embryonic Heart Looping. Biochem. Biophys. Res. Commun. *247*, 100–105.

Antic, D., Stubbs, J.L., Suyama, K., Kintner, C., Scott, M.P., and Axelrod, J.D. (2010). Planar cell polarity enables posterior localization of nodal cilia and left-right axis determination during mouse and Xenopus embryogenesis. PLoS One *5*.

Attisano, L., and Wrana, J.L. (2002). Signal transduction by the TGF-beta superfamily. Science (80-.). *296*, 1646–47.

Baeg, G.H., Selva, E.M., Goodman, R.M., Dasgupta, R., and Perrimon, N. (2004). The Wingless morphogen gradient is established by the cooperative action of Frizzled and Heparan Sulfate

Proteoglycan receptors. Dev. Biol. *276*, 89–100.

Beck, S., Le Good, J.A., Guzman, M., Haim, N. Ben, Roy, K., Beermann, F., and Constam, D.B. (2002). Extraembryonic proteases regulate Nodal signalling during gastrulation. Nat. Cell Biol. *4*, 981.

Belenkaya, T.Y., Han, C., Yan, D., Opoka, R.J., Khodoun, M., Liu, H., and Lin, X. (2004). Drosophila Dpp morphogen movement is independent of dynamin-mediated endocytosis but regulated by the glypican members of heparan sulfate proteoglycans. Cell *119*, 231–244.

Bell, E., Munoz-Sanjuán, I., Altmann, C.R., Vonica, A., and Brivanlou, A.H. (2003). Cell fate specification and competence by Coco, a maternal BMP, TGFbeta and Wnt inhibitor. Development *130*, 1381–1389.

Bellomo, D., Lander, A., Harragan, I., and Brown, N.A. (1996). Cell proliferation in mammalian gastrulation: the ventral node and notochord are relatively quiescent. Dev. Dyn. *205*, 471–485.

Belo, J.A., Bachiller, D., Agius, E., Kemp, C., Borges, A.C., Marques, C.L., Piccolo, S., and De Robertis, E.M. (2000). Cerberus-like is a secreted BMP and nodal antagonist not essential for mouse development. Genesis *26*, 265–270.

Berleth, T., Burri, M., Thoma, G., Bopp, D., Richstein, S., Frigerio, G., Noll, M., and Nüsslein-Volhard, C. (1988). The role of localization of bicoid RNA in organizing the anterior pattern of the Drosophila embryo. EMBO J. *7*, 1749–1756.

Bisgrove, B.W., Essner, J.J., and Yost, J.H. (1999). Regulation of midline development by antagonism of lefty and nodal signaling. Development *126*, 3253–3262.

Bisgrove, B.W., Snarr, B.S., Emrazian, A., and Yost, H.J. (2005). Polaris and Polycystin-2 in dorsal forerunner cells and Kupffer's vesicle are required for specification of the zebrafish left-right axis. Dev. Biol. *287*, 274–288.

Blanchet, M.-H., Le Good, J.A., Mesnard, D., Oorschot, V., Baflast, S., Minchiotti, G., Klumperman, J., and Constam, D.B. (2008). Cripto recruits Furin and PACE4 and controls Nodal trafficking during proteolytic maturation. EMBO J. *27*, 2580–2591.

Borovina, A., Superina, S., Voskas, D., and Ciruna, B. (2010). Vangl2 directs the posterior tilting and asymmetric localization of motile primary cilia. Nat. Cell Biol. *12*, 407–412.

Boskovski, M.T., Yuan, S., Pedersen, N.B., Goth, C.K., Makova, S., Clausen, H., Brueckner, M., and Khokha, M.K. (2013). The heterotaxy gene GALNT11 glycosylates Notch to orchestrate cilia type and laterality. Nature *504*.

Branford, W.W., Essner, J.J., and Yost, H.J. (2000). Regulation of gut and heart left-right asymmetry by context-dependent interactions between xenopus lefty and BMP4 signaling. Dev Biol. *223*, 291–

306.

Brennan, J., Norris, D.P., and Robertson, E.J. (2002). Nodal activity in the node governs left-right asymmetry. Genes Dev. *16*, 2339–2344.

Brody, S.L., Yan, X.H., Wuerffel, M.K., Song, S.-K., and Shapiro, S.D. (2000). Ciliogenesis and Left – Right Axis Defects in Forkhead Factor HFH-4 – Null Mice (Aka FOXJ1 Mutant Mice). Am. J. Respir. Cell Mol. Biol. *23*, 45–51.

Burdine, R.D., and Grimes, D.T. (2016). Antagonistic interactions in the zebrafish midline prior to the emergence of asymmetric gene expression are important for left–right patterning. Philos. Trans. R. Soc. B Biol. Sci. *371*, 20150402.

Campione, M., Steinbeisser, H., Schweickert, A., Deissler, K., van Bebber, F., Lowe, L.A., Nowotschin, S., Viebahn, C., Haffter, P., Kuehn, M.R., et al. (1999). The homeobox gene Pitx2: mediator of asymmetric left-right signaling in vertebrate heart and gut looping. Development *126*, 1225–1234.

Caron, A., Xu, X., and Lin, X. (2012). Wnt/beta-catenin signaling directly regulates Foxj1 expression and ciliogenesis in zebrafish Kupffer's vesicle. Development *139*, 514–524.

Cartwright, J.H.E., Piro, O., and Tuval, I. (2004). Fluid-dynamical basis of the embryonic development of left-right asymmetry in vertebrates. Proc. Natl. Acad. Sci. U. S. A. *101*, 7234–7239.

Cartwright, J.H.E., Piro, N., Piro, O., and Tuval, I. (2007). Embryonic nodal flow and the dynamics of nodal vesicular parcels. J. R. Soc. Interface *4*, 49–55.

Chen, Y., and Schier, A.F. (2002). Lefty proteins are long-range inhibitors of Squint-mediated Nodal signaling. Curr. Biol. *12*, 2124–2128.

Chen, J., Knowles, H.J., Hebert, J.L., and Hackett, B.P. (1998). Mutation of the mouse hepatocyte nuclear factor/forkhead homologue 4 gene results in an absence of cilia and random left-right asymmetry. J. Clin. Invest. *102*, 1077–1082.

Cheng, S.K., Olale, F., Brivanlou, A.H., and Schier, A.F. (2004). Lefty blocks a subset of TGFb signals by antagonizing EGF-CFC coreceptors. PLoS Biol. *2*.

Choksi, S.P., Lauter, G., Swoboda, P., and Roy, S. (2014). Switching on cilia: transcriptional networks regulating ciliogenesis. Development *141*, 1427–1441.

Collignon, J., Varlet, I., and Robertson, E.J. (1996). Relationship between asymmetric nodal expression and the direction of embryonic turning. Nat. Lett. *381*, 155–158.

Compagnon, J., Barone, V., Rajshekar, S., Kottmeier, R., Pranjic-Ferscha, K., Behrndt, M., and Heisenberg, C.-P. (2014). The notochord breaks bilateral symmetry by controlling cell shapes in the

zebrafish laterality organ. Dev. Cell *31*, 774–783.

Cooper, M.S., and D'Amico, L.A. (1996). A cluster of noninvoluting endocytic cells at the margin of the zebrafish blastoderm marks the site of embryonic shield formation. Dev. Biol. *180*, 184–198.

Corbit, K.C., Shyer, A.E., Dowdle, W.E., Gaulden, J., Singla, V., Chen, M.H., Chuang, P.T., and Reiter, J.F. (2008). Kif3a constrains b-catenin- dependent Wnt signalling through dual ciliary and non-ciliary mechanisms. Nat Cell Biol *10*, 70–76.

Danos, M.C., and Yost, H.J. (1996). Role of notochord in specification of cardiac left-right orientation in zebrafish and Xenopus. Dev Biol. *177*, 96–103.

Delling, M., DeCaen, P.G., Doerner, J.F., Febvay, S., and Clapham, D.E. (2013). Primary cilia are specialized calcium signalling organelles. Nature *504*, 311–314.

Delling, M., Indzhykulian, A.A., Liu, X., Li, Y., Xie, T., Corey, D.P., and Clapham, D.E. (2016). Primary cilia are not calcium-responsive mechanosensors. Nature *531*, 656–660.

Didon, L., Zwick, R.K., Chao, I.W., Walters, M.S., Wang, R., Hackett, N.R., and Crystal, R.G. (2013). RFX3 modulation of FOXJ1 regulation of cilia genes in the human airway epithelium. Respir. Res. *14*, 70.

England, S.J., Campbell, P.C., Banerjee, S., Swanson, A.J., and Lewis, K.E. (2017). Identification and Expression Analysis of the Complete Family of Zebrafish pkd Genes. Front. Cell Dev. Biol. *5*.

Essner, J.J., Branford, W.W., Zhang, J., and Yost, H.J. (2000). Mesendoderm and left-right brain, heart and gut development are differentially regulated by pitx2 isoforms. Development *127*, 1081–1093.

Essner, J.J., Amack, J.D., Nyholm, M.K., Harris, E.B., and Yost, H.J. (2005). Kupffer's vesicle is a ciliated organ of asymmetry in the zebrafish embryo that initiates left-right development of the brain, heart and gut. Development *132*, 1247–1260.

Ezratty, E.J., Stokes, N., Chai, S., Shah, A.S., Williams, S.E., and Fuchs, E. (2011). A Role for the Primary Cilium in Notch Signaling and Epidermal Differentiation during Skin Development. Cell *145*, 1129–1141.

Ferreira, R.R., Vilfan, A., Jülicher, F., and Supatto, W. (2017). Physical limits of flow sensing in the left-right organizer. Elife *6:e25078*, 1–27.

Field, S., Riley, K.-L., Grimes, D.T., Hilton, H., Simon, M., Powles-Glover, N., Siggers, P., Bogani, D., Greenfield, A., and Norris, D.P. (2011). Pkd1l1 establishes left-right asymmetry and physically interacts with Pkd2. Development *138*, 1131–1142.

Francescatto, L., Rothschild, S.C., Myers, A.L., and Tombes, R.M. (2010). The activation of membrane targeted CaMK-II in the zebrafish Kupffer's vesicle is required for left-right asymmetry. Development *137*, 2753–2762.

Fu, X., Wang, Y., Schetle, N., Gao, H., Pütz, M., von Gersdorff, G., Walz, G., and Kramer-Zucker, A.G. (2008). The subcellular localization of TRPP2 modulates its function. J. Am. Soc. Nephrol. *19*, 1342–1351.

Gokey, J.J., Ji, Y., Tay, H.G., Litts, B., and Amack, J.D. (2015). Kupffer's vesicle size threshold for robust left-right patterning of the zebrafish embryo. Dev. Dyn. *245*, 22–33.

Le Good, J.A., Joubin, K., Giraldez, A.J., Ben-Haim, N., Beck, S., Chen, Y., Schier, A.F., and Constam, D.B. (2005). Nodal Stability Determines Signaling Range. Curr. Biol. *15*, 31–36.

Gorgulho, R., Jacinto, R., Lopes, S.S., Pereira, S.A., Tranfield, E.M., Martins, G.G., Gualda, E.J., Derks, R.J.E., Correia, A.C., Steenvoorden, E., et al. (2017). Usefulness of zebrafish larvae to evaluate drug-induced functional and morphological renal tubular alterations. Arch. Toxicol. 1–13.

Gourronc, F., Ahmad, N., Nedza, N., Eggleston, T., and Rebagliati, M. (2007). Nodal activity around Kupffer's vesicle depends on the T-box transcription factors notail and spadetail and on Notch signaling. Dev. Dyn. *236*, 2131–2146.

Gritsman, K., Zhang, J., Cheng, S., Heckscher, E., Talbot, W.S., and Schier, A.F. (1999). The EGF-CFC protein one-eyed pinhead is essential for nodal signaling. Cell *97*, 121–132.

Hadjantonakis, A.-K., Pisano, E., and Papaioannou, V.E. (2008). Tbx6 regulates left/right patterning in mouse embryos through effects on nodal cilia and perinodal signaling. PLoS One *3*.

Hashimoto, H., Rebagliati, M., Ahmad, N., Muraoka, O., Kurokawa, T., Hibi, M., and Suzuki, T. (2004). The Cerberus/Dan-family protein Charon is a negative regulator of Nodal signaling during left-right patterning in zebrafish. Development *131*, 1741–1753.

Hashimoto, M., Shinohara, K., Wang, J., Ikeuchi, S., Yoshiba, S., Meno, C., Nonaka, S., Takada, S., Hatta, K., Wynshaw-Boris, A., et al. (2010). Planar polarization of node cells determines the rotational axis of node cilia. Nat. Cell Biol. *12*, 170–176.

Heckler, K., and Kroll, J. (2017). Zebrafish as a Model for the Study of Microvascular Complications of Diabetes and Their Mechanisms. Int. J. Mol. Sci. *18*.

Hentschel, D.M., Park, K.M., Cilenti, L., Zervos, A.S., Drummond, I., and Bonventre, J. V (2005). Acute renal failure in zebrafish: a novel system to study a complex disease. Am. J. Physiol. - Ren. Physiol. *288*, F923 LP-F929.

Hirokawa, N., Tanaka, Y., Okada, Y., and Takeda, S. (2006). Nodal Flow and the Generation of Left-

Right Asymmetry. Cell *125*, 33–45.

Hogan, B.M., and Schulte-Merker, S. (2017). How to Plumb a Pisces: Understanding Vascular Development and Disease Using Zebrafish Embryos. Dev. Cell *42*, 567–583.

Hojo, M., Takashima, S., Kobayashi, D., Sumeragi, A., Shimada, A., Tsukahara, T., Yokoi, H., Narita, T., Jindo, T., Kage, T., et al. (2007). Right-elevated expression of charon is regulated by fluid flow in medaka Kupffer's vesicle. Dev. Growth Differ. *49*, 395–405.

Howe, K., Clark, M.D., Torroja, C.F., Torrance, J., Berthelot, C., Muffato, M., Collins, J.E., Humphray, S., McLaren, K., Matthews, L., et al. (2013). The zebrafish reference genome sequence and its relationship to the human genome. Nature *496*, 498—503.

Huang, S., Hirota, Y., and Sawamoto, K. (2009). Various facets of vertebrate cilia: motility, signaling, and role in adult neurogenesis. Proc. Jpn. Acad. Ser. B. Phys. Biol. Sci. *85*, 324–336.

Huangfu, D., Liu, A., Rakeman, A.S., Murcia, N.S., Niswander, L., and Anderson, K. V. (2003). Hedgehog signalling in the mouse requires intraflagellar transport proteins. Nature *426*, 83–87.

Hummel, K.P., and Chapman, D.B. (1959). Visceral inversion and associated anomalies in the mouse. J. Hered. *50*, 9–13.

Inácio, J.M., Marques, S., Nakamura, T., Shinohara, K., Meno, C., Hamada, H., and Belo, J.A. (2013). The dynamic right-to-left translocation of Cerl2 is involved in the regulation and termination of Nodal activity in the mouse node. PLoS One *8*.

Ishimura, A., Chida, S., and Osada, S.-I. (2008). Man1, an inner nuclear membrane protein, regulates left-right axis formation by controlling nodal signaling in a node-independent manner. Dev. Dyn. *237*, 3565–3576.

Jacquet, B. V., Salinas-Mondragon, R., Liang, H., Therit, B., Buie, J.D., Dykstra, M., Campbell, K., Ostrowski, L.E., Brody, S.L., and Ghashghaei, H.T. (2009). FoxJ1-dependent gene expression is required for differentiation of radial glia into ependymal cells and a subset of astrocytes in the postnatal brain. Development *136*, 4021–4031.

Ji, Y., Buel, S.M., Amack, J.D., and Medical, U. (2016). Mutations in zebrafish pitx2 model congenital malformations in Axenfeld-Rieger syndrome but do not disrupt left-right placement of visceral organs. Dev. Biol. *416*, 69–81.

Jing, X. hong, Zhou, S. mei, Wang, W. qing, and Chen, Y. (2006). Mechanisms underlying long- and short-range nodal signaling in Zebrafish. Mech. Dev. *123*, 388–394.

Jurisch-Yaksi, N., Rose, A.J., Lu, H., Raemaekers, T., Munck, S., Baatsen, P., Baert, V., Vermeire, W., Scales, S.J., Verleyen, D., et al. (2013). Rer1p maintains ciliary length and signaling by regulating

γ-secretase activity and Foxj1a levels. J. Cell Biol. *200*, 709–720.

Kamel, M., and Ninov, N. (2017). Catching new targets in metabolic disease with a zebrafish. Curr. Opin. Pharmacol. *37*, 41–50.

Kamura, K., Kobayashi, D., Uehara, Y., Koshida, S., Iijima, N., Kudo, A., Yokoyama, T., and Takeda, H. (2011). Pkd1l1 complexes with Pkd2 on motile cilia and functions to establish the left-right axis. Development *138*, 1121–1129.

Karcher, C., Fischer, A., Schweickert, A., Bitzer, E., Horie, S., Witzgall, R., and Blum, M. (2005). Lack of a laterality phenotype in Pkd1 knock-out embryos correlates with absence of polycystin-1 in nodal cilia. Differentiation *73*, 425–432.

Katsu, K., Tokumori, D., Tatsumi, N., Suzuki, A., and Yokouchi, Y. (2012). BMP inhibition by DAN in Hensen's node is a critical step for the establishment of left-right asymmetry in the chick embryo. Dev. Biol. *363*, 15–26.

Kawasumi, A., Nakamura, T., Iwai, N., Yashiro, K., Saijoh, Y., Belo, J.A., Shiratori, H., and Hamada, H. (2011). Left-right asymmetry in the level of active Nodal protein produced in the node is translated into left-right asymmetry in the lateral plate of mouse embryos. Dev. Biol. *353*, 321–330.

Kicheva, A., Pantazis, P., Bollenbach, T., Kalaidzidis, Y., Bittig, T., Jülicher, F., and González-Gaitán, M. (2007). Kinetics of Morphogen Gradient Formation. Science (80-.). *315*, 521 LP-525.

Kim, S., Nie, H., Nesin, V., Tran, U., Outeda, P., Bai, C.-X., Keeling, J., Maskey, D., Watnick, T., Wessely, O., et al. (2016). The polycystin complex mediates Wnt/Ca2+ signalling. Nat. Cell Biol. *18*.

Kitajima, K., Oki, S., Ohkawa, Y., Sumi, T., and Meno, C. (2013). Wnt signaling regulates left-right axis formation in the node of mouse embryos. Dev. Biol. *380*, 222–232.

Kondo, S., Sato-Yoshitake, R., Noda, Y., Aizawa, H., Nakata, T., Matsuura, Y., and Hirokawa, N. (1994). KIF3A is a new microtubule-based anterograde motor in the nerve axon. J. Cell Biol. *125*, 1095–1107.

Kosaki, K., and Casey, B. (1998). Genetics of human left-right axis malformations. Sem. Cell Dev. Biol. *9*, 89–99.

Kramer-Zucker, A.G., Olale, F., Haycraft, C.J., Yoder, B.K., Schier, A.F., and Drummond, I.A. (2005a). Cilia-driven fluid flow in the zebrafish pronephros, brain and Kupffer's vesicle is required for normal organogenesis. Development *132*, 1907–1921.

Kramer-Zucker, A.G., Wiessner, S., Jensen, A.M., and Drummond, I.A. (2005b). Organization of the pronephric filtration apparatus in zebrafish requires Nephrin, Podocin and the FERM domain protein Mosaic eyes. Dev. Biol. *285*, 316–329.

Krebs, L.T., Iwai, N., Nonaka, S., Welsh, I.C., Lan, Y., Jiang, R., Saijoh, Y., O'Brien, T.P., Hamada, H., and Gridley, T. (2003). Notch signaling regulates left−right asymmetry determination by inducing Nodal expression. Genes Dev. *17*, 1207–1212.

Kreiling, J.A., Balantac, Z.L., Crawford, A.R., Ren, Y., Toure, J., Zchut, S., Kochilas, L., and Creton, R. (2008). Suppression of the endoplasmic reticulum calcium pump during zebrafish gastrulation affects left-right asymmetry of the heart and brain. Mech. Dev. *125*, 396–410.

Kumar, A., Novoselov, V., Celeste, A.J., Wolfman, N.M., ten Dijke, P., and Kuehn, M.R. (2001). Nodal signaling uses activin and transforming growth factor-beta receptor-regulated Smads. J. Biol. Chem. *276*, 656–661.

Lee, M.A., Heasman, J., and Whitman, M. (2001). Timing of endogenous activin-like signals and regional specification of the Xenopus embryo. Development *128*, 2939–2952.

Leitch, C.C., Lodh, S., Prieto-Echagüe, V., Badano, J.L., and Zaghloul, N.A. (2014). Basal body proteins regulate Notch signaling through endosomal trafficking. J. Cell Sci. *127*, 2407–2419.

Lenhart, K.F., Lin, S.-Y., Titus, T.A., Postlethwait, J.H., and Burdine, R.D. (2011). Two additional midline barriers function with midline lefty1 expression to maintain asymmetric Nodal signaling during left-right axis specification in zebrafish. Development *138*, 4405–4410.

Li, H., Findlay, I. a., and Sheppard, D.N. (2004). The relationship between cell proliferation, Cl- secretion, and renal cyst growth: A study using CFTR inhibitors. Kidney Int. *66*, 1926–1938.

Lin, X., and Xu, X. (2009). Distinct functions of Wnt/beta-catenin signaling in KV development and cardiac asymmetry. Development *136*, 207–217.

Logan, M., Pagán-Westphal, S.M., Smith, D.M., Paganessi, L., and Tabin, C.J. (1998). The transcription factor pitx2 mediates situs-specific morphogenesis in response to left-right asymmetric signals. Cell *94*, 307–317.

Long, S., Ahmad, N., and Rebagliati, M. (2003). The zebrafish nodal-related gene southpaw is required for visceral and diencephalic left-right asymmetry. Development *130*, 2303–2316.

Lopes, S.S., Lourenço, R., Pacheco, L., Moreno, N., Kreiling, J., and Saúde, L. (2010). Notch signalling regulates left-right asymmetry through ciliary length control. Development *137*, 3625–3632.

Lowe, L.A., Supp, D.M., Sampath, K., Yokoyama, T., Wright, C.V.E., Potter, S.S., Overbeek, P., and Kuehn, M.R. (1996). Conserved left-right asymmetry of nodal expression and alterations in murine situs inversus. Lett. to Nat. *381*, 158–161.

Madigan, C.A., Cameron, J., and Ramakrishnan, L. (2017). A Zebrafish Model of Mycobacterium leprae Granulomatous Infection. J. Infect. Dis. *216*, 776–779.

Marjoram, L., and Wright, C. (2011). Rapid differential transport of Nodal and Lefty on sulfated proteoglycan-rich extracellular matrix regulates left-right asymmetry in Xenopus. Development *138*, 475–485.

Marques, S., Borges, A.C., Silva, A.C., Freitas, S., Cordenonsi, M., and Belo, J.A. (2004). The activity of the Nodal antagonist Cerl-2 in the mouse node is required for correct L/R body axis. Genes Dev. *18*, 2342–2347.

McGrath, J., Somlo, S., Makova, S., Tian, X., and Brueckner, M. (2003). Two populations of node monocilia initiate left-right asymmetry in the mouse. Cell *114*, 61–73.

Meno, C., Saijoh, Y., Fujii, H., Ikeda, M., Yokoyama, T., Yokoyama, M., Toyoda, Y., and Hamada, H. (1996). Left-right asymmetric expression of the TGFβ-family member lefty in mouse embryos. Nature *381*, 151–155.

Meno, C., Shimono, A., Saijoh, Y., Yashiro, K., Mochida, K., Ohishi, S., Noji, S., Kondoh, H., and Hamada, H. (1998). Lefty-1 Is Required for Left-Right Determination As a Regulator of Lefty-2 and Nodal. Cell *94*, 287–297.

Minegishi, K., Hashimoto, M., Ajima, R., Takaoka, K., Shinohara, K., Ikawa, Y., Nishimura, H., McMahon, A.P., Willert, K., Okada, Y., et al. (2017). A Wnt5 Activity Asymmetry and Intercellular Signaling via PCP Proteins Polarize Node Cells for Left-Right Symmetry Breaking. Dev. Cell *40*, 439–452.

Mochizuki, T., Tsuchiya, K., and Yokoyama, T. (2002). Molecular cloning of a gene for inversion of embryo turning (inv) with cystic kidney. Nephrol. Dial. Transplant. *17*.

Montenegro-Johnson, T.D., Baker, D.I., Smith, D.J., and Lopes, S.S. (2016). Three-dimensional flow in Kupffer's Vesicle. J. Math Biol. *73*, 705–725.

Morgan, D., Goodship, J., Essner, J.J., Vogan, K.J., Turnpenny, L., Yost, H.J., Tabin, C.J., and Strachan, T. (2002). The left-right determinant inversin has highly conserved ankyrin repeat and IQ domains and interacts with calmodulin. Hum. Genet. *110*, 377–384.

Müller, P., Rogers, K.W., Jordan, B.M., Lee, J.S., Robson, D., Ramanathan, S., and Schier, A.F. (2012). Differential diffusivity of Nodal and Lefty underlies a reaction-diffusion patterning system. Science *336*, 721–724.

Müller, P., Rogers, K.W., Yu, S.R., Brand, M., and Schier, A.F. (2013). Morphogen transport. Development *140*, 1621–1638.

Nakamura, T., Mine, N., Nakaguchi, E., Mochizuki, A., Yamamoto, M., Yashiro, K., Meno, C., and Hamada, H. (2006). Generation of Robust Left-Right Asymmetry in the Mouse Embryo Requires a

Self-Enhancement and Lateral-Inhibition System. Dev. Cell *11*, 495–504.

Nakamura, T., Saito, D., Kawasumi, A., Shinohara, K., Asai, Y., Takaoka, K., Dong, F., Takamatsu, A., Belo, J.A., Mochizuki, A., et al. (2012). Fluid flow and interlinked feedback loops establish left-right asymmetric decay of Cerl2 mRNA. Nat. Commun. *3*, 1322.

Nakaya, M., Biris, K., Tsukiyama, T., Jaime, S., Rawls, J.A., and Yamaguchi, T.P. (2005). Wnt3a links left-right determination with segmentation and anteroposterior axis elongation. Development *132*, 5425–5436.

Nauli, S.M., Alenghat, F.J., Luo, Y., Williams, E., Vassilev, P., Li, X., Elia, A.E.H., Lu, W., Brown, E.M., Quinn, S.J., et al. (2003). Polycystins 1 and 2 mediate mechanosensation in the primary cilium of kidney cells. Nat. Genet. *33*, 129–137.

Nauli, S.M., Rossetti, S., Kolb, R.J., Alenghat, F.J., Consugar, M.B., Harris, P.C., Ingber, D.E., Loghman-Adham, M., and Zhou, J. (2006). Loss of polycystin-1 in human cyst-lining epithelia leads to ciliary dysfunction. J. Am. Soc. Nephrol. *17*, 1015–1025.

Navis, A., Marjoram, L., and Bagnat, M. (2013). Cftr controls lumen expansion and function of Kupffer's vesicle in zebrafish. Development *140*, 1703–1712.

Neugebauer, J.M., Amack, J.D., Peterson, A.G., and Bisgrove, B.W. (2009). FGF Signaling during embryo development regulates cilia length in diverse epithelia. Nature *458*, 651–654.

Neugebauer, J.M., Cadwallader, A.B., Amack, J.D., Bisgrove, B.W., and Yost, H.J. (2013). Differential roles for 3-OSTs in the regulation of cilia length and motility. Development *140*, 3892–3902.

Newton, F.G., zur Lage, P.I., Karak, S., Moore, D.J., Göpfert, M.C., and Jarman, A.P. (2012). Forkhead Transcription Factor Fd3F Cooperates with Rfx to Regulate a Gene Expression Program for Mechanosensory Cilia Specialization. Dev. Cell *22*, 1221–1233.

Noël, E.S., Verhoeven, M., Lagendijk, A.K., Tessadori, F., Smith, K., Choorapoikayil, S., den Hertog, J., and Bakkers, J. (2013). A Nodal-independent and tissue-intrinsic mechanism controls heart-looping chirality. Nat. Commun. *4*.

Nolan, K., and Thompson, T.B. (2014). The DAN family: Modulators of TGF-b signaling and beyond. Protein Sci. *23*, 999–1012.

Nonaka, S., Tanaka, Y., Okada, Y., Takeda, S., Harada, A., Kanai, Y., Kido, M., and Hirokawa, N. (1998). Randomization of left-right asymmetry due to loss of nodal cilia generating leftward flow of extraembryonic fluid in mice lacking KIF3B motor protein. Cell *95*, 829–837.

Nonaka, S., Shiratori, H., Saijoh, Y., and Hamada, H. (2002). Determination of left-right patterning of the mouse embryo by artificial nodal flow. Nature *418*, 96–99.

Nonaka, S., Yoshiba, S., Watanabe, D., Ikeuchi, S., Goto, T., Marshall, W.F., and Hamada, H. (2005). De novo formation of left-right asymmetry by posterior tilt of nodal cilia. PLoS Biol. *3*.

Ocaña, O.H., Coskun, H., Minguillón, C., Murawala, P., Tanaka, E.M., Galcerán, J., Muñoz-Chápuli, R., and Nieto, M.A. (2017). A right-handed signalling pathway drives heart looping in vertebrates. Nature *549*, 86–90.

Odate, T., Takeda, S., Narita, K., and Kawahara, T. (2016). 9+0 and 9+2 cilia are randomly dispersed in the mouse node. Microscopy *65*, 119–126.

Ohi, Y., and Wright, C.V.E. (2007). Anteriorward shifting of asymmetric Xnr1 expression and contralateral communication in left-right specification in Xenopus. Dev Biol. *301*, 447–463.

Okabe, N., Xu, B., and Burdine, R.D. (2008). Fluid dynamics in zebrafish Kupffer's vesicle. Dev. Dyn. *237*, 3602–3612.

Okada, Y., Nonaka, S., Tanaka, Y., Saijoh, Y., Hamada, H., and Hirokawa, N. (1999). Abnormal nodal flow precedes situs inversus in iv and inv mice. Mol. Cell *4*, 459–468.

Okada, Y., Takeda, S., Tanaka, Y., Belmonte, J.I., Hirokawa, N., and Jolla, L. (2005). Mechanism of Nodal Flow : A Conserved Symmetry Breaking Event in Left-Right Axis Determination. Cell *121*, 633–644.

Oki, S., Hashimoto, R., Okui, Y., Shen, M.M., Mekada, E., Otani, H., Saijoh, Y., and Hamada, H. (2007). Sulfated glycosaminoglycans are necessary for Nodal signal transmission from the node to the left lateral plate in the mouse embryo. Development *134*, 3893–3904.

Oki, S., Kitajima, K., Marques, S., Belo, J.A., Yokoyama, T., Hamada, H., and Meno, C. (2009). Reversal of left-right asymmetry induced by aberrant Nodal signaling in the node of mouse embryos. Development *136*, 3917–3925.

Osada, S.-I., Saijoh, Y., Frisch, A., Yeo, C.-Y., Adachi, H., Watanabe, M., Whitman, M., Hamada, H., and Wright, C.V.E. (2000). Activin/nodal responsiveness and asymmetric expression of a Xenopus nodal-related gene converge on a FAST-regulated module in intron 1. Development *127*, 2503–2514.

Oteíza, P., Köppen, M., Concha, M.L., and Heisenberg, C.-P. (2008). Origin and shaping of the laterality organ in zebrafish. Development *135*, 2807–2813.

Pala, R., Alomari, N., and Nauli, S.M. (2017). Primary cilium-dependent signaling mechanisms. Int. J. Mol. Sci. *18*.

Pearce, J.J.H., Penny, G., and Rossant, J. (1999). A Mouse Cerberus / Dan-Related Gene Family. Dev. Biol. *110*, 98–110.

Peng, H.-C., Wang, Y.-H., Wen, C.-C., Wang, W.-H., Cheng, C.-C., and Chen, Y.-H. (2010). Nephrotoxicity assessments of acetaminophen during zebrafish embryogenesis. Comp. Biochem. Physiol. Part C Toxicol. Pharmacol. *151*, 480–486.

Pennekamp, P., Karcher, C., Fischer, A., Schweickert, A., Skryabin, B., Horst, J., Blum, M., and Dworniczak, B. (2002). The ion channel polycystin-2 is required for left-right axis determination in mice. Curr. Biol. *12*, 938–943.

Peterson, R.T., and MacRae, C.A. (2012). Systematic Approaches to Toxicology in the Zebrafish. Annu. Rev. Pharmacol. Toxicol. *52*, 433–453.

Pham, D.-H., Zhang, C., and Yin, C. (2017). Using zebrafish to model liver diseases-Where do we stand? Curr. Pathobiol. Rep. *5*, 207–221.

Piccolo, S., Agius, E., Leyns, L., Bhattacharya, S., Grunz, H., Bouwmeester, T., and De Robertis, E.M. (1999). The head inducer cerberus is a multifunctional antagonist of nodal, BMP and Wnt signals. Nature *397*, 707–710.

Piedra, M.E., Icardo, J.M., Albajar, M., Rodriguez-Rey, J.C., and Ros, M.A. (1998). Pitx2 participates in the late phase of the pathway controlling left- right asymmetry. Cell *94*, 319–324.

Pintado, P., Sampaio, P., Tavares, B., Montenegro-Johnson, T.D., Smith, D.J., and Lopes, S.S. (2017). Dynamics of cilia length in left-right development. R. Soc. Open Sci. *4*, 161102.

Potts, K.S., and Bowman, T. V. (2017). Modeling Myeloid Malignancies Using Zebrafish. Front. Oncol. *7*, 1–13.

Rankin, C.T., Bunton, T., Lawler, A.M., and Lee, S.-J. (2000). Regulation of left-right patterning in mice by growth/differentiation factor-1. Nat. Genet. *24*, 262.

Raya, Á., Kawakami, Y., Rodríguez-Esteban, C., Buscher, D., Koth, C.M., Itoh, T., Morita, M., Raya, R.M., Dubova, I., Bessa, J.G., et al. (2003). Notch activity induces Nodal expression and mediates the establishment of left-right asymmetry in vertebrate embryos. Genes Dev. *17*, 1213–1218.

Rider, S.A., Tucker, C.S., del-Pozo, J., Rose, K.N., MacRae, C.A., Bailey, M.A., and Mullins, J.J. (2012). Techniques for the in vivo assessment of cardio-renal function in zebrafish (Danio rerio) larvae. J. Physiol. *590*, 1803–1809.

Rothschild, S.C., Francescatto, L., Drummond, I.A., and Tombes, R.M. (2011). CaMK-II is a PKD2 target that promotes pronephric kidney development and stabilizes cilia. Development *138*, 3387–3397.

Roxo-Rosa, M., Jacinto, R., Sampaio, P., and Lopes, S.S. (2015). The zebrafish Kupffer's vesicle as a model system for the molecular mechanisms by which the lack of Polycystin-2 leads to stimulation of

CFTR. Biol. Open *4*, 1356–1366.

Saijoh, Y., Adachi, H., Mochida, K., Ohishi, S., Hirao, A., and Hamada, H. (1999). Distinct transcriptional regulatory mechanisms underlie left – right asymmetric expression of lefty-1 and lefty-2. Genes Dev. 259–269.

Saijoh, Y., Adachi, H., Sakuma, R., Yeo, C.Y., Yashiro, K., Watanabe, M., Hashiguchi, H., Mochida, K., Ohishi, S., Kawabata, M., et al. (2000). Left-right asymmetric expression of lefty2 and nodal is induced by a signaling pathway that includes the transcription factor FAST2. Mol. Cell *5*, 35–47.

Saijoh, Y., Oki, S., Ohishi, S., and Hamada, H. (2003). Left-right patterning of the mouse lateral plate requires Nodal produced in the node. Dev. Biol. *256*, 160–172.

Sakuma, R., Ohnishi, Y., Meno, C., Fujii, H., Juan, H., Takeuchi, J., Ogura, T., Li, E., Miyazono, K., and Hamada, H. (2002). Inhibition of Nodal signalling by Lefty mediated through interactionwithcommon receptors and efficient diffusion. Genes Cells *7*, 401–412.

Sampaio, P., Ferreira, R.R., Guerrero, A., Pintado, P., Tavares, B., Amaro, J., Smith, A.A., Montenegro-Johnson, T., Smith, D.J., and Lopes, S.S. (2014). Left-right organizer flow dynamics: how much cilia activity reliably yields laterality? Dev. Cell *29*, 716–728.

Saund, R.S., Kanai-Azuma, M., Kanai, Y., Kim, I., Lucero, M.T., and Saijoh, Y. (2012). Gut endoderm is involved in the transfer of left-right asymmetry from the node to the lateral plate mesoderm in the mouse embryo. Development *139*, 2426–2435.

Schier, A.F. (2003). Nodal Signaling in Vertebrate Development. Annu. Rev. Cell Dev. Biol. *19*, 589–621.

Schmierer, B., and Hill, C.S. (2007). TGFβ–SMAD signal transduction: molecular specificity and functional flexibility. Nat. Rev. Mol. Cell Biol. *8*, 970.

Schneider, I., Houston, D.W., Rebagliati, M.R., and Slusarski, D.C. (2008). Calcium fluxes in dorsal forerunner cells antagonize beta-catenin and alter left-right patterning. Development *135*, 75–84.

Schneider, I., Schneider, P.N., Derry, S.W., Lin, S., Barton, L.J., Westfall, T., and Slusarski, D.C. (2010). Zebrafish Nkd1 promotes Dvl degradation and is required for left-right patterning. Dev. Biol. *348*, 22–33.

Schoenberg, D.R., and Maquat, L.E. (2012). Regulation of cytoplasmic mRNA decay. Nat. Rev. Genet. *13*.

Schottenfeld, J., Sullivan-Brown, J., and Burdine, R.D. (2007). Zebrafish curly up encodes a Pkd2 ortholog that restricts left-side-specific expression of southpaw. Development *134*, 1605–1615.

Schweickert, A., Vick, P., Getwan, M., Weber, T., Schneider, I., Eberhardt, M., Beyer, T., Pachur, A., and Blum, M. (2010). The nodal inhibitor Coco is a critical target of leftward flow in Xenopus. Curr. Biol. *20*, 738–743.

Shen, M.M., and Schier, A.F. (2000). The EGF-CFC gene family invertebrate development. Genet. *16*, 303–309.

Shen, M.M., Wang, H., and Leder, P. (1997). A differential display strategy identifies Cryptic, a novel EGF-related gene expressed in the axial and lateral mesoderm during mouse gastrulation. Development *124*, 429–442.

Shi, Y., and Massague, J. (2003). Mechanisms of TGF-beta signaling from cell membrane to the nucleus. Cell *113*, 685–700.

Shinohara, K., Kawasumi, A., Takamatsu, A., Yoshiba, S., Botilde, Y., Motoyama, N., Reith, W., Durand, B., Shiratori, H., and Hamada, H. (2012). Two rotating cilia in the node cavity are sufficient to break left–right symmetry in the mouse embryo. Nat. Commun. *3*.

Shinohara, K., Chen, D., Nishida, T., Misaki, K., Nishida, T., Misaki, K., and Yonemura, S. (2015). Absence of Radial Spokes in Mouse Node Cilia Is Required for Rotational Movement but Confers Ultrastructural Instability as a Trade-Off Article Absence of Radial Spokes in Mouse Node Cilia Is Required for Rotational Movement but Confers Ultrastructural In. Dev. Cell *35*, 236–246.

Smith, D.J., Gaffney, E.A., and Blake, J.R. (2007). Discrete cilia modelling with singularity distributions: application to the embryonic node and the airway surface liquid. Bull. Math. Biol. *69*, 1477–1510.

Smith, D.J., Montenegro-Johnson, T.D., and Lopes, S.S. (2014). Organized chaos in Kupffer's vesicle: How a heterogeneous structure achieves consistent left-right patterning. Bioarchitecture *4*, 119–125.

Song, H., Hu, J., Chen, W., Elliott, G., Andre, P., Gao, B., and Yang, Y. (2010). Planar cell polarity breaks the bilateral symmetry by controlling ciliary positioning. Nature *466*, 378–382.

Soroldoni, D., Bajoghli, B., Aghaallaei, N., and Czerny, T. (2007). Dynamic expression pattern of Nodal-related genes during left-right development in medaka. Gene Expr. Patterns *7*, 93–101.

Stubbs, J.L., Oishi, I., Izpisúa Belmonte, J.C., and Kintner, C. (2008). The forkhead protein Foxj1 specifies node-like cilia in Xenopus and zebrafish embryos. Nat. Genet. *40*, 1454–1460.

Sulik, K., Dehart, D.B., Inagaki, T., Carson, J.L., Vrablic, T., Gesteland, K., and Schoenwolf, G.C. (1994). Morphogenesis of the murine node and notochordal plate. Dev. Dyn. *201*, 260–278.

Supp, D.M., Witte, D.P., Potter, S.S., and Brueckner, M. (1997). Mutation of an axonemal dynein affects left-right asymmetry in inversus viscerum mice. Nature *389*, 963–966.

Supp, D.M., Brueckner, M., Kuehn, M.R., Witte, D.P., Lowe, L.A., McGrath, J., Corrales, J., and Potter, S.S. (1999). Targeted deletion of the ATP binding domain of left-right dynein confirms its role in specifying development of left-right asymmetries. Development *126*, 5495–5504.

Takeda, S., Yonekawa, Y., Tanaka, Y., Okada, Y., Nonaka, S., and Hirokawa, N. (1999). Left-right asymmetry and kinesin superfamily protein KIF3A: new insights in determination of laterality and mesoderm induction by kif3A-/- mice analysis. J. Cell Biol. *145*, 825–836.

Tanaka, C., Sakuma, R., Nakamura, T., Hamada, H., and Saijoh, Y. (2007). Long-range action of Nodal requires interaction with GDF1. Genes Dev. *21*, 3272–3282.

Tanaka, Y., Okada, Y., and Hirokawa, N. (2005). FGF-induced vesicular release of Sonic hedgehog and retinoic acid in leftward nodal flow is critical for left – right determination. Nature *435*, 172–177.

Tavares, B., Jacinto, R., Sampaio, P., Pestana, S., Gardner, R., Lopes, T., Lopes, S.S., Schilling, B., Henry, I., and Sau, L. (2017). Notch / Her12 signalling modulates , motile / immotile cilia ratio downstream of Foxj1a in zebrafish left-right organizer. Elife *6:e25165*, 1–26.

Tian, J., Andree, B., Jones, C.M., and Sampath, K. (2008). The pro-domain of the zebrafish Nodal-related protein Cyclops regulates its signaling activities. Development *135*, 2649–2658.

Tsukui, T., Capdevila, J., Tamura, K., Ruiz-Lozano, P., Rodriguez-Esteban, C., Yonei-Tamura, S., Magallon, J., Chandraratna, R.A.S., Chien, K., Blumberg, B., et al. (1999). Multiple left-right asymmetry defects in Shh-/- mutant mice unveil a convergence of the Shh and retinoic acid pathways in the control of Lefty-1. Proc. Natl. Acad. Sci. *96*, 11376–11381.

Turing, A.M. (1952). The chemical basis of morphogenesis. Philos. Trans. R. Soc. London *237*, 37–72.

Viotti, M., Niu, L., Shi, S.-H., and Hadjantonakis, A.-K. (2012). Role of the gut endoderm in relaying left-right patterning in mice. PLoS Biol. *10*, e1001276.

Vonica, A., and Brivanlou, A.H. (2007). The left-right axis is regulated by the interplay of Coco, Xnr1 and derriere in Xenopus embryos. Dev Biol. *303*, 281–294.

Walentek, P., Beyer, T., Thumberger, T., Schweickert, A., and Blum, M. (2012). ATP4a is required for Wnt-dependent Foxj1 expression and leftward flow in Xenopus left-right development. Cell Rep. *1*, 516–527.

Wang, X., and Yost, H.J. (2008). Initiation and propagation of posterior to anterior (PA) waves in zebrafish left-right development. Dev. Dyn. *237*, 3640–3647.

Wang, G., Cadwallader, A.B., Jang, D.S., Tsang, M., Yost, H.J., and Amack, J.D. (2011). The Rho kinase Rock2b establishes anteroposterior asymmetry of the ciliated Kupffer's vesicle in zebrafish. Development *138*, 45–54.

Wang, G., Manning, M.L., and Amack, J.D. (2012). Regional cell shape changes control form and function of Kupffer's vesicle in the zebrafish embryo. Dev. Biol. *370*, 52–62.

Wang, Y., Wang, X., Wohland, T., and Sampath, K. (2016). Extracellular interactions and ligand degradation shape the nodal morphogen gradient. Elife *5*, 1–19.

Westhoff, J.H., Giselbrecht, S., Schmidts, M., Schindler, S., Beales, P.L., Tönshoff, B., Liebel, U., and Gehrig, J. (2013). Development of an automated imaging pipeline for the analysis of the zebrafish larval kidney. PLoS One *8*, e82137.

Whitman, M. (2001). Nodal signaling in early vertebrate embryos: themes and variations. Dev. Cell 605–617.

Wingert, R.A., Selleck, R., Yu, J., Song, H.-D., Chen, Z., Song, A., Zhou, Y., Thisse, B., Thisse, C., McMahon, A.P., et al. (2007). The cdx genes and retinoic acid control the positioning and segmentation of the zebrafish pronephros. PLoS Genet. *3*, 1922–1938.

Wolpert, L. (1969). Positional information and the spatial pattern of cellular differentiation. J. Theor. Biol *25*.

Yamamoto, M., Mine, N., Mochida, K., Sakai, Y., Saijoh, Y., Meno, C., and Hamada, H. (2003). Nodal signaling induces the midline barrier by activating Nodal expression in the lateral plate. Development *130*, 1795–1804.

Yamanaka, Y., Tamplin, O.J., Beckers, A., Gossler, A., and Rossant, J. (2007). Live Imaging and Genetic Analysis of Mouse Notochord Formation Reveals Regional Morphogenetic Mechanisms. Dev. Cell *13*, 884–896.

Yamazaki, H., Nakata, T., Okada, Y., and Hirokawa, N. (1995). KIF3A/B: A heterodimeric kinesin superfamily protein that works as a microtubule plus end-directed motor for membrane organelle transport. J. Cell Biol. *130*, 1387–1399.

Yan, Y., Gritsman, K., Ding, J., Burdine, R.D., Corrales, J.D., Price, S.M., Talbot, W.S., Schier, A.F., and Shen, M.M. (1999). Conserved requirement for EGF – CFC genes in vertebrate left – right axis formation. Genes Dev. *13*, 2527–2537.

Yashiro, K., Saijoh, Y., Sakuma, R., Tada, M., Tomita, N., Amano, K., Matsuda, Y., Monden, M., Okada, S., and Hamada, H. (2000). Distinct transcriptional regulation and phylogenetic divergence of human LEFTY genes. Genes to Cells *5*, 343–357.

Yeo, C., and Whitman, M. (2001). Nodal signals to Smads through Cripto-dependent and Cripto-independent mechanisms. Mol. Cell 949–957.

Yokouchi, Y., Vogan, K.J., Pearse, R. V., and Tabin, C.J. (1999). Antagonistic signaling by Caronte, a

novel Cerberus-related gene, establishes left-right asymmetric gene expression. Cell *98*, 573–583.

Yokoyama, T., Copeland, N.G., Jenkins, N.A., Montgomery, C.A., Elder, F.F., and Overbeek, P.A. (1993). Reversal of left-right asymmetry: a situs inversus mutation. Science (80-.). *260*, 679 LP-682.

Yoshiba, S., Shiratori, H., Kuo, I.Y., Kawasumi, A., Shinohara, K., Nonaka, S., Asai, Y., Sasaki, G., Belo, J.A., Sasaki, H., et al. (2012). Cilia at the Node of Mouse Embryos Sense Fluid Flow for Left-Right Determination via Pkd2. Science (80-.). *338*, 226–231.

Yoshioka, H., Meno, C., Koshiba, K., Sugihara, M., Itoh, H., Ishimaru, Y., Inoue, T., Ohuchi, H., Semina, E. V., Murray, J.C., et al. (1998). Pitx2, a bicoid-type homeobox gene, is involved in a lefty-signaling pathway in determination of left-right asymmetry. Cell *94*, 299–305.

Yu, X., Ng, C.P., Habacher, H., and Roy, S. (2008). Foxj1 transcription factors are master regulators of the motile ciliogenic program. Nat. Genet. *40*, 1445–1453.

Yuan, S., Zhao, L., Brueckner, M., and Sun, Z. (2015). Intraciliary Calcium Oscillations Initiate Vertebrate Left-Right Asymmetry. Curr. Biol. *25*, 1–12.

Zhang, M., Zhang, J., Lin, S.-C., and Meng, A. (2012). β-Catenin 1 and β-catenin 2 play similar and distinct roles in left-right asymmetric development of zebrafish embryos. Development *139*, 2009–2019.

Zhou, X., Sasaki, H., Lowe, L.A., Hogan, B.L., and Kuehn, M.R. (1993). Nodal is a novel TGF-beta-like gene expressed in the mouse node during gastrulation. Nature *361*, 543–547.

Zhu, P., Xu, X., and Lin, X. (2015). Both ciliary and non-ciliary functions of Foxj1a confer Wnt/ -catenin signaling in zebrafish left-right patterning. Biol. Open *4*, 1376–1386.

CHAPTER 2

Notch/Her12 signalling modulates motile/immotile cilia ratio downstream of *Foxj1a* in zebrafish left-right organizer

"Now, when you work out where to draw the line your guess is as good as mine"

Coldplay, God put a smile upon your face

eLIFE elifesciences.org

RESEARCH ARTICLE

Notch/Her12 signalling modulates, motile/immotile cilia ratio downstream of *Foxj1a* in zebrafish left-right organizer

Barbara Tavares[1†], Raquel Jacinto[1†], Pedro Sampaio[1], Sara Pestana[1], Andreia Pinto[2], Andreia Vaz[1], Mónica Roxo-Rosa[1], Rui Gardner[3], Telma Lopes[3], Britta Schilling[4], Ian Henry[4], Leonor Saúde[5], Susana Santos Lopes[1*]

[1]CEDOC, Chronic Diseases Research Centre, NOVA Medical School - Faculdade de Ciências Médicas, Universidade Nova de Lisboa, Lisboa, Portugal; [2]Laboratório de Histologia e Patologia Comparada, Instituto de Medicina Molecular, Centro Académico de Medicina de Lisboa, Lisboa, Portugal; [3]Instituto Gulbenkian de Ciência, Oeiras, Portugal; [4]MPI of Molecular Cell Biology and Genetics, Dresden, Germany; [5]Instituto de Medicina Molecular e Instituto de Histologia e Biologia do Desenvolvimento, Faculdade de Medicina da Universidade de Lisboa, Lisboa, Portugal

Abstract Foxj1a is necessary and sufficient to specify motile cilia. Using transcriptional studies and slow-scan two-photon live imaging capable of identifying the number of motile and immotile cilia, we now established that the final number of motile cilia depends on Notch signalling (NS). We found that despite all left-right organizer (LRO) cells express *foxj1a* and the ciliary axonemes of these cells have dynein arms, some cilia remain immotile. We identified that this decision is taken early in development in the Kupffer's Vesicle (KV) precursors the readout being *her12* transcription. We demonstrate that overexpression of either *her12* or Notch intracellular domain (NICD) increases the number of immotile cilia at the expense of motile cilia, and leads to an accumulation of immotile cilia at the anterior half of the KV. This disrupts the normal fluid flow intensity and pattern, with consequent impact on *dand5* expression pattern and left-right (L-R) axis establishment.

DOI: https://doi.org/10.7554/eLife.25165.001

***For correspondence:** susana.lopes@fcm.unl.pt

[†]These authors contributed equally to this work

Competing interests: The authors declare that no competing interests exist.

Funding: See page 22

Received: 16 January 2017
Accepted: 03 September 2017
Published: 06 September 2017

Reviewing editor: Jeremy F Reiter, University of California, San Francisco, United States

Introduction

Embryonic motile cilia play an essential role in body laterality patterning by generating a directional fluid flow inside the vertebrate left-right organizer (LRO) (***Nonaka et al., 1998***; ***Takeda et al., 1999***; ***Nonaka et al., 2002***). The mouse LRO (or node) is lined with monociliated cells, presenting motile and immotile cilia (***McGrath et al., 2003***). While motile cilia in the pit region generate a directional fluid flow (the nodal flow), the immotile cilia, present mostly in the perinodal crown cells, are thought to be able to sense it (***McGrath et al., 2003***). This sensing mechanism is still unknown and continues to deserve tentative updates in the field both using the mouse model (***Delling et al., 2016***) and the zebrafish model (***Ferreira et al., 2017***). Whether it involves mechano- or chemosensation, or both, is still not demonstrated but it is known to lead to the activation of the channel Polycystin-2 (PKD2) (***Yoshiba et al., 2012***). This channel was elegantly shown to be necessary for the asymmetric expression of *dand5* (DAN domain family, member 5) on the right side of the mouse node (***Yoshiba et al., 2012***) and consequently allowing the propagation of Nodal into the left Lateral plate mesoderm (LPM) (***Marques et al., 2004***). This signal is amplified via a self-enhanced lateral-inhibition system (SELI) (***Nakamura et al., 2006***) at the left LPM, which consists in the activation of the genetic

cascade Nodal-Pitx2-Lefty2 and ends with the correct formation and asymmetric positioning of the visceral organs (**Nonaka et al., 2002**).

In zebrafish, the left-right (L-R) axis establishment starts in a fluid-filled organ designated Kupffer's vesicle (KV) (**Essner et al., 2005**; **Kramer-Zucker et al., 2005**). Functionally, this organ is the homologue of other vertebrate LROs like the mouse node (**Nonaka et al., 2002**) and the gastrocoel roof plate in *Xenopus* (**Schweickert et al., 2007**). The KV originates from a cluster of cells, the dorsal forerunner cells (DFCs), which migrate in the forefront of the shield during gastrulation (**Cooper and D'Amico, 1996**). At the end of gastrulation, the DFCs form an ellipsoid fluid filled vesicle. While KV lumen inflates each cell extends one cilium towards the lumen (**Amack et al., 2007**; **Oteíza et al., 2008**). As in the mouse node, the KV cilia also produce a directional fluid flow that leads to an asymmetric *dand5* gene expression (**Lopes et al., 2010**; **Sampaio et al., 2014**). Our previous work determined that KV cilia can also be divided into two populations according to whether they are functionally motile or immotile (**Sampaio et al., 2014**). We also showed that the DeltaD zebrafish mutant ($dld^{-/-}$) for Notch signalling (NS) presents an increase in the number of motile cilia in the LRO (**Sampaio et al., 2014**), suggesting that NS may modulate the number of motile cilia in this organ. Equivalently, Boskovski *et al.* reported that GALNT11, an *N*-acetylgalactosamine type *O*-glycosylation enzyme needed to activate NS, regulates the ratio between motile and immotile cilia in the *Xenopus'* LRO, where less NS also increased the number of motile cilia (**Boskovski et al., 2013**). The authors showed that changing the ratio between motile and immotile cilia caused downstream defects in L-R patterning of the laterality marker *pitx2c* (*paired-like homeodomain 2*), and in the correct heart looping of *Xenopus* embryos (**Boskovski et al., 2013**).

The transcription factor Forkhead box J1a (Foxj1a) has been established as the motile cilia master regulator in the KV cells (**Stubbs et al., 2008**; **Yu et al., 2008**). Without it cilia do not form, altering the expression of L-R markers and randomizing organ *situs* (**Tian et al., 2009**). Its transcription initiates during gastrulation in the DFCs, and Foxj1a is responsible for the transcriptional activation of several motility genes, such as *dnah7* (**Choksi et al., 2014**) and *dnah9* (axonemal heavy chain dyneins that mediate the movement of cilia by hydrolysing ATP) (**Yu et al., 2008**; **Choksi et al., 2014**). This suggests that in wild type (WT) embryos, where motile and immotile cilia are present in neighbouring cells (**Sampaio et al., 2014**), Foxj1a function may be antagonized by other factors, explaining why cilia remain immotile in some cells.

In order to understand the mechanisms behind the choice of motile *versus* immotile cilia, we manipulated NS and Foxj1a levels and evaluated their impact in the ratio of motile and immotile cilia in the zebrafish LRO. We concluded that, independently from variations in *foxj1a* mRNA levels, all cilia seem to acquire a motile ultrastructure. However, NS modulates the final number of functionally moving cilia early in the KV precursors, via a mechanism that involves the activity of Her12 (hairy-related 12), a transcription repressor so far only involved in somitogenesis (**Shankaran et al., 2007**). We then experimentally showed that Her12 mediated motile/immotile cilia ratio imbalance impacts not only on fluid flow intensity but also on its pattern. This supports our previous data showing that for the KV to develop a robust fluid flow, capable of promoting normal organ *situs*, it requires a minimum of 30 motile cilia and an anterior-dorsal cluster of motile cilia (**Sampaio et al., 2014**; **Smith et al., 2014**). Overall, the evidence presented demonstrates the importance of regulating the motile/immotile cilia ratio in the generation of a robust and functional fluid flow in the zebrafish LRO.

Results

Cilia in the KV become motile as development progresses

As the KV starts to form and inflate, cilia begin to emerge and some start to beat, generating a fluid flow (**Essner et al., 2005**; **Kramer-Zucker et al., 2005**), while others remain static (**Sampaio et al., 2014**). How this dichotomy evolves over time is unknown. We thus questioned whether the percentage of immotile cilia at the 8-somites stage (ss) was the same since the beginning of the LRO formation. To better understand this phenomenon, we injected WT zebrafish embryos at the 1 cell stage with a titrated, non-toxic concentration of *arl13b-GFP mRNA*, and performed live imaging in a two-photon microscope. By scanning the whole KV at a low speed (0.16 frames per second, fps) in a slow scanning mode by using a high pixel dwell time (22.4 microseconds) (**Video 1**; **Figure 1A**) it was

possible to accurately distinguish the motile cilia (***Figure 1B***) from the immotile cilia (***Figure 1C***), quantify them, and track them throughout the KV development. An higher pixel dwell time allows to better identify motile from immotile cilia, thus explaining some differences in quantification of immotile cilia in comparison with another recent work (***Ferreira et al., 2017***), We then imaged the same embryos from 3 to 8 ss (5 embryos; 294 cilia); we identified every motile and immotile cilium at each time point using the 3D stacks acquired, and then tracked them throughout time in 3D projections (***Video 2***).

The results showed that at 3 ss, the vast majority of cilia were immotile (***Figure 1D***) and cilia distribution and KV cell shape were homogeneous (***Figure 1F and G***). Between 3 and 5 ss, we observed the highest rate of increase in the percentage of motile cilia (***Figure 1D, F–K***), which then tended to stabilize at 6–8 ss (***Figure 1D, L–O***). This is accompanied with a change in KV cell shape and anterior-dorsal cluster formation as previously reported (***Wang et al., 2012***). While tracking cilia, we observed two main different types of cilia behaviour (***Figure 1E***; 4 embryos; 231 cilia). We found that 79 ± 7% of cilia transitioned from immotile at 3 ss to motile at 8 ss (***Figure 1E***), while 16 ± 8% of cilia never became motile during the time-window of the assay (***Figure 1E***). We reasoned that if immotile cilia are always immotile from the beginning to the end of the KV lifetime then something should be determining the fate of such cilia very early in development.

In agreement with the increase in number of motile cilia from 3 to 8 ss, we also observed changes in the pattern of the KV fluid flow throughout development (***Figure 2***). As we had previously reported (***Sampaio et al., 2014***) we can calculate the speed and direction of the KV fluid flow by tracking native particles present in the KV by bright field microscopy (***Figure 2—videos 1–3***). Therefore, at 3–4 ss we observed a complete absence of directional fluid flow (***Figure 2A and C***; 5 embryos; 258 tracks), with the native particles presenting what seemed to be Brownian motion (2.32 ± 0.95 µm s^{-1}; ***Figure 2—video 1***; ***Figure 2B***). This observation is in agreement with the low number of beating cilia found at 3 ss (6 ± 5%; ***Figure 1D***). Again, here our results contrast with those from ***Ferreira et al. (2017)***, which are built on numerical predictions of flow supported by a much lower number of immotile cilia. So, flow forces were calculated in different ways in the two studies, while we measured flow velocity by following native particles in live embryos averaged over a number of embryos, ***Ferreira et al. (2017)*** mapped cilia position and tilting in live embryos and then predicted the flow forces based on numerical simulations. As development progressed and the number of beating cilia increased (5 ss – 63 ± 23%; 6 ss – 76 ± 8%; ***Figure 1D***), we began to observe a weak directional fluid flow at 5–6 ss (6.61 ± 3.26 µm s^{-1}; ***Figure 2G***), which at this time was still homogeneous throughout the KV (***Figure 2—video 2***; ***Figure 2E*** – G; 5 embryos; 309 tracks). Finally, at 7–8 ss, when the number of beating cilia began to stabilize (8 ss – 83 ± 6%; ***Figure 1D***), the directional fluid flow acquired its characteristic velocity (9.81 ± 5.36 µm s^{-1}) and heterogeneous pattern (***Figure 2—video 3***) (***Sampaio et al., 2014***), presenting a faster flow at the anterior-left quadrant of the KV (***Figures 2I, K*** and ***3*** embryos, 128 tracks). While tracking native particles we could also account for cilia motility and thus by an independent method we confirmed our previous quantifications on the ratio between motile vs immotile cilia. This method was based on a high frame rate acquisitions (500 fps) using a high-speed video camera.. Again, we observed an increase in the percentage of motile cilia throughout development, ranging from 27% at 3–4 ss (4 embryos; 48 cilia; ***Figure 2D***), 70% at 5–6 ss (4 embryos; 63 cilia; ***Figure 2H***) to 84% at 7–8 ss (4 embryos; 89 cilia; ***Figure 2L***). We also determined the cilia beat frequency (CBF) at these three different stages and we found that

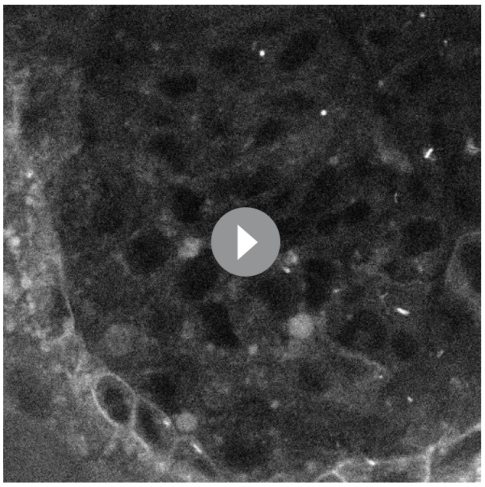

Video 1. Scan of Wild Type KV showing motile and immotile cilia. Embryo was injected with 400 pg Arl13b-GFP at 1 cell stage and imaged as described in ***Figure 1***. Anterior is to the top and Left is to left.
DOI: https://doi.org/10.7554/eLife.25165.004

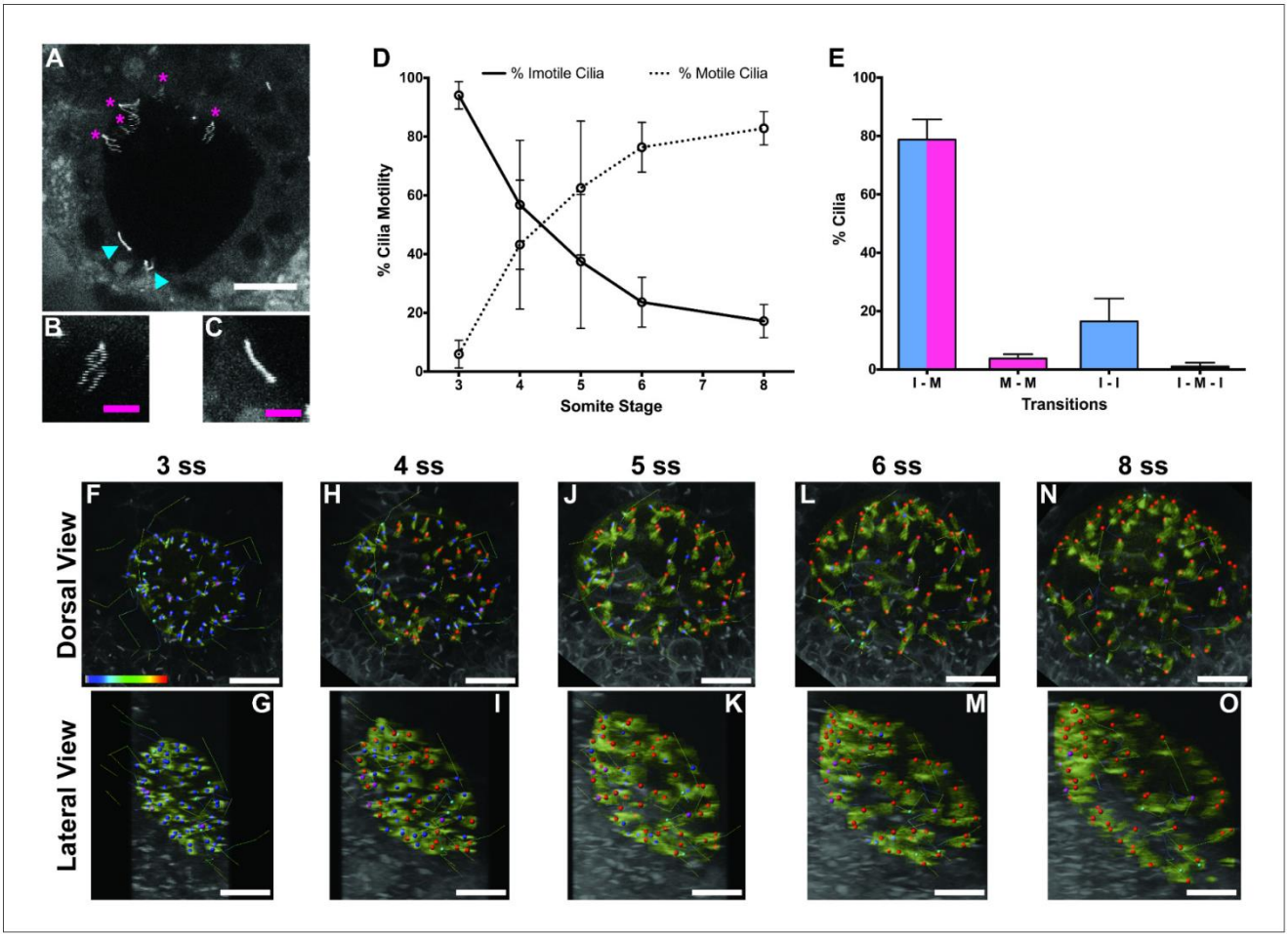

Figure 1. Immotile cilia are specified early in development. (**A**) Still from ***Video 1*** representing a wild-type embryo injected with 400 pg Arl13b-GFP at 1 cell stage. Anterior is up and Left is left. Blue arrowheads indicate – Immotile cilia; Magenta stars indicate Motile Cilia. Scale bar represents 20 μm. (**B–C**) Details of a Motile (**B**) and Immotile Cilia (**C**). Scale bar (magenta) represents 5 μm. (**D**) Changes in the % of Motile and Immotile Cilia in KV during zebrafish development from 3 to 8 somites stage (n_e = 5, n_c = 294). (**E**) Types of cilia motility behaviours found during the Time Lapse experiment (from 3 to 8 somites stage). I – M is 'Immotile to Motile', M – M is 'Always Motile', I – I is 'Always Immotile', and I – M – I is 'Immotile to Motile to Immotile' (n_e = 4, n_c = 231). (**F–O**) Stills from ***Video 2***, the time-lapse video obtained from a Control embryo injected with 400 pg Arl13b-GFP at 1 cell stage. Dorsal view – Anterior is to the top and Left is to left (**F, H, J, L, N**). Lateral view – Anterior is to the top and Dorsal is to left (**G, I, K, M, O**). Motile cilia (red), Immotile Cilia (blue), cilia that were always motile (from 3 to 8 ss – purple), cilia that remain always immotile (from 3 to 8 ss – cyan). In all images, scale bar represents 20 μm. n_e – number of embryos and n_c – number of cilia.

DOI: https://doi.org/10.7554/eLife.25165.002

The following source data is available for figure 1:

Source data 1. Contains data about the number of motile and immotile cilia from single embryos along development from 3 ss to 8 ss (n = 4).

DOI: https://doi.org/10.7554/eLife.25165.003

cilia beat faster as development progressed (***Figure 2D*** – L, right panels). The CBFs calculated were 33 ± 4 Hz (4 embryos; 8 cilia), 37 ± 5 Hz (4 embryos; 29 cilia), and 40 ± 4 Hz (4 embryos; 34 cilia) for the 3–4 ss, 5–6 ss and 7–8 ss, respectively. The ciliary frequency at 7–8 ss was significantly higher than at 3–4 ss. Overall the values found for the percentage of motile cilia together with the CBF may account for the differences found in the velocity of the fluid flow throughout development.

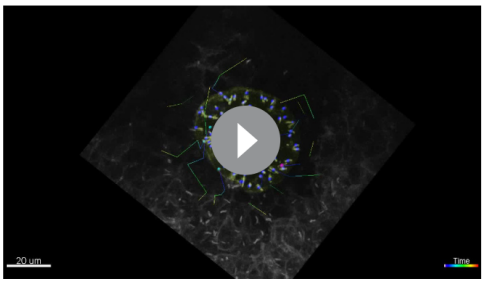

Video 2. Time lapse from 3 to 8 somites stage with respective cilia trackings. Tracking of the cilia was performed with Imaris software. Anterior is to the top and Left is to left.

DOI: https://doi.org/10.7554/eLife.25165.005

Transcriptomic studies support a boost of cilia motility gene expression in deltaD mutants

We have previously reported that *DeltaD* ($dld^{-/-}$) mutant embryos have more cilia moving in the KV than the WT (***Sampaio et al., 2014***), indicating that Notch signalling (NS) could be responsible for the decision between motility and immotility of cilia in the KV. To understand why $dld^{-/-}$ had more motile cilia than control embryos we performed a comparative transcriptomic analysis of DFCs from WT and $dld^{-/-}$ mutant zebrafish embryos (***Figure 3A–D***). After curation, we obtained a list of 706 genes with a linear fold change (FC) in transcription higher than 2 (Table S1a in ***Supplementary file 1***).

Our intention was to determine which genes in $dld^{-/-}$ mutants were implicated specifically in cilia motility. Therefore, we decided to use the $Cildb_{v2}$ reference base (***Arnaiz et al., 2009***) and Genevenn algorithm (***Pirooznia et al., 2007***) to determine the hits in our list that had orthologues already associated with cilia motility in other model organisms. We chose *Caenorhabditis elegans*, a primary cilia model; and *Chlamydomonas reinhardtii*, a motile cilia/flagella model (Table S1b in ***Supplementary file 1***). The intersection analysis between these models permitted us to distinguish the ciliary genes specific for motility in our list. Because *foxj1a* was up-regulated (FC = 1.62, p value = 0.029) in the microarray, we also compared our gene list with the list of Foxj1a-induced genes published by ***Choksi et al. (2014)***. The result of these intersections showed that 18% (129 genes) of the genes in our original list were related to ciliogenesis and of those, 67% (86 genes) were specifically related to motility (Table S1b in ***Supplementary file 1***). Motility specific column). Among these were the known motility axonemal genes *dnah7* and *dnah10* (Dynein, Axonemal, Heavy Chain 7 and 10), *rsph3* and *rsph9* (Radial Spoke Head 3 and 9) together with *dld*, *foxj1a* and *rfx2*. The axonemal genes were up-regulated in $dld^{-/-}$ mutants and were therefore good candidates to explain the increased number of motile cilia. To validate some of the motility-associated genes obtained in the microarray, we focused on the following genes: the ciliogenesis master regulator, *rfx2* (*regulator master x 2*) (***Swoboda et al., 2000***); the motile cilia master regulator *foxj1a*, the notch ligand, *dld*; and two motile cilia axonemal components, *dnah7* and *rsph3*. We performed quantitative PCR (qPCR) using mRNA extracted from fluorescently activated cell sorted DFCs. Of these 5 tested genes, only 3 (*foxj1a*, *dld*, and *dnah7*) showed consistent changes in transcription regulation between the two methods (***Figure 3E and F***), the microarray and qPCR analyses, also confirmed by in situ hybridization in bud stage and 8 somite stage (***Figure 3—figure supplement 1***).

Motile cilia fate decision is regulated by Notch signalling independently of Foxj1a

In order to check if Foxj1a, the master regulator of motility, was expressed in all KV cells or KV precursor cells, we decided to look at a zebrafish line that expresses GFP under a *foxj1a* minimal promoter (Tg:*foxj1a:GFP*) (***Caron et al., 2012***) and determined whether all WT KV cells were GFP positive. Our reasoning was that if we found that Foxj1a was absent in around 16–20% of WT DFCs, this alone could account for the lack of motility observed at 8 ss (***Figure 1D***). We fixed embryos at 8 ss and by immunofluorescence with an antibody against GFP and another against acetylated alpha-tubulin (***Figure 4—figure supplement 1C–E***; ***Video 3***), we confirmed that the number of *foxj1a*-positive cells and the number of cilia present in each KV were concordant (***Figure 4—figure supplement 1F***; p=0.9479, 7 embryos, 514 cells, 513 cilia). This experiment showed that *foxj1a:GFP* was present in all KV cells despite the fact that some cells have immotile cilia throughout development. So, we then questioned how this *foxj1a* promoter related to the actual mRNA expression. We confirmed that, as reported before by ***Yu et al. (2008)*** *foxj1a* mRNA is strongly expressed in the DFCs at bud stage (***Figure 4—figure supplement 1A***) (***Yu et al., 2008***). However, this early expression is

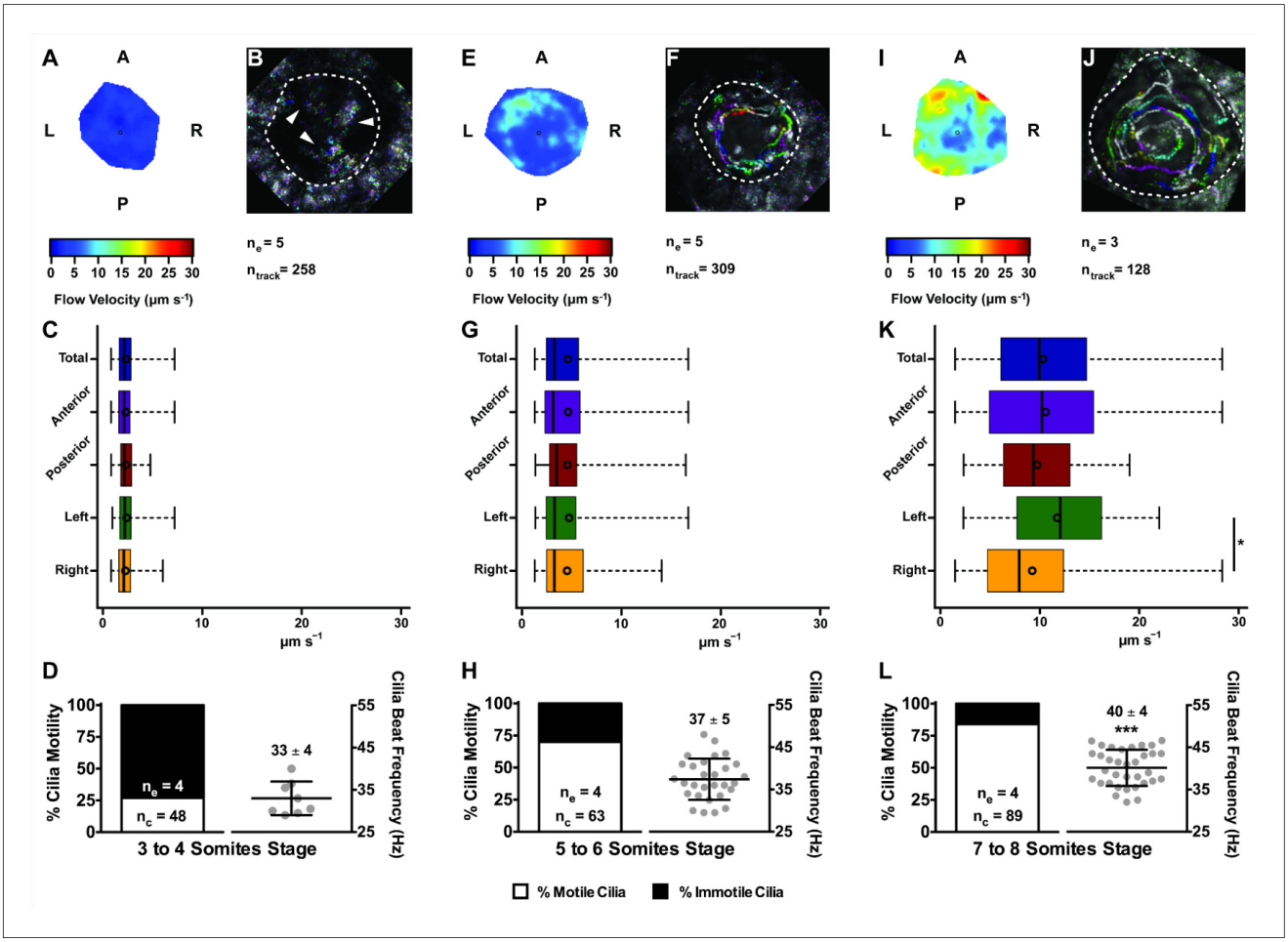

Figure 2. Changes in KV flow and CBF through development observed in uninjected WT embryos. Data was pooled from embryos at 3–4 (**A–D**), 5–6 (**E–H**), and 7–8 (**I–L**) somites stage. (**A, E, I**) Heat maps of flow speed showing detailed regions within the KV for pooled embryos in each experimental condition: 3–4 ss (**A**), 5–6 ss (**E**), and 7–8 ss (**I**). The pseudo-colour scale represents flow speed in µm s^{-1}, where red represents high speed versus low speed in blue. (**B, F, J**) Representative KV particle flow map for a WT embryo at 3–4 ss (**B**), 5–6 ss (**F**), and 7–8 ss (**J**). Each second is represented by a different colour. The particle Brownian motion in (**B**) is marked with white arrowheads. Anterior is to the top and Left is to left. (**C, G, K**) Box plots for instantaneous flow speed measured at different locations of the KVs, based on the same data set used to generate the heat maps, in each experimental condition: 3–4 ss (**C**), 5–6 ss (**G**), and 7–8 ss (**K**). Box plots display the median with a vertical line, and the whiskers represent the minimum and maximum values observed. Means are represented as small circles. *p<0.05, Wilcoxon test. (**D, H, L**) display the %motile and %immotile cilia found in the KV midplane (left panels) and the CBF measured in the motile cilia (right panels) of WT embryos in each experimental condition: 3–4 ss (**D**), 5–6 ss (**H**), and 7–8 ss (**L**). Values for CBF are Mean ±SD, ***p<0.001, ANOVA with Bonferroni's multiple comparisons test. n_e – number of embryos; n_{tracks} – number of tracks followed; n_c – number of cilia.

DOI: https://doi.org/10.7554/eLife.25165.006

Source data 1. Contains data from the native particles tracked to generate the flow maps on ***Figure 2***.

DOI: https://doi.org/10.7554/eLife.25165.010

Figure 2—video 1. Wild-type fluid flow at 3 ss. Movie from 1 WT, non-injected embryo. At this development stage, the native particles only present Brownian motion. Anterior is to the top and Left is to left. 30 frames per second.

DOI: https://doi.org/10.7554/eLife.25165.007

Figure 2—video 2. Wild-type fluid flow at 5 ss. Movie from 1 WT, non-injected embryo. At this development stage the KV presents a homogeneous directional fluid flow. Anterior is to the top and Left is to left. 30 frames per second.

DOI: https://doi.org/10.7554/eLife.25165.008

Figure 2—video 3. Wild-type fluid flow at 8 ss. Movie from 1 WT, non-injected embryo. At this development stage, the directional fluid flow is no longer homogeneous, presenting higher speeds at the anterior-left part of the KV. Anterior is to the top and Left is to left. 30 frames per second.

Figure 2 continued on next page

Figure 2 continued

DOI: https://doi.org/10.7554/eLife.25165.009

not yet seen with the *foxj1a*:GFP minimum promoter described by **Caron et al. (2012)** (**Figure 4—figure supplement 1**) (**Caron et al., 2012**). On the other hand, at 8 ss the mRNA expression of *foxj1a* is no longer observed in the KV, while it is detectable in the pronephros and neural tube, but the reporter shows GFP in all KV cells (**Figure 4—figure supplement 1B and C–E**, respectively). So, we must conclude that this promoter is not faithfully representing the *foxj1a* gene expression along time. However, by comparing the foxj1a *in situs* with another reporter line for DFCs, the sox17:GFP reporter, we showed that the *foxj1a* mRNA staining closely matches the sox17:GFP labelling (**Figure 4A–C**). Altogether these experiments suggest that *foxj1a* is expressed in all DFCs and that the foxj1a:GFP observed at 8 ss is due to a delayed reporter and/or GFP perdurance.

Moreover, the information that *foxj1a* was up-regulated in *dld*$^{-/-}$ mutant DFC cells (Table S1a in **Supplementary file 1** suggested a regulation of *foxj1a* expression by NS. Therefore, in order to understand the crosstalk between NS and *foxj1a* in regulating cilia motility, we monitored the transcription levels of *her12* (*hairy-related 12*), *dnah7* and *foxj1a* itself while manipulating NS and Foxj1a protein levels. These genes were chosen because: i) *her12* is a NS direct transcription target in the tail bud and somites (**Shankaran et al., 2007**) and in this study we found that it is highly expressed in DFCs at bud stage, and down-regulated in *dld*$^{-/-}$ mutants (Table S1a in **Supplementary file 1**) as previously described (**Thisse and Thisse, 2004**); and ii) *dnah7* was reported to be a transcriptional target of Foxj1a (**Choksi et al., 2014**) and an essential structural component of motile cilia, without which zebrafish KV cilia become static (**Sampaio et al., 2014**). Similar to the expression levels of *foxj1a*, we found *dnah7* significantly up-regulated in *dld*$^{-/-}$ mutants (**Figure 4—figure supplement 1H**) and expressed in DFCs at bud stage (Table S1a in **Supplementary file 1**). The restricted expression patterns of *her12*, *foxj1a* and *dnah7* at bud stage indicated that it was possible to use mRNA from whole embryos to determine their expression levels by qPCR (**Neugebauer et al., 2013**; **Jurisch-Yaksi et al., 2013**). As a control of this procedure, we tested *dnah9* and *rfx4*, two genes that, despite being transcribed in DFCs were not influenced by NS, according to our microarray and qPCR data (**Figure 4—figure supplement 1H**).

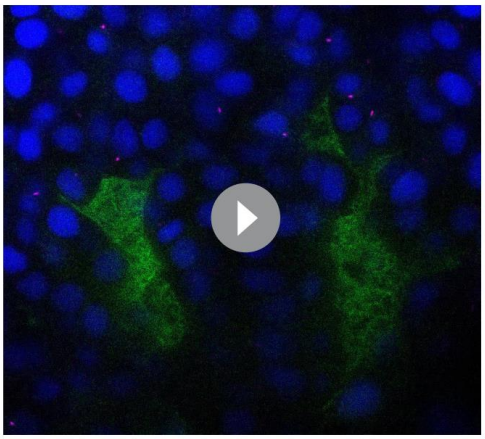

Video 3. Immuno-staining of a KV of an 8 ss embryo from the transgenic line Foxj1a:GFP. In blue are the nuclei stained with DAPI; in green the *foxj1a* positive KV cells; and in magenta are the KV cilia stained with antibody against acetylated α-tubulin. This experiment allowed us to determine if all monociliated KV cells expressed Foxj1a. Anterior is to the top and Left is to left.

DOI: https://doi.org/10.7554/eLife.25165.020

We then set out to manipulate the levels of NS by using the single mutants *dld*$^{-/-}$ and *delta like c* (*dlc*$^{-/-}$), and the double mutant *dlc*$^{-/-}$;*dld*$^{-/-}$. In order to increase NS we overexpressed Notch intracellular domain (NICD OE). Showing the efficiency of NS manipulations, the *her12* transcription levels behaved accordingly, being significantly lower in the *dld*$^{-/-}$;*dlc*$^{-/-}$ double mutant (**Figure 4D**), and significantly higher in the NICD OE (**Figure 4D**).

For each NS manipulation we also interfered with the levels of Foxj1a. This was assured either by knocking down the *foxj1a* expression with a morpholino against *foxj1a* translation start site (Foxj1a KD) or by overexpressing it *via* the injection of *Danio rerio foxj1a* mRNA (Foxj1a OE). As expected, the *dnah7* expression served as readout of the Foxj1a manipulation efficiency, as its expression significantly correlated both with the endogenous levels of Foxj1a (Foxj1a Not Manipulated; NM) and upon its overexpression (Foxj1a OE) (**Figure 4E**; Pearson's correlation coefficient: r = 0.8799, p value = 0.0208; and r = 0.9523, p value = 0.0034, respectively). Moreover, when compared to the WT situation, the *dnah7* mRNA levels were significantly higher upon the Foxj1a

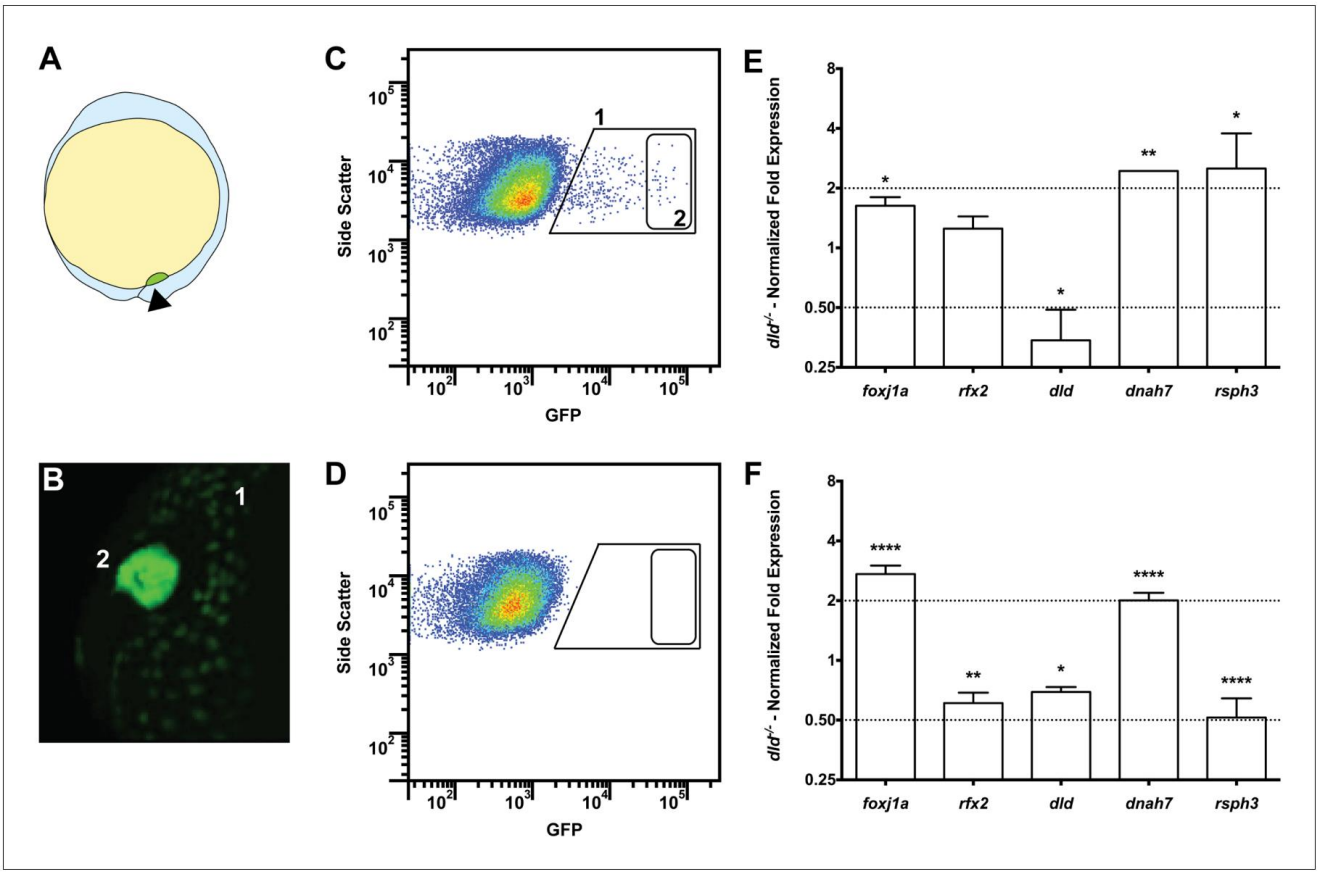

Figure 3. Tissue specific microarray identifies motility genes differentially expressed in *dld*$^{-/-}$ mutants. (**A**) Representation of a zebrafish embryo at Bud stage (10 hpf). The arrowhead shows the tail bud. In green are represented the DFCs. (**B**) At bud stage, sox17:GFP zebrafish Tg line, the DFCs strongly express GFP (2). At this same stage, endoderm cells also express GFP but at significantly lower levels (1). (**C**) FACS profiles for sox17:GFP (AB and *dld*$^{-/-}$) Tg lines and (**D**) WT line without GFP for assessing embryo auto-fluorescence. In (**C**) the cells contained in (1) correspond to the endoderm cells, and the cells contained in (2) correspond to the DFCs. (**E**) Normalized fold expression (log2) of several motility related genes in *dld*$^{-/-}$ mutant embryos as determined in the microarray. t-test; *p<0.05, **p<0.01. (**F**) qPCR validation in normalized fold expression (log2) of the microarray results in the cells selected by FACS as in (**C**). Welsh t-test or the Mann–Whitney U-test; *p<0.05, **p<0.01, ****p<0.0001.

DOI: https://doi.org/10.7554/eLife.25165.011

The following source data and figure supplement are available for figure 3:

Source data 1. Contains data on the relative expression levels of several genes by quantitative PCR.

DOI: https://doi.org/10.7554/eLife.25165.013

Source data 2. GO annotation for gene groups obtained with the R package clusterProfiler.

DOI: https://doi.org/10.7554/eLife.25165.014

Figure supplement 1. In situ hybridization with *dnah7* specific probe in zebrafish embryos.

DOI: https://doi.org/10.7554/eLife.25165.012

OE (***Figure 4E***). This observation is in agreement with ***Choksi et al. (2014)*** who previously showed that *dnah7* is induced by Foxj1a. Concordantly, the transcription levels of *dnah7* were lower in the Foxj1a KD than in the control situation (***Figure 4E***), demonstrating the efficiency of the morpholino in blocking the *foxj1a* mRNA translation. Interestingly, we observed that the changes in *dnah7* expression were dependent only on the variations in Foxj1a, irrespectively of the NS background (***Figure 4D and E***; Pearson's correlation coefficient: r = −0.1859, p value = 0.4198).

The quantification of the expression data led us to conclude that the regulation of *foxj1a* transcription by NS, uncovered in our microarray, was dependent on the NS context (***Figure 4—figure supplement 1I***). In short, the qPCR analysis showed that NS impacts indirectly on the transcription

of *dnah7* by affecting *foxj1a* transcription levels. This data confirms the results obtained in the comparative transcriptome analysis between *dld*$^{-/-}$ mutants and WT for the genes in question: *her12*, *foxj1a* and *dnah7*.

Next, to independently evaluate the impact on the combined manipulation of NS and Foxj1a levels on KV cilia motility we performed live imaging of KV cilia at 8 ss. We selected three NS conditions: *dld*$^{-/-}$;*dlc*$^{-/-}$ double mutants (low NS); WT embryos (normal NS); and embryos injected with *NICD* mRNA at 1 cell stage (high NS), while simultaneously manipulating the levels of Foxj1a by overexpressing it in the three experimental groups. We chose not to knockdown Foxj1a because this would lead to the loss of cilia altogether (**Yu et al., 2008**). We decided to use the double mutants *dld*$^{-/-}$;*dlc*$^{-/-}$ because we had previously observed laterality defects in both *dld*$^{-/-}$ and *dlc*$^{-/-}$ single mutants (**Lopes et al., 2010**) and more importantly, we wanted to avoid redundancy among the genes coding for the two Delta ligands. We filmed ciliary motility at 8 ss because by this stage we know that the anterior and left flow hotspots are established (**Figure 2I**), which we demonstrated before to be crucial for the L-R patterning (**Sampaio et al., 2014**; **Smith et al., 2014**; **Montenegro-Johnson et al., 2016**).

The live imaging analysis showed that when NS is reduced, the number of immotile cilia in the KV decreased significantly from 20 ± 5% in controls to 12 ± 4% in *dld*$^{-/-}$;*dlc*$^{-/-}$ mutants (**Figure 4F**; 24 embryos, 1047 total cilia in control; 7 embryos, 304 total cilia in *dld*$^{-/-}$;*dlc*$^{-/-}$ mutants). Conversely, when NS is increased, the number of immotile cilia increased from 20 ± 5% in controls to 31 ± 10% (**Figure 4F**; 8 embryos, 353 total cilia in NICD OE;). Importantly, NS levels interfered with the motile/immotile cilia ratio and not with the total number of cilia (24 embryos, 44 ± 12 cilia in Control versus 8 embryos, 44 ± 11 cilia in NICD OE,; p=0.9154) or with cilia length (**Figure 4—figure supplement 2A**). Regarding cilia length, we evaluated the cilia length from all treatments done in **Figure 4F**. These experiments were done using a 50 pg of arl13b-GFP so that we could observe the cilia motion live. Using the same movies we have also measured cilia length in 3D. We found no differences between any treatment (**Figure 4—figure supplement 2A**). Using the arl13b-GFP overexpression we have normalized cilia length. In this way, we could overcome the cilia length differences that Notch signaling manipulations produce and successfully uncouple cilia length from cilia motility.

So, despite the qPCR data showing a significant increase in both *dnah7* and *foxj1a* transcription levels after *foxj1a* was over-expressed (**Figure 4E** and **Figure 4—figure supplement 1I**, respectively), live imaging experiments showed that there were no changes in the actual number of motile cilia when *foxj1a* was over-expressed, irrespective of the NS background (**Figure 4F**; nine embryos, 380 total cilia in Foxj1a OE; eight embryos, 368 total cilia in *dld*$^{-/-}$;*dlc*$^{-/-}$ mutants + Foxj1 a OE; eight embryos, 347 total cilia in NICD OE +Foxj1 a OE). We conclude that the failure of Foxj1a OE to increase the number of motile cilia, and specifically the failure in rescuing the loss of motile cilia in the NICD OE embryos (**Figure 4F**) strongly suggests that the KV cells are already committed to a certain motility fate. We propose NS modulates such functional decision downstream of Foxj1a function.

Next, we investigated whether a higher level of *foxj1a* transcription, as the one found in the *dld*$^{-/-}$ mutants, was causing increased CBFs on motile cilia. However, by overexpressing Foxj1a, we observed no significant change in motile cilia CBF (WT = 37.27 ± 7.202 Hz, Foxj1a OE = 36.30 ± 6.877 Hz; p=0.4990; **Figure 4—figure supplement 1G**). This experiment also agreed with the fact that in *dld*$^{-/-}$ mutants, we did not observe an increase in CBF (**Sampaio et al., 2014**). Our results suggest that this level of Foxj1a overexpression, despite eliciting the transcription of the downstream target *dnah7* (**Figure 4—figure supplement 1I**) has no consequences in KV cilia motility, contrary to our initial assumptions.

Next, we investigated whether the Her12 transcription factor was directly involved in the regulation of the ratio between motile and immotile cilia. In order to test this hypothesis we overexpressed Her12 (Her12 OE) by injecting its mRNA at 1 cell stage and imaging the embryos at 8 ss. We observed a significant increase in the percentage of immotile cilia from 20% in controls to 27% (**Figures 4F**, 9 embryos, 305 total cilia), recapitulating the results observed in the NICD OE assay (**Figure 4F**).

Overall these observations indicate that, in parallel to the activation of the motile cilia program by *foxj1a* transcription, which should occur in all DFCs, NS decides which cilia will be stopped. Since both *foxj1a* and *her12* are expressed at bud stage in the DFCs (**Thisse and Thisse, 2004**; **Neugebauer et al., 2013**; **Jurisch-Yaksi et al., 2013**), we reason that on one hand, Foxj1a specifies

cilia capable of moving, while on the other hand, NS prevents the fulfilment of the motile cilia Foxj1a-activated program. This could be achieved either by structurally changing cilia (e.g. preventing the assembly of dynein arms), or by somehow inhibiting the motility of structurally motile cilia (e.g. switching off the dynein motors). To tackle these different scenarios in the absence of appropriate zebrafish antibodies, we cloned the coding sequence of *dnal1*, fused it to the mCherry fluorescent tag and injected this construct in *arl13b-GFP* transgenic embryos that enable live imaging of motile and immotile cilia. As Dnal1 is a light chain outer dynein arm axonemal dynein motor required for cilia movement (***Horváth et al., 2005***; ***Mazor et al., 2011***), we reasoned that if only motile cilia expressed this construct then we could favour the hypothesis that motile cilia were likely to be structurally different. On the other hand if immotile KV cilia also expressed the Dnal1 construct then we could predict that all KV cilia might be structurally similar. In this last scenario, perhaps some other factor capable of switching off the dynein motors ATPase activity could be occurring.

Our results showed that Dnal1 was present in both motile and immotile KV cilia (***Figure 4G*** – R; six embryos; compare K, N, Q with L, O, R). The quantification for the injection of the construct *dnal1*-mCherry was done in a sample of 56 cilia in a total of 4 embryos. In the sample of cilia positive for *dnal1*-mCherry, we saw 72% of motile cilia and 28% of immotile cilia. This ratio is not statistically different from the one for the controls used in ***Figure 4F*** (p=0.17, Fisher test) meaning that the *dnal1*-mCherry construct did not affect the cilia motility status and that both motile and immotile cilia can express *dnal1*-mCherry. Importantly, primary cilia from the tail region around the KV were all negative for *dnal1*-mCherry, which shows that in a mild overexpression scenario, this construct cannot enter a primary cilium (***Figure 4J,M,P***). Overall this experiment suggests that most KV cilia have dynein arms, i.e., may have the necessary machinery to move.

In order to have a definitive answer as to whether all KV cilia structurally belong to the sub-type of motile cilia, we performed transmitted electron microscopy by sampling the full KV of 3 embryos. We used 10 ss embryos and sectioned their KVs with 5–7 micron intervals (***Figure 4—figure supplement 4S***). We imaged a total of 101 cilia, providing an average of 34 cilia per KV, which according to ***Figure 4—figure supplement 2B***, represents on average a random coverage of 77% of the cilia population of each KV. Our findings demonstrated that all cilia imaged had an ultra-structure characteristic of motile cilia. Some cilia had a clearly visible central pair while others showed an unfocused central pair and all cilia had visible dynein arms (***Figure 4U*** - W; ***Table 1***). So, we conclude that it is very likely that all KV cilia are equipped with motility apparatus.

her12 localization in DFCs agrees with immotile cilia distribution at later stages

From the microarray and qPCR validations we discovered that *her12*, a homologue of the mammalian *hes5* that belongs to a family of transcription repressors (reviewed in (***Kageyama et al., 2007***)), was a likely candidate to mediate the cilia immotility regulation. Furthermore, we showed that over-expressing *her12* induced a significant increase in immotile cilia, and thus recapitulated the NICD overexpression phenotype. Next we asked how many cells in the cluster of DFCs were expressing *her12* at bud stage, because we reasoned that if Her12 was mediating the establishment of immotile cilia, then the number of immotile cilia should be similar to the number of *her12* positive cells. For this assay we used the transgenic line *sox17:GFP*, which allowed us to identify the DFCs while detecting *her12* expression pattern by fluorescent in situ hybridization (***Figure 5—videos 1*** and ***2***; ***Figure 5A–F***).

Importantly, we showed that in the control situation 29 ± 8% of the DFCs were *her12* positive (***Figure 5M***; 9 embryos) which represent 10% more than the percentage of immotile cilia detected at 8 ss in the motility assay (***Figure 4F***). We also checked how was *her12* in NICD OE embryos (***Figure 5—videos 3*** and ***4***; ***Figure 5G–L***). We found a significant increase of 14% in the percentage of *her12* positive DFCs (***Figure 5M***; from 30 to 44 ± 11%; 9 embryos). This represents a 14% more than the percentage of immotile cilia detected at 8 ss for this treatment (***Figure 4F***). This differences between *her12* positive cells and immotile cilia percentages could be explained by the existence of a fine-tuning mechanism (***Basch et al., 2016***).

Additionally, we noticed that these cells were preferentially located at the posterior half of the DFC 3-dimensional cluster (***Figure 5N***; 40 ± 5% and 60 ± 5% for the anterior and the posterior halves, respectively; 9 embryos). When NICD is over-expressed, regarding cell distribution, we

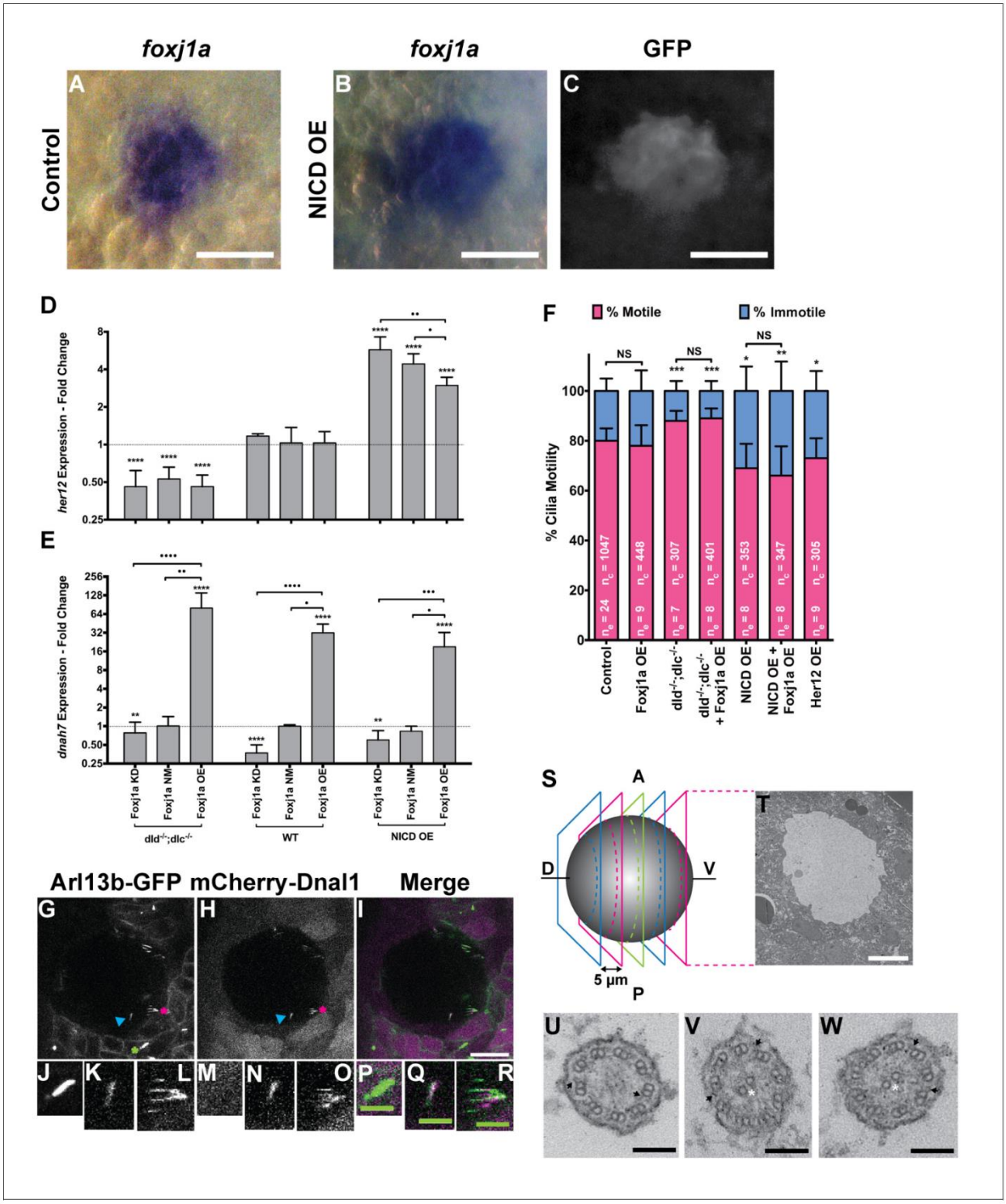

Figure 4. *foxj1a* is expressed in dorsal forerunner cells structurally specifying all cilia as motile cilia. (**A-C**) In situ hybridization with *foxj1a* at bud stage in the dorsal forerunner cells (DFCs), in a control representative embryo (**A**) and upon NICD overexpression (**B**). (**C**) Performing immune-staining with an antibody anti-GFP in the same embryos revealed co-localization with sox17:GFP, a marker for DFCs at bud stage. (**D–E**) Fold change (log2) in expression levels of *her12* (**D**), and *dnah7* (**E**) in whole embryos with different Notch Signalling and Foxj1a manipulations at bud stage. *dld*$^{-/-}$;*dlc*$^{-/-}$ –

Figure 4 continued on next page

Figure 4 continued

deltaD and deltaC double mutant; WT – Wild Type, non-injected controls; NICD OE – overexpression of Notch Intracellular Domain by injecting *NICD* mRNA; Foxj1a KD – knock-down of Foxj1a by Morpholino injection; Foxj1a NM – Foxj1a non-manipulation; and Foxj1a OE – overexpression of Foxj1a by injecting *foxj1a* mRNA. Statistical significance tested with Mann-Whitney U-test (**p<0.01 and ****p<0.0001). Kruscal-Wallis one-way analysis of variance with Dunn's correction for multiple comparisons was used to determine significant differences between different Foxj1a treatments in the same NS assay (*p<0.05, **p<0.01, ***p<0.001, and ****p<0.0001). (**F**) Changes in the % of Immotile and Motile Cilia after manipulation of NS and/or of Foxj1a levels, and imaged by Multiphoton fluorescence microscopy at 0.16 frames per second. Unpaired Welch t-test (Control *vs* Foxj1a OE; Control *vs* Her12 OE) and one-way ANOVA with Bonferroni's correction for multiple comparisons (Control *vs* NICD OE *vs* NICD OE +Foxj1 a OE; Control *vs* $dld^{-/-};dlc^{-/-}$ *vs* $dld^{-/-};dlc^{-/-}$ + Foxj1 a OE). *p<0.05; **p<0.01; ***p<0.001. NS stands for non significant. (**G–I**) Live KV from Arl13b-GFP *Tg* zebrafish embryo at 8 ss, over-expressing mCherry-Dnal1 (**M–O**). Of note are the positive GFP and mCherry signals present in both Immotile (**K, N, Q**) and Motile KV cilia (**L, O, R**). Primary cilium showed no mCherry signal (**J, M, P**). In the sample of cilia positive for *dnal1*-mCherry, we scored 72% motile cilia and 28% immotile cilia (n = 56 cilia in a total of 4 embryos). Scale bars represent 20 μm (white) and 5 μm (green). Blue arrow – immotile cilia; magenta asterisk – motile cilia; green asterisk – primary cilia. Ss -somite stage. (**S–W**) Transmission electron microscopy (TEM) micrographs of the kupffer's vesicle from 10 ss wild type zebrafish embryos. (**S**) Schematics of the sampling methodology sectioning every 5–7 microns to recover full transverse sections such as the one shown in (**T**). (**U-W**) Examples of the two types of cilia ultrastructure observed, (**U**) without visible central pair but showing visible outer and inner dynein arms (arrows) or with visible central pair and dynein arms (**U, V**).

DOI: https://doi.org/10.7554/eLife.25165.015

The following source data and figure supplements are available for figure 4:

Source data 1. Contains data on *foxj1a* gene expression by in situ hybridization and by qPCR.

DOI: https://doi.org/10.7554/eLife.25165.018

Source data 2. Relative expression levels of *dnah7*, *her12*, *dnah9*, *rfx4* and *foxj1a* by qPCR for different Notch signalling manipulations.

DOI: https://doi.org/10.7554/eLife.25165.019

Figure supplement 1. *foxj1a* expression analysis and loss and gain of function assays.

DOI: https://doi.org/10.7554/eLife.25165.016

Figure supplement 2. Arl13b-GFP enables live imaging of cilia motility and normalizes cilia length.

DOI: https://doi.org/10.7554/eLife.25165.017

noticed that *her12* positive cells became homogeneously distributed in both the anterior and posterior halves of the DFC cluster in contrast to the control situation (***Figure 5N***; 9 embryos).

Posterior to anterior cell transitions induce a bias in the distribution of immotile cilia upon NICD overexpression

It is well established that KV maturation involves changes in cell shape to form an anterior-dorsal cluster (***Roxo-Rosa et al., 2015***) crucial for the anterior-left fluid flow hotspots (***Sampaio et al., 2014***; ***Smith et al., 2014***; ***Wang et al., 2012***; ***Montenegro-Johnson et al., 2016***). However, in light of the bias of *her12* positive DFCs at the posterior part of the DFC cluster in control embryos (at bud stage ***Figure 5C,D,F,N***), this led us to test a new hypothesis. Knowing that at 8 ss there is no anterior-posterior bias in the position of immotile cilia (***Sampaio et al., 2014***) we postulated that in a WT embryo with 3 ss, more cells bearing immotile cilia would be present in the posterior part of the KV, judging from the expression pattern of *her12*. We thus predict that some of those cells will be pushed to the anterior part of the KV, as previously reported (***Wang et al., 2012***) and also confirmed here, leading to a homogeneous final distribution of immotile cilia (***Figure 5O***; immotile cilia in blue) at 8 ss. On the other hand, when NICD was overexpressed, we found that the posterior bias of *her12* positive DFCs was lost (***Figure 5N***), which should lead to a homogenous distribution of immotile cilia in the KV at 3 ss, prior to cell shape changes. Therefore, upon KV maturation, we predict an accumulation of immotile cilia in the anterior half (***Figure 5P***). To test this hypothesis, we looked again to the KVs scanned at 8 ss, and used them to create 3D reconstructions and to map the position of each immotile cilia for all treatments. Using the principles of the Cartesian referential

Table 1. Transmitted electron microscopy sampling of cilia from the Kupffer's vesicle.

# KV	Total number of cilia observed	Central-pair	Dynein arms	Microns covered
1	37	35	37	65
2	40	39	40	70
3	24	20	24	58

DOI: https://doi.org/10.7554/eLife.25165.021

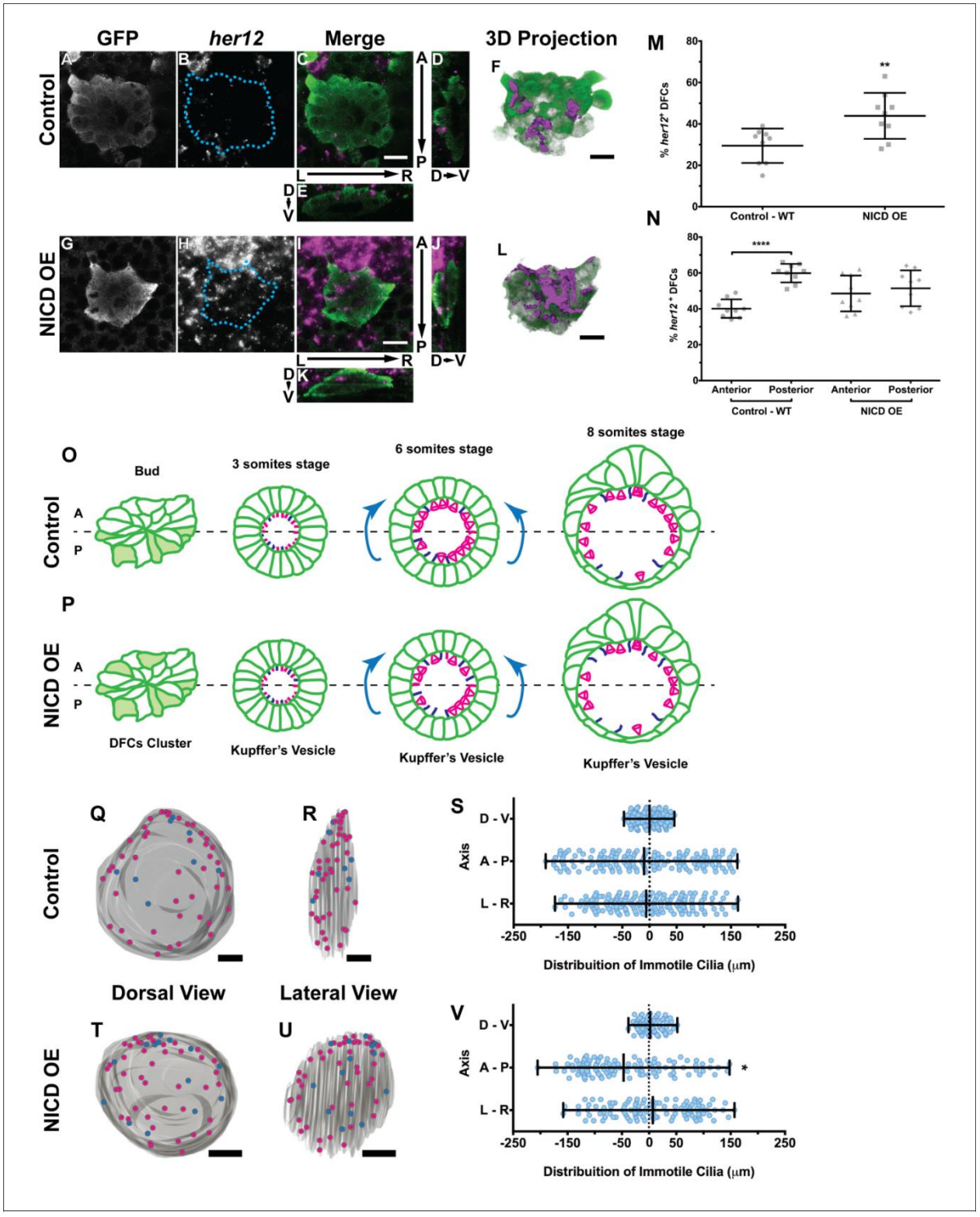

Figure 5. Expression of *her12* agrees with future immotile cilia *distribution*. In situ hybridization with *her12* specific probe in sox17:GFP transgenic embryos at bud stage in Control (**A–E**) and NICD over-expression embryos (**G–K**). An antibody anti-GFP was simultaneously used in order to highlight the DFCs (**A, G**). *her12* expression visualized with the Fast Red (Roche) fluorescent precipitate (**B, H**). In all images, scale bar represents 20 μm. Anterior is to the top and Left is to left. (**D–E, J–K**) Orthogonal projections emphasising *her12* expression in the DFC cluster. (**D, J**) Anterior is to the top and

Figure 5 continued on next page

Figure 5 continued

Dorsal is to left. (**E, K**) Dorsal is to the top and Left is to left. (**M**) % *her12* positive cells in the DFC cluster in Control (•) and NICD over-expression assay (■). (**N**) % *her12* present in the Anterior or in the Posterior halves of the DFC cluster in Control (•, ■) and NICD over-expression (p, ◆). Unpaired t-test with Welsh's correction; **p<0.01 and ****p<0.0001. (**O–P**) Models describing how the cellular reorganization that transforms a DFC cluster into a fully mature KV impacts on the position of the immotile cilia in Control (**O**) and NICD OE (**P**) embryos. (**Q, R, T, U**) 3D projections of representative KVs, where the positions of motile (magenta dots) and immotile cilia (blue dots) are shown for Control (**Q–R**) and NICD OE (**T–U**). (**Q, T**) Dorsal view – Anterior is to the top and Left is to left. (**R, U**) Lateral view – Anterior is to the top and Dorsal is to left. In all images, scale bar represents 20 µm. (**S, V**) Distribution of the position of the immotile cilia along the three axes: D – V (Dorsal – Ventral); A – P (Anterior – Posterior); L – R (Left – Right), in Control (**S**) (17 embryos; 159 cilia) and NICD OE (**V**) (8 embryos; 107 cilia). Distance from centre represents the distance from the origin of the Cartesian referential (placed at the KV's centre). *p<0.05, Fisher's Exact Test.

DOI: https://doi.org/10.7554/eLife.25165.022

Source data 1. Contains data on *her12* positive DFC number and its anterior posterior location within the DFC cluster.
DOI: https://doi.org/10.7554/eLife.25165.025
Source data 2. Provides data on the coordinates of immotile cilia denoting posterior to anterior transitions.
DOI: https://doi.org/10.7554/eLife.25165.026
Figure supplement 1. Immotile cilia are homogeneously distributed in the KV.
DOI: https://doi.org/10.7554/eLife.25165.023
Figure supplement 2. Positions of immotile cilia in the anterior-posterior axis change through development.
DOI: https://doi.org/10.7554/eLife.25165.024
Figure 5—video 1. In situ hybridization + immuno staining with *her12* RNA probe and antibody anti-GFP of a cluster of DFCs at bud stage from a *sox17:GFP* embryo.
DOI: https://doi.org/10.7554/eLife.25165.027
Figure 5—video 2. 3D reconstruction of the WT *her12* expression in the DFCs cluster at bud stage.
DOI: https://doi.org/10.7554/eLife.25165.028
Figure 5—video 3. In situ hybridization + immuno staining with *her12* RNA probe and antibody anti-GFP of a cluster of DFCs at bud stage from a *sox17:GFP* embryo injected with 100 pg of *NICD* mRNA at 1 cell stage.
DOI: https://doi.org/10.7554/eLife.25165.029
Figure 5—video 4. 3D reconstruction of *her12* expression in the DFCs cluster in an embryo over-expressing NICD at bud stage.
DOI: https://doi.org/10.7554/eLife.25165.030
Figure 5—video 5. 3D reconstruction of the WT DLD localization around the DFCs cluster at bud stage.
DOI: https://doi.org/10.7554/eLife.25165.031

and, establishing the centre of the KV as the origin (0, 0, 0) of the three coordinate axes, it was possible to attribute Cartesian coordinates (*x*, *y*, *z*) to each immotile cilium. Using this information, we were able to plot the distribution of the immotile cilia along the anterior-posterior, the dorsal–ventral, and the left–right axes (***Figure 5Q–V*** and ***Figure 5—figure supplement 1A–F***). Our results showed that the position of immotile cilia was homogeneous across all 3 axes in the control (***Figure 5Q–S***; 17 embryos; 159 cilia), when *foxj1a* is overexpressed (***Figure 5—figure supplement 1A–C***; 9 embryos; 89 cilia), and in the double mutant $dld^{-/-};dlc^{-/-}$ (***Figure 5—figure supplement 1D–F***; 7 embryos; 38 cilia). Only when NICD was overexpressed, was there a significant accumulation of immotile cilia at the anterior part of the KV (***Figure 5T–V***; 8 embryos; 107 cilia), thus supporting our hypothesis. To quantify which transitions in cell position were occurring (anterior to posterior, left to right, dorsal to ventral, or vice-versa) we revisited our time-lapse results and tracked the immotile cilia through development for the control situation. Overall, our results showed that in WT embryos, posterior to anterior transitions are the most common (***Figure 5—figure supplement 2A*** – B, four embryos, nine cilia transitions, 19 immotile cilia tracked), further confirming our model. Here we show one such immotile cilium transitioning from the posterior part of the KV (at three ss), to an anterior position (at eight ss). We found a total of 4 immotile cilia transitioning from a posterior position to a more anterior position in as many embryos. If we assume an average KV with 44 ± 12 cilia (***Figure 4—figure supplement 2B***), 20% of these cilia will be immotile, giving an approximate number of 8 immotile cilia. Since at bud stage, 60% of the *her12* positive cells are located at the posterior part of the DFCs cluster, five immotile cilia (60% of total immotile cilia) start at a more posterior position, while 3 (40% of total immotile cilia) will be positioned more anteriorly. Therefore, one immotile cilia transition from posterior to anterior would suffice in order to evenly distribute immotile cilia at eight ss. This analysis is concordant with the observed number of transitions.

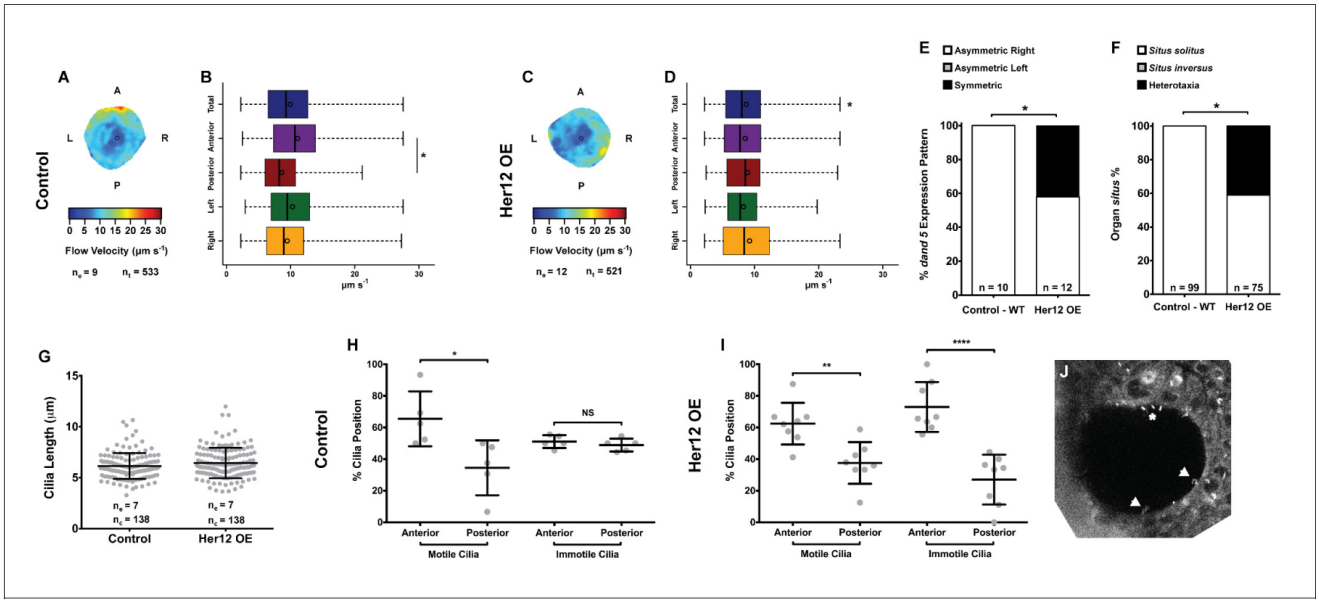

Figure 6. Overexpression of *her12* impacts on fluid flow dynamics, *dand5* expression pattern and organ *situs*. Fluid flow pattern and intensity found in Control (**A–B**) and in Her12 OE (**C–D**) embryos. (**A, C**) Heat maps of flow speed showing detailed regions within the KV for pooled embryos in Control (**A**) and Her12 OE (**C**). The pseudo-colour scale represents flow speed in µm s^{-1}, where red represents high speed versus low speed in blue. n_e – number of embryos; n_{tracks} – number of tracks followed. (**B, D**) Box plots for instantaneous flow speed measured at different locations of the KVs, based on the same data set used to generate the heat maps, in Control (**B**) and Her12 OE (**D**). Box plots display the median with a vertical line, and the whiskers represent the minimum and maximum values observed. Means are represented as small circles. *p<0.05, Wilcoxon test. (**E**) Percentages of *dand5* expression pattern at 8 ss, as determined by in situ hybridization in the same embryos used to study the fluid flow, in Control and Her12 OE. (**F**) Organ *situs* determined by observing the heart position at 30hpf, and the liver and pancreas positions at 53 hpf, by in situ hybridization with a probe for *foxa3*, in Control and Her12 OE. *Situs solitus* stands for left heart and liver; *Situs inversus* stands for right heart and liver; Heterotaxia stands for any other possible combination for the heart and liver position. *p<0.05, Fisher's Exact Test. (**G**) KV cilia length from 8 somite stage embryos in Control (7 embryos, 138 cilia) and Her12 OE (7 embryos, 138 cilia). The cilia were measured in 3D in fixed samples. (**H–I**) Immotile and motile cilia distribution along the Anterior – Posterior axis in Control (5 embryos) (**H**) and Her12 OE (9 embryos) (**I**) 8 somite stage embryos. Unpaired t-test with Welsh's correction; *p<0.05 **p<0.01 and ****p<0.0001. (**J**) Depicts a KV slice where motile (white arrows) and immotile cilia can be observed (white asterisk).

DOI: https://doi.org/10.7554/eLife.25165.032

The following source data is available for figure 6:

Source data 1. Provides data on flow speed and CBF upon *her12* overexpression.

DOI: https://doi.org/10.7554/eLife.25165.033

Notch signalling occurs between DFCs and surrounding cells

Finally, the accumulation of *her12* positive cells in the posterior half of the DFC cluster of control embryos led us to question how NS was occurring, i.e. which cells were DeltaD positive. Using a DeltaD specific antibody, we looked for the expression of DeltaD at bud stage in the vicinity of DFCs (***Figure 5—video 2***; ***Figure 5—figure supplement 2C–G***). This assay showed that DeltaD protein is mainly present in the cells surrounding posteriorly, laterally and dorsally to the cluster of DFCs (***Figure 5—video 5***; ***Figure 5—figure supplement 2E,G and F***, respectively). We thus conclude that NS occurs between the DeltaD positive cells, forming a crescent posteriorly to the DFCs, depicted in our model in ***Figure 5—figure supplement 2H***. *notch1b* positive DFCs (FC = 3.3 in Table S1a, ***Supplementary file 1***) together with *notch1a*, *notch2* and *notch3* are also expressed in the DFCs at bud stage. Some DFCs, preferentially at the posterior boundary, will transcribe *her12* (***Figure 5—figure supplement 2H***) and we postulate that those are the ones where ciliary motility will be inhibited.

Excess of anterior immotile cilia affects flow pattern, dand5 expression and organ situs

To determine whether the 7% increase in immotile cilia observed upon *her12* overexpression is relevant for the determination of laterality (***Figure 4F***) we measured fluid flow and scored *dand5* expression in the same embryos, this time without co-injecting *arl13b*-GFP. Furthermore, we scored the heart position by observing it in the live embryo at 30 hpf and the liver position at 53 hpf by ISH with a *foxa3* probe. Fluid flow analysis showed that *her12* overexpression leads to, not only a loss of the dorsal-anterior flow hotspot (compare ***Figure 6A–B*** with ***Figure 6C-D***) but also a 12.5% reduction in flow velocity (***Figure 6B,D***; from 9.94 ± 4.47 in WT to 8.70 ± 4.26 µm s^{-1} in Her12 OE; 9 and 12 embryos, respectively; 533 and 521 tracks, respectively). Regarding *dand5* expression pattern, it correlated with the difference in the fluid flow: in contrast to 100% of asymmetric on the right in control embryos (***Figures 6E***, 10 embryos), 42% of embryos overexpressing Her12 showed a symmetric expression pattern (***Figures 6E***, 12 embryos). In terms of organ *situs*, 41% of Her12 overexpressing embryos displayed heterotaxia (incorrect positioning of either the heart or liver; ***Figures 6F***, 75 embryos) while 100% of the control embryos showed left heart and left liver (*situs solitus*; ***Figures 6F***, 99 embryos). To test if the observed decrease in flow speed and pattern, as well as the change in *dand5* expression pattern and organ *situs* were not due to a change in cilia length we measured the cilia length from 7 KVs upon Her12 OE (without arl13b-GFP). The results showed that there was no significant difference between treated and control experiments (***Figure 6G***). In order to check if the Her12 OE really recapitulated the NICD effect leading to an increase in the anterior immotile cilia, we then counted the motile and immotile cilia that were present on the Anterior-Posterior halves of each KV. These results confirmed an increase in the number of immotile cilia at the anterior KV halves upon Her12 overexpression (***Figure 6H–I***). Altogether, we demonstrated that the change in location of immotile cilia and its accumulation at the anterior half of the KV had a significant effect in fluid flow dynamics, impacting on *dand5* expression pattern and consequently in organ *situs*.

Discussion

In this manuscript we show the progressive increase of cilia motility in the KV from 3 ss to 8 ss using two independent methods: slow scanning two-photon microscopy allowing for cilia beat pattern trajectories to be revealed and fast acquisition transmitted light imaging by high speed videomicroscopy allowing for slow-motion video analysis (***Figures 1*** and ***2***). This increase in motility occurs as immotile cilia start acquiring motility throughout development as previously reported (***Yuan et al., 2015***). We report here an increase in the intensity of the fluid flow velocity together with a significant increase in the CBF from 3 to 8 ss (***Figure 2***). The changes in fluid flow velocity as the number of motile cilia increased are in line with our previous predictions (***Sampaio et al., 2014***), which dictated that a minimum of 30 cilia is necessary for a robust fluid flow showing anterior-left hotspots at 8 ss (***Smith et al., 2014***; ***Montenegro-Johnson et al., 2016***). By performing live imaging in a two-photon microscope we could establish that the average number of cilia in a KV is 44 ± 12 (***Figure 4—figure supplement 2B***; 1047 cilia in 24 embryos), which according with our previous predictions (***Sampaio et al., 2014***)is more than sufficient to create a robust fluid flow at 8 ss, even accounting for the observed 20% of immotile cilia in WT embryos.

In order to understand why *dld*$^{-/-}$ mutants had more motile cilia in the KV we performed a tissue specific comparative transcriptomic analysis that showed differential expression of genes known to be Foxj1a-induced (***Choksi et al., 2014***) (Table S1b in ***Supplementary file 1***) We also found that the *dld*$^{-/-}$ mutant presented a significant up-regulation of *foxj1a* (FC = 1.62), which indicated a possible regulation in transcription of this gene and its downstream targets by NS. To determine if that was in fact the case we observed the KV cilia in action, using fluorescent live imaging at 0.16 frames per second (fps) and a resolution of 512 × 512 pixels. Contrary to our expectations, we showed that the number of motile cilia was not affected by overexpressing *foxj1a*. Furthermore, we demonstrated that the balance between motile and immotile cilia is regulated by NS, similarly to what was reported in the *Xenopus* LRO (***Boskovski et al., 2013***). However we did not detect the same interaction between NS and *foxj1a* as suggested by ***Boskovski et al. (2013)***. Interactions between NS and Foxj1a have also been suggested by ***Jurisch-Yaksi et al. (2013)*** who showed that decreased levels of Rer1 (retention in endoplasmic reticulum sorting receptor 1), lead to increased γ-secretase activity

and consequently increased NS, which lead to decreased *foxj1a* levels in zebrafish embryos (**Jurisch-Yaksi et al., 2013**). They showed this interaction occurs in several ciliated organs, such as neuromasts, pronephros, olfactory pits, and the sensory patch of the inner ear. In KV, Rer1 knockdown causes the decrease of *foxj1a* expression, but unlike in other organs, when NS is increased, *foxj1a* levels remain unchanged (**Jurisch-Yaksi et al., 2013**). This last observation concurs with our qPCR results that show that when NICD is over expressed, the expression of *foxj1a* is unchanged (**Figure 4—figure supplement 1I**).

It is also known that NS affects Gemc1/MCIDAS, which are required for Foxj1 expression and multiciliated cell fate determination (**Kyrousi et al., 2015**). In this context NS indirectly regulates the pattern of multicilliated cells in the epidermis of *Xenopus laevis* embryos and in the human airway epithelium, by the process of lateral inhibition (**Deblandre et al., 1999**; **Marcet et al., 2011a**). Additionally, the epithelia of the pronephric ducts from zebrafish embryos also present two types of cells, a multiciliated cell and a monociliated principal cell. Their differentiation and patterning is also determined by a NS-dependent lateral inhibition mechanism (**Ma and Jiang, 2007**; **Liu et al., 2007**). In this organ, multiciliogenesis is also inhibited by NS, with multiciliated cells expressing *rfx2* and *jagged2*, and principal cells expressing *notch3* and *her9* (hairy-related 9, a NS downstream target) (**Ma and Jiang, 2007**; **Liu et al., 2007**). In the three multicilliogenesis models discussed, it was suggested that NS inhibited multiciliogenesis by blocking the early expression of either *foxj1* (**Marcet et al., 2011a**; **Marcet et al., 2011b**) or *rfx2* (**Ma and Jiang, 2007**; **Liu et al., 2007**). There was an exclusion of expression patterns for *foxj1/rfx2* and *notch*, and it was this exclusion that triggered cell fate specification and differentiation. **Boskovski et al. (2013)** also suggest that NS functions upstream of Foxj1 and Rfx2 in determining the cilia type at the Xenopus LRO. Nevertheless, they never tested whether overexpressing *foxj1a* would rescue the immotility phenotype observed when NS was up-regulated (**Boskovski et al., 2013**). We were the first to show in the present study that *foxj1a* overexpression fails to rescue the immotile cilia number caused by the up-regulation of NS provided by NICD injection (**Figure 4F**). We propose here that Foxj1a acts early to specify all KV cilia as motile cilia and then Notch signalling triggers an immotility switch. Our strongest evidence comes from the random sampling by transmitted electron microscopy that clearly points to all KV cilia being of the motile sub-type. As far as we are aware we were the first to sample the whole KV by transmitted electron microscopy and to provide a high number of analysed cilia. Collectively, our results show that NS is acting downstream of Foxj1a to establish immotility.

Additionally, this study provides a new player involved in the motility decision: Her12, a paralogue of the mouse Hes5, known as a *bona fide* NS transcriptional target (**Shankaran et al., 2007**). In our hands *her12* transcription proved a faithful NS readout in the KV cell precursors. We thus suggest that DeltaD binds to Notch1a [as suggested by **Shankaran et al. (2007)**] to activate transcription of *her12*. Subsequently, Her12 perhaps together with other factors, restricts the number of motile cilia, most likely by inhibiting the early transcription of a yet unknown crucial motility switch. Here we determined that overexpressing *her12* resulted in a significant increase of immotile cilia in the anterior half of the KV, thereby softening the difference between anterior and posterior flow speed (**Figure 6A–D**). We demonstrate that this flow pattern/intensity disruption impacted on the expression pattern of *dand5* (making it symmetric) and on organ *situs* generating heterotaxia (**Figure 6E–F**). We would like to emphasize that the results presented here on motile/immotile cilia ratio were uncoupled from the cilia length defects that Notch signalling causes (**Figure 4—figure supplement 2A** and **Figure 6G**) (**Lopes et al., 2010**).

A recent work by **Ferreira et al. (2017)** determined a considerably smaller percentage of immotile cilia in the zebrafish LRO. This discrepancy can be explained by the different pixel dwell times used during acquisition in the two different studies. The pixel dwell time was ten times higher in our study, meaning that while we spent 22.4 microseconds per pixel, Ferreira et al. spent 2.4 microseconds. This parameter measures the time that is spent scanning on each pixel, so the longer the dwell time on a particular pixel, the more signal will be detected and the less it will be distorted. In opposition, the faster the scanning the more distorted becomes the imaged object and any cilia movement, even when caused passively by the KV flow bending immotile cilia, will produce a cilium blur that may be inaccurately scored as a motile cilium. Therefore, a longer pixel dwell time is crucial because it will produce a very sharp image of the trajectory of each cilium, reconstituting the beating pattern of a motile cilium (**Figure 1B**), or in the case of an immotile cilium it will show a very bright stiff cilium (**Figure 1C**). Additionally, the number of discarded cilia by Ferreira et al. may have biased

the ratio between motile and immotile cilia. We are aware that immotile cilia can be difficult to detect in 3D reconstructions due to cilia passive motion. In our own study to accurately identify immotile cilia we compared the 3D stacks side by side with the corresponding 3D reconstruction. For some immotile cilia this was crucial due to the smoother blur these may show in a 3D reconstruction. According to Ferreira et al. some embryos at 8 somites show 0% of immotile cilia which contrasts with the 20% we have detected by two independent methods.

Finally, the reason why immotile cilia detection method is important to be clarified is because ***Ferreira et al. (2017)*** refute the immotile cilia mechanosensory hypothesis based on their results. We therefore cannot agree with such conclusion. In fact, according to Ferreira et al. own theory for mechanosensation to work, we would need at least 3 immotile cilia on each LR side to discern noise from productive flow. Therefore based on our results and their theory, we can conclude that from 5 to 6 somite stage, we have enough immotile cilia per KV to be able to sense flow (13 cilia at 5 ss and 9 cilia at 8 ss, on average, which is more than 3 cilia on each side). So, overall we propose that the mechanosensing hypothesis cannot be excluded until demonstration of a chemosensing or mixed mechanism emerges.

Taken together it is possible to conclude that the balance between motile and immotile LRO cilia in zebrafish needs to be tightly regulated for the proper establishment of the L-R axis, by producing a robust, and most importantly, a heterogeneous patterned fluid flow. We would like to stress that in opposition to the mouse embryo (***Shinohara et al., 2012***) the fish LRO is very sensitive to motile cilia number and localization, most likely because of the different topographies of these two LROs. Whereas in mouse all motile cilia are on the floor of the node contributing to the effective flow, in zebrafish ventral pole cilia are antagonistic to the desired flow (***Smith et al., 2014***).

Materials and methods

Zebrafish lines

For the microarray and respective qPCR assays we used transgenic sox17:GFP zebrafish on WT AB background (gift from Carl-Philipp Heisenberg) and on deltaD/aei^{tr233} homozygous mutant AB background. The later line was generated by crossing *dld*$^{-/-}$ mutants with the sox17:GFP line, growing the progeny to adulthood and then incrossing and selecting the GFP fluorescent *dld*$^{-/-}$ mutant fish by their somite phenotype (***Tübingen 2000 Screen Consortium et al., 2005***). For the motility assays (live imaging and qPCR) we used WT zebrafish line, and the homozygous double mutant line *dld*$^{-/-}$;*dlc*$^{-/-}$ line, both from AB background. This last line was obtained by crossing the homozygous mutant lines *dld*$^{-/-}$ and *dlc*$^{-/-}$, growing the progeny to adulthood and then incrossing and selecting the *dld*$^{-/-}$;*dlc*$^{-/-}$ mutant fish by their *dlc*$^{-/-}$ somite phenotype, and genotyping for the presence of the aei^{tr233} mutation. To genotype the deltaD/aei^{tr233} mutation in *dld*$^{-/-}$;*dlc*$^{-/-}$ double mutants, we isolated genomic DNA from individual adults' tails, amplified it and sequenced it. Homozygous mutant DeltaC/bea$^{tm98/tm98}$ fish and the transgenic zebrafish line *Tg(Foxj1a:GFP)* were gifts from Leonor Saúde lab. All these zebrafish lines were maintained and used as described in ***Westerfield, 2000***. Embryos were kept at either 32°C (for Fluorescence Activated Cell Sorting, qPCR, and for CBFs measurements from 3 to 8 ss), or overnight (ON) at 25°C (for live imaging), in the dark and in E3 embryo medium, and were staged according to ***Kimmel et al. (1995)***. The procedures performed to zebrafish were approved by the Portuguese Veterinary General Administration (DGAV - Direcção Geral de Alimentação e Veterinária).

Fluorescence activated cell sorting (FACS)

Embryos at bud stage (10hpf) were dechorionated with pronase (2 mg ml^{-1}) and washed extensively in Danieu's buffer. Cells were dissociated by manual pipetting in CO_2 independent medium (Gibco) complemented with 0.5 mM EDTA. Cells were centrifuged at 700 g and re-suspended in 4 ml of the same medium (step performed 3 times). The cells were then re-suspended in 1 ml and filtered with a 30 µm filter (CellTrics) directly into a round bottom tube. FACS was performed with a FACSAria bench top High Speed Cell Sorter (Becton Dickinson) at 140 kPa (20 psi) and with a 70 µm nozzle, using a 488 nm laser and a 530/40 nm bandpass filter to excite and detect GFP, respectively. GFP positive cells present both in WT and in *dld*$^{-/-}$ mutant embryos were selected, collected into RTL

buffer from the RNeasy micro Kit (Qiagen Inc., Valencia, CA), and immediately frozen at −80°C. We collected three independent samples for WT and mutant embryos, each with around 20 000 cells.

Microarray

RNA isolation and quality evaluation

Total RNA was isolated with the RNeasy micro Kit following the manufacturer's instructions. RNA quantification was done by using a *nanophotometer P-class* (Implen) and integrity was confirmed using an Agilent 2100 Bioanalyzer for an Eukaryote total RNA pico assay (Agilent Technologies). Three biological replicates were produced with an equivalent number off cells and used in the microarray.

Target preparation

2 ng total RNA were used to produce amplified single stranded (ss) cDNA with the Ovation Pico WTA System (NuGEN Technologies). 3 µg of the ss cDNA were used to produce double stranded (ds) cDNA with the WT-Ovation Exon Module (NuGEN Technologies). Target labelling was performed using the One-Color DNA Labelling Kit (Roche NimbleGen, Inc.) with 1 µg ds cDNA as input material. All procedures were performed according to the manufacturer's recommendations.

Hybridization, washing and scanning

6 µg Cy3-labeled cDNA target was hybridized to Zebrafish Gene Expression 385K Arrays (Roche NimbleGen, Inc., Design ID 090506_Zv7_EXPR) following the instructions in the 'NimbleGen Arrays User's Guide: Gene Expression Analysis v3.2.

Data analysis

Normalized datasets (Gene Calls: _RMA.calls files) were created during data extraction in the software NimbleScan according to the 'NimbleGen Arrays User's Guide. Statistical data analysis was performed using the GeneSpring GX software (Agilent Technologies, Version 11.0.2). An unpaired T-test without multiple testing corrections was applied to the data and differences in expression were considered significant when $p<0.05$. A list of sequence IDs was created with sequences that had a fold change in transcription >2, and expression values > 8 in at least 3 out of the 6 datasets. The list of Ensembl gene IDs was later updated to a more current Ensembl release and genome build (Ensembl release-80, ZV10) by remapping the original probes against the updated transcriptome. The list of genes was then curated to remove those with repetitive probes, unspecific probes with more than one gene target or genes with insufficient probes mapping to them. The resulting gene list was then analysed with clusterProfiler, an R package for comparing biological themes among gene clusters (http://bioconductor.org/packages/release/bioc/html/clusterProfiler.html [***Yu et al., 2012***]). The data was also analysed with $Cildb_{v2}$ (http://cildb.cgm.cnrs-gif.fr/, [***Arnaiz et al., 2009***]) and with Genevenn (http://genevenn.sourceforge.net/, [***Pirooznia et al., 2007***]) in order to filter gene targets associated with motility. These lists are in Table S1a and Table S1b in ***Supplementary file 1***.

Validation of microarray expression data

We performed quantitative PCR (qPCR) using cDNA from KV's cells at bud stage (selected as in the microarray experiment). Total RNA from WT and $dld^{-/-}$ mutant embryos was isolated as previously described and reverse-transcribed using iScript cDNA Synthesis Kit (Bio-Rad) according to the manufacturer's instruction. qPCR was performed on the CFX96 Real-Time PCR Detection System (BIO-RAD, Hercules, CA) using the SsoFast EvaGreen Supermix (BIO-RAD, Hercules, CA). Primers for amplification of *foxj1a* (forkhead box J1a), *dnah7* (Dynein, Axonemal, Heavy Chain 7), *rsph3* (Radial Spoke 3 Homolog), *rfx2* (Regulatory Factor X, 2), and *dld* (delta D) were designed with Primer-BLAST (NCBI). Two reference genes *sox17* (Sex Determining Region Y-Box 17) and *eef1al1* (eukaryotic elongation factor 1 alpha 1 like 1) were used. Primers can be found in Table S1c in ***Supplementary file 1***. All reactions were performed with two biological replicates and three technical replicates. Results were evaluated with the Bio-Rad CFX Manager 2.0 software (BIO-RAD, Hercules, CA). Significant differences in the transcription level were determined using either the Welsh t-test or the Mann–

Whitney U-test ($p<0.05$), depending on the normality of the populations as established by the KS normality test.

Injections of morpholino oligonucleotides and/or mRNA

Morpholino blocking translation of Foxj1a was used as previously described (**Tian et al., 2009**; **Echeverri and Oates, 2007**). *Danio rerio her12* coding sequence was cloned into a pCS2 +vector with the primers 5' TCAAGCTTCGAAATGGCACCCCACTCAGC (forward) and 5' CTGGAGACCC TGGTAGTCTAGAAGCGGC (reverse). *Danio rerio dnal1* coding sequence was cloned into a pCS2 +mCherry vector, with mCherry at the N-terminus of Dnal1, with the primers 5' TCAAGC TTCGAAATGGCAAAAGCAACAACTATTAAAGAGGC (forward) and 5' CGCTGGATCCTTAACTC TCCCCTTCAGTTTCC (reverse). *her12*, mCherry-Dnal1, Notch-intracellular domain (NICD) (**Takke and Campos-Ortega, 1999**), full-length *foxj1a* (**Lopes et al., 2010**), and Arl13b-GFP (a gift from Helena Soares) constructs were used to produced mRNA with the mMESSAGE mMACHINE kit (Ambion). The RNA was purified with the kit RNA Clean and Concentrator-5 (Zymo) and injected at one-cell stage at a concentration of 50 pg, 200 pg, 100 pg, 100 pg, and 400 pg respectively. Embryos were left to develop at 32°C or 25°C until the desired stage.

Quantitative PCR

Total RNA was extracted from groups of zebrafish embryos at bud stage using the Qiagen RNeasy Mini Kit and reverse transcribed using both oligo$(dT)_{18}$ and random hexamer primers with the RevertAid First Strand cDNA Synthesis Kit following the manufacturers' instructions. This procedure was repeated for the 3 biological replicates. Expression was quantified using Roche SYBR Green I Master and the PCR was run in a Roche LightCycler 96 Real-Time PCR System with 3 technical replicates for each biological replicate. Results were analysed and depicted as fold-change of transcript levels in injected embryos relative to transcript levels in control embryos. *foxj1a, rfx4* (Regulatory factor X, 4), *dnah7, dnah9* (dynein, axonemal, heavy chain 9) *and her12* (Hairy-related 12) levels were normalized in relation to *eef1al1* and *rpl13a* (ribosomal protein L13a) expression. Significant differences in the transcription level were determined using either the Welsh t-test or the Mann–Whitney U-test ($p<0.05$), depending on the normality of the populations as established by the Shapiro-Wilks normality test. Significant differences between different Foxj1a treatments in the same NS assay were established with a Kruskal–Wallis one-way analysis of variance ($p<0.05$). Primer sequences summarized in Table S1c in **Supplementary file 1**. A biological replicate results from the cDNA produced from the total RNA extracted from 25 zebrafish embryos at bud stage. The technical replicates use the same cDNA (of each biological replicate) in the qPCR reactions. All valid replicates are used in the statistical analysis.

Live imaging and time-lapse

Embryos were mounted live in 1% (w/v) low-melting agarose at either 2 or 7 somites stage, and covered with E3 medium. Live imaging was performed in a Prairie Multiphoton fluorescence microscope with Olympus 40x water immersion lens (NA 0.8) at 28°C. To assess motility, whole KVs were scanned with z sections of 0.5 µm, with an acquisition rate of 9.6 slices per minute (6.25 s per slice), which provided a pixel dwell time of 22,4 µs. Each experiment was repeated either two (WT vs Foxj1a OE; $dld^{-/-};dlc^{-/-}$ vs $dld^{-/-};dlc^{-/-}$ + Foxj1 a OE; WT vs NICD OE vs NICD OE +Foxj1 OE) or three times (WT vs Her12 OE). Each time an experiment was repeated, both control (WT) and tests were assayed in equal numbers until enough *n* was obtained. Time lapses were performed starting at the third somite stage and stacks were acquired every 30 min up until the sixth somite stage and 1 hr later at the eight somite stage. Since only two embryos could be imaged in this manner, this experiment was repeated 4 times in order to gather enough *n*.

3D identification of immotile and motile cilia and length measurement

Stacks were reconstructed and surfaces of the KVs were obtained by image segmentation in Imaris software (Bitplane, UK). Cilia were labelled with a red or blue dot based on whether they were motile or immotile, respectively. This was done for 4 embryos throughout time. Certain conditions were tracked through all time-points: immotile cilia that remained so from the first time point to the last, cilia that were motile from the beginning of the time-lapse (3 somites stage), cilia that started

immotile, became motile and then stopped moving again, and cilia that started immotile and became motile as development progressed. In order to determine the 3D coordinates of the immotile cilia in the KV, we used the stacks obtained at 8 ss in the different treatments. These were reconstructed as described, the cilia were labelled and the Cartesian coordinates (*x*, *y*, *z*) of each cilium were calculated by establishing the centre of the Cartesian referential as the centre of the KV.

3D cilia length were measured using the 'Simple Neurite Tracer' plugin (***Longair et al., 2011***). In live imaged KV's only immotile cilia were sampled for each condition from 8 ss embryos expressing arl13b-GFP (400 pg). In total we analysed: WT – 36 cilia, 11 embryos; Foxj1a OE – 18 cilia, 5 embryos; $dld^{-/-}$;$dlc^{-/-}$ – 24 cilia, 6 embryos; $dld^{-/-}$;$dlc^{-/-}$ + Foxj1a OE – 25 cilia, 7 embryos; NICD OE – 29 cilia, 8 embryos; NICD OE +Foxj1 a OE – 24 cilia, 7 embryos; Her12 OE – 18 cilia, 7 embryos. Specifically to compare WT and Her12 OE cilia length, 8 somite-stage embryos were fixed and the axonemal skeleton of the cilia was labeled with acetylated alpha tubulin. In this way we analyzed: WT - 138 cilia, 7 embryos; Her12 OE - 138 cilia, 7 embryos.

Fluid flow and CBF measurements

We followed the methods described previously (***Sampaio et al., 2014***) for mounting and filming embryos, and calculating the fluid flow and the cilia beat frequency. We tracked native particles and calculated the respective flow velocity with an R script (***Supplementary file 2***) in WT embryos from 3 to 8 ss. Embryos were kept at 32˚C until desired stage and then filmed at room temperature. We imaged ciliary movement for beating frequency analysis in embryos overexpressing Foxj1a at 8 ss and the corresponding non-injected WT siblings (embryos kept at 25˚C until desired stage and then filmed at room temperature). Each fluid flow and CBF measurement experiments were repeated once.

Transmission electron microscopy

Zebrafish embryos with 14 hpf (10 ss) were fixed for 16 hr at 4˚C in 0.1 M sodium cacodylate buffer, pH 7.3, containing 2,5% gluteraldehyde (v/v) enriched with sucrose and calcium chloride. After washings with sucrose enriched buffer the fragments were post-fixed for 1 hr (on ice) in 1% (aq.) osmium tetroxide and contrasted in block in 1% (aq.) uranyl acetate for 30 min. Dehydration was made using ethanol gradient (50-70-95–100%). Samples were embedded in bottle neck beem capsules (Ted Pella) using EPON resin (Electron microscopy sciences) and hardened at 60˚C for 72 hr. After polymerization the tip containing the embryo was sawed and the embryo was re-embed in flat silicon mold for better orientation (KV parallel to the section plan). Resin blocks were sectioned using an ultramicrotome UC7 (Leica microsystems), semi-thin sections (300 nm) were stained with toluidine blue for optic light microscopy, semi-thin were collected until the KV start appearing. Ultra-thin sections (80 nm), were obtained systematically, 2 grids with 2 sections every 5–8 µm until the end of the vesicle. Sections were collected into formvar coated copper slot grids (AGAR scientific), and counter-stained with uranyl acetate and lead citrate (Reynold recipe), the whole KV was screened in a Hitachi H-7650 transmission electron microscope at 100kV acceleration, cilia were tilted in order to check for ultrastructural features, pictures were taken using a XR41M mid mount AMT digital camera.

Antibody staining, immunofluorescence, immuno-in situ hybridization, and confocal microscopy

We followed the methods described previously (***Neugebauer et al., 2009***) for immunostaining. The mixed immunofluorescence and in situ hybridization technique was adapted (***Thisse and Thisse, 2008***) as follows: on the second day, we added the antibody anti-GFP together with the antibody Anti-Digoxigenin-AP Fab Fragments (Roche) and incubated over night at 4˚C in a horizontal rotator; on the third day, we added the secondary antibody anti-rabbit Alexa Fluor 488 and incubated over night at 4˚C in a horizontal rotator; on the fourth day, we developed the RNA probe with Fast-Red substrate (Roche) until a red deposit was observed and the reaction was stopped with 4% PFA (in PBS) for 5 min. *her12* RNA probe was a gift from Leonor Saude. Antibodies used were anti-acetylated α-tubulin (1:300; T7451 from Sigma), anti-GFP (1:500; ab290 from Abcam), anti-DlD (1:50; zdd2 monoclonal antibody [***Itoh et al., 2003***]), anti-mouse Alexa Fluor 564, and anti-rabbit Alexa Fluor 488 (1:500; Invitrogen). Nuclei were stained with DAPI (1:500). Flat-mounted embryos were

examined with a Zeiss LSM 710 Meta confocal microscope and a Zeiss 40x water immersion C-Apochromat lens (1.2 NA). Three-colour confocal z-series images were acquired using sequential laser excitation, and analysed using Fiji software (LSM Reader) (**Schindelin et al., 2012**).

In situ hybridization *on* whole-mount embryos

Whole-mount in situ hybridization was performed as described previously (**Thisse and Thisse, 2008**). Digoxigenin RNA probes were synthesized from DNA templates of *dnah7* (**Sampaio et al., 2014**), *dand5* (**Hashimoto et al., 2004**), *foxa3* (**Monteiro et al., 2008**) and *foxj1a* (**Yu et al., 2008**). Images of flat-mounted embryos were acquired in a Zeiss Z2 Widefield Microscope with Zeiss air EC Plan-Neofluar 5x (0.16 NA) and 10x (0.3 NA) lenses. Whole-mount in situ hybridization to detect the expression of *dand5* and *foxa3*.

Data statistical analysis

Statistical analysis was performed with Prism 6 and R (Wilcoxon test and Fisher's Exact Test). Data populations were tested for normality with the Shapiro-Wilks or the KS normality tests and the different statistical tests were used accordingly. These are specified in the materials and methods section and on the Figures' legend. The values presented are Means ± SD, unless stated otherwise.

Acknowledgements

The authors wish to thank Julian Lewis for the DeltaD antibody, Carl-Philipp Heisenberg for the gift of the transgenic zebrafish line Tg(sox17:GFP), Leonor Saúde for the gift of the transgenic zebrafish line *Tg(foxj1a:GFP)*, the homozygous mutant DeltaC/bea$^{tm98/tm98}$, and the *her12 in situ* probe, and Helena Soares for the Arl13b-GFP construct. We would like to thank Idan Tuval, Domingos Henrique, Rita Teodoro and Adán Guerrero for insightful discussion of the manuscript. We also want to thank the IGC Advanced Image Facility, mainly to Gabriel Martins for advice and the use of Imaris software, and the IGC and CEDOC Fish Facilities. R.J. was supported by the Mechanisms of Disease and Regenerative Medicine (ProRegeM) PhD programme.

Additional information

Funding

Funder	Grant reference number	Author
Fundação para a Ciência e a Tecnologia	PTDC/BEX-BID/1411/2014	Susana Santos Lopes
Fundação para a Ciência e a Tecnologia	FCT-ANR/BEX-BID/0153/2012	Sara Pestana
Fundação para a Ciência e a Tecnologia	PTDC/SAU-OBD/103981/2008	Andreia Vaz
Fundação para a Ciência e a Tecnologia	PD/BD/52420/2013	Raquel Jacinto
Fundação para a Ciência e a Tecnologia	SFRH/BPD/77258/2011	Barbara Tavares
Fundação para a Ciência e a Tecnologia	SFRH/BD/111611/2015	Pedro Sampaio
Fundação para a Ciência e a Tecnologia	IF/00951/2012	Susana Santos Lopes

The funders had no role in study design, data collection and interpretation, or the on the decision to submit the work for publication.

Author contributions

Barbara Tavares, Raquel Jacinto, Conceptualization, Data curation, Formal analysis, Investigation, Methodology, Writing—original draft, Writing—review and editing; Pedro Sampaio, Data curation, Formal analysis, Investigation, Methodology, Writing—review and editing; Sara Pestana,

Investigation, Methodology; Andreia Pinto, Investigation, Visualization, Methodology; Andreia Vaz, Formal analysis, Investigation, Methodology; Mónica Roxo-Rosa, Validation, Writing—review and editing; Rui Gardner, Data curation, Formal analysis; Telma Lopes, Britta Schilling, Data curation, Formal analysis, Methodology; Ian Henry, Data curation, Formal analysis, Validation, Investigation, Methodology; Leonor Saúde, Writing—review and editing; Susana Santos Lopes, Conceptualization, Formal analysis, Supervision, Funding acquisition, Investigation, Methodology, Project administration, Writing—review and editing

Author ORCIDs

Raquel Jacinto, http://orcid.org/0000-0002-4029-0204
Susana Santos Lopes, http://orcid.org/0000-0002-6733-6356

Decision letter and Author response

Decision letter https://doi.org/10.7554/eLife.25165.037
Author response https://doi.org/10.7554/eLife.25165.038

Additional files

Supplementary files

- Supplementary file 1. Microarray data. Excel file that contains Table S1a - List of 706 genes with significantly altered transcription. This list contains 706 genes with a fold change in transcription higher than 2, in the DFCs from *dld*$^{-/-}$ mutant zebrafish embryos. Table S1b – List of motility associated genes from the Table S1a that have been associated with cilia in the different model organisms. Analysis performed with Cildb v2. Table S1c – List of primers sequences used for genotyping *dld*$^{-/-}$ mutant zebrafish embryos and for qPCR validations.

DOI: https://doi.org/10.7554/eLife.25165.034

- Supplementary file 2. Contains the R script for creating and analysing the flow maps.

DOI: https://doi.org/10.7554/eLife.25165.035

- Transparent reporting form

DOI: https://doi.org/10.7554/eLife.25165.036

References

Amack JD, Wang X, Yost HJ. 2007. Two T-box genes play independent and cooperative roles to regulate morphogenesis of ciliated Kupffer's vesicle in zebrafish. *Developmental Biology* **310**:196–210. DOI: https://doi.org/10.1016/j.ydbio.2007.05.039, PMID: 17765888

Arnaiz O, Malinowska A, Klotz C, Sperling L, Dadlez M, Koll F, Cohen J. 2009. Cildb: a knowledgebase for centrosomes and cilia. *Database* **2009**:bap022. DOI: https://doi.org/10.1093/database/bap022, PMID: 20428338

Basch ML, Brown RM, Jen HI, Semerci F, Depreux F, Edlund RK, Zhang H, Norton CR, Gridley T, Cole SE, Doetzlhofer A, Maletic-Savatic M, Segil N, Groves AK. 2016. Fine-tuning of Notch signaling sets the boundary of the organ of Corti and establishes sensory cell fates. *eLife* **5**:e19921. DOI: https://doi.org/10.7554/eLife.19921, PMID: 27966429

Boskovski MT, Yuan S, Pedersen NB, Goth CK, Makova S, Clausen H, Brueckner M, Khokha MK. 2013. The heterotaxy gene GALNT11 glycosylates Notch to orchestrate cilia type and laterality. *Nature* **504**:456–459. DOI: https://doi.org/10.1038/nature12723, PMID: 24226769

Caron A, Xu X, Lin X. 2012. Wnt/β-catenin signaling directly regulates Foxj1 expression and ciliogenesis in zebrafish Kupffer's vesicle. *Development* **139**:514–524. DOI: https://doi.org/10.1242/dev.071746, PMID: 22190638

Choksi SP, Babu D, Lau D, Yu X, Roy S. 2014. Systematic discovery of novel ciliary genes through functional genomics in the zebrafish. *Development* **141**:3410–3419. DOI: https://doi.org/10.1242/dev.108209, PMID: 25139857

Cooper MS, D'Amico LA. 1996. A cluster of noninvoluting endocytic cells at the margin of the zebrafish blastoderm marks the site of embryonic shield formation. *Developmental Biology* **180**:184–198. DOI: https://doi.org/10.1006/dbio.1996.0294, PMID: 8948584

Deblandre GA, Wettstein DA, Koyano-Nakagawa N, Kintner C. 1999. A two-step mechanism generates the spacing pattern of the ciliated cells in the skin of Xenopus embryos. *Development* **126**:4715–4728. PMID: 10518489

Delling M, Indzhykulian AA, Liu X, Li Y, Xie T, Corey DP, Clapham DE. 2016. Primary cilia are not calcium-responsive mechanosensors. *Nature* **531**:656–660. DOI: https://doi.org/10.1038/nature17426, PMID: 27007841

Echeverri K, Oates AC. 2007. Coordination of symmetric cyclic gene expression during somitogenesis by Suppressor of Hairless involves regulation of retinoic acid catabolism. *Developmental Biology* **301**:388–403. DOI: https://doi.org/10.1016/j.ydbio.2006.10.003, PMID: 17098223

Essner JJ, Amack JD, Nyholm MK, Harris EB, Yost HJ. 2005. Kupffer's vesicle is a ciliated organ of asymmetry in the zebrafish embryo that initiates left-right development of the brain, heart and gut. *Development* **132**:1247–1260. DOI: https://doi.org/10.1242/dev.01663, PMID: 15716348

Ferreira RR, Vilfan A, Jülicher F, Supatto W, Vermot J. 2017. Physical limits of flow sensing in the left-right organizer. *eLife* **6**:e25078. DOI: https://doi.org/10.7554/eLife.25078

Hashimoto H, Rebagliati M, Ahmad N, Muraoka O, Kurokawa T, Hibi M, Suzuki T. 2004. The Cerberus/Dan-family protein Charon is a negative regulator of Nodal signaling during left-right patterning in zebrafish. *Development* **131**:1741–1753. DOI: https://doi.org/10.1242/dev.01070, PMID: 15084459

Horváth J, Fliegauf M, Olbrich H, Kispert A, King SM, Mitchison H, Zariwala MA, Knowles MR, Sudbrak R, Fekete G, Neesen J, Reinhardt R, Omran H. 2005. Identification and analysis of axonemal dynein light chain 1 in primary ciliary dyskinesia patients. *American Journal of Respiratory Cell and Molecular Biology* **33**:41–47. DOI: https://doi.org/10.1165/rcmb.2004-0335OC, PMID: 15845866

Itoh M, Kim CH, Palardy G, Oda T, Jiang YJ, Maust D, Yeo SY, Lorick K, Wright GJ, Ariza-McNaughton L, Weissman AM, Lewis J, Chandrasekharappa SC, Chitnis AB. 2003. Mind bomb is a ubiquitin ligase that is essential for efficient activation of Notch signaling by Delta. *Developmental Cell* **4**:67–82. DOI: https://doi.org/10.1016/S1534-5807(02)00409-4, PMID: 12530964

Jurisch-Yaksi N, Rose AJ, Lu H, Raemaekers T, Munck S, Baatsen P, Baert V, Vermeire W, Scales SJ, Verleyen D, Vandepoel R, Tylzanowski P, Yaksi E, de Ravel T, Yost HJ, Froyen G, Arrington CB, Annaert W. 2013. Rer1p maintains ciliary length and signaling by regulating γ-secretase activity and Foxj1a levels. *The Journal of Cell Biology* **200**:709–720. DOI: https://doi.org/10.1083/jcb.201208175, PMID: 23479743

Kageyama R, Ohtsuka T, Kobayashi T. 2007. The Hes gene family: repressors and oscillators that orchestrate embryogenesis. *Development* **134**:1243–1251. DOI: https://doi.org/10.1242/dev.000786, PMID: 17329370

Kimmel CB, Ballard WW, Kimmel SR, Ullmann B, Schilling TF. 1995. Stages of embryonic development of the zebrafish. *Developmental Dynamics* **203**:253–310. DOI: https://doi.org/10.1002/aja.1002030302, PMID: 8589427

Kramer-Zucker AG, Olale F, Haycraft CJ, Yoder BK, Schier AF, Drummond IA. 2005. Cilia-driven fluid flow in the zebrafish pronephros, brain and Kupffer's vesicle is required for normal organogenesis. *Development* **132**:1907–1921. DOI: https://doi.org/10.1242/dev.01772, PMID: 15790966

Kyrousi C, Arbi M, Pilz GA, Pefani DE, Lalioti ME, Ninkovic J, Götz M, Lygerou Z, Taraviras S. 2015. Mcidas and GemC1 are key regulators for the generation of multiciliated ependymal cells in the adult neurogenic niche. *Development* **142**:3661–3674. DOI: https://doi.org/10.1242/dev.126342, PMID: 26395491

Liu Y, Pathak N, Kramer-Zucker A, Drummond IA. 2007. Notch signaling controls the differentiation of transporting epithelia and multiciliated cells in the zebrafish pronephros. *Development* **134**:1111–1122. DOI: https://doi.org/10.1242/dev.02806, PMID: 17287248

Longair MH, Baker DA, Armstrong JD. 2011. Simple Neurite Tracer: open source software for reconstruction, visualization and analysis of neuronal processes. *Bioinformatics* **27**:2453–2454. DOI: https://doi.org/10.1093/bioinformatics/btr390, PMID: 21727141

Lopes SS, Lourenço R, Pacheco L, Moreno N, Kreiling J, Saúde L. 2010. Notch signalling regulates left-right asymmetry through ciliary length control. *Development* **137**:3625–3632. DOI: https://doi.org/10.1242/dev.054452, PMID: 20876649

Ma M, Jiang YJ. 2007. Jagged2a-notch signaling mediates cell fate choice in the zebrafish pronephric duct. *PLoS Genetics* **3**:e18–145. DOI: https://doi.org/10.1371/journal.pgen.0030018, PMID: 17257056

Marcet B, Chevalier B, Coraux C, Kodjabachian L, Barbry P. 2011b. MicroRNA-based silencing of Delta/Notch signaling promotes multiple cilia formation. *Cell Cycle* **10**:2858–2864. DOI: https://doi.org/10.4161/cc.10.17.17011, PMID: 21857154

Marcet B, Chevalier B, Luxardi G, Coraux C, Zaragosi LE, Cibois M, Robbe-Sermesant K, Jolly T, Cardinaud B, Moreilhon C, Giovannini-Chami L, Nawrocki-Raby B, Birembaut P, Waldmann R, Kodjabachian L, Barbry P. 2011a. Control of vertebrate multiciliogenesis by miR-449 through direct repression of the Delta/Notch pathway. *Nature Cell Biology* **13**:694–701. DOI: https://doi.org/10.1038/ncb2241, PMID: 21602795

Marques S, Borges AC, Silva AC, Freitas S, Cordenonsi M, Belo JA. 2004. The activity of the Nodal antagonist Cerl-2 in the mouse node is required for correct L/R body axis. *Genes & Development* **18**:2342–2347. DOI: https://doi.org/10.1101/gad.306504, PMID: 15466485

Mazor M, Alkrinawi S, Chalifa-Caspi V, Manor E, Sheffield VC, Aviram M, Parvari R. 2011. Primary ciliary dyskinesia caused by homozygous mutation in DNAL1, encoding dynein light chain 1. *The American Journal of Human Genetics* **88**:599–607. DOI: https://doi.org/10.1016/j.ajhg.2011.03.018, PMID: 21496787

McGrath J, Somlo S, Makova S, Tian X, Brueckner M. 2003. Two populations of node monocilia initiate left-right asymmetry in the mouse. *Cell* **114**:61–73. DOI: https://doi.org/10.1016/S0092-8674(03)00511-7, PMID: 12859898

Monteiro R, van Dinther M, Bakkers J, Wilkinson R, Patient R, ten Dijke P, Mummery C. 2008. Two novel type II receptors mediate BMP signalling and are required to establish left-right asymmetry in zebrafish. *Developmental Biology* **315**:55–71. DOI: https://doi.org/10.1016/j.ydbio.2007.11.038, PMID: 18222420

Montenegro-Johnson TD, Baker DI, Smith DJ, Lopes SS. 2016. Three-dimensional flow in Kupffer's Vesicle. *Journal of mathematical biology* **73**:705–725. DOI: https://doi.org/10.1007/s00285-016-0967-7, PMID: 26825450

Nakamura T, Mine N, Nakaguchi E, Mochizuki A, Yamamoto M, Yashiro K, Meno C, Hamada H. 2006. Generation of robust left-right asymmetry in the mouse embryo requires a self-enhancement and lateral-inhibition system. *Developmental Cell* **11**:495–504. DOI: https://doi.org/10.1016/j.devcel.2006.08.002, PMID: 17011489

Neugebauer JM, Amack JD, Peterson AG, Bisgrove BW, Yost HJ. 2009. FGF signalling during embryo development regulates cilia length in diverse epithelia. *Nature* **458**:651–654. DOI: https://doi.org/10.1038/nature07753, PMID: 19242413

Neugebauer JM, Cadwallader AB, Amack JD, Bisgrove BW, Yost HJ. 2013. Differential roles for 3-OSTs in the regulation of cilia length and motility. *Development* **140**:3892–3902. DOI: https://doi.org/10.1242/dev.096388, PMID: 23946439

Nonaka S, Shiratori H, Saijoh Y, Hamada H. 2002. Determination of left-right patterning of the mouse embryo by artificial nodal flow. *Nature* **418**:96–99. DOI: https://doi.org/10.1038/nature00849, PMID: 12097914

Nonaka S, Tanaka Y, Okada Y, Takeda S, Harada A, Kanai Y, Kido M, Hirokawa N. 1998. Randomization of left-right asymmetry due to loss of nodal cilia generating leftward flow of extraembryonic fluid in mice lacking KIF3B motor protein. *Cell* **95**:829–837. DOI: https://doi.org/10.1016/S0092-8674(00)81705-5, PMID: 9865700

Oteíza P, Köppen M, Concha ML, Heisenberg CP. 2008. Origin and shaping of the laterality organ in zebrafish. *Development* **135**:2807–2813. DOI: https://doi.org/10.1242/dev.022228, PMID: 18635607

Pirooznia M, Nagarajan V, Deng Y. 2007. GeneVenn - A web application for comparing gene lists using Venn diagrams. *Bioinformation* **1**:420–422. DOI: https://doi.org/10.6026/97320630001420, PMID: 17597932

Roxo-Rosa M, Jacinto R, Sampaio P, Lopes SS. 2015. The zebrafish Kupffer's vesicle as a model system for the molecular mechanisms by which the lack of Polycystin-2 leads to stimulation of CFTR. *Biology Open* **4**:1356–1366. DOI: https://doi.org/10.1242/bio.014076, PMID: 26432887

Sampaio P, Ferreira RR, Guerrero A, Pintado P, Tavares B, Amaro J, Smith AA, Montenegro-Johnson T, Smith DJ, Lopes SS. 2014. Left-right organizer flow dynamics: how much cilia activity reliably yields laterality? *Developmental Cell* **29**:716–728. DOI: https://doi.org/10.1016/j.devcel.2014.04.030, PMID: 24930722

Schindelin J, Arganda-Carreras I, Frise E, Kaynig V, Longair M, Pietzsch T, Preibisch S, Rueden C, Saalfeld S, Schmid B, Tinevez JY, White DJ, Hartenstein V, Eliceiri K, Tomancak P, Cardona A. 2012. Fiji: an open-source platform for biological-image analysis. *Nature Methods* **9**:676–682. DOI: https://doi.org/10.1038/nmeth.2019, PMID: 22743772

Schweickert A, Weber T, Beyer T, Vick P, Bogusch S, Feistel K, Blum M. 2007. Cilia-driven leftward flow determines laterality in Xenopus. *Current Biology* **17**:60–66. DOI: https://doi.org/10.1016/j.cub.2006.10.067, PMID: 17208188

Shankaran SS, Sieger D, Schröter C, Czepe C, Pauly MC, Laplante MA, Becker TS, Oates AC, Gajewski M. 2007. Completing the set of h/E(spl) cyclic genes in zebrafish: her12 and her15 reveal novel modes of expression and contribute to the segmentation clock. *Developmental Biology* **304**:615–632. DOI: https://doi.org/10.1016/j.ydbio.2007.01.004, PMID: 17274976

Shinohara K, Kawasumi A, Takamatsu A, Yoshiba S, Botilde Y, Motoyama N, Reith W, Durand B, Shiratori H, Hamada H. 2012. Two rotating cilia in the node cavity are sufficient to break left-right symmetry in the mouse embryo. *Nature Communications* **3**:622. DOI: https://doi.org/10.1038/ncomms1624, PMID: 22233632

Smith DJ, Montenegro-Johnson TD, Lopes SS. 2014. Organized chaos in Kupffer's vesicle: how a heterogeneous structure achieves consistent left-right patterning. *BioArchitecture* **4**:119–125. DOI: https://doi.org/10.4161/19490992.2014.956593, PMID: 25454897

Stubbs JL, Oishi I, Izpisúa Belmonte JC, Kintner C. 2008. The forkhead protein Foxj1 specifies node-like cilia in Xenopus and zebrafish embryos. *Nature Genetics* **40**:1454–1460. DOI: https://doi.org/10.1038/ng.267, PMID: 19011629

Swoboda P, Adler HT, Thomas JH. 2000. The RFX-type transcription factor DAF-19 regulates sensory neuron cilium formation in C. elegans. *Molecular Cell* **5**:411–421. DOI: https://doi.org/10.1016/S1097-2765(00)80436-0, PMID: 10882127

Takeda S, Yonekawa Y, Tanaka Y, Okada Y, Nonaka S, Hirokawa N. 1999. Left-right asymmetry and kinesin superfamily protein KIF3A: new insights in determination of laterality and mesoderm induction by kif3A-/- mice analysis. *The Journal of Cell Biology* **145**:825–836. DOI: https://doi.org/10.1083/jcb.145.4.825, PMID: 10330409

Takke C, Campos-Ortega JA. 1999. her1, a zebrafish pair-rule like gene, acts downstream of notch signalling to control somite development. *Development* **126**:3005–3014. PMID: 10357943

Thisse B, Thisse C. 2004. Fast release clones: A high throughput expression analysis. In: *ZFIN Direct Data Submission (Http://zfin.org) [Internet.*

Thisse C, Thisse B. 2008. High-resolution in situ hybridization to whole-mount zebrafish embryos. *Nature Protocols* **3**:59–69. DOI: https://doi.org/10.1038/nprot.2007.514, PMID: 18193022

Tian T, Zhao L, Zhang M, Zhao X, Meng A. 2009. Both foxj1a and foxj1b are implicated in left-right asymmetric development in zebrafish embryos. *Biochemical and Biophysical Research Communications* **380**:537–542. DOI: https://doi.org/10.1016/j.bbrc.2009.01.111, PMID: 19284996

Tübingen 2000 Screen Consortium, Jülich D, Geisler R, Holley SA. 2005. Integrinalpha5 and delta/notch signaling have complementary spatiotemporal requirements during zebrafish somitogenesis. *Developmental Cell* **8**:575–586. DOI: https://doi.org/10.1016/j.devcel.2005.01.016, PMID: 15809039

Wang G, Manning ML, Amack JD. 2012. Regional cell shape changes control form and function of Kupffer's vesicle in the zebrafish embryo. *Developmental Biology* **370**:52–62. DOI: https://doi.org/10.1016/j.ydbio.2012.07.019, PMID: 22841644

Westerfield M. 2000. The Zebrafish Book. In: *A Guide for the Laboratory Use of Zebrafish (Danio Rerio)*. 4th Edn. Eugene: University of Oregon Press.

Yoshiba S, Shiratori H, Kuo IY, Kawasumi A, Shinohara K, Nonaka S, Asai Y, Sasaki G, Belo JA, Sasaki H, Nakai J, Dworniczak B, Ehrlich BE, Pennekamp P, Hamada H. 2012. Cilia at the node of mouse embryos sense fluid flow for left-right determination via Pkd2. *Science* **338**:226–231. DOI: https://doi.org/10.1126/science.1222538, PMID: 22983710

Yu G, Wang LG, Han Y, He QY, Q-y H. 2012. clusterProfiler: an R package for comparing biological themes among gene clusters. *OMICS: A Journal of Integrative Biology* **16**:284–287. DOI: https://doi.org/10.1089/omi.2011.0118, PMID: 22455463

Yu X, Ng CP, Habacher H, Roy S. 2008. Foxj1 transcription factors are master regulators of the motile ciliogenic program. *Nature Genetics* **40**:1445–1453. DOI: https://doi.org/10.1038/ng.263, PMID: 19011630

Yuan S, Zhao L, Brueckner M, Sun Z. 2015. Intraciliary calcium oscillations initiate vertebrate left-right asymmetry. *Current Biology* **25**:556–567. DOI: https://doi.org/10.1016/j.cub.2014.12.051, PMID: 25660539

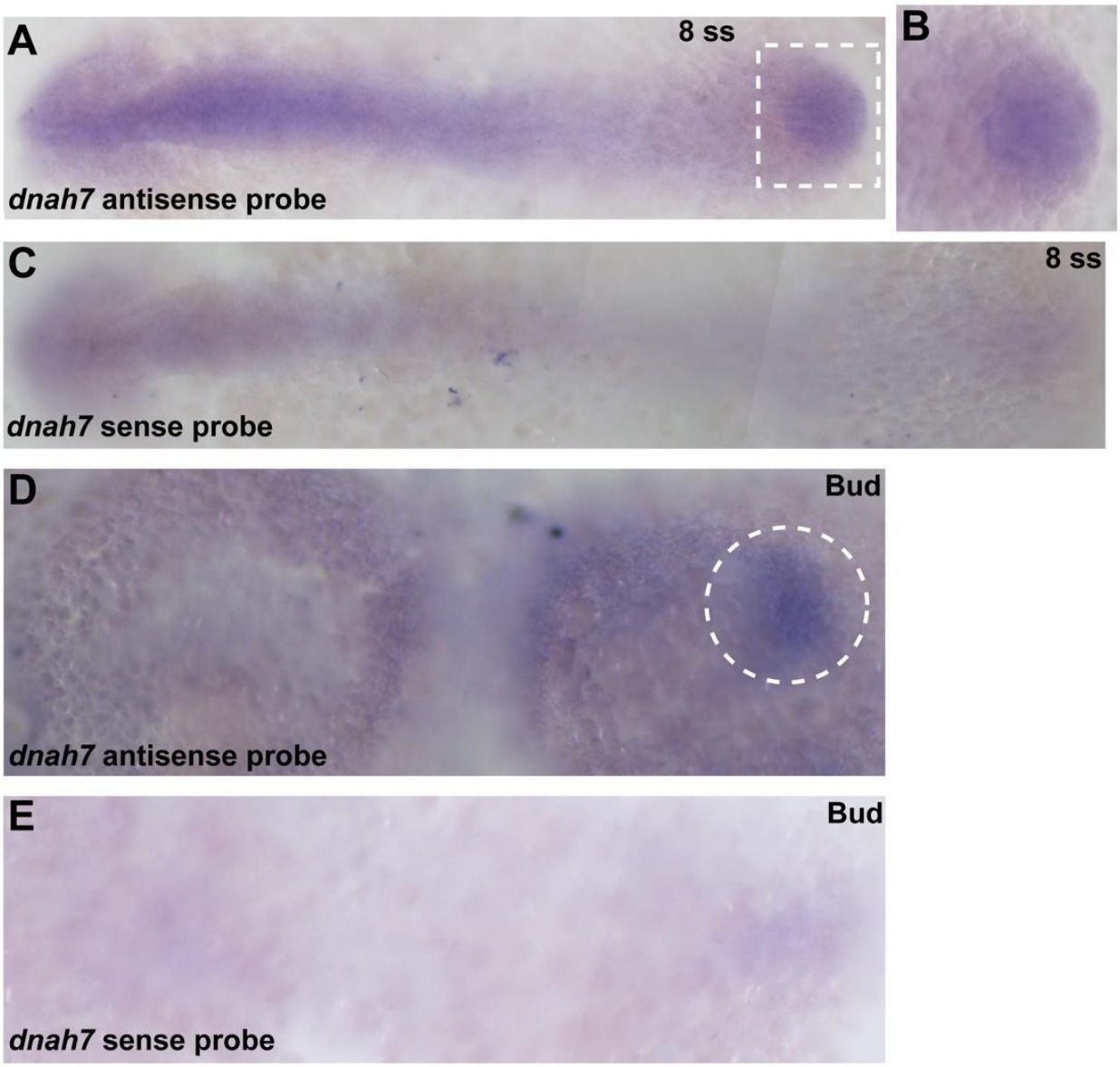

Figure 3 – figure supplement 1

***In situ* hybridization with *dnah7* specific probe in zebrafish embryos.**

(**A–C**) WT 8 ss zebrafish embryo stained with antisense (**A–B**) and sense (**C**) *dnah7* specific probes. (**A**) White dotted square delimits the KV, which is detailed in (**B**). (**D–E**) WT zebrafish embryos at bud stage, stained with antisense (**D**) and sense (**E**) *dnah7* specific probes. White dotted line circles the DFCs in (**D**). In all images Anterior is to left and Posterior is to right.

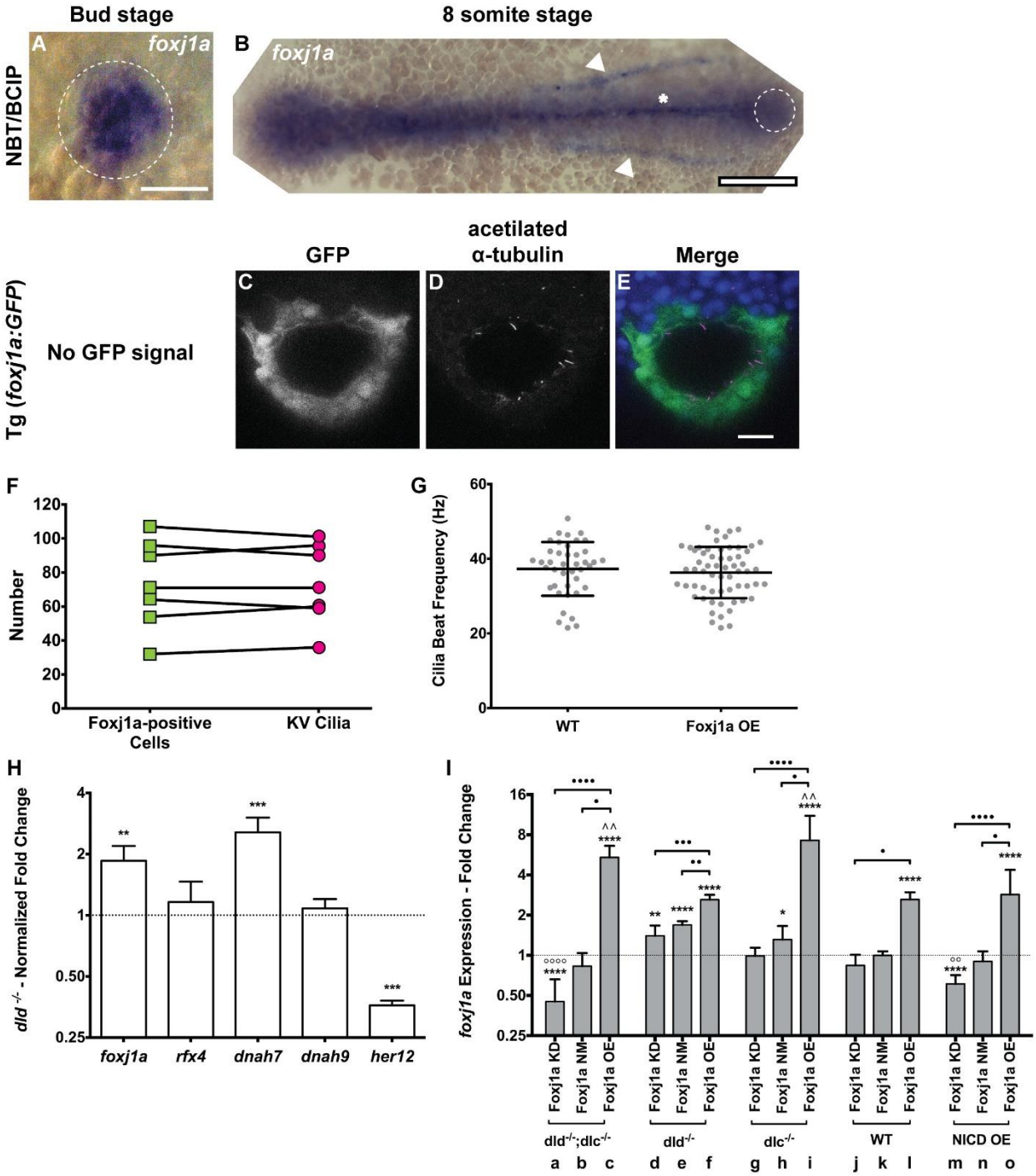

Figure 4 – figure supplement 1

foxj1a expression analysis and loss and gain of function assays.

(**A–B**) In situ hybridization with *foxj1a* riboprobe; (**A**) at bud stage showing the labelled purple dorsal forerunner cells; (**B**) later at 8 somite-stage showing the purple staining

is absent from the KV cells (dotted circle) but is visible in the neural tube (asterisk) and in both pronephros (arrow heads). (**C–E**) Still from Video 3 representing the immuno-staining of a KV from the transgenic line Foxj1a:GFP. *foxj1a*-positive KV cells in green (anti-GFP antibody) (**C**), and KV cilia in magenta (anti-acetylated α-tubulin antibody) (**D**). (**E**) Nuclei stained with DAPI. Anterior is to the top and Left is to left. Scale bar represents 20 μm. (**F**) Relation between the number of *foxj1a*-positive cells (green ■) and the number of cilia (magenta ●) in zebrafish embryos at 8 ss. Averages were not significantly different (p=0.9479, paired t-test; 8 embryos, 514 cells, 513 cilia). (**G**) Cilia Beat Frequency (CBF) in WT (37.27 ± 7.202 Hz, 8 embryos, 41 cilia), and in Foxj1a OE (36.30 ± 6.877 Hz, 12 embryos, 61 cilia). p=0.4990, unpaired t-test with Welsh's correction (averages not significantly different). (**H**) Transcription levels of several genes in whole zebrafish embryos. Normalized fold change (log2) in expression levels of *foxj1a, rfx4, dnah7, dnah9,* and *her12* in whole embryos at bud stage from the *dld*$^{-/-}$ mutant. Unpaired t-test with Welsh's correction; **p<0.01 and ***p<0.001. (**I**) Transcription levels for *foxj1a*. Fold change (log2) in expression levels of f*oxj1a* in whole embryos with different Notch Signalling and Foxj1a manipulations at bud stage (a – o). *dld*$^{-/-}$;*dlc*$^{-/-}$ – deltaD and deltaC double mutant; *dld*$^{-/-}$ – *deltaD* mutant; *dlc*$^{-/-}$ – *deltaC* mutant; WT – Wild Type, non-injected controls; NICD OE – overexpression of Notch Intracellular Domain by injecting NICD mRNA; Foxj1a KD – knock-down of *foxj1a* by Morpholino injection; Foxj1a NM – Foxj1a no-manipulation; Foxj1a OE – overexpression of Foxj1a by injecting *foxj1a* mRNA. Statistical significance tested with Mann-Whitney U-test (*p<0.05, **p<0.01, and ****p<0.0001). Kruscal-Wallis one-way analysis of variance with Dunn's correction for multiple comparisons was used to determine significant differences between different Foxj1a treatments in the same NS assay (*p<0.05,**p<0.01, ***p<0.0001, and ****p<0.0001), and to determine significant differences between different NS treatments in the same Foxj1a assay (Foxj1a KD – **p<0.01, and ****p<0.0001. Foxj1a OE – **p<0.01).

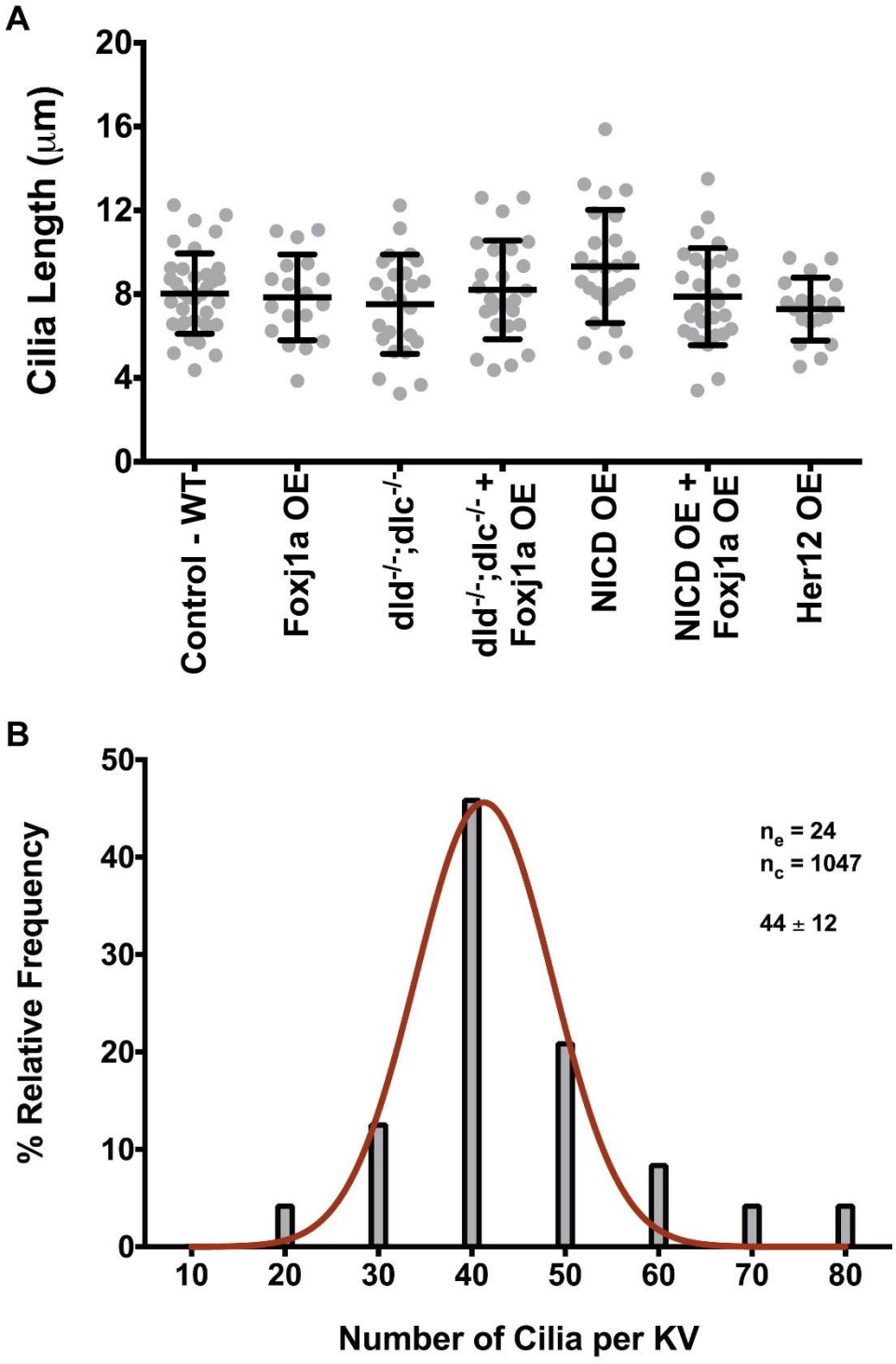

Figure 4 – figure supplement 2

Arl13b-GFP enables live imaging of cilia motility and normalizes cilia length.

(**A**) KV cilia length was measured in 3D in live imaged KVs, immotile cilia were sampled for each condition from 8 ss embryos expressing arl13b-GFP (400 pg). In total we analyzed: WT – 36 cilia, 11 embryos; Foxj1a OE – 18 cilia, 5 embryos; dld$^{-/-}$;dlc$^{-/-}$ – 24

cilia, 6 embryos; dld$^{-/-}$;dlc$^{-/-}$ + Foxj1a OE – 25 cilia, 7 embryos; NICD OE – 29 cilia, 8 embryos; NICD OE +Foxj1 a OE – 24 cilia, 7 embryos; Her12 OE – 18 cilia, 7 embryos. (**B**) Frequence distribution of the cilia number per KV in a population of WT zebrafish from the AB background. Data was acquired from the WT live embryos at 8 ss used in our assays from Figure 4F. Fiji software was used to visualize and count the number of cilia found in each KV (24 embryos; 1047 cilia). The histogram was fitted with a Gaussian expression (Amplitude = 45.61, Mean = 41.30, SD = 7.318).

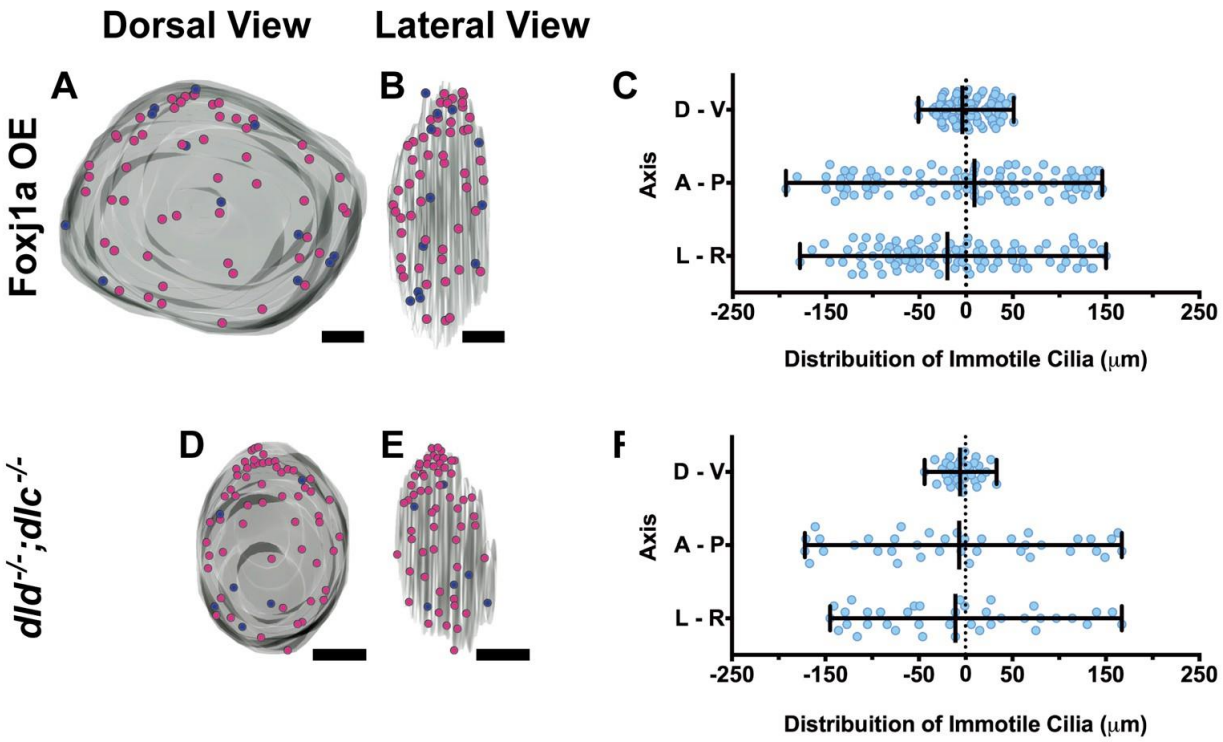

Figure 5 – figure supplement 1

Immotile cilia are homogeneously distributed in the KV.

3D projections of representative KVs, where the position of motile (red dots) and immotile cilia (blue dots) is shown in Foxj1a OE (**A–C**), and *dld*$^{-/-}$;*dlc*$^{-/-}$ (**D–F**). (**A**, **D**) Dorsal view – Anterior is to the top and Left is to left. (**B**, **E**) Lateral view – Anterior is to the top and Dorsal is to left. In all images, scale bar represents 20 μm. (**C, F**) Distribution of the position of the immotile cilia along the three axes: D – V (Dorsal – Ventral); A – P (Anterior – Posterior); L – R (Left – Right), in Foxj1a OE (C) (9 embryos; 89 cilia), and *dld*$^{-/-}$;*dlc*$^{-/-}$ (**F**) (7 embryos; 38 cilia). Distance from center represents the distance from the origin of the Cartesian referential (placed at the KV's center). Fisher's Exact Test, $p<0.05$.

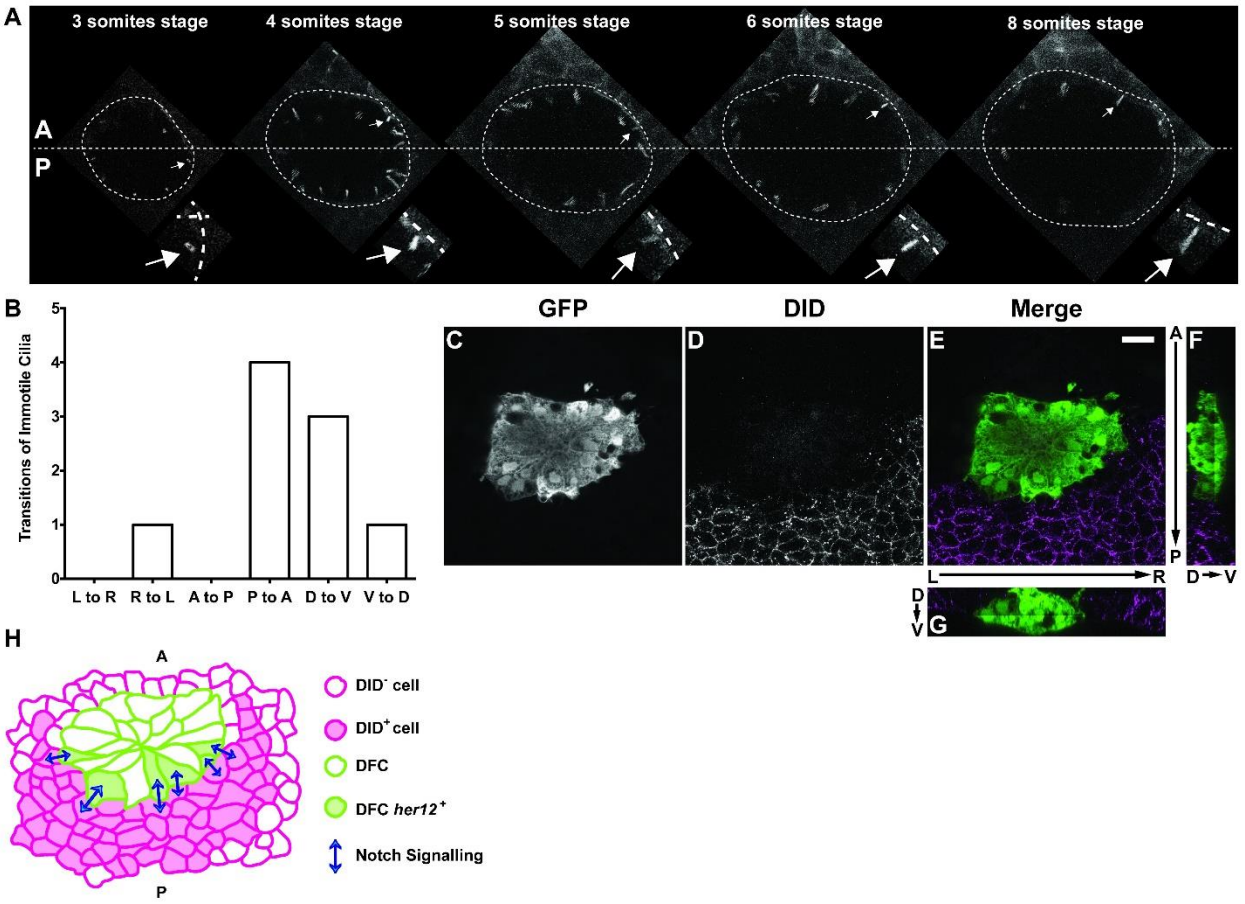

Figure 5 – figure supplement 2

Positions of immotile cilia in the anterior-posterior axis change through development.

(**A**) Transition of an immotile cilium from a Posterior position to an ever more Anterior position as development of the embryo progresses from 3 ss to 8 ss. (**B**) Number and type of transitions of Immotile cilia along the three axes (Anterior – Posterior; Dorsal – Ventral; Left – Right) from 3 to 8 somites stage (4 embryos, 9 cilia transitions, 19 immotile cilia tracked). L to R – Left to Right; R to L – Right to Left; A to P – Anterior to Posterior; P to A – Posterior to Anterior; D to V – Dorsal to Ventral; V to D – Ventral to Dorsal. (**C–G**) Localization of the DlD ligand by immune-histochemistry with an antibody anti-DlD (**D**) in sox17:GFP transgenic embryos at bud stage in Control. An antibody anti-GFP was simultaneously used in order to highlight the DFCs (**C**), with the resulting merged image in (**E**). Scale bar represents 20 μm. Anterior is to the top and Left is to left. (**F–G**) Orthogonal projections emphasising DLD expression. (**F**) Anterior is to the top and Dorsal is to left. (**G**) Dorsal is to the top and Left is to left. (**H**) Model depicting how the NS is occurring between the DLD positive surrounding cells and the Notch positive DFC in the posterior region of the cluster.

Video Legends

Video 1 - Scan of Wild Type KV showing motile and immotile cilia.
Embryo was injected with 400 pg Arl13b-GFP at 1 cell stage and imaged as described in Figure 1. Anterior is to the top and Left is to left.
https://doi.org/10.7554/eLife.25165.004

Video 2 - Time lapse from 3 to 8 somites stage with respective cilia trackings.
Tracking of the cilia was performed with Imaris software. Anterior is to the top and Left is to left.
https://doi.org/10.7554/eLife.25165.005

Video 3 - Immuno-staining of a KV of an 8 ss embryo from the transgenic line Foxj1a:GFP.
In blue are the nuclei stained with DAPI; in green the foxj1a positive KV cells; and in magenta are the KV cilia stained with antibody against acetylated α-tubulin. This experiment allowed us to determine if all monociliated KV cells expressed Foxj1a. Anterior is to the top and Left is to left.
https://doi.org/10.7554/eLife.25165.020

Figure 2 – video 1 - Wild-type fluid flow at 3 ss.
Movie from 1 WT, non-injected embryo. At this development stage, the native particles only present Brownian motion. Anterior is to the top and Left is to left. 30 frames per second.
https://doi.org/10.7554/eLife.25165.007

Figure 2 – video 2 - Wild-type fluid flow at 5 ss.
Movie from 1 WT, non-injected embryo. At this development stage the KV presents a homogeneous directional fluid flow. Anterior is to the top and Left is to left. 30 frames per second.
https://doi.org/10.7554/eLife.25165.008

Figure 2 – video 3 - Wild-type fluid flow at 8 ss.
Movie from 1 WT, non-injected embryo. At this development stage, the directional fluid flow is no longer homogeneous, presenting higher speeds at the anterior-left part of the KV. Anterior is to the top and Left is to left. 30 frames per second.
https://doi.org/10.7554/eLife.25165.009

Figure 5 – video 1 - *In situ* hybridization + immuno staining with *her12* RNA probe and antibody anti-GFP of a cluster of DFCs at bud stage from a *sox17:GFP* embryo.
In green are the DFCs (*sox17:GFP* positive cells) highlighted by the anti-GFP antibody. *her12*expression is visualized with the Fast Red (Roche) fluorescent precipitate in magenta. Anterior is to the top and Left is to left.
https://doi.org/10.7554/eLife.25165.027

Figure 5 – video 2 - 3D reconstruction of the WT *her12* expression in the DFCs cluster at bud stage.
3D reconstruction was performed with Amira software. Anterior is to the top and Left is to left.
https://doi.org/10.7554/eLife.25165.028

Figure 5 – video 3 - *In situ* hybridization + immuno staining with *her12* RNA probe and antibody anti-GFP of a cluster of DFCs at bud stage from a *sox17:GFP* embryo injected with 100 pg of *NICD* mRNA at 1 cell stage.
In green are the DFCs (*sox17:GFP* positive cells) highlighted by the anti-GFP antibody. *her12*expression is visualized with the Fast Red (Roche) fluorescent precipitate in magenta. Anterior is to the top and Left is to left.
https://doi.org/10.7554/eLife.25165.029

Figure 5 – video 4 - 3D reconstruction of *her12* expression in the DFCs cluster in an embryo over-expressing NICD at bud stage.
3D reconstruction was performed with Amira software. Anterior is to the top and Left is to left.
https://doi.org/10.7554/eLife.25165.030

Figure 5 – video 5 - 3D reconstruction of the WT DLD localization around the DFCs cluster at bud stage.
3D reconstruction was performed with Amira software. Anterior is to the top and Left is to left.
https://doi.org/10.7554/eLife.25165.031

Additional files

Supplementary file 1 - Microarray data.
Excel file that contains Table S1a - List of 706 genes with significantly altered transcription. This list contains 706 genes with a fold change in transcription higher than 2, in the DFCs from *dld*$^{-/-}$ mutant zebrafish embryos. Table S1b – List of motility associated genes from the Table S1a that have been associated with cilia in the different model organisms. Analysis performed with Cildb v2. Table S1c – List of primers sequences used for genotyping *dld*$^{-/-}$ mutant zebrafish embryos and for qPCR validations.

https://doi.org/10.7554/eLife.25165.034
Download elife-25165-supp1-v2.xlsx

Supplementary file 2 - Contains the R script for creating and analysing the flow maps.

https://doi.org/10.7554/eLife.25165.035
Download elife-25165-supp2-v2.pdf

CHAPTER 3

No fluid flow and different levels of Pkd2-mediated sensing affect left-right axis establishment in the same manner

"I suppose it is tempting, if the only tool you have is a hammer, to treat everything as if it were a nail."

Abraham Maslow, Toward a Psychology of Being (1962)

No fluid flow and different levels of Pkd2-mediated sensing affect left-right axis establishment in the same manner

Raquel Jacinto[1,2], Pedro Sampaio[1,2], Mónica Roxo-Rosa[1] and Susana S. Lopes[1]

1-CEDOC, Chronic Diseases Research Center, NOVA Medical School / Faculdade de Ciências Médicas, Universidade Nova de Lisboa, Campo dos Mártires da Pátria, 130, 1169-056 Lisboa, Portugal

2- Co first author

Summary

The left-right (LR) field recognizes the importance of the mechanism involving the calcium permeable channel Polycystin-2 (Yuan et al., 2015; Yoshiba et al., 2012; Field et al., 2011; Kamura et al., 2011). However, whether the early LR symmetry breaking mechanism is exclusively occurring via Polycystin-2 has not been fully tested.

By stopping the extracellular fluid flow, we negated any potential mechanosensory and flow-derived morphogen gradient mechanisms. We then asked whether this situation was similar to impairing the calcium permeable Polycystin-2 channel (Pkd2), crucial for correct LR patterning in mouse and zebrafish (Bisgrove et al., 2005; Pennekamp et al., 2002; Schottenfeld et al., 2007). Unfortunately, we could not make this comparison using the zebrafish mutant *pkd2*$^{-/-}$/*cup*$^{-/-}$ or the *pkd2* morphant at 1 cell stage because affecting Pkd2 in the whole embryo also affected the architecture of zebrafish left-right organizer and thereby influenced fluid flow dynamics. The only approach to get rid of Pkd2 contribution that minimizes the impact on architecture and flow dynamics was the DFC-specific pkd2 knockdown that still left Pkd2 protein and resulted in LRO with a slower fluid flow. Still, all our manipulations gave the same result: majority of symmetric *dand5* and randomization of organ *situs*.

Introduction

The presence of asymmetric intracellular calcium in LR axis establishment seems to be a constant in many model organisms, such as chick (Raya et al., 2004), zebrafish and *Xenopus* (Webb and Miller, 2006; Yuan et al., 2015)and mouse (McGrath et al., 2003). Although the exact role and time-window of action might vary, calcium seems to act as a very important player in this early process. In mice and zebrafish, the calcium oscillations seem to typically happen as a response to the directional fluid flow seen in the LRO of both models (node and Kupffer's vesicle KV, respectively), which is generated by the action of rotating cilia - hair-like structures on the surface of cells (Essner et al., 2005; Supp et al., 1997). Importantly, these calcium oscillations seem to be downstream of the calcium channel Pkd2 and influence the asymmetric expression of genes from the nodal signalling pathway (Bisgrove et al., 2005; Pennekamp et al., 2002; Schottenfeld et al., 2007; Yoshiba et al., 2012). In zebrafish it has also been shown that calcium is important not only at KV stages (Yuan et al., 2015) but also earlier to allow the correct migration of KV cell precursors, the dorsal forerunner cells (DFCs) and proper KV establishment (Schneider et al., 2008). It has been shown that calcium can interact with wnt signalling (Schneider et al., 2008) in zebrafish DFCs and with notch signalling in the chick embryo Hensen's node (Raya et al., 2004) for correct left-right axis establishment.

Polycystin 2 (Pkd2) is a known calcium channel that has been described as part of a mechanosensory complex first described in kidney cells (Nauli et al., 2003). Paired with its sensory partner Pkd1, which is capable of sensing urine fluid flow by the N terminus extracellular part, that supposedly signals to Pkd2 by the interacting C terminal parts of both proteins. The signalling output responds by opening the channel and allowing calcium to enter the kidney cells. Absence of either one of the partners leads to polycystic kidney disease, which is characterized by the formation of large fluid filled cyst due to overactivation of CFTR (Harris and Torres, 2009). Recent work from our lab established the zebrafish KV as an organ model for a fluid filled cyst, since the KV inflation is also

dependent on the crosstalk between Pkd2 and CFTR. *pkd2* knockdown induces an increase in KV volume via CFTR activation (Roxo-Rosa et al., 2015). Such volume is proportional to the levels of Pkd2 and provide an indirect indication of the amount of Pkd2 protein present in the KV cells. In this study the authors also confirmed that the *pkd2* knockdown technology results in the presence of less Pkd2 protein than the pool of Pkd2 that remains in *cup*$^{-/-}$ mutants, likely due to maternal contribution in the mutants (Roxo-Rosa et al., 2015). By *in situ* hybridization, *pkd2* and *pkd1l1* are strongly expressed in DFCs and KV cells from 8.3 to 12 hours post fertilization (England et al., 2017). Pkd2 protein is expressed in all KV cells in the cytosol around the nucleus and along the cilia in a punctuated manner and it has been shown in both models, zebrafish and mouse, to be important for left-right axis establishment (Bisgrove et al., 2005; Pennekamp et al., 2002; Schottenfeld et al., 2007; Yoshiba et al., 2012; Yuan et al., 2015). It is known that for left-right, Pkd2 sensory partner is Polycystin 1-like 1 (Pkd1l1) in mice and medaka (Field et al., 2011; Kamura et al., 2011).

There are two main hypotheses for left-right axis establishment: the chemosensory hypothesis and the mechanosensory hypothesis. The first is now based on the observation of nodal vesicular parcels (NVPs), small membrane-bound vesicles traveling in the mouse node. Their production and release are dependent of FGF signalling and they seem to transport sonic hedgehog and retinoic acid towards the left, which seemed to have an impact on the calcium elevation. Blocking FGF leads to a loss of calcium elevation on the left that was partially rescued by providing SHH and RA (Tanaka et al., 2005). The second is based on the clear regional distinction between motile and immotile cilia present in the mice node, where an enrichment of immotile cilia in the crown cells surround the motile cilia in the pit (McGrath et al., 2003). This distinction allows the regional separation of functions: while the motile cilia are responsible for generating fluid-flow, the immotile cilia can sense it and respond accordingly (McGrath et al., 2003). The fact that the presence of Pkd2 on the crown cells is crucial for left-right establishment is

very strong evidence that these are the sensory cells (Yoshiba et al., 2012). However, the evidence that cilia are the sensory organelles where Pkd2 exerts its function comes from an elegant experiment where restoration of primary cilia in crown cells of *kif3a* mutants rescued the response to the artificial flow and allowed normal laterality to be recovered (Yoshiba et al. 2012).

The KV architecture in zebrafish does not show any clear distinction between the localization of the two cilia types, in fact, Tavares et al. (2017) have shown that 20% of the cilia population is immotile and randomly distributed. However, morphologically, KV cilia are all equal and even after an ultrastructural study where three KVs were sampled every 5 microns, all KV cilia showed dynein arms despite that 20% are immotile (Tavares et al. 2017). In zebrafish, it was showed that the motile/immotile cilia ratio is very important for robust fluid flow pattern and strength (Sampaio et al., 2014; Tavares et al., 2017). Nevertheless, Tavares et al. (2017) did not advocate for mechano- or chemosensation because both models are compatible with their observations. A piece of evidence that strongly supports the mechanosensory hypothesis was provided by Yuan et al, (2015) using a genetically encoded calcium indicator (GECIs) targeted specifically into cilia via fusion with Arl13b (arl13b-GCaMP6). They observed a burst of intracellular calcium on the left side of the KV preceded by intraciliary calcium oscillations (ICOs) that then propagated into the left sided tissue. This was also dependent on Pkd2 – knockdown of *pkd2* completely abrogated the ICOs and the left sided intracellular calcium wave (Yuan et al., 2015). On the other hand, subsequent work by Clapham's group has challenged the view that the immotile cilia in the mouse node can act as a mechanosensors. By using another calcium molecular sensor, (Arl13b-mCherry-GECO1.2) they saw that the first calcium signals did not originate in the cilium, but rather started in the cytoplasm and then propagated back into the cilium. They also showed that physiological flow could not induce a calcium response in the cilium (Delling et al., 2016). So, either they are correct and their discoveries will have a big impact in field by making

everybody redesign their hypotheses or their technology is not sensitive enough or have the appropriate time-resolution to discern the very first calcium events.

Pkd2 is expressed in the ciliary and cytoplasmic membranes and in the endoplasmic reticulum (ER), so this raised the question: which Pkd2 compartment, is the important one for left-right? There is evidence from rescue assays in zebrafish supporting a stronger role in LR for the pool of Pkd2 at the ER rather than the pool in cilia. This was showed by using three different constructs: a WT version, TRPP2^{S812A} and TRPP2^{S812D}. The first mutation inhibited the interaction of TRPP2/Pkd2 with PACS proteins on the ER, allowing for the trafficking of TRPP2 to other subcellular compartments, while the second enhanced the interaction with PACS, thereby trapping it in the ER. TRPP2^{S812D} rescued LR defects more effectively than either WT and TRPP2^{S812A} versions, suggesting a stronger role of Pkd2 pool present in the ER in LR axis establishment (Fu et al., 2008). Also, Vermont's lab recently showed by mathematical models that the noise inside the KV might be too high for mechanosensory to reliably work with the amount of immotile cilia reported by them, which is less than 5% (Ferreira et al., 2017). However, work from Tavares et al. (2017) found 20%, which would be a good enough number to distinguish between noise and real signal, according to the mathematical models from Ferreira et al. (2017). In the end, is it possible that both hypotheses for left-right, mechanosensory and chemosensory, are working together for robust left-right axis establishment.

Problems either in cilia motility or cilia flow sensing capability can lead to laterality defects with various degrees of severity: *situs inversus,* a mirror image of the normal *situs* (*situs solitus*) or various abnormal combinations of thoracic and abdominal *situs* – heterotaxy - which is more severe and can even result in early death in humans (Fliegauf et al., 2007). Whether heterotaxy is increased by impaired ciliary motility or defective ciliary signalling through Pkd2, or both, is a question we address here. One of the advantages of using zebrafish to answer this question is the ability to manipulate cilia in early development, and later assess flow and *situs* in the exact same embryo. We previously characterized

flow maps inside the KV by following native particles present in this organ (Sampaio et al., 2014). We reported that there are two main spots of faster flow in the WT, one in the anterior and one in the left side. The latter inversely correlates with expression of *dand5* (ortholog of *cerl2*) mainly present on the right side (Sampaio et al., 2014). As in mouse (Marques et al., 2004; Nakamura et al., 2012; Oki et al., 2009) and xenopus (Schweickert et al., 2010), *dand5* starts to be symmetrically expressed and by a flow dependent process that is still unclear, its expression decreases on the left side. This early *dand5* asymmetry is fundamental for generating the left sided *nodal* cascade of gene expression (Hojo et al., 2007; Lopes et al., 2010; Sampaio et al., 2014).

We previously demonstrated that by knocking down an inner dynein arm (*dnah7*) present in motile cilia, we were able to generate embryos with flow speeds close to zero, i.e where all cilia were stopped upon verification by high-speed videomicroscopy (Sampaio et al., 2014). This 'no flow' experimental setting allowed us to address a fundamental basic question that remains unanswered in the LR field: is 'no flow' the same as impaired Pkd2, or do these treatments render different outcomes, which would indicate the presence of other potential players apart from Pkd2. We also wanted to investigate if the absence of both flow and Pkd2 resulted in a worse *situs* scenario, i.e in more heterotaxy. Our study involved careful confirmation of all the premises required for such comparison to be made, such as decreasing Pkd2 without impacting on flow and stopping flow without removing cilia. Additionally, for the 'no flow' experiments we imaged the embryos to select those with total cilia immotility upon manipulations.

Experimental Procedures

Fish stocks and genetics

The following zebrafish lines were maintained and used as described elsewhere (Westerfield, 2000): wild-type (AB), *Tg(foxj1a:GFP)* (Caron et al., 2012) and cup(+/-;*Tg(foxj1a:GFP)*)^{tc321}. Embryos were raised at 28 or 30ºC, depending on the experiment, in E3 embryo media and

staged accordingly (Kimmel et al., 1995). Procedures with zebrafish were approved by the Portuguese DGAV (Direcção Geral de Alimentação e Veterinária).

Injections of morpholino oligonucleotides and Ouabain treatment

dnah7 morpholino (Sampaio et al., 2014) was diluted in sterile water and injected at one cell stage at a dose of 3 ng per embryo. *pkd2* morpholino (Schottenfeld et al., 2007) was diluted in sterile water and injected at one cell stage at a dose of 2.5ng per embryo. To generate chimeric *pkd2* knockdown in DFCs, *pkd2* morpholino (Schottenfeld et al., 2007) was diluted in 10,000 MW rhodamine-dextran solution (1:4; Sigma-Aldrich) and injected at a dose of 4.2 ng per embryo into the yolk of 512 to 1000-cell-stage embryos as previously described (Amack and Yost, 2004). Morpholino injection efficiency was thoroughly controlled as follows: specific *pkd2* MO targeting to DFCs (called *pkd2*MO^{DFCs}) was determined by the rhodamine lineage tracer in KV and yolk cells of the selected embryos (Amack and Yost, 2004) (Fig. 2A, A' and A''); embryos injected with *dnah7* morpholino oligonucleotide were carefully screened by high speed-videomicroscopy for confirming cilia immotility throughout the entire KV. Double morphant (called DM^{DFCs}) were generated by injecting dnah7 morpholino at 1 cell stage embryos and later *pkd2* morpholino into the yolk of 512 to 1000-cell-stage embryos. Embryos were screened as explained above. A mismatch *pkd2* morpholino was injected in the same conditions (4.2ng per embryo) as control. Treatments with 5μM Ouabain were performed as detailed in Roxo-Rosa et al., 2015.

Live imaging for flow recording

Mounted embryos between 13–14 hpf were set under the 100x/1.30 NA oil immersion objective lens on a Nikon Eclipse Ti-U inverted microscope at room temperature (26ºC). All images were taken with the dorsal roof of the KV facing the objective lens. Bright field images were recorded with a FASTCAM MC2camera (Photron Europe, Limited) controlled with PFV (Photron FASTCAM Viewer) software. Native KV particles were filmed at 60 fps for 30 seconds while cilia were recorded at 500 fps for 2 seconds. KV flow and CBF measurements were analysed using Fiji software as described previously (Sampaio et al., 2014). We have successfully analysed 8 WT embryos, 7 *pkd2*MO 1-cell stage, 4 *dnah7*MO injected embryos, 6 *pkd2*MO^{DFCs} injected embryos and 8 Double Morphants(DM)^{DFCs} injected embryos.

Immunofluorescence and in *in situ* hybridization

Whole-mount immunostaining and *in situ* hybridization were performed as described previously (Lopes et al., 2010). Antibodies used for immunostaining were mouse anti-acetylated alpha-tubulin (1:400; Sigma), Goat anti-mouse Alexa Fluor 488 (Invitrogen; 1:500) and Alexa fluor 546 Phalloidin (Invitrogen/ molecular probes 1:100). Pkd2 immunostaining was performed as described in Roxo-Rosa et al., 2015. Individual *dand5 in situ* hybridizations were performed at 8-10 somite stage in 37 WT embryos, 13 *pkd2*MO in 1-cell stage, 14 *pkd2*MO^{DFCs}, 9 *dnah7* MO and 11 DM^{DFCs}. *foxa3 in situ* hybridizations at 53 hpf were performed as described elsewhere (Thisse and Thisse, 2008) and were used 205 WT controls, 56 *pkd2*MO^{DFCs}, 112 cup-/- mutants, 140 *pkd2*MO in 1 cell-stage, 31 *dnah7*MO and 15 DM^{DFCs}. Gene expression and *situs* scoring were performed double blind by two investigators and the results were analysed by Fisher's exact test with Bonferroni correction for multiple comparisons and by Binomial exact test for comparisons in the same genetic background.

Cell shape and cilia motility assay

cup(+/-;*Tg(foxj1a:GFP)*)^{tc321} embryos were mounted live in 2% (w/v) agarose mold and covered with E3 medium for confocal microscopy live imaging in a Zeiss LSM710 with a Olympus 40x water immersion lens (NA 0.8) at room temperature. To assess cell shape, whole KVs were scanned with z sections of 0.5 µm, with an acquisition rate of less than 1 fps. After acquisition, embryos were retrieved from the agarose mold and let develop for heart *situs* scoring and to observe curved or straight tail phenotypes. We successfully imaged 12 cup$^{-/-}$ embryos and 19 sibling embryos. *pkd2*MO 1 cell-stage, *pkd2*MO^{DFCs} and DM^{DFCs} injected embryos were immunostained at 14 hpf for actin cytoskeleton and mounted in PBS 1X for confocal epifluorescence microscopy in the same conditions. We imaged 15 controls, 11 *pkd2*MO 1 cell-stage, 15 *pkd2*MO^{DFCs}, 5 DM^{DFCs} embryos and 4 embryos *pkd2*MO 1 cell-stage treated with 5µM Ouabain. Selected stacks were subsequently analysed in Amira for 3D cell shape in KV midplane (5 to 6 embryos for each condition). Results were statistically analysed by using the paired t-test and statistical significance was set at p-value < 0.05. For cilia motility, embryos were injected with 400pg of Arl13b-mCherry mRNA and 2.5ng of *pkd2* morpholino into 1-cell stage. Embryos were allowed to develop until 8 somite stage and then mounted live as explained above. Live imaging was performed in the same conditions as described above. To assess motility, whole KVs were scanned with z sections of 0.5 µm, with an acquisition rate of 9.6 slices per minute (6.25 sec per slice) (Tavares et al., 2017).

Stacks were then processed in Fiji for identification of motile and immotile cilia. We analysed 8 controls and 5 *pkd2* morphant embryos.

Heart and gut laterality

At 30 hpf we evaluated heart jogging using a stereoscopic zoom microscope (SMZ745, Nikon Corporation) to observe the embryos from the ventral side. These embryos were then allowed to develop in separated petri dishes and at 53 hpf, embryos were fixed and processed for *foxa3 in situ* hybridizations to assess gut laterality. We could then pair the heart *situs* with gut *situs* for each treatment and attribute an embryo *situs*. We scored organ *situs* in 159 WT, 31 dnah7 knockdown embryos, 56 *pkd2* DFCs knockdown embryos, 15 double morphants and 31 *pkd2* mismatch control-MO^{DFCs} injected embryos.

Quantitative PCR

Four groups of eight to ten embryos were used; one group for untreated (control) and the others were injected as explained above and let develop until 8-10 somite stage. After thorough scoring of rhodamin expression only in KV and yolk cell and complete cilia immotility, total RNA was extracted using the Qiagen RNeasy Mini Kit (ref number 74104) and reverse transcribed using both oligo(dT)$_{18}$ and random hexamer primers with the RevertAid First Strand cDNA Synthesis Kit (ref number K1622) following the manufacturers' instructions. This was repeated three times for three different biological replicates. Expression was quantified by PCR using Roche SYBR Green I Master (ref number 04887352001) and run in a Roche LightCycler® 96 Real-Time PCR System. Results were analysed and depicted as fold-change of transcript levels in injected embryos relative to transcript levels in control embryos. The p-value represents significance in the pairwise comparison of transcript levels between injected and control embryos as determined using the paired t-test. Statistical significance was set at p-value < 0.05. *dand5* levels were normalized in relation to *eukaryotic elongation factor 1 alpha 1 like 1* (*eef1al1*) and *ribosomal protein L13a* (*rpl13a*) expression. Primer sequences used were as follows: *dand5* forward 5′-CCGCAATCCTGACCCATAGCAA-3′ and reverse 5′-CTCCTCCGTTATGCGCTGTGTA-3′; *eef1al1*

forward 5'-CCTTCAAGTACGCCTGGGTGTT-3' and reverse 5'-CACAGCACAGTCAGCCTGAGAA-3'; *rpl13a* forward 5'-TGACAAGAGAAAGCGCATGGTT-3' and reverse 5'-GCCTGGTACTTCCAGCCAACTT-3'.

Results

Different Pkd2 levels affect KV volume and architecture and impact on fluid flow pattern

To understand if no flow and no Pkd2-mediated sensing rendered the same LR phenotypes, we had to find the best Pkd2 manipulation possible to compare with our well established no flow situation. First, we decided to explore the already published *pkd2* morpholino (Schottenfeld et al., 2007). To evaluate the flow speed, we recorded the native particles inside the KV of multiple embryos at 8 somite-stage (ss) using high speed videomicroscopy (Sampaio et al., 2014). Sampaio et al. (2014) had already described the typical flow pattern: stronger flow in the anterior region compared with the posterior region and also stronger on the left side than on the right side (Figure 1A). Knockdown of *pkd2* with a morpholino led to a decrease in total flow speed (from 10 in the WT to 4μms^{-1} in *pkd2* morphants, Figure 1A and C respectively), with a loss of the anterior and left hotspots of strong flow. Also, we observed a significant decrease in cilia beat frequency (from 34Hz in WT controls to 32Hz in *pkd2* MO 1 cell-stage, Wilcox test p-value <0.05, Figure 1B and D respectively). Morphants also showed strong volume increase (59pL in WT to 92pL in *pkd2* morphants, Roxo-Rosa et al., 2015). Interestingly, when we looked for the ratio of motile/immotile cilia with the same method used in Tavares et al. (2017) in *pkd2* morphants, there was a significant increase of the immotile cilia population at the expense of motile cilia (from 20% of immotile cilia in WT controls to 35% in *pkd2* morphants p-value<0.05, Figure 1). All these features together could explain why the flow is much slower in *pkd2* morphants, since bigger KVs with less motile cilia that beat slower

can account for an overall slower fluid flow speed. In sum, we could not use a 1-cell injection *pkd2* morphants in our comparison since they also showed problems with flow pattern.

It has been previously reported that Pkd2 is present in many tissues, including notochord (Mangos et al., 2010) which has been recently shown to play an important role in KV architecture (Compagnon et al., 2014). Therefore, we decided to inject the *pkd2* MO in a later developmental stage and specifically target the precursors of the KV – the dorsal

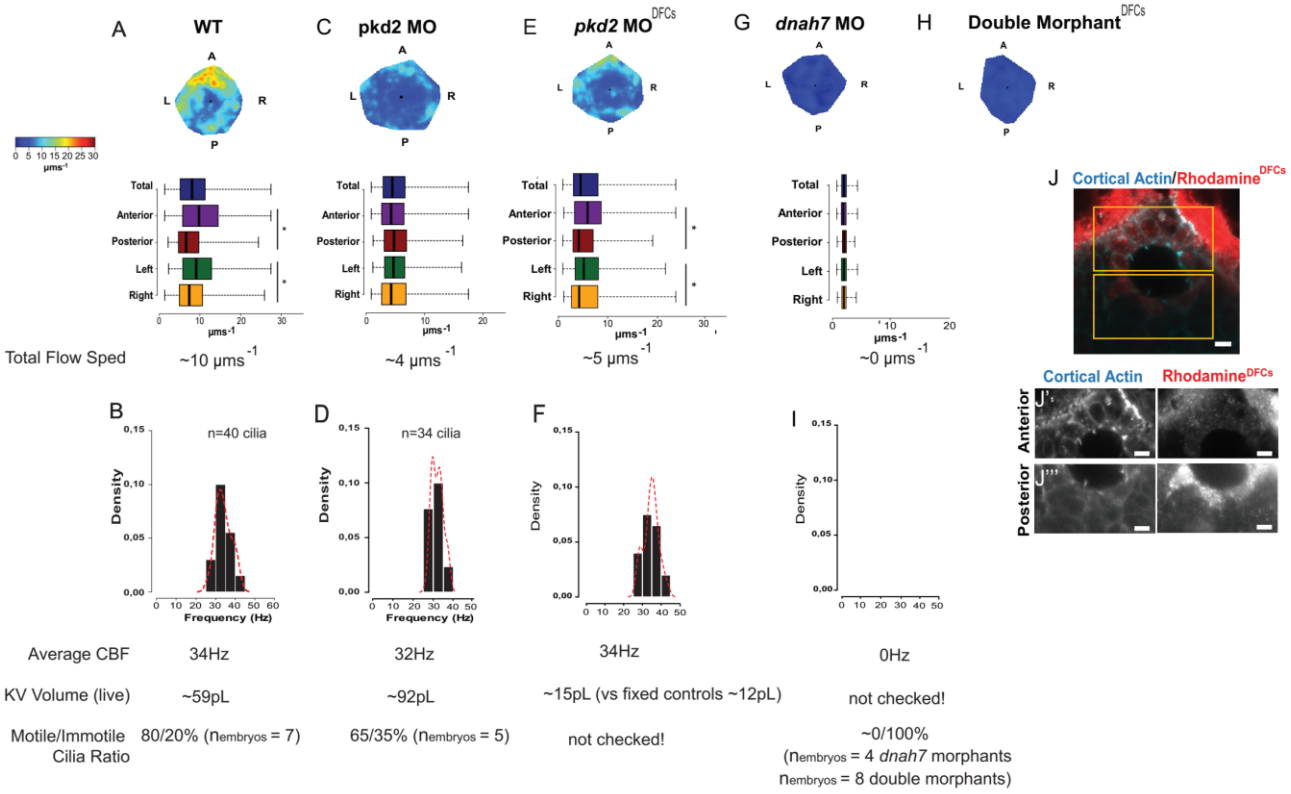

Figure 1. Different *pkd2* manipulations impact on fluid flow pattern and KV volume.

(A, C, E, G and H) Fluid flow heatmap and quantification of WT siblings (n=8) and *pkd2* knockdown into 1-cell stage morphants (n=140), *pkd2* MO^{DFCs} (n=6), *dnah7* MO (n=4) and DM^{DFCs} (n=8), respectively. Asterisks represent statistical significance (Wilcoxon Test, p-value < 0.05). L left, R right, A anterior and P posterior. (B, D, F and I) Cilia beat frequency (CBF) of WT, *pkd2* knockdown into 1-cell stage morphants, *pkd2* MO^{DFCs} morphants and *dnah7* MO/Double Morphants^{DFCs}; WT embryos an average of 34Hz, *pkd2* knockdown into 1-cell stage morphants an average of 32Hz, *pkd2*MODFCs an average of 34Hz and dnah7MO/Double Morphants^{DFCs} an average of zero (paired t-test, p-value < 0.05). (J) Immunostaining for cortical actin and rhodamine showing the result of a successful injection of *pkd2* MO into KV precursors, anterior (J') and posterior (J'') panels in the different channels allow for better contrast/brightness balance.

forerunner cells (DFCs) (Essner et al., 2005). By co-injecting the *pkd2* MO with the lineage tracer rhodamine-dextran, we could later select the embryos that only showed fluorescence in the yolk cell and the KV (Figure 1J, J' and J''). Below we shall refer to these embryos as *pkd2*MO^{DFCs}. This treatment did not significantly increased KV volume (Roxo-Rosa et al., 2015). We checked the flow maps and found that embryos injected with *pkd2*MO^{DFCs} had significant differences between anterior/posterior and left/right KV regions (Figure 1E), as in WT embryos (Figure 1A). These characteristics generated a heterogeneous flow map similar to that found in controls, though with a slower total speed (average 5 μms^{-1} while controls have average 10 μms^{-1}, Figure 1E and Figure 1A, respectively). Since we do not see differences in cilia beat frequency with this KV-targeted knockdown (Figure 1F), a possible explanation for this slower flow could be the motile/ immotile cilia ratio, where in this situation we might see more immotile cilia, similar to the *pkd2* knockdown in 1 cell-stage embryos. It would be important to check cilia motility in this treatment. Still, this situation is also not ideal: although with normal pattern, we have in general slower flow. We could not truly compare a no Pkd2-mediated sensing with a no flow situation since this manipulation of *pkd2* still affected flow speed.

KV volume seems to impact on flow pattern. Alterations in KV volume lead to differences in KV cell shape and overall architecture (Roxo-Rosa et al., 2015). To further evaluate this, we measured length and width of cells in the midplane of the KV and calculated the length width ratio (LWR) of cells in the anterior and the posterior part of the KV midplane. Typically, from 6-7 somite stage onwards, WT KVs present cells in the anterior region that have higher lengths and smaller widths (LWR>1), while cells in the posterior region are smaller in length and higher in width (LWR<1) (Figure 2A). This re-shaping is what allows for the formation of an anterior dorsal cluster that is responsible for the hotspot of flow in the anterior region (Compagnon et al., 2014; Sampaio et al., 2014; Smith et al., 2014; Wang et al., 2011). In contrast to what was found in the WT KVs, *pkd2* morphants had significant differences in LWR compared to controls, with both cells in the anterior and

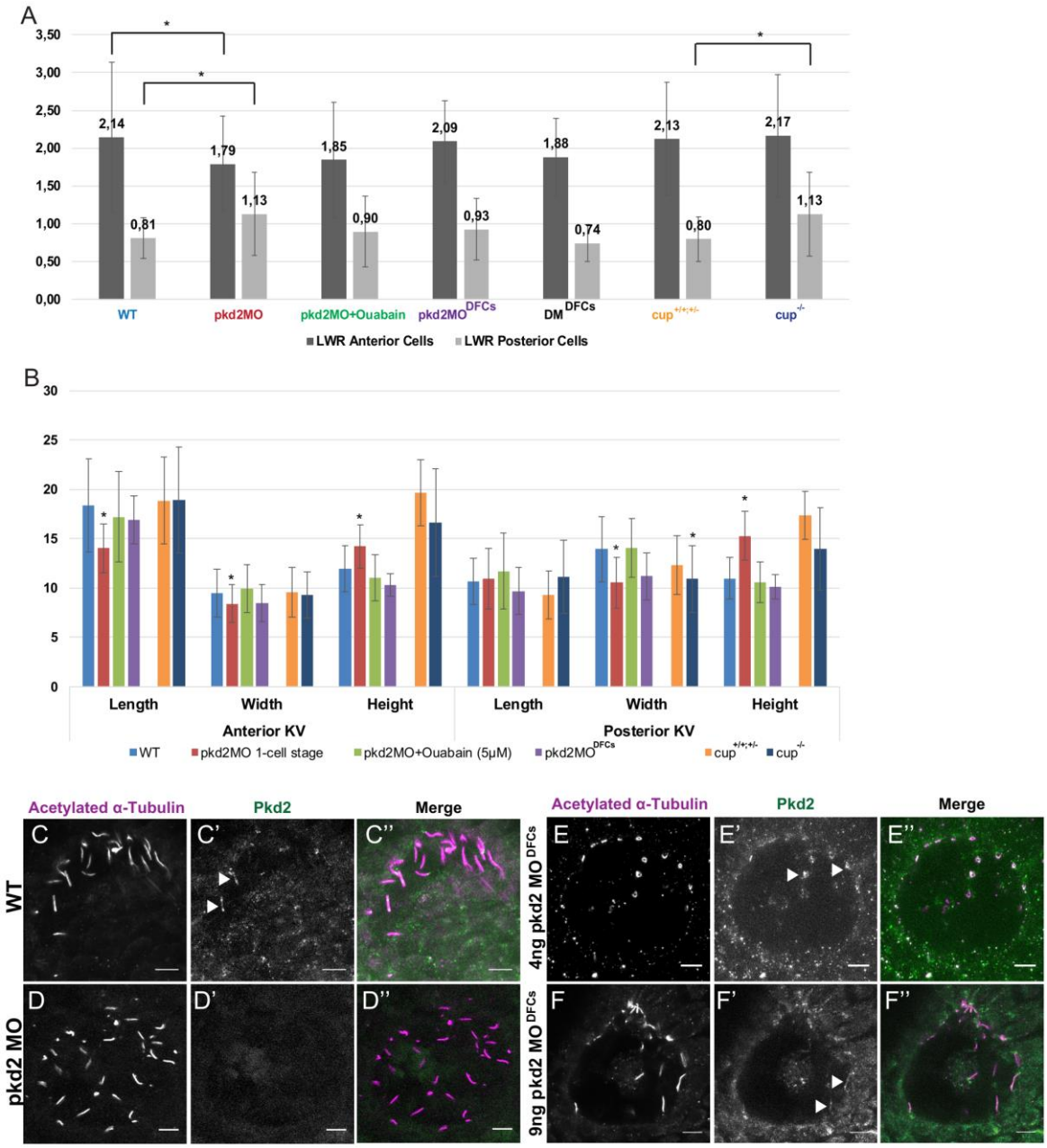

Figure 2. *pkd2* knockdown in the DFCs rescues KV fluid flow pattern but is still present in KV cilia.

(A) Quantification of the differences in length to width ratio in the KV of WT, *pkd2* knockdown into 1-cell stage (*pkd2*MO), *pkd2* knockdown into 1-cell stage morphants treated with 5µM Ouabain, *pkd2* MO^{DFCs}, DM^{DFCs}, *cup*$^{+/+;+/-}$ and *cup*$^{-/-}$ embryos. Asterisks represent statistical significance; t-student p-value<0.05 **(B)** Quantification of the differences in cellular length, width and height, in WT, *pkd2* knockdown into 1-cell stage (*pkd2*MO), *pkd2* knockdown into 1-cell stage morphants treated with 5µM Ouabain and *pkd2* MO^{DFCs} injected embryos. Asterisks represent statistical significance; t-student p-value<0.05 **(C-F, C'-F' and C''-F'')** Pkd2 and acetylated α-tubulin immunostaining for WT **(C-C')**, *pkd2* knockdown into 1-cell stage morphants **(D-D')**, 4ng pkd2MO^{DFCs} **(E-E')** and 9ng pkd2MO^{DFCs} **(F-F')** morphants.

posterior part more severely affected (Figure 2A, p-value<0.05). Cells in the anterior part had lower lengths and cells in the posterior region had lower widths, both compensating the increase in volume by increasing their heights in the z-axis (Figure 2B, blue bars *versus* red bars; p-value<0.05). This caused the dilution of the anterior dorsal cluster and a loss of the anterior-posterior bias that cilia typically show, which had a strong impact on the flow pattern of the morphants. To confirm that the architectural problems seen in this situation resulted only from the increase in volume and not directly from the absence of Pkd2, i.e., an indirect outcome of the absence of Pkd2, we treated *pkd2* morphants with 5μM of Ouabain. This drug impacts on CFTR activity and abrogates the increase in volume that we observed with *pkd2* knockdown (Roxo-Rosa et al. 2015). By using this treatment, cells in the anterior and posterior part of the KV presented normal LWR (Figure 2A), with all 3 measurements (length, width and height) similar to the controls (Figure 2B, green bars). Therefore, we conclude that the architectural problems seen in the KV are likely due to the increase in volume resulting from an overactivation of CFTR when *pkd2* is knockdown.

We then checked if the KV architecture was compromised in *pkd2*MO^{DFCs}. Cells in the anterior and posterior region of *pkd2*MO^{DFCs} presented normal LWR (Figure 2A, WT controls are not statistically different from either *pkd2*MO^{DFCs}), which was a good indicator that the anterior dorsal cilia cluster could generate the crucial anterior flow hotspot (Montenegro-Johnson et al., 2016; Sampaio et al., 2014; Smith et al., 2014).The only difference was that in embryos injected with 4 ng of *pkd2*MO^{DFCs}, KV cells had slightly smaller heights than control cells (Figure 2B, purple bars; p-value < 0.05). We also checked LWR in the zebrafish homozygous mutant line for *pkd2* called *curly up*$^{-/-}$ (*cup*$^{-/-}$) mutant line *tc321* that likely generates a non-functional truncated protein and the *pkd2* morpholino injected in 1-cell stage (Schottenfeld et al., 2007). We knew from previous work that the cup-/- mutants also had problems with KV volume (Roxo-Rosa et al., 2015). Our analysis showed that *cup*$^{-/-}$ mutants still retained the anterior normal cell shape, with

length to width ratio (LWR) >1, while the more posterior cells were significantly less wide compared to their siblings, showing a LWR proximate to 1, which indicates square cells (Figure 2A, p-value<0.05). When analysed in more detail, we found that posterior KV cells in *cup*$^{-/-}$ mutants had different widths than those from their siblings (Figure 2B, dark blue versus orange bars, p-value < 0.05), likely to accommodate the differences in volume previously seen. Considering the number of cells surrounding the KV in *cup*$^{-/-}$ mutants was not significantly different from their siblings (12 cells average in cup$^{+/+;+/-}$ WT and 13 cells average in cup$^{-/-}$ mutant siblings), we therefore concluded that differences in cell morphology affected the spacing between posterior KV cilia, resulting in a higher concentration of cilia in the posterior region of *cup*$^{-/-}$ mutants and should affect flow pattern. In summary, through attempting to impair the mechanosensory pathway using *cup*$^{-/-}$ mutants and 1 cell stage *pkd2* morphants, we generated fluid flow problems that were not anticipated. While this situation remains interesting from a fluid mechanics point of view, it also rendered these mutants and these morphants inadequate to answer our original question. The volume problems could only be averted by either controlling for volume increase with the CFTR inhibitor or targeting *pkd2* morpholino into DFCs, which created other problems on their own.

Finally, we checked by immunostaining how Pkd2 protein was being affected by our manipulations. While injecting *pkd2* morpholino into 1 cell-stage was very effective to bring down Pkd2 protein (compare Figure 2C' to 2D'; white arrowheads mark Pkd2-positive cilia), injecting the same morpholino in 500 cell-stage to target DFCs still showed Pkd2 in KV cells and along the ciliary axoneme (compare Figure 2C' with E'; white arrowheads mark Pkd2-positive cilia). Even when injected with a higher dose of morpholino, we could still see Pkd2-positive cilia (Figure 2F'; white arrowheads mark Pkd2-positive cilia). If there is a difference in protein levels, it is not one that we can easily assess by immunostaining. An alternative method to test this difference would be doing a western blot, but since the injection targeted only the KV precursors, performing a

western with samples of whole embryos would not be sensitive enough to detect differences either. The alternative would be to FACS the KV cells and do a western on that purified sample. Unfortunately, the amount of cells needed for such an experiment was not feasible.

In sum, none of the used approaches for knocking down *pkd2* rendered a perfect manipulation: taking all Pkd2 affected KV volume and therefore flow pattern, while targeting only to KV cells did not take enough protein to be visible by immunostaining. Still, we decided to proceed with the original experimental design until the end. The reason why was the observation that $cup^{-/-}$ mutants also have more Pkd2 protein due to maternal contribution and still have severe left-right defects in heart and gut *situs* (Roxo-Rosa et al., 2015; Schottenfeld et al., 2007). Therefore, we could be in a position where different levels of Pkd2 protein could have different ranges of phenotypes and that would be an interesting result. Additionally, a 'no flow' situation and a double knockdown situation (where Pkd2 was knocked down from KV cells and ~100% of cilia were rendered immotile – called DM^{DFCs}) were also evaluated (Figure 1G and H). DM^{DFCs} did not show any significant differences in LWR (Figure 2A).

Impairment of Pkd2 and fluid flow affect *dand5* expression pattern similarly, but show differences in expression level

For this comparative experiment we used two readouts: a) *dand5* expression, a nodal inhibitor known to be the first asymmetric expressed gene during the left-right axis establishment (Lopes et al., 2010) and b) internal organ *situs*. In WT embryos, *dand5* is mainly expressed on the right side from 8 somites onwards (Lopes et al., 2010) (Figure 3A). Our results showed that in the 'no flow' scenario (as in Sampaio et al., 2014), *dand5* became predominantly symmetric (Figure 3D, Fisher test with Bonferroni correction, p-value<0.0125). Next, when we impaired Pkd2-mediated sensing mechanism either in whole embryo or specifically in the KV, and these treatments also resulted in a symmetric *dand5* expression pattern (Figure 3B and C, respectively; Fisher test with Bonferroni

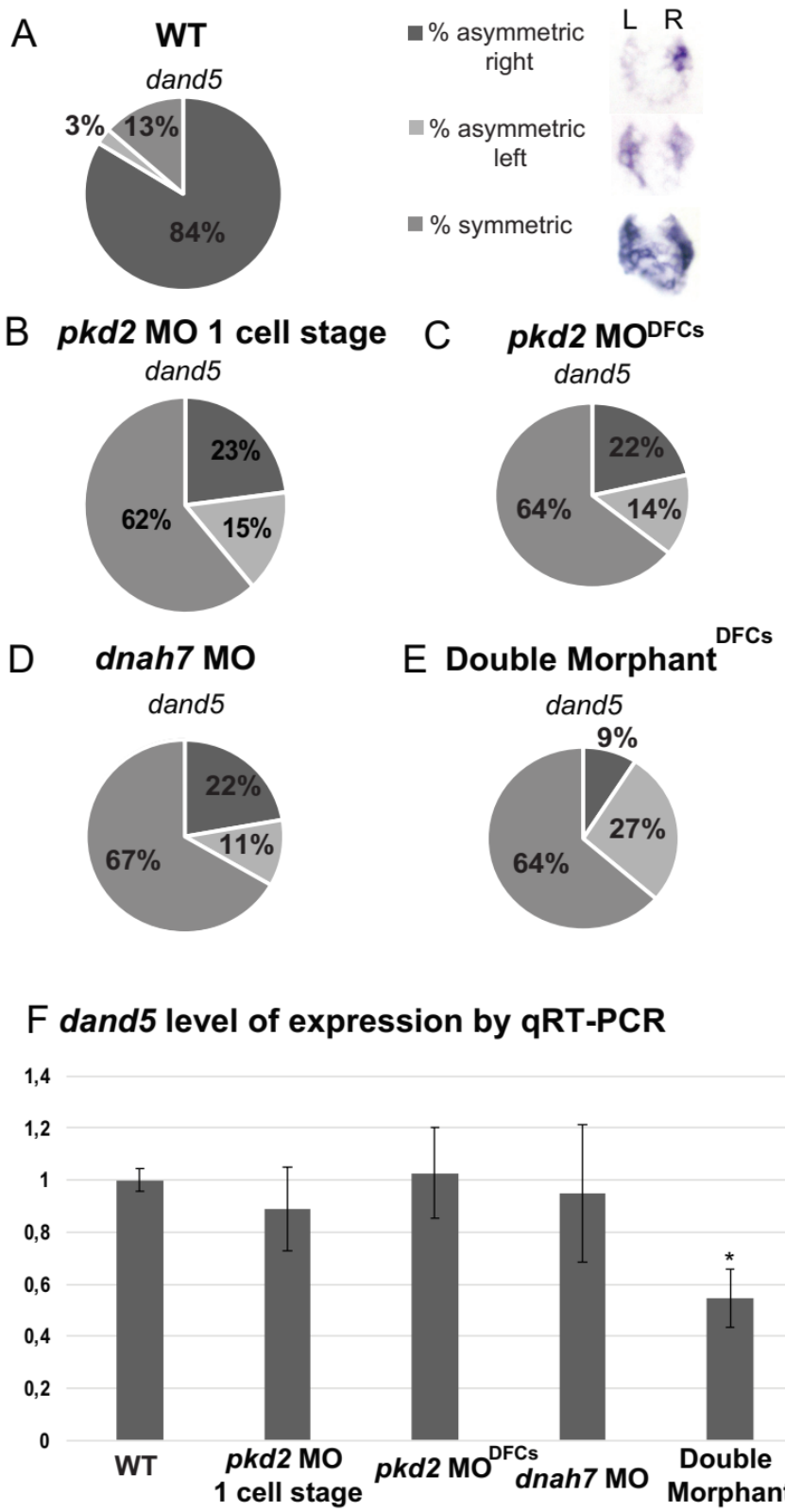

Figure 3. Impact of lack of fluid flow and knockdown of *pkd2* in *dand5* expression pattern and level

(A-E) *dand5* expression pattern quantification by in situ hybridization of WT embryos, *pkd2* MO 1 cell stage, *pkd2* MO^{DFCs}, *dnah7* MO and DM^{DFCs}. **(F)** *dand5* expression level in fold change quantified by qRT-PCR; asterisks represent statistical significance (paired t-test, p-value<0.05).

correction, p-value<0.0125). In addition, we found that when both processes were affected, the expression pattern distribution was again very similar to the previous cases (Figure 3E; Fisher test with Bonferroni correction, p-value<0.0125). This points to the fact that, in terms of expression pattern, *dand5* becomes highly symmetric both when there is 'no flow' (67%), when there is 'reduced *pkd2* mediated sensing' of that flow (64%), or both (64%). This fact confirms that Pkd2-mediated flow sensing is very important to define *dand5* expression pattern, which in WT embryos may be accomplished by higher degradation rates of its mRNA on the left side of the LRO (Nakamura et al., 2012; Schweickert et al., 2010; Oki et al., 2009). After comparing all different treatments between each other, we found no statistically significant differences between them (Fisher test with Bonferroni correction, p-value>0.008).

As for mRNA expression quantification of *dand5*, qRT-PCRs were performed for each condition. For all the cases where motility was abolished, embryos were observed with high-speed videomicroscopy to ensure that all cilia were immotile. Although there were no differences between WT, *pkd2* MO at 1 cell stage, *pkd2* MO^{DFCs} and *dnah7* MO, embryos injected with both morpholinos expressed significantly less *dand5* (Figure 3F; t-student, p-value<0.05). So, regardless of the expression pattern being mainly symmetric in all conditions, abolishing both processes seem to additionally affect *dand5* mRNA expression level. This could indicate the presence of a downstream effector of both flow and Pkd2-mediated sensing, responsible for maintaining *dand5* expression levels independently of its pattern. Such an effector would be sensitive to the combined 'no flow'/no Pkd2 mediated sensing situation, but would still be active in an independent 'no flow or 'no Pkd2' situation.

Fluid flow abrogation shows more severe effects on organ *situs* than *pkd2* knockdown

Lastly, we analysed organ *situs*. Controls typically display a left heart and left liver (97.5% of the cases), which means *situs solitus* in zebrafish (Figure 4A). All three *pkd2*

knockdown treatments randomize *situs*, making it equally possible to fall in one of the three categories (Figure 4B-D; Fisher test with Bonferroni correction, p-value<0.007). In fact, there are no statistically significant differences in terms of organ *situs* between these three approaches (Figure 4G; Fisher test with Bonferroni correction, p-value>0.008) and they are not different from a total randomization (Figure 4G in the last column all situations were compared with a random fate of 33%; Fisher test with Bonferroni correction, p-value>0.006). This points to the hypothesis that even when Pkd2 protein is marginally reduced, it still has a huge impact on left-right axis establishment, pointing to a minimal threshold. This result is different from what happens with the volume increase, since it seems you need a more complete *pkd2* knockdown to see a big impact on CFTR activation and therefore KV volume.

Abrogation of flow also led to a randomization of organ *situs* (Figure 4E and last column in Figure 4G; Fisher test with Bonferroni correction, p-value>0.006). Blocking both flow and Pkd2-mediated sensing showed the same phenotype (Figure 4F and M). This is in line with what we saw with *dand5* expression pattern, since there were also no differences between treatments. The only difference observed was the level of *dand5* expression in the double morphants. We can hypothesize that the reason why we do not observe a stronger phenotype in the double morphants in terms of organ *situs* might be because, without flow, more or less *dand5* has no impact on organ *situs*. On the other hand, our results seem to suggest that flow and Pkd2 are important for the maintenance of *dand5* levels of expression and not only for the correct pattern. Without flow but with normal levels of Pkd2, *dand5* is symmetric but has a normal level of expression (Figure 3F). The same happens when the flow has a normal pattern and we knockdown *pkd2* (Figure 3F). Only when we affect both we also affect the maintenance of *dand5* levels (Figure 3F).

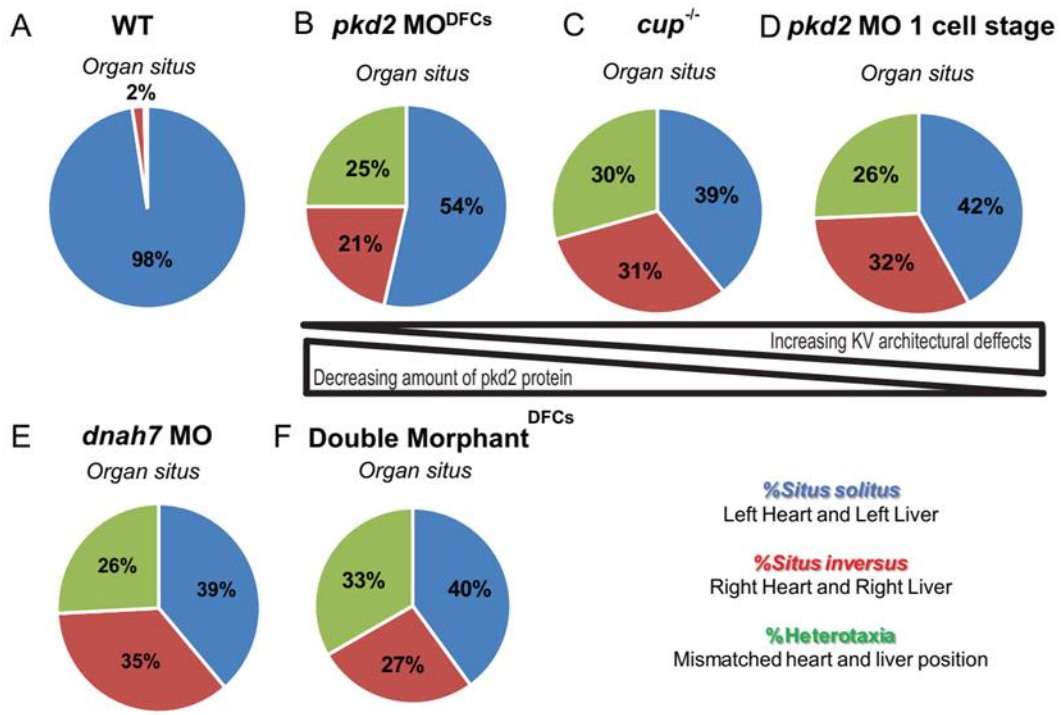

G Statistical analysis of organ *situs* for different treatments with Fisher test and Bonferroni Correction for multiple comparissons

	SS	SI	H	p-value WT vs…	p-value pkd2MO DFCs vs…	p-value cup-/- vs…	p-value pkd2MO 1cell stage vs…	p-value dnah7MO vs…	p-value DM DFCs vs…	p-value all vs random (33%)
WT	200	4	1							2,20E-16
4ng pkd2MO DFCs	30	12	14	4,40E-16						4,84E-02
cup-/-	44	35	33	2,20E-16	2,03E-01					6,77E-01
2,5ng pkd2MO 1 cell-stage	59	45	36	2,20E-16	2,58E-01	8,17E-01				3,13E-01
3ng dnah7MO	12	11	8	8,00E-16	3,08E-01	9,05E-01	9,67E-01			7,35E-01
Double Morphant DFCs	6	4	5	1,01E-09	5,96E-01	9,42E-01	8,34E-01	8,57E-01		9,40E-01
4ng pkd2-MisMo	26	0	5	3,05E-04	2,76E-03	3,74E-06	4,44E-06	9,66E-05	1,75E-03	4,34E-07
p-value < error with Bonferroni correction				7,14E-03	8,33E-03					6,25E-03

Figure 4. Comparison of organ *situs* between lack of fluid flow and different knockdown levels of Pkd2

(A-F) Organ *situs* quantification by scoring heart and liver laterality in the same larvae; experimental conditions involved injecting *dnah7* MO, *pkd2* MO 1 cell stage, *pkd2* MO^{DFCs} and DM^{DFCs} and *cup*$^{-/-}$ mutants. **(G)** Statistical analysis of organ *situs* for different treatments using a Fisher test with p-value corrected for multiple comparisons with Bonferroni correction. SS – *situs solitus*; SI – *situs inversus*; H – heterotaxia. Green values show tests where H_0 could be rejected and red values show tests where H_0 could not be rejected.

Discussion

What started as a simple question - is no flow the same as no Pkd2-mediated sensing for left-right axis establishment – ended in a realization that manipulating Pkd2, was trickier than we first anticipated. Changing the amount of Pkd2 in the zebrafish KV not only had an impact on left-right but also influenced the whole KV architecture and flow pattern and strength. Although we tried all manipulations currently available, the best compromise we could achieve was a situation where we still had a considerable amount of Pkd2 protein and normal flow pattern but weaker in strength (compare *pkd2*MO in 1 cell-stage in Figure 1C with *pkd2*MO^{DFCs} in Figure 1E). The reason why we still have Pkd2 protein might be explained by the fact that a later injection is not as efficient at blocking the maternal contribution and the half-life of this channel makes it very stable for a long period of time. How fair is to compare this *pkd2*MO^{DFCs} with weaker flow to a no flow situation is very debatable. We cannot assure that, although we see the same range of LR phenotypes, both in terms of *dand5* expression and organ *situs* (Figure 3 and 4), this actually results from a slower flow. When we increased the amount of morpholino injected into DFCs (from 4 to 9ng) we started to see KVs with more volume, meaning that we were likely succeeding in taking more Pkd2 protein out (Roxo-Rosa et al., 2015). However, we still saw Pkd2 protein by immunostaining in KV cells and cilia despite we saw the same degree of defects in organ *situs* (48% of *situs solitus*, 18% of *situs inversus* and 33% of heterotaxia). On the other hand, *cup*$^{-/-}$ mutants showed that, with maternal contribution alone, there were minimal architectural problems (when compared with *pkd2*MO in 1 cell-stage) and still had a randomization of organ *situs*. Also, one study reports that the KV size is not tightly controlled during development, impacting on organ *situs* only if exceeding a certain threshold (Gokey et al., 2015). Further work should be done to address the differences found between mutant and morphant. An alternative would be to chemically maintain the volume (with Ouabain or a more specific CFTR inhibitor, CFTRinh-172) in the hope that this would keep the KV architecture constant and

do a stronger knockdown for Pkd2 by injecting the morpholino into 1 cell-stage (where it was proven to be more effective). It is still interesting to note that it was needed a stronger *pkd2* knockdown to see a volume and architectural problem than to see left-right problems, which would suggest that left-right must be more sensitive to decreases in Pkd2 protein doses in this system.

A big problem that we faced with our approaches was the flow speed. This could be happening either because the KV was too big for proper flow speed or because there were more immotile cilia and therefore less motile cilia producing flow. In our *pkd2*MODFCs situation, we had a proper flow pattern, but slower flow, which made us ask what is the minimum flow speed necessary for correct LR axis establishment. Some works from the mice model states that all LR decisions in the node are done when flow is still very slow: asymmetric gene expression is established prior to stronger flow and the fact that only two motile cilia can still produce enough flow for correct LR establishment (Shinohara et al., 2012). It the zebrafish model, *dand5* asymmetric expression is only established after the flow is strong, becoming weaker in the cells on the left side that feel the strongest flow (Sampaio et al., 2014). When flow is abrogated, dand5 becomes mostly symmetric, stronger on both sides, which coincide with the absence of flow (Sampaio et al., 2014). On the other hand, Yuan et al. (2015) shows that the intraciliary calcium oscillations on the left side happen earlier, when flow is weaker, pointing to the beginning of the process happening before strong flow. More experiments should be done in the zebrafish model in order to clarify if LR decisions are made with weak or stronger flow. Either way, mice and zebrafish LRO have very different topologies. The mice model has all cilia present in the dorsal roof of the LRO (Sulik et al., 1994) and being useful for flow production, while zebrafish has cilia all around the LRO, with more incidence in the dorsal anterior region (Wang et al., 2012) .

Autossomal dominant polycystic kidney disease (ADPKD) is the most common genetic disorders and result from mutations in PKD1 and/or PKD2. The clinical manifestations of this disease include renal cysts that lead to kidney failure, cyst in many other organs like liver, mitral valve prolapse and intracranial aneurysms (Grantham et al., 2006; Pirson, 2010; Pirson et al., 2005). Although mutations on PKD2 can only account for 15% of all the ADPKD disease, there are 278 different PKD2 mutations already described to be associated with this disease, which 48 are reported as being nonsense mutations and most likely leading to having no protein at all (Autosomal Dominant Polycystic Kidney Disease: Mutation Database - http://pkdb.mayo.edu/index.html). Despite that fact, there are only 3 cases of unrelated patients both presenting PKD2 mutations and laterality problems: a large deletion in one patient with dextrocardia and two different duplications (one in exon 1 and another in exon 3) in two patients with *situs inversus totalis* (Bataille et al., 2011). This makes laterality problems deriving from PKD2 mutations an extremely rare situation. At this point, we must ask if PKD2 in humans has the same importance for left-right as observed in other animal models like mice and zebrafish. There can be some explanations for this lack of penetrance of laterality disorders. There might be haplo-sufficiency for PKD2 in the human node, where half of the normal protein amount is sufficient for left-right to be established normally. Or maybe other calcium channels like a PKD2L1 and several others (as reviewed in Nauli et al., 2016) might be expressed in the human node and compensate the lack of PKD2 in left-right axis establishment. Or the mutations are so lethal that are not even reported due to early miscarriages. Either way, more work is needed to understand how different are humans from our current model animals in terms of Pkd2 and left-right.

Acknowledgements

The authors thank J. Vermot and L. Saúde for the *cup*^{tc321} mutant and the Tg(*foxj1a*:GFP) zebrafish lines, respectively. We also thank the IGC Image and Fish Facilities for great support.

References

Amack, J.D., and Yost, H.J. (2004). The T box transcription factor no tail in ciliated cells controls zebrafish left-right asymmetry. Curr. Biol. *14*, 685–690.

Bataille, S., Demoulin, N., Devuyst, O., Audrézet, M.P., Dahan, K., Godin, M., Fonts, M., Pirson, Y., and Burtey, S. (2011). Association of PKD2 (Polycystin 2) mutations with left-right laterality defects. Am. J. Kidney Dis. *58*, 456–460.

Bisgrove, B.W., Snarr, B.S., Emrazian, A., and Yost, H.J. (2005). Polaris and Polycystin-2 in dorsal forerunner cells and Kupffer's vesicle are required for specification of the zebrafish left-right axis. Dev. Biol. *287*, 274–288.

Caron, A., Xu, X., and Lin, X. (2012). Wnt/beta-catenin signaling directly regulates Foxj1 expression and ciliogenesis in zebrafish Kupffer's vesicle. Development *139*, 514–524.

Compagnon, J., Barone, V., Rajshekar, S., Kottmeier, R., Pranjic-Ferscha, K., Behrndt, M., and Heisenberg, C.-P. (2014). The notochord breaks bilateral symmetry by controlling cell shapes in the zebrafish laterality organ. Dev. Cell *31*, 774–783.

Delling, M., Indzhykulian, A.A., Liu, X., Li, Y., Xie, T., Corey, D.P., and Clapham, D.E. (2016). Primary cilia are not calcium-responsive mechanosensors. Nature *531*, 656–660.

England, S.J., Campbell, P.C., Banerjee, S., Swanson, A.J., and Lewis, K.E. (2017). Identification and Expression Analysis of the Complete Family of Zebrafish pkd Genes. Front. Cell Dev. Biol. *5*.

Essner, J.J., Amack, J.D., Nyholm, M.K., Harris, E.B., and Yost, H.J. (2005). Kupffer's vesicle is a ciliated organ of asymmetry in the zebrafish embryo that initiates left-right development of the brain, heart and gut. Development *132*, 1247–1260.

Ferreira, R.R., Vilfan, A., Jülicher, F., and Supatto, W. (2017). Physical limits of flow sensing in the left-right organizer. Elife *6:e25078*, 1–27.

Field, S., Riley, K.-L., Grimes, D.T., Hilton, H., Simon, M., Powles-Glover, N., Siggers, P., Bogani, D., Greenfield, A., and Norris, D.P. (2011). Pkd1l1 establishes left-right asymmetry and physically interacts with Pkd2. Development *138*, 1131–1142.

Fliegauf, M., Benzing, T., and Omran, H. (2007). When cilia go bad: cilia defects and ciliopathies. Nat. Rev. Mol. Cell Biol. *8*, 880–893.

Fu, X., Wang, Y., Schetle, N., Gao, H., Pütz, M., von Gersdorff, G., Walz, G., and Kramer-Zucker, A.G. (2008). The subcellular localization of TRPP2 modulates its function. J. Am. Soc. Nephrol. *19*, 1342–1351.

Gokey, J.J., Ji, Y., Tay, H.G., Litts, B., and Amack, J.D. (2015). Kupffer's vesicle size threshold for robust left-right patterning of the zebrafish embryo. Dev. Dyn. *245*, 22–33.

Grantham, J.J., Torres, V.E., Chapman, A.B., Guay-Woodford, L.M., Bae, K.T., King, B.F., Wetzel, L.H., Baumgarten, D.A., Kenney, P.J., Harris, P.C., et al. (2006). Volume Progression in Polycystic Kidney Disease. N. Engl. J. Med. *354*, 2122–2130.

Harris, P.C., and Torres, V.E. (2009). Polycystic Kidney Disease. Annu Rev Med *60*, 321–337.

Hojo, M., Takashima, S., Kobayashi, D., Sumeragi, A., Shimada, A., Tsukahara, T., Yokoi, H., Narita, T., Jindo, T., Kage, T., et al. (2007). Right-elevated expression of charon is regulated by fluid flow in medaka Kupffer's vesicle. Dev. Growth Differ. *49*, 395–405.

Kamura, K., Kobayashi, D., Uehara, Y., Koshida, S., Iijima, N., Kudo, A., Yokoyama, T., and Takeda, H. (2011). Pkd1l1 complexes with Pkd2 on motile cilia and functions to establish the left-right axis. Development *138*, 1121–1129.

Kimmel, C.B., Ballard, W.W., Kimmel, S.R., Ullmann, B., and Schilling, T.F. (1995). Stages of embryonic development of the zebrafish. Dev. Dyn. *203*, 253–310.

Lopes, S.S., Lourenço, R., Pacheco, L., Moreno, N., Kreiling, J., and Saúde, L. (2010). Notch signalling regulates left-right asymmetry through ciliary length control. Development *137*, 3625–3632.

Mangos, S., Lam, P., Zhao, A., Liu, Y., Mudumana, S., Vasilyev, A., Liu, A., and Drummond, I.A. (2010). The ADPKD genes pkd1a/b and pkd2 regulate extracellular matrix formation. Dis. Model. Mech. *3*, 354–365.

Marques, S., Borges, A.C., Silva, A.C., Freitas, S., Cordenonsi, M., and Belo, J.A. (2004). The activity of the Nodal antagonist Cerl-2 in the mouse node is required for correct L/R body axis. Genes Dev. *18*, 2342–2347.

McGrath, J., Somlo, S., Makova, S., Tian, X., and Brueckner, M. (2003). Two populations of node monocilia initiate left-right asymmetry in the mouse. Cell *114*, 61–73.

Montenegro-Johnson, T.D., Baker, D.I., Smith, D.J., and Lopes, S.S. (2016). Three-dimensional flow in Kupffer's Vesicle. J. Math Biol. *73*, 705–725.

Nakamura, T., Saito, D., Kawasumi, A., Shinohara, K., Asai, Y., Takaoka, K., Dong, F., Takamatsu, A., Belo, J.A., Mochizuki, A., et al. (2012). Fluid flow and interlinked feedback loops establish left-right asymmetric decay of Cerl2 mRNA. Nat. Commun. *3*, 1322.

Nauli, S.M., Alenghat, F.J., Luo, Y., Williams, E., Vassilev, P., Li, X., Elia, A.E.H., Lu, W., Brown, E.M., Quinn, S.J., et al. (2003). Polycystins 1 and 2 mediate mechanosensation in the primary cilium of kidney cells. Nat. Genet. *33*, 129–137.

Nauli, S.M., Pala, R., and Kleene, S.J. (2016). Calcium Channels in Primary Cilia. Curr Opin Nephrol Hypertens *165*, 1789–1802.

Oki, S., Kitajima, K., Marques, S., Belo, J.A., Yokoyama, T., Hamada, H., and Meno, C. (2009). Reversal of left-right asymmetry induced by aberrant Nodal signaling in the node of mouse embryos. Development *136*, 3917–3925.

Pennekamp, P., Karcher, C., Fischer, A., Schweickert, A., Skryabin, B., Horst, J., Blum, M., and Dworniczak, B. (2002). The ion channel polycystin-2 is required for left-right axis determination in mice. Curr. Biol. *12*, 938–943.

Pirson, Y. (2010). Extrarenal manifestations of autosomal dominant polycystic disease. Adv Chronic Kidney Dis. *17*, 173–180.

Pirson, Y., Chauveau, D., and Devuyst, O. (2005). Autosomal-dominant polycystic kidney disease. In Oxford Textbook of Clinical Nephrology Vol 3, A.M. Davison, ed. (New York, NY: Oxford University Press), pp. 2304–2321.

Raya, A., Kawakami, Y., Rodríguez-Esteban, C., Ibañes, M., Rasskin-Gutman, D., Rodríguez-León, J., Büscher, D., Feijó, J.A., and Izpisúa Belmonte, J.C. (2004). Notch activity acts as a sensor for extracellular calcium during vertebrate left-right determination. Nature *427*, 121–128.

Roxo-Rosa, M., Jacinto, R., Sampaio, P., and Lopes, S.S. (2015). The zebrafish Kupffer's vesicle as a model system for the molecular mechanisms by which the lack of Polycystin-2 leads to stimulation of CFTR. Biol. Open *4*, 1356–1366.

Sampaio, P., Ferreira, R.R., Guerrero, A., Pintado, P., Tavares, B., Amaro, J., Smith, A.A.,

Montenegro-Johnson, T., Smith, D.J., and Lopes, S.S. (2014). Left-right organizer flow dynamics: how much cilia activity reliably yields laterality? Dev. Cell *29*, 716–728.

Schneider, I., Houston, D.W., Rebagliati, M.R., and Slusarski, D.C. (2008). Calcium fluxes in dorsal forerunner cells antagonize beta-catenin and alter left-right patterning. Development *135*, 75–84.

Schottenfeld, J., Sullivan-Brown, J., and Burdine, R.D. (2007). Zebrafish curly up encodes a Pkd2 ortholog that restricts left-side-specific expression of southpaw. Development *134*, 1605–1615.

Schweickert, A., Vick, P., Getwan, M., Weber, T., Schneider, I., Eberhardt, M., Beyer, T., Pachur, A., and Blum, M. (2010). The nodal inhibitor Coco is a critical target of leftward flow in Xenopus. Curr. Biol. *20*, 738–743.

Shinohara, K., Kawasumi, A., Takamatsu, A., Yoshiba, S., Botilde, Y., Motoyama, N., Reith, W., Durand, B., Shiratori, H., and Hamada, H. (2012). Two rotating cilia in the node cavity are sufficient to break left–right symmetry in the mouse embryo. Nat. Commun. *3*.

Smith, D.J., Montenegro-Johnson, T.D., and Lopes, S.S. (2014). Organized chaos in Kupffer's vesicle: How a heterogeneous structure achieves consistent left-right patterning. Bioarchitecture *4*, 119–125.

Sulik, K., Dehart, D.B., Inagaki, T., Carson, J.L., Vrablic, T., Gesteland, K., and Schoenwolf, G.C. (1994). Morphogenesis of the murine node and notochordal plate. Dev. Dyn. *201*, 260–278.

Supp, D.M., Witte, D.P., Potter, S.S., and Brueckner, M. (1997). Mutation of an axonemal dynein affects left-right asymmetry in inversus viscerum mice. Nature *389*, 963–966.

Tanaka, Y., Okada, Y., and Hirokawa, N. (2005). FGF-induced vesicular release of Sonic hedgehog and retinoic acid in leftward nodal flow is critical for left – right determination. Nature *435*, 172–177.

Tavares, B., Jacinto, R., Sampaio, P., Pestana, S., Gardner, R., Lopes, T., Lopes, S.S., Schilling, B., Henry, I., and Sau, L. (2017). Notch / Her12 signalling modulates , motile / immotile cilia ratio downstream of Foxj1a in zebrafish left-right organizer. Elife *6:e25165*, 1–26.

Thisse, C., and Thisse, B. (2008). High-resolution in situ hybridization to whole-mount zebrafish embryos. Nat. Protoc. *3*, 59–69.

Wang, G., Cadwallader, A.B., Jang, D.S., Tsang, M., Yost, H.J., and Amack, J.D. (2011). The Rho kinase Rock2b establishes anteroposterior asymmetry of the ciliated Kupffer's vesicle in zebrafish. Development *138*, 45–54.

Wang, G., Manning, M.L., and Amack, J.D. (2012). Regional cell shape changes control form and function of Kupffer's vesicle in the zebrafish embryo. Dev. Biol. *370*, 52–62.

Webb, S.E., and Miller, A.L. (2006). Ca2+ signaling and early embryonic patterning during the Blastula and Gastrula Periods of Zebrafish and Xenopus development. Biochim. Biophys. Acta - Mol. Cell Res. *1763*, 1192–1208.

Westerfield, M. (2000). The Zebrafish Book. A Guide for the Laboratory Use of Zebrafish (Danio rerio) (University of Oregon Press, Eugene).

Yoshiba, S., Shiratori, H., Kuo, I.Y., Kawasumi, A., Shinohara, K., Nonaka, S., Asai, Y., Sasaki, G., Belo, J.A., Sasaki, H., et al. (2012). Cilia at the Node of Mouse Embryos Sense Fluid Flow for Left-Right Determination via Pkd2. Science (80-.). *338*, 226–231.

Yuan, S., Zhao, L., Brueckner, M., and Sun, Z. (2015). Intraciliary Calcium Oscillations Initiate Vertebrate Left-Right Asymmetry. Curr. Biol. *25*, 1–12.

CHAPTER 4

Pkd2 downstream targets and how they affect left-right axis establishment

"If it looks like a duck, swims like a duck and quacks like a duck, then it probably is a duck"

Duck test of Abductive Reasoning

Pkd2 downstream targets and how they affect left-right axis establishment

Raquel Jacinto[1,2], Mónica Roxo-Rosa[1,2] and Susana S. Lopes[1]

1-CEDOC, Chronic Diseases Research Center, NOVA Medical School / Faculdade de Ciências Médicas, Universidade Nova de Lisboa, Campo dos Mártires da Pátria, 130, 1169-056 Lisboa, Portugal

2- Co first author

Summary

Calcium permissive channel Polycystin-2 plays an important role on Left-Right axis establishment in many animal models (Field et al., 2011; Kamura et al., 2011; Yoshiba et al., 2012; Yuan et al., 2015). However, what are the activated or blocked targets downstream of the activation of this permissive calcium channel and the calcium oscillations and waves that follow are not yet known.

By performing a tissue specific microarray in WT embryos vs *pkd2* morphant embryos (using the morpholino referred by Schottenfeld et al., 2007), we got a list of differentially expressed genes between these two conditions. Among these we selected four genes of interest to further assess their impact on left-right: *parvalbumin 6*, *frizzled-related protein*, *calcyclin binding protein* and *nicalin 1*. First, we evaluated their expression patterns; second, we manipulated them in order to mimic the same up or downregulation as found in the microarray. Our readouts were both *dand5* expression pattern and mRNA expression levels and later we assessed the effect of our manipulations in organ *situs*. Subsequently, we evaluated the impact on left-right of the inverse manipulations. Finally, we summarized the results in a model, where we put these new players in their potential new roles for left-right axis establishment.

INTRODUCTION

Vertebrates establish left-right (LR) organization of the internal organs during development. This starts by the action of rotating cilia – hair-like structures on the surface of cells – in the left-right organizer (LRO) known as the node in mammalians and Kupffer's vesicle (KV) in fish (Essner et al., 2005). Zebrafish motile cilia generate an anticlockwise fluid flow that is stronger anteriorly and on the left side of the KV (Sampaio et al., 2014). Independently, corresponding asymmetric intracellular calcium oscillations (ICOs) (Yuan et al., 2015) were detected in the first layers of cells surrounding the KV. Such ICOs were observed mainly on the left side of the KV midplane and were shown to be dependent on the presence of Pkd2. Therefore, in zebrafish predominant anterior and left flow forces and ICOs in the LRO seem to precede a left-sided calcium wave in the adjacent tissues and a left-biased asymmetric expression of genes in the lateral plate mesoderm (such as *nodal*, *pitx2* and *lefty2*). Later, this asymmetric genetic cascade will lead to laterality formation revealed by the asymmetric localization of internal organs (for review see Pennekamp et al., 2015).

The cation channel Pkd2 together with the mechanosensor Pkd1, form a complex, which in the kidney has the ability to sense the urine flow and induce an intracellular calcium signal (Nauli et al., 2003). Pkd2 and its new partner Pkd1l1 have also been proposed as the mechanosensor channel complex responsible for sensing the flow in the LRO and conveying the information into the adjacent tissues (Field et al., 2011; Kamura et al., 2011). Despite working as a complex, it has been shown that decreasing the levels of Pkd2 alone is sufficient for a strong LR randomization both in mice (Yoshiba et al., 2012) and in zebrafish (Bisgrove et al., 2005; Schottenfeld et al., 2007). However, how the extracellular fluid flow is 'perceived' by the node/KV cells, is still controversial and has not been demonstrated. One explanation provided by the 'two-cilia hypothesis', is based on the fact that there are two types of cilia in the mouse node cells: one immotile, the alleged sensory type, capable of detecting changes in the flow, and another population of motile rotating cilia generating the fluid flow movement (McGrath et al., 2003). An important finding supporting this hypothesis was that absence of Pkd2 in perinodal mouse cells inhibits the usual asymmetric expression of cerberus-like2 (*cerl2 or dand5*) on the right side, important for further LR asymmetry, but a tissue specific perinodal rescue

recovers normal LR patterns (Yoshiba et al., 2012). The perinodal cells are enriched in immotile cilia promoting the idea that these are the important sensors in the murine system. Motile and immotile cilia have also been found in the zebrafish KV but in a intermingled arrangement (Sampaio et al., 2014; Tavares et al., 2017) and Pkd2 is present in all zebrafish KV cells including ciliary axoneme and basal body (Roxo-Rosa et al., 2015). As in mice, knockdown of *pkd2* in zebrafish leads to symmetric *dand5* expression (Yoshiba et al., 2012). Altogether, there is evidence indicating a possible connection between the rise of intracellular calcium and *dand5* decrease in expression on the left side of the LRO, possibly through the stimulation of more Pkd2 channels in a sided manner. In mice, Pkd2 dependent calcium signalling seems to be upstream the initial degradation of *dand5* mRNA on the left side that is then further established by a positive feedback loop involving Wnt3 (Nakamura et al., 2012). However, such mechanism remains to be formally demonstrated in other animal models. At this stage we can ask if apart from *dand5* regulation there are other left-right targets of the intracellular calcium signalling mediated by Pkd2. And what is the mechanism by which intracellular calcium modulates gene expression. To answer these questions, we decided to do a tissue-specific mRNA profiling of the KV ciliated cells. To do this, we used a zebrafish line that specifically labels KV cells (tg(foxj1a:GFP) (Caron et al., 2012) and then performed *pkd2* knockdown experiments using a well established translation blocking morpholino (Schottenfeld et al., 2007). The results were analysed and clustered and candidate genes were chosen and validated by qRT-PCR for further testing. We chose four potential candidates to further analyse their mRNA and protein localization, when possible. Then we manipulated these genes by overexpression and knockdown to assess their individual impact on left-right axis establishment by looking at *dand5* expression pattern and levels and later scoring for organ *situs*.

EXPERIMENTAL PROCEDURES

Fish stocks and genetics

Wild-type (AB) and *Tg(foxj1a:GFP)* (Caron et al., 2012) zebrafish lines were maintained and used as described elsewhere (Westerfield, 2000). Embryos were raised at 28ºC, depending on the experiment,

in E3 embryo media and staged accordingly (Kimmel et al., 1995). Procedures with zebrafish were approved by the Portuguese DGAV (Direcção Geral de Alimentação e Veterinária).

Fluorescence activated cell sorting (FACS)

pkd2 morpholino (Schottenfeld et al., 2007) and *pkd2* mismatch morpholino was diluted in sterile water and injected at one cell stage at a dose of 2.5ng per embryo from the *Tg(foxj1a:GFP)* zebrafish line. Embryos were allowed to develop until 16 hours post-fertilization (hpf) and dechorionated using pronase (MERCK)(2mg ml^{-1}). Embryos were then rinsed 3 times with Danieu's solution and collected into 15mL falcons. To deyolk embryos, 1mL of CO_2-independent medium (Gibco™) complemented with 5mM EDTA was added to the falcons and embryos were dissociated by gently pipetting up-and-down with filter tips. Then 4mL of medium was added and falcons were centrifuged at room temperature for 3 minutes at 700g. The supernatant was removed and new medium was added. The dissociation and centrifuge was repeated until the removed supernatant was pink. Cells were then finally resuspended in 1mL of medium and transferred into FACS tubes. Cells were then FACS sorted and GFP positive cells were collected to 75uL of RLT Buffer from the RNeasy® micro Kit (Qiagen Inc., Valencia, CA), and stored at -80ºC. We collected three independent samples for WT, *pkd2* morphant embryos and *pkd2* mismatch morphant embryos, each with around 15000 cells per sample.

Microarray

RNA isolation and quality evaluation: Total RNA was isolated with the RNeasy® micro Kit following the manufacturer's instructions. RNA quantification was done by using a *nanophotometer P-class* (Implen) and integrity was confirmed using an Agilent 2100 Bioanalyzer for an Eukaryote total RNA pico assay (Agilent Technologies). Three biological replicates were produced with an equivalent number off cells and used in the microarray.

The foxj1a:GFP reporter line was injected with pkd2-augMO. This procedure blocked pkd2 translation and allowed us to identify the genes that were affected transcriptionally in motile ciliated cells expressing the foxj1a reporter. Embryos were raised until 10 somites stage. We have also injected embryos from the foxj1a:GFP background with the control MO mismatch. We have as predicted in TASK 4 performed Fluorescent Activated Cell Sorter (FACS) on these embryos that are on the

foxj1a:GFP transgenic background. So, we selected the foxj1a:GFP positive cells by FACS. We have used a FACSAria High- Speed Cell Sorter (BD) available at the IGC facilities. We collected 100306 cells from non-injected, 56353 cells from MO-pkd2 injected and 39383 cells from MO mismatch injected embryos. For each situation, the collected cells were in three replicates and the total RNA was isolated with a micro RNAeasy kit (Qiagen). The quality of the total RNA was analyzed on the Agilent 2100 Bioanalyzer (Affymetrix Core Facility in the IGC). Demonstrating the quality of the extracted RNA, all the samples presented a RIN factor above 7.70.

Microarray procedure: The new Zebrafish Gene 1.1 ST Array Strip (Affymetrics) was used. This array is based on the Zv9 version of the zebrafish genome. The strips were run on the GeneAtlas System at the IGC Gene expression facility. This allowed us to analyze and compare the expression of 23878 properly annotated genes.

The crossing between the results from the MO pkd2 with MO mismatch and wt was very informative because we could exclude all the genes that were being differentially expressed due to Morpholino toxicity. After excluding differences caused by MO toxicity, we found 623 genes to be differentially expressed in the pkd2-morphants compared to wt embryos. We have only considered genes presenting an expression 1.3 times higher or lower in the pkd2 morphants compared to wt embryos. Strengthening our results, among the differentially expressed genes we found some encoding proteins that are dependent of Ca^{2+}.

Validation of microarray expression data: We performed quantitative PCR (qPCR) using cDNA from KV's cells at 10 somite stage (selected as in the microarray experiment). qPCR was performed on the Roche Real-Time PCR Detection System using the Roche SybrGreen. Primers for amplification of *cacybp* (calcyclin binding protein)*, pvalb6* (parvalbumin 6), *frzb* (frizzled-related protein) and *ncl1* (nicalin 1) were designed with Primer-BLAST (NCBI). Two reference genes *rpl13a* (ribosomal protein L13a) and *eef1al1* (eukaryotic elongation factor 1 alpha 1 like 1) were used. All reactions were performed with three biological replicates and three technical replicates. Significant differences in the transcription level were determined using t-student test ($p < 0.05$).

Cloning for overexpression and *in situ* hybridization and Morpholinos

Primers were designed to amplify full coding sequence of *pvalb6*, *cacybp*, *frzb* and *ncl1* into a pCS2+ plasmid. Primer sequences: *pvalb6* forward 5'- GCGATATGGATCCATGGCGATGAGCAGCATC-3' and reverse 5'-CGCGCGAATTCTTCACGAACCAGAGCAGCAAAC-3'; *frzb* forward 5'-GCGCCGGCGGATCCATGCAAAACATGTTTTCCTACG-3' and reverse 5'-GCGCGCGGAATTCTTAGTGGTGGTTCCATTTGG-3'; *cacybp* forward 5'-GCGGCGCATGGATCCATGGACATCAATGAAC-3' and reverse 5'-GCGGGCGCCCCGCGAATTCTTAGAAGTCAAAATCATCTGG-3'; *ncl1* forward 5'-GCTGCTATCGATATGTTCGAGGAGGCTGGT-3' and reverse 5'-GCGCAGAATTCTCAGTGCTGCTTGACCCG-3'. PCRs were performed using iProof™ High-Fidelity DNA Polymerase (Bio Rad). Double digestions were performed in the plasmid and amplified genes, according to primer design (data summarized in Table 1) and T4 ligation (NEB) was performed overnight at 16ºC. DH5α competent *E. coli* were transformed with ligation product and plated in LB-Agar (Carl Roth) with 100mg/mL Ampicilin resistance. Colonies were screened by PCR using pCS2+ specific primers and positive colonies were sent to sequence to assess the quality of PCR amplification. Colonies with correct sequences for all 4 genes were selected and grown on secondary cultures. High quality and very concentrated plasmids were obtained with a ZymoPURE™ Plasmid Midiprep kit. The same plasmid can be linearized for mRNA production and *in situ* hybridization probe synthesis. For mRNA production, 2μg of linearized plasmid were processed with mMESSAGE mMACHINE™ Sp6 Transcription Kit (Ambion), aliquoted and stored at -80ºC. For *in situ* hybridization probe synthesis, 2μg of linearized plasmid were processed with T7 RNA Polymerase (Promega) and labelled with DIG (Roche) and finally diluted 30-50ng in 200μL of Hybridization Mix.

Morpholinos targeting the 5'UTR excluding the initial ATG for all 4 genes were ordered online from GeneTools: *pvalb6* 5'-AACGAGACCGGCAACGCACAGACAG-3'; *frzb* 5'-AGCGGAGTTGATAGAAGAATGACAT-3'; *cacybp* 5'-TGCTGTCTTGGAAAAACCTCTGTAT-3'; *ncl1* 5'- CGGGAGATTCCCACCGACAGAAACA-3'.

Overexpression and Knockdown experiments

WT (AB) embryos were injected at 1 cell stage with several doses of each morpholino and mRNA. Toxicity was assessed by discarding all doses that produced high mortality rates. The doses chosen for the final experiments were: 3ng of *pvalb6* morpholino (KD), 800pg of *pvalb6* mRNA (OE), 800pg of *frzb* mRNA (OE), 2ng of *frzb* morpholino (KD), 3ng of *cacybp* morpholino (KD), 1000pg *cacybp* mRNA (OE), 1000pg *ncl1* OE, 3ng *ncl1* morpholino (KD), 1000pg *ncl1* OE/800pg *frzb* OE/3ng *cacybp* KD and finally 2,5ng of *pkd2* morpholino (KD). Embryos were allowed to develop to the desire stages to study *dand5* expression pattern and level, heart and gut *situs*.

Immunofluorescence and in *in situ* hybridization

Whole-mount immunostaining for parvalbumin was performed as described previously (Lopes et al., 2010). Antibodies used for immunostaining were mouse anti-parvalbumin (1:400; clone PARV-19, Sigma), Goat anti-mouse Alexa Fluor 488 (Invitrogen; 1:500) and Alexa fluor 546 Phalloidin (Invitrogen/ molecular probes 1:100). Whole-mount in *situ* hybridizations for all 4 genes were performed at 8-10 somite stage and 24hpf in wt embryos as described in Thisse Lab - In situ Hybridization Protocol 2010 update Zfin (https://goo.gl/XdcfCH). *dand5 in situ* hybridizations were performed at 8ss as described elsewhere (Thisse and Thisse, 2008) and were used 241 WT controls, 53 *frzb* OE, 43 *cacybp* KD, 49 *ncl1* OE, 75 *pvalb6* OE, 101 *cacybp* OE and 45 *ncl1* KD. The results were analysed by Fisher's exact test with Bonferroni correction for multiple comparisons.

Heart and gut laterality

At 30 hpf we evaluated heart jogging using a stereoscopic zoom microscope (SMZ745, Nikon Corporation) to observe the embryos from the ventral side. These embryos were then allowed to develop in separated petri dishes and at 53 hpf, embryos were fixed and processed for *foxa3 in situ* hybridizations to assess gut laterality. We could then pair the heart *situs* with gut *situs* for each treatment and attribute an embryo *situs*. We scored organ *situs* in 1438 WT, 55 *pvalb6* KD, 120 *pvalb6* OE, 103 *frzb* OE, 76 *frzb* KD, 18 *cacybp* KD, 84 *cacybp* OE, 79 *ncl1* OE, 188 *ncl1* KD, 84 *ncl1* OE/ *frzb* OE/ *cacybp* KD and 140 *pkd2* KD.

Quantitative PCR

Embryos from different treatments were pooled in 3 groups of 20-50 embryos in order to have three different biological replicates. Total RNA was extracted using the Qiagen RNeasy Mini Kit (ref number 74104) and reverse transcribed using both oligo(dT)$_{18}$ and random hexamer primers with the RevertAid First Strand cDNA Synthesis Kit (ref number K1622) following the manufacturers' instructions. Expression was quantified by PCR using Roche SYBR Green I Master (ref number 04887352001) and run in a Roche LightCycler® 96 Real-Time PCR System. Results were analysed and depicted as fold-change of transcript levels in injected embryos relative to transcript levels in control embryos. The p-value represents significance in the pairwise comparison of transcript levels between injected and control embryos as determined using the paired t-test. Statistical significance was set at p-value < 0.05. Expression levels of all our genes of interest were normalized in relation to *eukaryotic elongation factor 1 alpha 1 like 1* (*eef1al1*) and *ribosomal protein L13a* (*rpl13a*) expression. Primer sequences used were as follows: *dand5* forward 5′-CCGCAATCCTGACCCATAGCAA-3′ and reverse 5′-CTCCTCCGTTATGCGCTGTGTA-3′; *pvalb6* forward 5'-GCGAAGGCATCTGACGATGTGAA-3' and reverse 5'-GCAAACTCTTCCGCTCCAATCTT-3'*;* *frzb* forward 5'-ACTTCCAGCACGACCCGATCAA-3' and reverse 5'-GAATTATCTGGCCCCTCCGCTT-3'*;* *cacybp* forward 5'-GCAGCTTCACAGAGAGAGGCTT-3' and reverse 5'-ACTTGTGTCAAGCAGTCCCACTT-3'*;* *ncl1* forward 5'- CGTCGCTATACTGCTGGAGCTT-3' and reverse 5'-GAGCAGACTGGCATCTGTGTGAT-3'*;* *eef1al1* forward 5'-CCTTCAAGTACGCCTGGGTGTT-3' and reverse 5'-CACAGCACAGTCAGCCTGAGAA-3'; *rpl13a* forward 5'-TGACAAGAGAAAGCGCATGGTT-3' and reverse 5'-GCCTGGTACTTCCAGCCAACTT-3'.

RESULTS

Expression patterns of downstream targets of Pkd2 in left-right axis establishment

To identify what target genes are downstream of the Pkd2 signalling pathway and how it influences the early left-right axis specification, a tissue-specific mRNA profiling of the KV ciliated cells was performed. To achieve this, a foxj1a:GFP transgenic line was used where all the ciliated cells of the

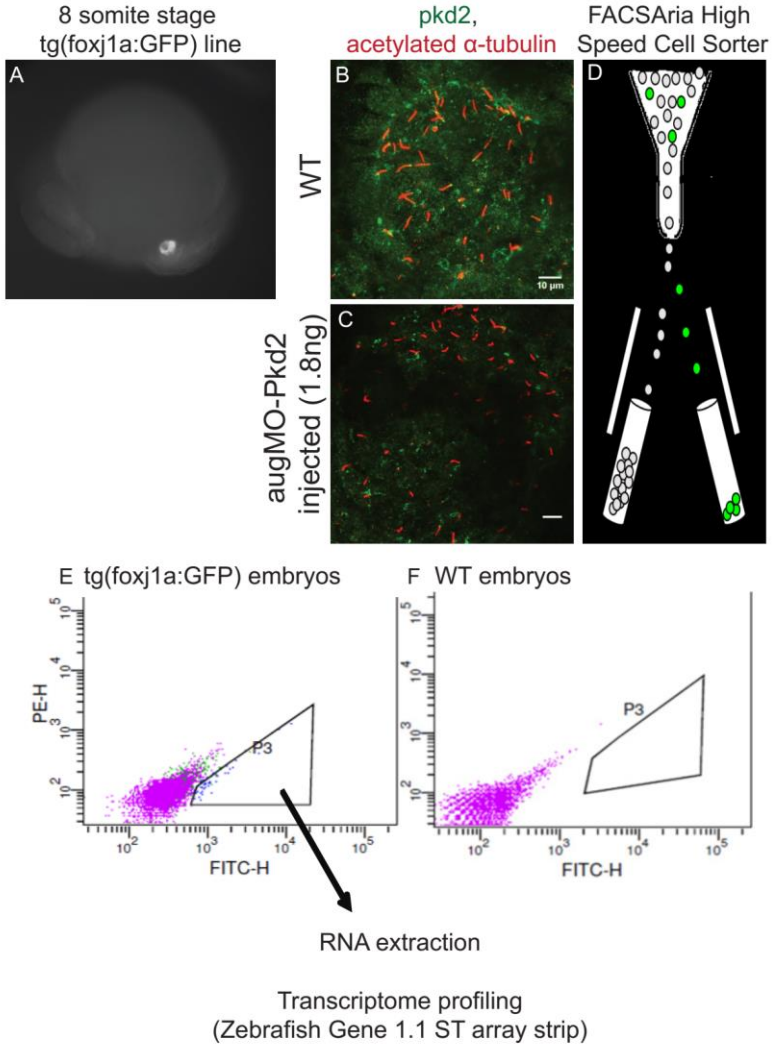

Figure 1. KV specific microarray of WT versus Pkd2 morphant embryos. **(A)** Zebrafish embryo at 8 somite stage from the transgenic line tg(Foxj1a:GFP), showing in bright grey the KV cells. **(B-C)** Pkd2 (in green) and acetylated α-tubulin (in red) immunostaining in WT **(A)** and pkd2 morphant **(B)** embryos, focusing in the KV cilia. Scale bars represent 10µm. **(D)** Schematics of the FACS sorting of GFP-positive cells. **(E-F)** GFP-positive cells that were selected for RNA extraction that are only present in the transgenic line (E), but not in a pool of WT embryos (F). **(G)** Table summarizing the results of the transcriptome profiling separated by clusters and further validated by qRT-PCR. In green are the genes followed during this study.

G Results of the transcriptome profiling separated by clusters and validated by qRT-PCR

Gene Cluster	Gene	Microarray	qRT-PCR validation
Ion Channel	Calcium channel voltage-dependent gamma subunit 2a/8b	up	No detected
Wnt signalling	wnt4a	up	No
	Forkhead box O3B	up	Yes
	Casein Kinase 1g1	up	No
	Frizzled-related protein	up	Yes
Calcium Binding	Parvalbumin6	down	Yes
	Ras-related GTP binding Ca	up	Yes
	Calcyclin binding protein	down	Yes
Other signalling pathways	Crumbs 2a	up	Yes
	Forkhead box I1	up	Yes
	Antizyme inhibitor 1	up	Yes
	Delta-like 1	up	Not detected
	Nicalin 1	up	Yes
	Leukotrien	down	No
	Myosin Light Chain Kinase	up	No

KV are GFP-positive (Figure 1A). This line was injected with 1,8ng of Pkd2 augMO (Schottenfeld et

al., 2007) that blocks translation and can successfully abrogate the Pkd2 that is present along the KV cilia (Figure 1B and C). After this, embryos were let to develop until 10 somite stage and then the KV cells were sorted through an optimized protocol using the Fluorescent Activated Cell Sorter (FACSAria High-Speed Cell) (Figure 1D-F). This tissue-specific screen allowed a strict selection and avoided contaminations with cells that are not from the KV. After the sorting, RNA was extracted with a microRNAeasy kit. cDNA was produced and the transcripts were investigated with the Zebrafish Gene 1.1 ST Array Strip from Affymetrics and run in the GeneAtlas System in the IGC. The results were analysed by Hierarchical Clustering to reveal potential genes that are being regulated by the Pkd2 signalling pathway. The qRT-PCR results were normalized with two housekeeping genes: *eukaryotic elongation factor 1 like 1* (eef1l1) and *ribosomal protein L13a* (rpl13a).

A list with 16 targets that were differently expressed between wt and *pkd2* morphants was curated and several genes of interest were clustered into four categories, such as Ion channel, wnt signalling, calcium binding and others (summarized in Figure 1G). In the ion channels class we found that there was an up regulation of two genes coding for subunits of a voltage dependent calcium channel which in Paramecium is important to control the frequency and direction of ciliary beating (Thiele and Schultz, 1981). Since this gene was the only calcium channel to be differentially expressed in our array, it was a very interesting gene to study. Unfortunately, we were not able to validate this gene through qRT-PCR due to its very low level of expression, rendering this gene unfit for further investigation. For further study, we chose *frizzled related protein (frzb)* from the wnt signalling cluster, *parvalbumin 6 (pvalb6)* and *calcyclin binding protein* (*cacybp*) from the calcium binding cluster and *nicalin1* (*ncl1*) from the others cluster. First we assessed if any of these genes had an asymmetric gene expression like *dand5*, a known inhibitor of nodal signalling that has been shown to be important for left-right axis establishment.

Parvalbumin 6 (pvalb6)

Parvalbumin is a well-known calcium binding protein expressed at high levels in muscle and neuronal cells. In muscle it can bind intracellular Ca^{2+}, increasing the rate of muscle relaxation (Müntener et al., 1995). In neuronal cells it might act as a cytosolic intracellular Ca^{2+} buffer, protecting the neurons from

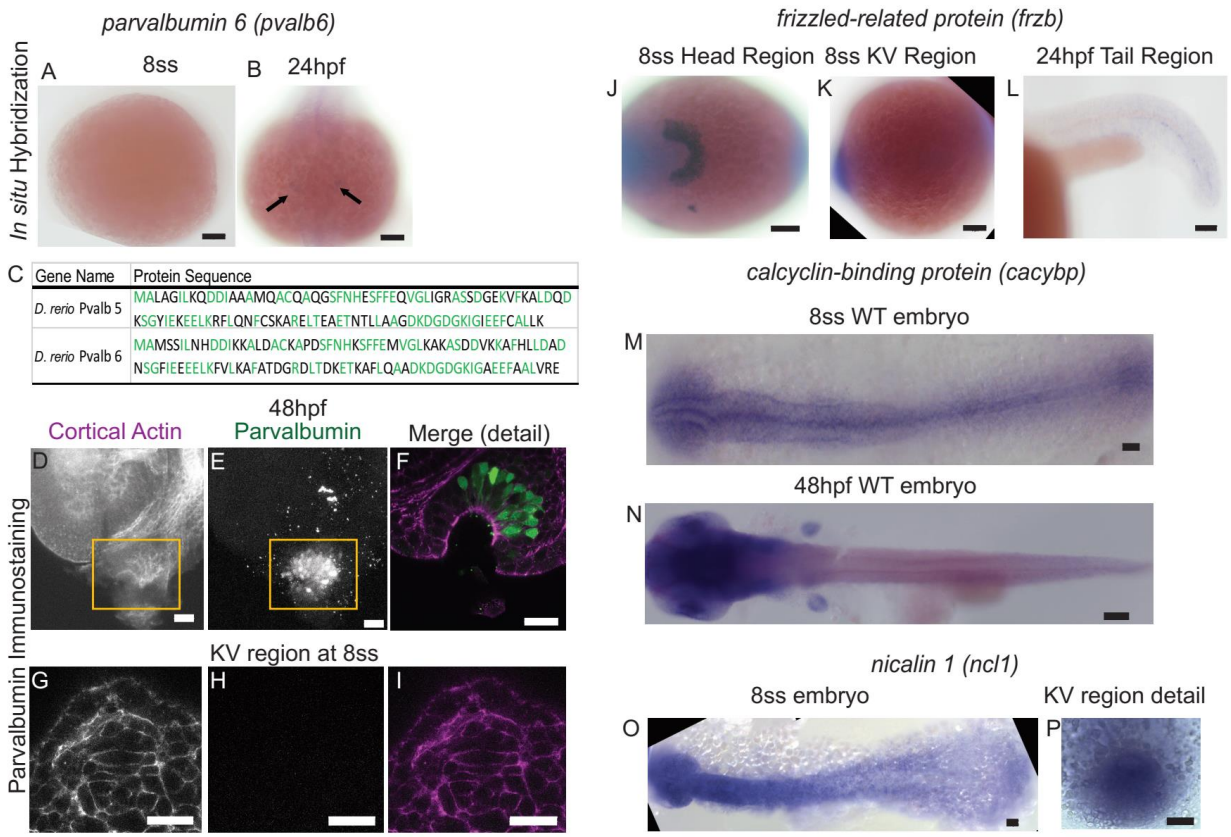

Figure 2. Expression pattern of parvalbumin 6, frizzled-related protein, calcyclin-binding protein and nicalin 1.

(A-B) *In situ* hybridization of parvalbumin 6 in embryos at 8 somite stage (A) and 24 hours post-fertilization (hpf) (B). Black arrows identify the acoustic ganglion. **(C)** Table comparing the protein sequence of Pvalb5 and Pvalb6, showing in green conserved amino acids between the two sequences. **(D-I)** Immunostaining of cortical actin (in magenta, D and G) and Parvalbumin (in green, E and H) in the olfactory pit in embryos at 48 hours post fertilization (F) and in the KV region in embryos at 8 somite stage (I). **(J-L)** *In situ* hybridization of frizzled-related protein in the head region (J) and KV region (K) of embryos at 8 somite-stage and in the tail region of 24 hours post fertilization (L). **(M-N)** *In situ* hybridization of calcyclin-binding protein in WT embryos at 8 somite stage (M) and 48 hours post fertilization (N). **(O-P)** *In situ* hybridization of nicalin 1 in WT embryos at 8 somite stage (O) and a detail of the KV region (P). Scale bars represent 20μm.

high cytotoxic amounts of intracellular Ca^{2+}, facilitating a more efficient signalling (Chard et al., 1993). Parvalbumin does not alter resting intracellular Ca^{2+} levels, only seems to reduce the peak and the rate of rise, promoting a faster decay (John et al., 2001). In zebrafish, there are 9 different Parvalbumins, more widely known for their role in retina neuron specification and muscle. Importantly,

Parvalbumin has been recently used as a tool for abolishing intracellular calcium signalling in the KV by Yuan et al. (2015). By targeting *Xenopus* Parvalbumin specifically to cilia, by fusing it to arl13b, Yuan et al. (2015) were able to reduce the intracellular calcium oscillations found in cilia, which they showed to be important for propagating the calcium wave into the left lateral plate mesoderm. Importantly, our array showed that all nine *parvalbumin* genes are expressed in the KV cells but only one (*pvalb6*) is significantly different between WT and *pkd2* knockdown being downregulated in morphant embryos. According to John et al. (2001), we predict that downregulating *pvalb6* gene would help to increase the calcium peak as well as the rate of rise, slowing down the decay. Therefore, even with low calcium due to absence of Pkd2, it might still be possible for the KV cells to detect slight changes in calcium downstream of flow.

The *in situ* hybridization probe showed no expression of this gene in embryos of 8-10 somite stage (Figure 2A), as already had been reported (Thisse and Thisse, 2004). This indicates that microarray and qRT-PCR are much more sensitive to low doses of expression than *in situ* hybridizations. When we compared the levels of relative expression found by qRT-PCR of *pvalb6* and for example *dand5*, a gene that is well visible by *in situ*, we realized that these values were much lower than the ones presented for *dand5* (*pvalb6* relative expression was 0.009 while *dand5* relative expression was 5). To confirm that the lack of expression at 8ss was not due to a defective *in situ* hybridization probe, we used it in embryos with 24hpf and it successfully showed expression in the acoustic ganglion as predicted by Thisse and Thisse, (2004) (Fig 2B, black arrows). For further confirmation that indeed the level of expression was very low in WT and lower even in morphants, a commercial monoclonal antibody against a frog Parvalbumin from Sigma was used to assess the expression of this protein in the KV. Zebrafish has 9 Parvalbumins and although many are present in muscle (Pvalb 1, 2, 3, 4 and 7), others exist in other structures like the olfactory pit (Pvalb5) and the acoustic ganglion and ganglion cell layer of the retina (Pvalb6). Since the commercial antibody detects cells of the olfactory pit (Figure 2D-F) and the Amacrine cell subtype of Zebrafish retina (Zhang et al., 2014), it must identify a conserved region between Pvalb5 and Pvalb6 proteins. When comparing the sequence of these two Parvalbumins, they have 56% peptide sequence homology (Figure 2C). Despite all this, the antibody

did not show any staining in the KV (Figure 2G-I). This shows further confirmation that the level of expression is so low that is likely not to produce any protein.

Frizzled-related protein (frzb)

This gene was up-regulated in *pkd2* morphants in our microarray and qPCR validation experiments (Figure 1G). Frizzled related proteins are molecules with a similar frizzled motif but without the transmembrane domains and containing a signal sequence, which means they can be secreted (as reviewed in Zorn, 1997). Frzb has been shown to be capable of acting as a Wnt signalling inhibitor by binding to Wnt ligands and inhibiting their binding to frizzled receptor (Leyns et al., 1997; Wang et al., 1997a). Frzb-1 has been described to be able to antagonize Wnt1 and Wnt8 but not Wnt3A, Wnt5A or Wnt11 (Wang et al., 1997b). Wnt signalling is an important pathway in the KV formation and ciliogenesis. Intracellular calcium release at 60% epiboly in the DFC (dorsal forerunner cells, the KV precursors) is required for regulation of β-catenin activity and therefore KV formation. Without early Wnt function, KV cells appear to be unable to coalesce into a vesicle (Schneider et al., 2008). Also, Wnt/β-catenin signalling is important for *foxj1a* expression and ciliogenesis (Caron et al., 2012; Zhu et al., 2015) and knockdown of *wnt8* or *wnt3* leads to reduced cilia length and less *dand5* expression (Lin and Xu, 2009).

Pkd2 morphants and mutants still develop a KV with cilia (Bisgrove et al., 2005; Schottenfeld et al., 2007), which points out to the fact that these initial steps of KV formation, where Wnt signalling is acting, must be independent of Pkd2. Wnt5A has been shown to induce calcium signalling responses in developing embryos in 8-16 cell stage (Slusarski et al., 1997) and has also been shown in the mice model to antagonize Wnt canonical pathway by promoting β-catenin degradation via E3 ubiquitin ligases like Siah-1 during limb development (Topol et al., 2003). In mice, it was shown that *dand5* left sided degradation happens through a negative feedback loop via Wnt3 (Nakamura et al., 2012). Therefore, we envisage that an upregulation of *frzb* at this developmental stage might be negatively regulating Wnt signalling in the process of left-right establishment in zebrafish, more likely affecting *dand5* expression pattern and levels.

In situ hybridyzation experiments performed at 8-10ss in WT embryos showed expression only in a structure called polster (Figure 2J), a hatching gland rudiment as reported before (Thisse et al., 2001). No other structures were visibly stained, particularly in the tail region (Figure 2K). Even though our microarray identified *frzb* in the KV cells, again we could not detect it by *in situ*. Similar to what was found for *pvalb6*, *frzb* has a very low relative expression when compared with *dand5* (relative expression detected by qRT-PCR was 0.08). As a control for effective probe production we also detected expression in cells of the hypochord in the tail region at 24hpf (Figure 2L). We know from unpublished work in our lab, that these cells can derive from the KV cells after the KV lumen closes.

Calcyclin binding protein (cacybp)

On the calcium binding cluster (Table 1), one of the genes selected was the *calcyclin binding protein* (*cacybp*), this gene was found to be down-regulated in *pkd2* morphants. *cacybp* encodes a protein with three domains: a N-terminal and a central domain of globular character and a C-terminal domain that is unstructured (Bhattacharya et al., 2005). It is a multi-ligand protein, capable of binding to S100 proteins (mainly S100A6, which is also known as Calcyclin), components of E3 ubiquitin ligases like Siah-1 and Skp1, cytoskeletal proteins and ERK1/2 (Topolska-Woś et al., 2016). Cacybp seems to be mainly present in several organ tissues in the mouse model, such as stomach, skeletal muscle, heart, lung, kidney and spleen, mainly present in fibroblasts and epithelial cells (Filipek et al., 2008). In addition, its presence in the cerebellum at postnatal day 21 points to a role in rat brain development (Jastrzebska et al., 2000). Most interesting to this study is the fact that it has been previously shown that Cacybp is normally present in the cytoplasm and has the ability to translocate to the perinuclear region or nucleus after an increase in the intracellular calcium (Schneider and Filipek, 2011). In addition, there is a link of Cacybp with β-catenin degradation through E3 ubiquitin ligases (Topolska-Woś et al., 2016). So, we selected it because we predicted that downregulation of *cacybp* could mean a transcriptional response to less calcium entry in *pkd2* morphants and thus downregulation of *cacybp* alone would show how important this gene was in the Pkd2 pathway.

By *in situ* hybridization in WT embryos, *cacybp* seemed to be a widely expressed gene (Figure 2M), as was previously shown (Thisse and Thisse, 2004). At 48hpf the expression became more restricted to the head (Figure 2N).

Nicalin1 (ncl1)

The gene transcripts for *ncl1* was found to be upregulated in the absence of Pkd2. Nicalin1 is a transmembrane protein distantly related to the γ-secretase component Nicastrin but with a different function, since interfering with Ncl1 failed to produce phenotypes related to Notch signalling deficiencies (Haffner et al., 2004). Its major binding partner is a protein called Nomo (Nicalin-Nodal modulator, also expressed in our array), forming a complex that is mainly expressed in the endoplasmic reticulum. They are type I proteins with a large luminal and a short cytoplasmic domain (Haffner et al., 2007). Ncl1 and Nomo have been reported to collaborate to modulate the activity of Nodal (Haffner et al., 2004). These authors showed that while ectopic expression of both factors interferes with midline development, generating cyclopic eyes, blocking Nomo function increases the amount of anterior mesendodermal derivatives at the expense of the posterior ones, in a dose-dependent manner. Nomo is also able to counteract the effect of Nodal inhibitor Lefty. All these experiments were interpreted as suggesting that Nomo/Ncl1 act as Nodal modulators in a dose-dependent manner (Haffner et al., 2004). Due to its presence on the ER, this complex might be affecting Nodal signalling by modifying and/or trapping Nodal pathway components that route through the ER (Haffner et al., 2004, 2007). Ncl1 looked like an interesting candidate for further analysis because upregulation of this gene might reflect a cell transcriptional regulation trying to increase the control over the secretion of proteins such as Nodal pathway players. For instance, in *pkd2* morphants we do see more *spaw* being expressed which could mean that more protein Spaw is being made since Spaw regulates its own expression.

ncl1 in situ hybridization in WT embryos showed widely spread expression, very strong in the head and along the somites (Figure 2O). A zoom in the KV region shows some diffuse expression (Figure 2P).

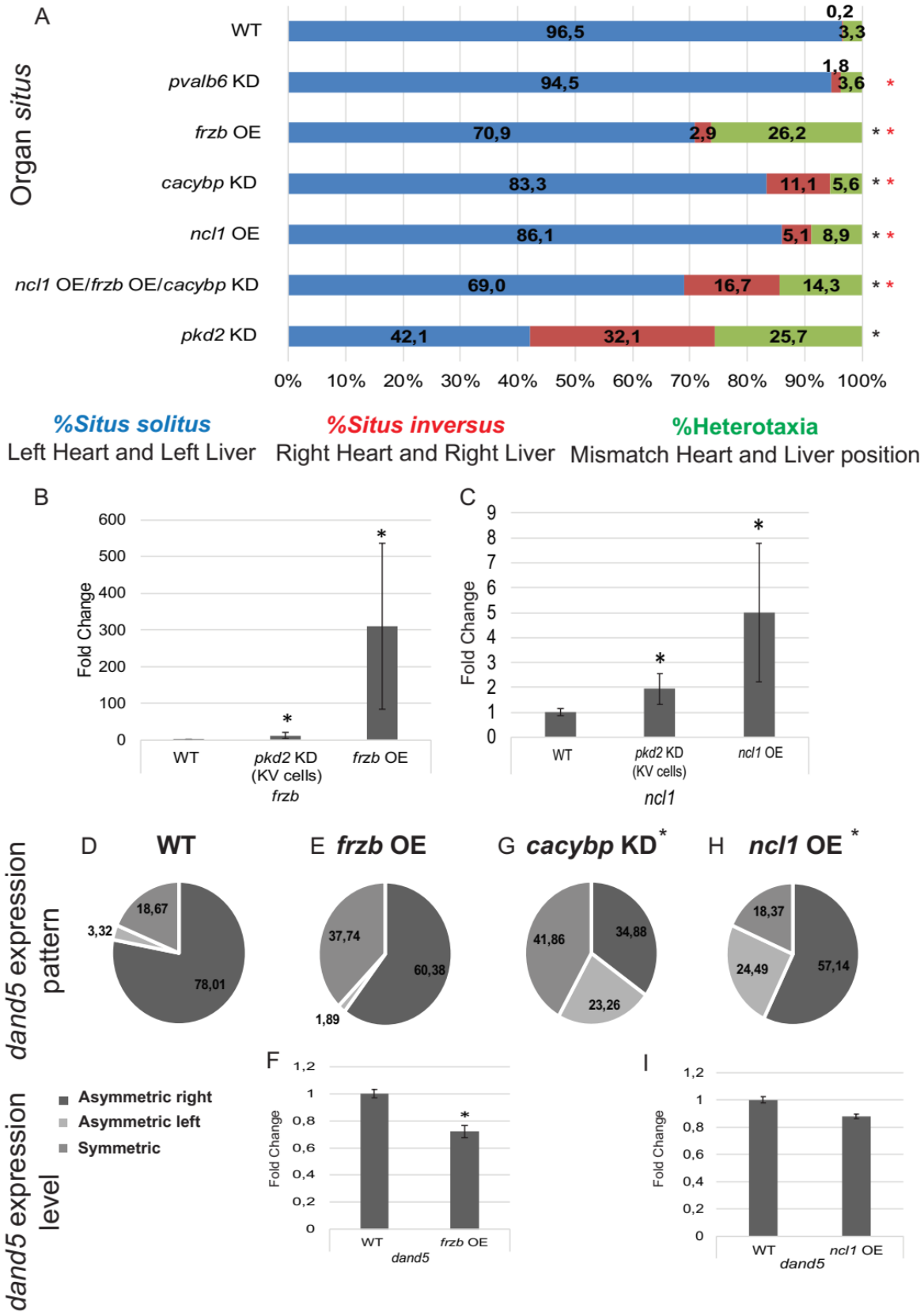
A
Organ situs
WT
pvalb6 KD
frzb OE
cacybp KD
ncl1 OE
ncl1 OE/frzb OE/cacybp KD
pkd2 KD
96,5
0,2
3,3
94,5
1,8
3,6
70,9
2,9
26,2
83,3
11,1
5,6
86,1
5,1
8,9
69,0
16,7
14,3
42,1
32,1
25,7
0% 10% 20% 30% 40% 50% 60% 70% 80% 90% 100%
%Situs solitus
Left Heart and Left Liver
%Situs inversus
Right Heart and Right Liver
%Heterotaxia
Mismatch Heart and Liver position
B
Fold Change
WT
pkd2 KD (KV cells)
frzb OE
frzb
C
Fold Change
WT
pkd2 KD (KV cells)
ncl1 OE
ncl1
dand5 expression pattern
dand5 expression level
D WT
E frzb OE
G cacybp KD*
H ncl1 OE*
18,67
3,32
78,01
37,74
60,38
1,89
41,86
34,88
23,26
18,37
24,49
57,14
Asymmetric right
Asymmetric left
Symmetric
F
Fold Change
WT
frzb OE
dand5
I
Fold Change
WT
ncl1 OE
dand5

Figure 3. Organ *situs* and *dand5* expression phenotypes resulting from manipulating the four candidate genes as in the Microarray.

(A) Organ *situs* quantification by scoring heart and liver laterality in the same larvae; experimental conditions involved injecting at 1-cell stage (A) pkd2 KD, *pvalb6* KD, *frzb* OE, *cacybp* KD, *ncl1* OE and the three together (*ncl1*OE/*frzb* OE/*cacybp* KD). Statistical analysis of organ *situs* for different treatments was performed using a Fisher test with p-value corrected for multiple comparisons with Bonferroni correction: black asterisks represent statistical significance when comparing treatments with WT; red asterisks represent statistical significance when comparing treatments with *pkd2* KD. **(B-C)** Quantification by qRT-PCR of the performed overexpressions: *frzb* (B), *ncl1* (C); asterisks represent statistical significance (paired t-test, p-value < 0.05). **(D, E, G, H)** *dand5* expression pattern quantification by *in situ* hybridization of WT embryos (D), *frzb* OE (E), *cacybp* KD (G), *ncl1* OE (H). Asterisks represent statistical significance (Fisher test with Bonferroni correction for multiple comparisons). **(F and I)** *dand5* expression level in fold change quantified by qRT-PCR; asterisks represent statistical significance (paired t-test, p-value < 0.05).

In sum, not one of the genes analysed showed a typical asymmetric expression around the KV like *dand5* shows. Also, in terms of levels of expression, only *ncl1* shows similar levels to the ones observed for *dand5*, meaning we can trust that it might be actually coding for a functional protein.

Manipulating the four candidates as observed in the microarray induces milder organ *situs* and *dand5* expression phenotypes than *pkd2* knockdown alone

Despite the fact that none of these genes has an expression similar to the known left-right genes like *dand5* and *spaw*, we decided to manipulate their levels to assess their impact on left-right.

First, we manipulated the levels according to what was observed in the microarray. Therefore, we individually knockdown *pvalb6* and *cacybp* with specific morpholinos and overexpressed *frzb* and *ncl1*. The objective was to understand if any of these genes was strong enough to mimic what we observed with the *pkd2* knockdown. That would indicate that one of them could be the direct downstream effector of the calcium oscillations observed upon Pkd2 activation by Yuan et al. (2015).

We evaluated their impact on organ *situs* (Figure 3A) and on both *dand5* expression pattern and levels (Figure 3D-I). Overexpression of *frzb* and *ncl1* were controlled by qRT-PCR and compared with the overexpressions obtained with *pkd2* knockdown (Figure 3B and C, respectively). While *pkd2* knockdown produced a statistical significant *frzb* mRNA overexpression of 12 ± 9.3 fold change (T-test p-value<0.05), our overexpression had a much greater impact (310 ± 226.7 fold change, T-test p-

value<0.05) (Figure 3B). The same was observed in *ncl1* overexpression (Figure 3C): when comparing the overexpression levels with those previously found for *pkd2* morphants (2-fold increase, T-test p-value<0.05), we observed that our overexpression led to a 5 fold-change increase (Figure 3C, T-test p-value<0.05). Despite our stronger manipulations, we realized that none of them alone was similar to *pkd2* knockdown in terms of organ *situs*. The strongest manipulation was the overexpression of *frzb* showing around 30% of defects, but it was still statistically different and weaker than *pkd2* knockdown (more than 50% defects, Figure 3A; Fisher test with Bonferroni correction for multiple comparisons, red asterisk p-value<0.0083). Still, all manipulations but *pvalb6* knockdown had significant impact on organ *situs* (Figure 3A, Fisher test with Bonferroni correction for multiple comparisons, black asterisk p-value<0.005). Then we evaluated the impact on *dand5* expression level and pattern of *frzb* and *ncl1* overexpression and *cacybp* knockdown. *frzb* overexpression did not affect *dand5* pattern in a significant way (Figure 3E; Fisher test with Bonferroni correction for multiple comparisons, p-value>0.007), but affected its expression level (Figure 3F, T-test p-value<0.05). This might explain that the dose of *dand5* protein produced might not be enough to restrain *spaw* expression solely on the left side of the lateral plate mesoderm and therefore impact on organ *situs*. On the other hand, *cacybp* knockdown and *ncl1* overexpression affected greatly *dand5* expression pattern (Figure 3G and H, respectively; Fisher test with Bonferroni correction for multiple comparisons, p-value<0.007), but *ncl1* overexpression did not affect *dand5* expression levels (Figure 3I; T-test p-value>0.05).

At this point, as *pvalb6* did not show any organ *situs* defects we did not used it for the next experiments. Next, we asked if a combined manipulation of the three genes (*ncl1, frzb* and *cacybp*) could render a stronger phenotype than each manipulation alone. Since manipulating *pkd2* alone affected so many different genes, maybe they all contribute to left-right axis correct establishment in a cumulative way. Doing the triple manipulation (*ncl1* OE; *frzb* OE and *cacybp* KD) in the same wt embryos did not produce a stronger phenotype than overexpressing *frzb* alone (Figure 3A, around 30% of defects; Fisher test with Bonferroni correction for multiple comparisons, black asterisk shows different from control experiment p-value<0.005, red asterisk shows different from *pkd2* knockdown p-value<0.008).

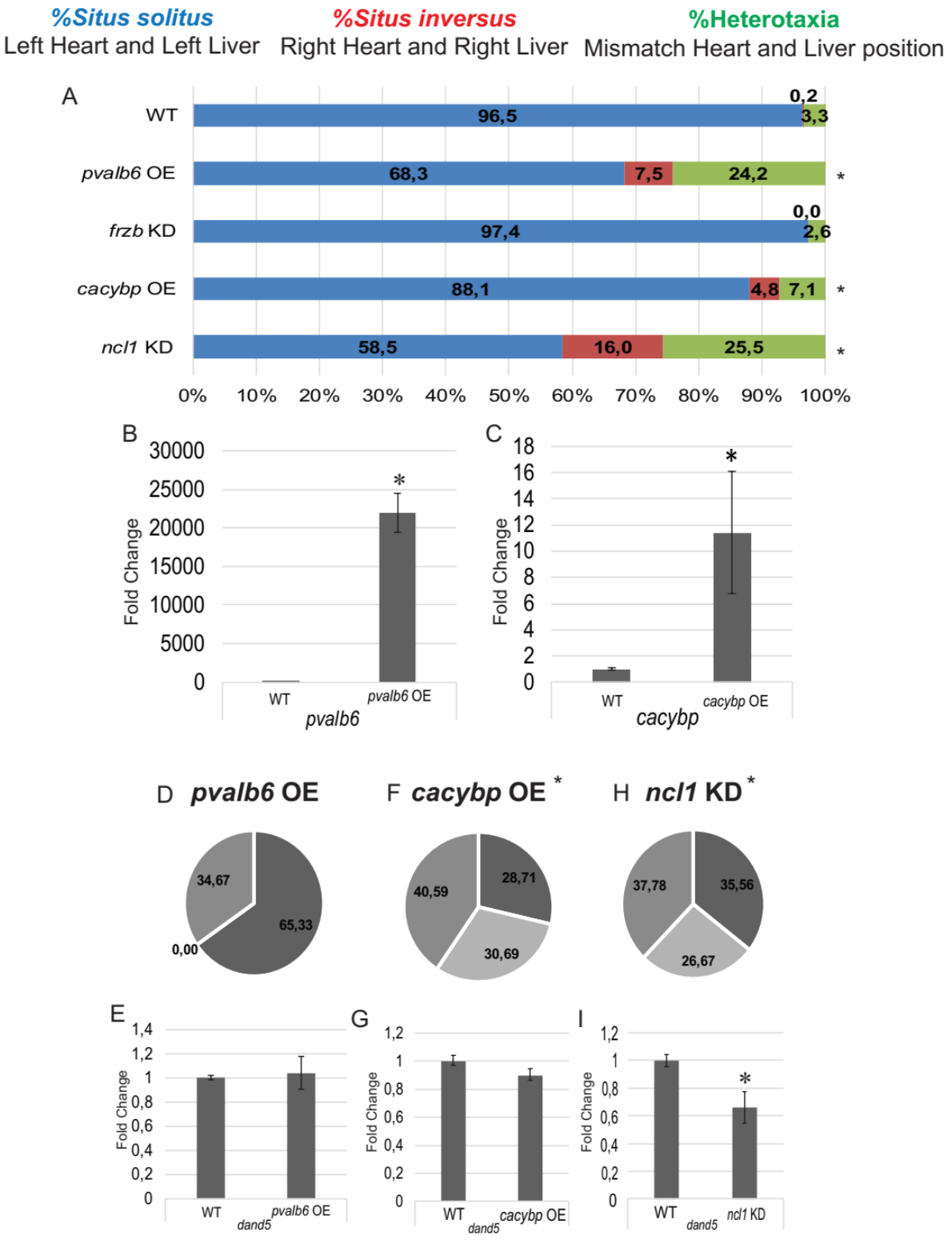
%Situs solitus
Left Heart and Left Liver
%Situs inversus
Right Heart and Right Liver
%Heterotaxia
Mismatch Heart and Liver position
A
WT
pvalb6 OE
frzb KD
cacybp OE
ncl1 KD
96,5
3,3
0,2
68,3
7,5
24,2
97,4
2,6
0,0
88,1
4,8
7,1
58,5
16,0
25,5
0%
10%
20%
30%
40%
50%
60%
70%
80%
90%
100%
B
Fold Change
pvalb6
WT
pvalb6 OE
C
cacybp
cacybp OE
D pvalb6 OE
34,67
65,33
0,00
F cacybp OE
40,59
28,71
30,69
H ncl1 KD
37,78
35,56
26,67
E
G
I
dand5
ncl1 KD

Figure 4. Organ *situs* and *dand5* expression phenotypes resulting from manipulating the four candidate genes in the opposite direction.

(A) Organ *situs* quantification by scoring heart and liver laterality in the same larvae; experimental conditions involved injecting at 1-cell stage (A) *pvalb6* OE, *frzb* KD, *cacybp* OE and *ncl1* KD. Statistical analysis of organ *situs* for different treatments was performed using a Fisher test with p-value corrected for multiple comparisons with Bonferroni correction: black asterisks represent statistical significance when comparing treatments with WT; red asterisks represent statistical significance when comparing treatments with *pkd2* KD. **(B-C)** Quantification by qRT-PCR of the performed overexpressions: *pvalb6* (B) and *cacybp* (C); asterisks represent statistical significance (paired t-test, p-value < 0.05). **(D, F, H)** *dand5* expression pattern quantification by *in situ* hybridization of *pvalb6* OE (D), *cacybp* OE (F), *ncl1* KD (H). Asterisks represent statistical significance (Fisher test with Bonferroni correction for multiple comparisons). **(E, G, I)** *dand5* expression level in fold change quantified by qRT-PCR; asterisks represent statistical significance (paired t-test, p-value < 0.05).

In sum, not one of the genes studied rendered a left-right as strong as the *pkd2* knockdown alone. This might suggest that there could be other genes in our profiling list that might explain the strong phenotype of *pkd2* knockdown in left-right axis establishment.

Manipulating the four genes in the opposite direction uncovered new roles in left-right

To complete our study, we then decided to look at the impact of each of these four genes when manipulated in the opposite direction of what we found to be in the microarray. Therefore, we overexpressed *pvalb6* and *cacybp* and we knocked-down *frzb* and *ncl1*. Again, we confirmed the overexpressions by qRT-PCR. We could observe that overexpressing *pvalb6* led to a 20-thousand-fold change increase when compared with controls (Figure 4B; T-test p-value<0.05) and overexpression of *cacybp* led to a 10-fold increase (Figure 4C; T-test p-value<0.05). Also, overexpressing *cacybp* led to mild organ *situs* defects (Figure 4A) and, although *dand5* expression level was not affected (Figure 4G; T-test p-value>0.05), its expression pattern was significantly affected (Figure 4F; Fisher test with Bonferroni correction for multiple comparisons, p-value<0.007). This is a very strange result and should be further investigated, since these levels of *dand5* pattern defects typically have huge impact on organ *situs*. On the other hand, *pvalb6* overexpression led to stronger phenotypes on organ *situs* (Figure 4A, more than 30% defects; Fisher test with Bonferroni correction, p-value<0.005) but not a huge impact on *dand5* expression pattern (Figure 4D; Fisher test Bonferroni correction, p-value>0.007) or levels (Figure 4E; T-test p-value>0.05). Therefore, overexpression of *pvalb6* might be

affecting some other pathway that impacts on organ *situs* that is independent of *dand5*. Interestingly, knockdown of *frzb* showed no organ *situs* phenotype (Figure 4A), while as we described before, its overexpression led to a significant phenotype (compare with Figure 3A). Finally, *ncl1* knockdown led to the strongest organ *situs* phenotypes (Figure 4A, more than 40% of LR defects were detected; Fisher test with Bonferroni correction, p-value<0.005). We observed a complete randomization of *dand5* expression pattern (Figure 4H; Fisher test with Bonferroni correction, p-value<0.07) and also a downregulation of *dand5* expression levels (Figure 4I; T-test p-value<0.05).

In sum, from four genes we uncovered some interesting new potential roles for two of them, *pvalb6* and *ncl1* on left-right axis establishment.

DISCUSSION

The link between intracellular calcium oscillations, asymmetric *dand5* and left-right axis establishment is far from being completely understood. Our microarray allows a quick look into this process in a very specific time-point. It has advanced some interesting new players like *parvalbumin6*, *calcyclin binding protein, frizzled related protein* and *nicalin1.* Although none of them presented an asymmetric expression pattern like *dand5* (Figure 2), they all impacted left-right one way or another.

parvalbumin6 expression was not detected by *in situ* hybridization and only produced left-right defects when was overexpressed. This made sense since all other *parvalbumin* genes were present in the KV gene profiling and therefore could compensate its absence upon knockdown. When overexpressed, it did not affect *dand5* expression pattern or level, but affected organ *situs* in a significant way. This requires further repetition. Parvalbumin can work as a calcium modulator, affecting its peak and allowing a faster decay (John et al., 2001). Overexpressing *pvalb6* in the KV might affect calcium normal homeostasis, which has been proved to have impact of left right development in mice (McGrath et al., 2003). However, the fact that it does not affect *dand5* pattern might indicate that the levels of intracellular calcium were not that affected and only calcium imaging could test this suspicion.

Another gene that was not detected by *in situ* hybridization was *frzb* and, in a similar fashion to *pvalb6*, only affected left-right establishment when overexpressed. Overexpressing *frzb* gave the strongest

phenotype, in terms of organ *situs,* of all the single manipulations that mimicked what we saw in the microarray (Figure 3A). Yet, it did not affect *dand5* expression pattern, only decreased *dand5* expression level. This is interesting and in line with what has already been seen for Wnt signalling downregulation with *wnt3* and *wnt8* knockdown in zebrafish (Lin and Xu, 2009). These authors showed that knockdown of *wnt8* and/or *wnt3* led to reduced cilia length and significantly less *dand5*. Also, although the midline was structurally normal, it no longer showed normal *lefty1* expression, meaning it is no longer signalling properly. Overexpression of *frzb* might be affecting the KV cilia length and midline in a similar fashion, which would need further experiments to confirm. Also, our overexpression of *frzb* is far stronger than what we see in a *pkd2* morphant context. This might explain the phenotypic differences observed since our overexpression is likely to have a stronger inhibition of Wnt signalling. This can be further confirmed by looking at cilia length and midline's *lefty1* expression as in Lin and Xu (2009).

cacybp expression in the KV region was diffuse and both types of manipulations (overexpression and knockdown) led to randomization of *dand5* expression pattern. However, this randomization was accompanied by very mild organ *situs* defects. This situation in uncommon and should be further addressed in future experiments. Nevertheless, Cacybp is a very interesting candidate for further studies mainly because it can connect to calcium binding proteins and E3 ubiquitin ligases like Siah-1 (present in our microarray) that degrade β-catenin (Topolska-Woś et al., 2016). β-catenin plays an important role in DFCs migration and KV formation (Schneider et al., 2008). In a WT situation we should have normal levels of Cacybp and therefore normal levels of β-catenin. Some β-catenin will be in the Adherens Junctions (AJ), impacting on the cell-cell adhesions and cell shape, or in the nuclei acting as a transcription factor downstream of canonical Wnt signalling (Figure 5A and B). Also, accumulation of β-catenin might be helping stabilize *dand5* mRNA, since this role of β-catenin has already been described for other RNAs (Briata et al., 2003). These authors discovered that *pitx2* mRNA becomes more stable upon Wnt/β-catenin signalling activation by targeting of the AU-rich elements present in its 3'UTR by β-catenin. Indeed, further analysis of *dand5* mRNA 3'UTR revealed the presence of some AU-rich elements. So, we could speculate that the raise of intracellular calcium on the left side might induce the degradation of *dand5* mRNA (Figure 5A), while on the right side the

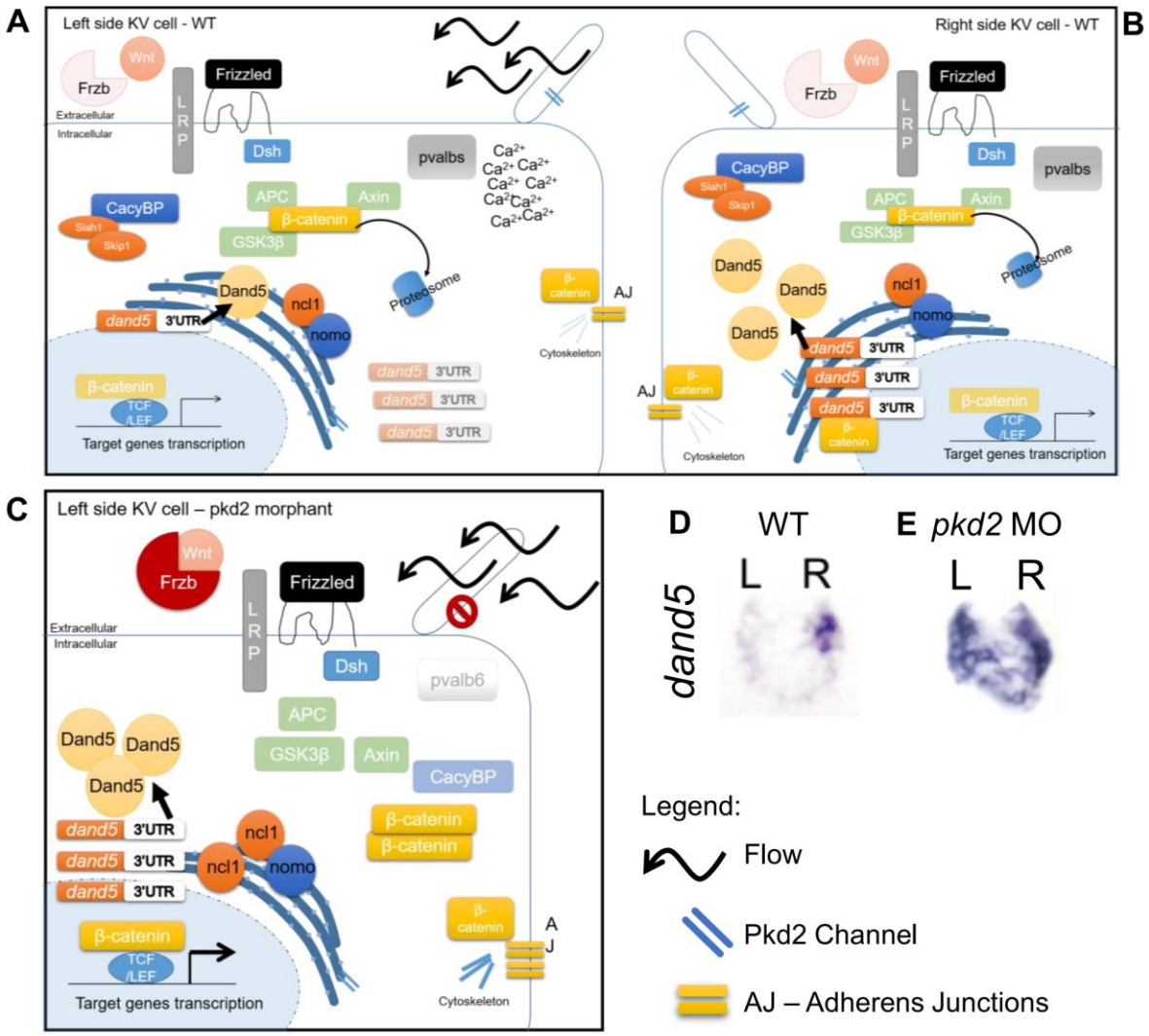

Figure 5. Model integrating the four new genes in the KV cells in WT and *pkd2* KD situations.

(A-B) WT situation: (A) represents a typical cell on the left side of the KV while (B) represents a typical cell on the right side of the KV. Flow induces a calcium rise on the left side that induces the degradation of *dand5* mRNA, possible because β-catenin is being targeted for degradation and therefore cannot stabilize *dand5* mRNA. On the right side, absence of flow and Wnt signalling induces an accumulation of β-catenin on the cytoplasm and therefore an accumulation of dand5 mRNA, explaining the observed asymmetry by *in situ* hybridization **(D)**. **(C)** KV cell on the left side of a *pkd2* KD embryo. Absence of *cacybp* can lead to an accumulation of β-catenin in the cytoplasm and a stabilization of *dand5* mRNA on the left side, resulting in the loss of *dand5* asymmetry as observed in *pkd2* morphant embryos **(E)**.

absence of calcium and maybe some Wnt signalling might be increasing β-catenin levels and

therefore stabilizing the mRNA there, explaining the asymmetry (Figure 5B and D). To better understand the differences occurring between both sides of the *dand5* expression pattern, we could try to obtain separate KV cells from the left and from the right side and then perform gene expression studies. Then we would see which pathways are activated on one side vs the other. When we reduce Pkd2, *cacybp* becomes downregulated, which could indicate that there might be an accumulation of β-catenin in the cytoplasm (Figure 5C and E). This could have an impact on the adherens junctions and therefore on the cytoskeleton, changing the cell shape, or could activate gene expression. Indeed, we have evidence for both processes: cell shape changes (Roxo-Rosa et al., 2015; Chapter 2 of this Thesis) and microarray data for some upregulated genes that are known downstream targets of β-catenin, like Follistatin (significant increase from 4.4 in WT sample to 5.1 in pkd2 morphant sample) and BMP2b (significant increase from 3.6 in WT sample to 4.3 in pkd2 morphant sample). To further confirm if indeed increasing β-catenin leads to stabilization of *dand5* mRNA, we could manipulate β-catenin in time and space and assess the impact on *dand5* expression pattern. Interestingly, we might see the overexpression of *frzb* in the *pkd2* morphant context as an attempt to bring down β-catenin, by inhibiting Wnt signalling and sending it to degradation.

Finally, *nicalin1* was the last gene chosen for further studies. There was not a lot known about this gene, besides the fact that it codes for a transmembrane protein that works in a complex with at least two other proteins (Nomo and TMEM147) (Dettmer et al., 2010; Haffner et al., 2004). This complex is present on the endoplasmic reticulum and affects Lefty trafficking to the extracellular space, impacting on Nodal signalling and consequently dorsal-ventral axis establishment (Haffner et al., 2004, 2007). It has never been associated with left-right and it is known that *ncl1* overexpression alone is not effective in producing Nodal signalling phenotypes during gastrulation, since it also needs the overexpression of its partner *nomo*. Still, since only *ncl1* but not *nomo,* was differently expressed in our microarray, we decided to only manipulate *ncl1* levels. Like *cacybp*, it has a general ubiquitous expression pattern and is strongly expressed. Overexpression of this gene led to mild defects in both *dand5* expression and organ *situs*. It might be interesting to do a co-overexpression with *nomo* to further assess their impact on left-right. On the other hand, knocking down *ncl1* revealed a strong phenotype in all the parameters assessed: strong impact on organ *situs*, randomization of *dand5* and less expression level of *dand5*.

These results suggest that lack of Ncl1 somehow affects *dand5* expression level, probably in an indirect way. Due to what is already known for the function of this protein, we suggest it might even affect the trafficking of both Lefty and Dand5 from the KV cells to the extracellular environment.

Although our approach to interpret the microarray data revealed some new interesting players, as far as we could detect, it did not reveal any new gene that might work at the same level as *dand5*. So, at this point, we cannot confidently say that *dand5* might be the only player with a direct effect on left-right. One thing we realized with this work was that, when looking at the microarray data, it will be important in the future to look more carefully at the expression levels *per se* and compare those with known control genes. One important control, *dand5*, is highly expressed but not differently expressed between WT and *pkd2* morphants. The pattern is affected, but not its expression level. Expression levels might work as an additional factor when choosing future candidates. Also, since zebrafish genome is still not completely annotated, we are still missing some unnamed genes with number codes that could in the future reveal to be interesting candidates as well. This work showed that knocking down *pkd2* led to a variety of gene expression changes, revealing a higher level of complexity downstream of this pathway. We realized that even by manipulating three genes at the same time and respecting the same trend as found in the microarray, we could not reproduce the phenotype of *pkd2* knockdown. This confirms that much more remains to be understood downstream of this protein.

REFERENCES

Bhattacharya, S., Lee, Y.T., Michowski, W., Jastrzebska, B., Filipek, A., Kuznicki, J., and Chazin, W.J. (2005). The modular structure of SIP facilitates its role in stabilizing multiprotein assemblies. Biochemistry *44*, 9462–9471.

Bisgrove, B.W., Snarr, B.S., Emrazian, A., and Yost, H.J. (2005). Polaris and Polycystin-2 in dorsal forerunner cells and Kupffer's vesicle are required for specification of the zebrafish left-right axis. Dev. Biol. *287*, 274–288.

Briata, P., Ilengo, C., Corte, G., Moroni, C., Rosenfeld, M.G., Chen, C.Y., and Gherzi, R. (2003). The Wnt/β-catenin→Pitx2 pathway controls the turnover of Pitx2 and other unstable mRNAs. Mol. Cell *12*, 1201–1211.

Caron, A., Xu, X., and Lin, X. (2012). Wnt/beta-catenin signaling directly regulates Foxj1 expression and ciliogenesis in zebrafish Kupffer's vesicle. Development *139*, 514–524.

Chard, P.S., Bleakman, D., Christakos, S., Fullmer, C.S., and Miller, R.J. (1993). Calcium bufferin properties of calbindin D28K and parvalbumin in rat sensory neurones. J. Physiol. *472*, 341–357.

Dettmer, U., Kuhn, P.H., Abou-Ajram, C., Lichtenthaler, S.F., Krüger, M., Kremmer, E., Haass, C., and Haffner, C. (2010). Transmembrane protein 147 (TMEM147) is a novel component of the Nicalin-NOMO protein complex. J. Biol. Chem. *285*, 26174–26181.

Essner, J.J., Amack, J.D., Nyholm, M.K., Harris, E.B., and Yost, H.J. (2005). Kupffer's vesicle is a ciliated organ of asymmetry in the zebrafish embryo that initiates left-right development of the brain, heart and gut. Development *132*, 1247–1260.

Field, S., Riley, K.-L., Grimes, D.T., Hilton, H., Simon, M., Powles-Glover, N., Siggers, P., Bogani, D., Greenfield, A., and Norris, D.P. (2011). Pkd1l1 establishes left-right asymmetry and physically interacts with Pkd2. Development *138*, 1131–1142.

Filipek, A., Michowski, W., and Kuznicki, J. (2008). Involvement of S100A6 (calcyclin) and its binding partners in intracellular signaling pathways. Adv. Enzyme Regul. *48*, 225–239.

Haffner, C., Frauli, M., Topp, S., Irmler, M., Hofmann, K., Regula, J.T., Bally-Cuif, L., and Haass, C. (2004). Nicalin and its binding partner Nomo are novel Nodal signaling antagonists. EMBO J. *23*, 3041–3050.

Haffner, C., Dettmer, U., Weiler, T., and Haass, C. (2007). The nicastrin-like protein nicalin regulates assembly and stability of the Nicalin-Nodal modulator (NOMO) membrane protein complex. J. Biol. Chem. *282*, 10632–10638.

Jastrzebska, B., Filipek, A., Nowicka, D., Kaczmarek, L., and Kuznicki, J. (2000). Calcyclin (S100A6) Binding Protein (CacyBP) Is Highly Expressed in Brain Neurons. J. Histochem. Cytochem. *48*, 1195–1202.

John, L.M., Mosquera-caro, M., Camacho, P., and Lechleiter, J.D. (2001). Control of IP3-mediated Ca2+ puffs in Xenopus laevis oocytes by the Ca2+ -binding protein parvalbumin. J. Physiol. *535*, 3–16.

Kamura, K., Kobayashi, D., Uehara, Y., Koshida, S., Iijima, N., Kudo, A., Yokoyama, T., and Takeda, H. (2011). Pkd1l1 complexes with Pkd2 on motile cilia and functions to establish the left-right axis. Development *138*, 1121–1129.

Kimmel, C.B., Ballard, W.W., Kimmel, S.R., Ullmann, B., and Schilling, T.F. (1995). Stages of embryonic development of the zebrafish. Dev. Dyn. *203*, 253–310.

Leyns, L., Bouwmeester, T., Kim, S.H., Piccolo, S., and De Robertis, E.M. (1997). Frzb-1 is a secreted antagonist of Wnt signaling expressed in the Spemann organizer. Cell *88*, 747–756.

Lin, X., and Xu, X. (2009). Distinct functions of Wnt/beta-catenin signaling in KV development and cardiac asymmetry. Development *136*, 207–217.

Lopes, S.S., Lourenço, R., Pacheco, L., Moreno, N., Kreiling, J., and Saúde, L. (2010). Notch signalling regulates left-right asymmetry through ciliary length control. Development *137*, 3625–3632.

McGrath, J., Somlo, S., Makova, S., Tian, X., and Brueckner, M. (2003). Two populations of node monocilia initiate left-right asymmetry in the mouse. Cell *114*, 61–73.

Müntener, M., Käser, L., Weber, J., and Berchtold, M.W. (1995). Increase of skeletal muscle relaxation speed by direct injection of parvalbumin cDNA. Proc. Natl. Acad. Sci. U. S. A. *92*, 6504–6508.

Nakamura, T., Saito, D., Kawasumi, A., Shinohara, K., Asai, Y., Takaoka, K., Dong, F., Takamatsu, A., Belo, J.A., Mochizuki, A., et al. (2012). Fluid flow and interlinked feedback loops establish left-right asymmetric decay of Cerl2 mRNA. Nat. Commun. *3*, 1322.

Nauli, S.M., Alenghat, F.J., Luo, Y., Williams, E., Vassilev, P., Li, X., Elia, A.E.H., Lu, W., Brown, E.M., Quinn, S.J., et al. (2003). Polycystins 1 and 2 mediate mechanosensation in the primary cilium of kidney cells. Nat. Genet. *33*, 129–137.

Pennekamp, P., Menchen, T., Dworniczak, B., and Hamada, H. (2015). Situs inversus and ciliary abnormalities: 20 years later, what is the connection? Cilia *4*.

Roxo-Rosa, M., Jacinto, R., Sampaio, P., and Lopes, S.S. (2015). The zebrafish Kupffer's vesicle as a model system for the molecular mechanisms by which the lack of Polycystin-2 leads to stimulation of CFTR. Biol. Open *4*, 1356–1366.

Sampaio, P., Ferreira, R.R., Guerrero, A., Pintado, P., Tavares, B., Amaro, J., Smith, A.A., Montenegro-Johnson, T., Smith, D.J., and Lopes, S.S. (2014). Left-right organizer flow dynamics: how much cilia activity reliably yields laterality? Dev. Cell *29*, 716–728.

Schneider, G., and Filipek, A. (2011). S100A6 binding protein and Siah-1 interacting protein (CacyBP/SIP): Spotlight on properties and cellular function. Amino Acids *41*, 773–780.

Schneider, I., Houston, D.W., Rebagliati, M.R., and Slusarski, D.C. (2008). Calcium fluxes in dorsal forerunner cells antagonize beta-catenin and alter left-right patterning. Development *135*, 75–84.

Schottenfeld, J., Sullivan-Brown, J., and Burdine, R.D. (2007). Zebrafish curly up encodes a Pkd2 ortholog that restricts left-side-specific expression of southpaw. Development *134*, 1605–1615.

Slusarski, D.C., Yang-Snyder, J., Busa, W.B., and Moon, R.T. (1997). Modulation of embryonic intracellular Ca2+ signaling by Wnt-5A. Dev. Biol. *182*, 114–120.

Tavares, B., Jacinto, R., Sampaio, P., Pestana, S., Gardner, R., Lopes, T., Lopes, S.S., Schilling, B., Henry, I., and Sau, L. (2017). Notch / Her12 signalling modulates , motile / immotile cilia ratio downstream of Foxj1a in zebrafish left-right organizer. Elife *6:e25165*, 1–26.

Thiele, J., and Schultz, J.E. (1981). Ciliary membrane vesicles of paramecium contain the voltage-sensitive calcium channel. Proc. Natl. Acad. Sci. U. S. A. *78*, 3688–3691.

Thisse, B., and Thisse, C. (2004). Fast Release Clones: A High Throughput Expression Analysis.

Thisse, C., and Thisse, B. (2008). High-resolution in situ hybridization to whole-mount zebrafish embryos. Nat. Protoc. *3*, 59–69.

Thisse, B., Pflumio, S., Fürthauer, M., Loppin, B., Heyer, V., Degrave, A., Woehl, R., Lux, A., Steffan, T., Charbonnier, X.Q., et al. (2001). Expression of the zebrafish genome during embryogenesis.

Topol, L., Jiang, X., Choi, H., Garrett-Beal, L., Carolan, P.J., and Yang, Y. (2003). Wnt-5a inhibits the canonical Wnt pathway by promoting GSK-3-independent β-catenin degradation. J. Cell Biol. *162*, 899–908.

Topolska-Woś, A.M., Chazin, W.J., and Filipek, A. (2016). CacyBP/SIP — Structure and variety of functions. Biochim. Biophys. Acta - Gen. Subj. *1860*, 79–85.

Wang, S., Krinks, M., Lin, K., Luyten, F.P., and Moos, M. (1997a). Frzb, a secreted protein expressed in the Spemann organizer, binds and inhibits Wnt-8. Cell *88*, 757–766.

Wang, S., Krinks, M., and Moos Jr, M. (1997b). Frzb-1, an antagonist of Wnt-1 and Wnt-8, does not block signaling by Wnts -3A, -5A, or -11. Biochem. Biophys. Res. Commun. *236*, 502–504.

Westerfield, M. (2000). The Zebrafish Book. A Guide for the Laboratory Use of Zebrafish (Danio rerio)

(University of Oregon Press, Eugene).

Yoshiba, S., Shiratori, H., Kuo, I.Y., Kawasumi, A., Shinohara, K., Nonaka, S., Asai, Y., Sasaki, G., Belo, J.A., Sasaki, H., et al. (2012). Cilia at the Node of Mouse Embryos Sense Fluid Flow for Left-Right Determination via Pkd2. Science (80-.). *338*, 226–231.

Yuan, S., Zhao, L., Brueckner, M., and Sun, Z. (2015). Intraciliary Calcium Oscillations Initiate Vertebrate Left-Right Asymmetry. Curr. Biol. *25*, 1–12.

Zhang, L., Bonilla, S., Zhang, Y., and Leung, Y.F. (2014). p35 Promotes the Differentiation of Amacrine Cell Subtype in the Zebrafish Retina Under the Regulation of egr1. Dev. Dyn. *243*, 315–323.

Zhu, P., Xu, X., and Lin, X. (2015). Both ciliary and non-ciliary functions of Foxj1a confer Wnt/ -catenin signaling in zebrafish left-right patterning. Biol. Open *4*, 1376–1386.

Zorn, A.M. (1997). Cell – cell signalling : Frog frizbees. 501–504.

CHAPTER 5

Dand5 and Nicalin1: two Nodal signalling inhibitors compared *de novo* in the Left-Right context

"When the going gets tough, the tough get going"

Proverb

Dand5 and Nicalin1: two Nodal signalling inhibitors compared *de novo* in the Left-Right context

Raquel Jacinto[1], Pedro Sampaio[1] and Susana S. Lopes[1]

1-CEDOC, Chronic Diseases Research Center, NOVA Medical School / Faculdade de Ciências Médicas, Universidade Nova de Lisboa, Campo dos Mártires da Pátria, 130, 1169-056 Lisboa, Portugal

Summary

Dand5 is a well-established Nodal pathway inhibitor in left-right (LR) axis establishment. It is also common between mice, zebrafish, medaka and xenopus (Bell et al., 2003; Belo et al., 2000; Hashimoto et al., 2004; Hojo et al., 2007; Pearce et al., 1999). To the present day, it is the only Nodal antagonist present in the Left-Right Organizer (LRO) cells. Here we describe another nodal inhibitor with a broad expression pattern that had not yet been associated with LR. A LRO-specific microarray performed in our lab identified Nicalin1, a nicastrin-like protein without γ-secretase activity. Nicalin1 was described to be present in the endoplasmic reticulum in a complex with two other partners (Dettmer et al., 2010; Haffner et al., 2004) and to play a role in mesendoderm patterning in the zebrafish model (Haffner et al., 2004).

In this study we have showed that while overexpression of *nicalin1* (*ncl1)* leads to mild defects in LR patterning, knocking-down its function causes increasing defects in LR in a dose-dependent fashion. We were able to rescue some of these defects by injecting *ncl1* mRNA. *ncl1* morphants presented weaker LRO fluid-flow speed and a clear randomization of the main nodal pathway components like *dand5* and *spaw* expression patterns. Interestingly, knockdown embryos presented higher percentage of heterotaxy than *situs solitus* or *situs inversus*. Experiments where we knocked-down both *dand5* and *ncl1* led to more defects than just affecting each one separately, indicating a potential new epistatic effect. *ncl1* overexpression cannot rescue *dand5*$^{-/-}$ mutant organ *situs* and *dand5* overexpression cannot rescue *ncl1* knockdown, pointing to two separate pathways. All data combined pointed to a potential new antagonist of the Nodal signalling pathway in zebrafish LR.

INTRODUCTION

Nodal signalling was first associated with left-right axis establishment in the chick embryo, with the finding that cNR-1 (chick Nodal Related gene 1) was expressed on the anterior left side of the Hensen's node and was stronger on the left lateral plate mesoderm (LPM) (Levin et al., 1995). One year later the same was described for mice, with the observation that *nodal* mRNA started symmetric on both sides of the node to then becoming asymmetric towards the left of the node. At the same time, expression on the left LPM was reported to start and expand (Lowe et al., 1996). It has been shown that the side of nodal expression correlates well with heart laterality and that mice lacking *nodal* expression around the node led to its absent expression in the LPM and consequently to multiple organ *situs* defects (Brennan et al., 2002; Collignon et al., 1996). Concomitantly with asymmetric *nodal* expression around the node it was also possible to observe asymmetric activation of Nodal signalling itself by using an antibody against phosphorylated Smad2/3, that showed a stronger signal on the left side of the node and left LPM (Kawasumi et al., 2011). Also in zebrafish, *southpaw* (*spaw*, nodal homolog) was observed to be expressed bilaterally around the Kupffer's vesicle (KV, node homolog in zebrafish) and in the left LPM (Long et al., 2003). Knocking-down *spaw* did not abolish its KV domains of expression but caused LPM absent *spaw* expression, lack of *cyclops, lefty1/2* and *pitx2* expression, together with disruption of heart and gut *situs* (Long et al., 2003). These other components of the nodal pathway were described to participate in LR establishment, like the two inhibitors *lefty1*, which shows an mRNA expression in the left diencephalon, and *lefty2* that presents an mRNA expression in the anterior left LPM, in the cardiac field (Bisgrove et al., 1999). Antibodies for these inhibitors were never described to work in zebrafish. Since Nodal can indirectly activate its own transcription and the transcription of its own inhibitors *lefty1*/2 through activation of the transcription factor FAST2 (Saijoh et al., 1999, 2000), it was found that there are physical and molecular barriers present to help define nodal expression domains. For instance, there is a midline molecular barrier provided by *lefty1* mRNA expression, that prevents the traveling of Nodal molecules from left to right LPM (Bisgrove et al., 1999). Also, there are two additional barriers described by Lenhart et al. (2011): a posterior barrier of BMP signalling independent of Lefty1 that impedes nodal propagation through the posterior LPM; and

an anterior barrier mediated by Lefty2, seen by mRNA delimited expression, in the left cardiac field that avoids transfer of nodal towards the right LPM and downward propagation (Lenhart et al., 2011).

On the actual left-right organizer (LRO), it is possible to find a common Nodal antagonist named Dand5, that is asymmetrically expressed towards the right side, known previously as *cerl2* in mice (Marques et al., 2004), *coco* in Xenopus (Schweickert et al., 2010) and *charon/dand5* in zebrafish and medaka (Hashimoto et al., 2004). In mice, *cerl2* KO mice show randomization of organ *situs* which can be partially rescued with the removal of one nodal allele (Marques et al., 2004). The asymmetric expression of *cerl2* mRNA seems to be a downstream target of fluid flow typically observed in the LRO (Nakamura et al., 2006) and this was further confirmed in xenopus model (Schweickert et al., 2010). Elegant work has showed that *cerl2* mRNA decay occurs in the apical region of LRO cells, initiated by the leftward fluid flow and further established by a Wnt3-mediated degradation at the *cerl2* 3'UTR (Nakamura et al., 2012). Interestingly, Cerl2 protein localization seems not to correlate with its mRNA expression pattern (Inácio et al., 2013). While *cerl2* mRNA first starts symmetric and then gradually becomes asymmetric towards the right until it completely disappears at 5-6 somite stage, Cerl2 protein first localizes and prevents Nodal activation on the right side (Inácio et al., 2013). However, later, Cerl2 protein was observed to gradually become bilateral and then to become restricted to the left-side. This protein shifting seemed to be a flow dependent process, because this localization was not observed in iv/iv mutant mice. This translocation of the Cerl2 protein was interpreted as having a role in stopping Nodal activity on the left side of the LRO (Inácio et al., 2013).

In zebrafish, *dand5* knockdown leads to bilateral expression of *spaw*, *lefty1*/2 and *pitx2*, as well as organ *situs* defects (Hashimoto et al., 2004), but nothing is known about the protein dynamics. So far, Dand5 is the only known Nodal antagonist present in the LRO cells. However, a recent KV-specific microarray performed by our lab revealed the presence of another Nodal inhibitor expressed at the same levels as *dand5* mRNA. Nicalin1 is a 60kDa protein, part of a previously unknown membrane protein complex that localizes to the endoplasmic reticulum with another two transmembrane proteins: Nomo (Nodal modulator, previously known as pM5, with 130kDa) and TMEM147 (Dettmer et al., 2010; Haffner et al., 2004, 2007). TMEM147 is highly conserved with a putative topology similar to APH-1

(another component of the γ-secretase complex)(Dettmer et al., 2010). All the three known components of this complex appear expressed in our microarray. Previous studies by Haffner et al. (2004) reported that ectopic expression of both Nicalin1 and Nomo in zebrafish can cause cyclopia and mesendoderm patterning defects that are mediated by Nodal signalling pathway. Downregulation of Nomo leads to increase of anterior axial mesendoderm and development of an enlarged hatching gland. Inhibition of Nodal signalling by overexpression of *lefty1* was rescued when Nomo levels were reduced. This suggested that Ncl1/Nomo have an antagonistic role on Nodal signalling (Haffner et al., 2004). Work with cell culture showed that Nicalin1 and Nomo become unstable in the absence of the respective binding partner, with Nomo being produced in excess and Ncl1 acting as the limiting reagent (Haffner et al., 2007). To this date, there is no report on these proteins having a role on left-right axis establishment. Therefore, in this work, we use the zebrafish model to explore the role of Nicalin1 in LR and we further compare it with the known Nodal antagonist, Dand5. Since *ncl1* has a very broad expression pattern (Haffner et al., 2004), it was important to first understand which LR players could be interacting with Ncl1. For this, we first assessed the expression patterns of known LR elements like *lefty1*, *spaw* and *dand5* in the vicinity of the zebrafish LRO. Then we manipulated *ncl1* and *dand5* and compared the results in terms of flow pattern and the expression pattern/level of *dand5*, *pitx2* and *spaw*. We proceeded to knockdown *ncl1* with a morpholino and compared its LR readouts with those for the *dand5*$^{-/-}$ mutant. In the end, we tried to rescue the phenotypes observed in *dand5*$^{-/-}$ mutants and *ncl1* KD embryos with overexpression of *ncl1*/*nomo* and *dand5*, respectively. Finally, we showed preliminary data on the *ncl1*$^{-/-}$ mutant generated by CRISPR-Cas9 and hypothesize on what role can this new player have in LR axis establishment.

EXPERIMENTAL PROCEDURES

Fish stocks and genetics

dand5$^{+/-}$ mutant line was kindly given by Alex Schier. Wild-type (AB) and *dand5*$^{-/-}$ mutant lines were maintained and used as described elsewhere (Westerfield, 2000). Embryos were raised at 28ºC, depending on the experiment, in E3 embryo media and staged accordingly (Kimmel et al., 1995).

Procedures with zebrafish were approved by the Portuguese DGAV (Direcção Geral de Alimentação e Veterinária).

Cloning full length *ncl1*, *dand5* and *nomo*

Primers were designed to amplify full coding sequence of *ncl1, nomo* and *dand5* into a pCS2+ plasmid. Primer sequences: *dand5* forward 5'-ATATATGGATCCCATGACTTTTCAGGTCGGC-3' and reverse 5'- CCCCCCGAATTCTTATAAATTAAACATATCTGTGTTCTG-3'; *nomo* forward 5'-ATATATGGATCCATGGGTGGAATTAAAGAGCTAGC-3' and reverse 5'-ATATATCTCGAGTCATGTACGTCTCGTCTTCG-3'; *ncl1* forward 5'-GCTGCTATCGATATGTTCGAGGAGGCTGGT -3' and reverse 5'-GCGCAGAATTCTCAGTGCTGCTTGACCCG-3'. PCRs were performed using iProof™ High-Fidelity DNA Polymerase (Bio Rad). Double digestions were performed in the pCS2+ plasmid and amplified genes, according to primer design and T4 ligation (NEB) was performed overnight at 16ºC. DH5α competent *E. coli* were transformed with ligation product and plated in LB-Agar (Roth) with 100mg/mL Ampicilin resistance. Colonies were screened by PCR using pCS2+ specific primers and positive colonies were sent to sequence to assess the quality of PCR amplification. Colonies with correct sequences for all 4 genes were selected and grown on secondary cultures. High quality and very concentrated plasmids were obtained with a ZymoPURE™ Plasmid MidiPrep kit.

***In vitro* RNA synthesis for overexpression, *in situ* hybridization and morpholino**

For mRNA for overexpression production, plasmids were linearized downstream of the polyA tail and 2μg of linearized plasmid were processed with mMESSAGE mMACHINE™ Sp6 Transcription Kit (Ambion). For *in situ* hybridization probes, plasmids were linearized and 2μg of linearized plasmid were transcribed *in vitro* using Promega T7 RNA polymerase. Both RNAs were further processed with Zymo RNA Clean and Concentrated and quantified using nanodrop. The mRNA was aliquoted and stored at -80ºC while the *in situ* hybridization probe was diluted in Hybridization Mix (30-50ng in 200μL). Morpholino targeting the 5'UTR excluding the initial ATG for *ncl1* was ordered online from GeneTools: *ncl1* 5'- CGGGAGATTCCCACCGACAGAAACA-3'.

Overexpression and Knockdown experiments

WT (AB) and dand5$^{-/-}$ mutant embryos were injected at 1 cell-stage or 500 cell-stage with several doses of *ncl1* morpholino and mRNA of *ncl1*, *nomo* and *dand5*. Toxicity was assessed by discarding all doses that produced high mortality rates. The doses chosen for the final experiments were: 3ng and 4,5ng of *ncl1* morpholino (KD), 500pg of *ncl1* mRNA (OE), 500pg of *nomo* mRNA (OE), 100pg *dand5* mRNA (OE). Embryos were allowed to develop to the desire stages to study the expression pattern of several genes and organ *situs*.

Fluid flow speed and pattern quantification

We used the methods described in previous work (Sampaio et al., 2014) for mounting and filming embryos and quantifying fluid flow. We tracked native particles and calculated flow velocity with an R script in WT and treated embryos at 8-10 somite stage (Tavares et al., 2017). Embryos were developed at 25ºC until the desired stage and then filmed at room temperature. We used 9 WT control embryos, 9 embryos injected with *ncl1* full length mRNA, 4 *ncl1* MO injected embryos and 8 embryos mutants for dand5$^{-/-}$.

***In situ* hybridization and immunostaining**

Whole-mount immunostaining-*in situ* hybridization was performed by combining the two protocols on the second day of the *in situ* hybridization, as described in Tavares et al., 2017. The new steps were added to the *in situ* hybridization protocol as follows: on the second day, antibody anti-GFP 1:200 was added with antibody Anti-Digoxigenin AP Fab Fragments (Roche) 1:5000 in blocking solution and incubated at 4ºC in a horizontal rotator; on the third day, the secondary antibody anti-rabbit Alexa Fluor 488 (Invitrogen) 1:500 was added to blocking solution and incubated overnight at 4ºC in a horizontal rotator; on the fourth day, embryos were developed with Fast-Red tablets substrate (Roche) in 0.1mM Tris-HCl pH 8 at 37ºC until red fluorescence was observed in a fluorescent stereoscope. They were then flat-mounted for confocal microscopy. The probes used were for *dand5*, *spaw* and *lefty1* at 8-10 somite stage. Whole-mount in *situ* hybridizations for *dand5* at 8-10 somite stage, *pitx2* and *spaw* at 14-16 somite stage, and *foxa3* at 53 hours post fertilization (hpf) as described in Thisse

Lab - *In situ* Hybridization Protocol 2010 update ZFIN. For *dand5 in situ* hybridization used 273 WT controls, 56 *ncl1* MO, 57 *ncl1* OE and 80 dand5$^{-/-}$ mutant embryos; for *pitx2* used 82 WT controls, 92 *ncl1* MO, 47 *ncl1* OE and 63 dand5$^{-/-}$ mutant embryos; for *spaw* used 53 WT controls, 69 *ncl1* MO, 50 *ncl1* OE and 66 dand5$^{-/-}$ mutant embryos. The results were analysed by Fisher's exact test with Bonferroni correction for multiple comparisons.

Heart and gut laterality

At 30 hpf we evaluated heart jogging using a stereoscopic zoom microscope (SMZ745, Nikon Corporation) to observe the embryos from the ventral side. These embryos were then allowed to develop in separated petri dishes and at 53 hpf, embryos were fixed and processed for *foxa3 in situ* hybridizations to assess gut laterality. We could then pair the heart *situs* with gut *situs* for each treatment and attribute an embryo *situs* as *situs solitus*, *situs inversus* or heterotaxy. The results were analysed by Fisher's exact test with Bonferroni correction for multiple comparisons.

Quantitative PCR

Embryos from different treatments were pooled in 3 groups of 20-50 embryos in order to have three different biological replicates. Protocol was implemented as described previously (Tavares et al., 2017). Primer sequences used were as follows: *dand5* forward 5′-CCGCAATCCTGACCCATAGCAA-3′ and reverse 5′-CTCCTCCGTTATGCGCTGTGTA-3′; *lefty1* forward 5'-CCAGACGACAACACTCTGGGAAAA-3' and reverse 5'- ACTGTTCCCTGCAGCACATTTCA-3'*; spaw* forward 5'-CTTTGCCGGCGGGTTGATATGT-3' and reverse 5'-GCTCCGGTTGGTAGAGCTTCAA-3'*; eef1al1* forward 5'-CCTTCAAGTACGCCTGGGTGTT-3' and reverse 5'-CACAGCACAGTCAGCCTGAGAA-3'; *rpl13a* forward 5'-TGACAAGAGAAAGCGCATGGTT-3' and reverse 5'-GCCTGGTACTTCCAGCCAACTT-3'.

***ncl1* CRISPR-Cas9 approach**

Two short guide RNAs targeting the beginning of the ncl1 coding sequence were found using the website CRISPRscan (www.crisprscan.org) with the sequences 5'-GGTGTCGTTCCCGCTCAGCC-3' and 5'-GGTGTTGGAGAACATGCTGA-3'. These were ordered as DNA sequences with BsaI

restriction sites and were cloned into the pDR274 vector. These were used to transform bacteria and sent to sequencing for further confirmation. These vectors were linearized and transcribed *in vitro* into RNA. Then, 50ng/μL of each short guide was co-injected with 100pg/μL of Cas9 mRNA into 1-cell stage embryos and let develop until 24 hours post fertilization. At 24hpf, 3 batches of 8 embryos each were used to extract DNA and perform PCR to amplify a 200bp region flanking the target sequence. These were run in a 15% PAGE gel for 3h at 150V. Batches that showed a mixture of indel mutations and WT alleles, forming heteroduplexes and homoduplexes of DNA, indicated the success of the injection and sibling embryos were let develop until adulthood. This generation was genotyped by outcross each fish with a WT fish and repeating the PAGE protocol in batches of 8 embryos until heteroduplexes were found in the progeny. Sibling embryos of these batches were allowed to grow until adulthood and were genotyped by fin clip and repeating the PAGE protocol. Heterozygotes were crossed and the progeny was genotyped by sequencing and evaluated for gross morphology defects and heart *situs* (n=82 embryos).

RESULTS

3D gene expression patterns for left-right genes around the KV

In the mouse model, the periphery cells of the node both express *nodal* and *dand5*, with nodal becoming asymmetric towards the left and *dand5* asymmetric towards the right (Lowe et al., 1996; Marques et al., 2004). In the zebrafish model, the published expression patterns for these two genes did not seem to overlap in the LRO cells (Hashimoto et al., 2004; Long et al., 2003). To confirm, we started by looking at the three-dimensional expression pattern of three players of Nodal pathway in left-right at 8 somite-stage. We first looked at *lefty1*, an inhibitor expressed in the midline (Figure 1A). By using Fast Red *in situ* hybridization in a tg(sox17:GFP) line and confocal microscopy, we could visualize that *lefty1* domain of expression is indeed dorsal to the KV (Figure 1B, B' and B'' and Figure 1C and C'). Despite the fact that a microarray produced in our lab has identified *lefty1* expressed in KV, we could not detect any expression there by *in situ* hybridization, maybe due to a very low level of expression (2,5 compared with 8,4 of *dand5*). This could be explained by very low levels of expression that are undetectable by *in situ* hybridization. We think we can exclude contamination of midline cells

because we used FACS technique to isolate KV cells labelled by a foxj1a:GFP reporter line that at that time is specific for the KV cells (Caron et al., 2012).

The second gene that we investigated by the same techniques was *spaw* (Figure 1D). This gene was also expressed in KV cells by the same KV-specific microarray, at the same level as *lefty1*. Fluorescent i*n situ* hybridization showed that *spaw* expression pattern was dorsal to the KV cells labelled by sox17:GFP (Figure 1E, E' and E''). There was no KV cell that was positive for *spaw* expression. We confirmed this in different Anterior-Posterior slices and also checked in the Dorsal-Ventral Axis (Figure 1E'', E1 and E2). As for differences between left and right sides, more embryos should be analysed to have a meaningful quantification. In sum, 3D reconstruction showed broad expression domains on both left and right sides, in the neighbouring cells dorsal to the KV (Figure 1F and F´).

The third gene studied was *dand5* (Figure 1G). This gene was expressed in KV cells, stronger and more broadly in the right side by being expressed in more cell layers surrounding the KV (Figure 1H and I). In a more dorsal level (KV upper level) we could see more cell layers on the right side expressing *dand5* than on the left side (Figure J, J' and J''). By looking at a KV mid-plane level, we could clearly observe that all KV cells expressed this gene (Figure 1K, K' and K''). Indeed, *dand5* level of expression in our KV-specific microarray was much higher than the expression levels found for *lefty1* and *spaw*.

Looking at the expression of all these genes together (Figure 1L and L'), we can say that there are three expression domains: 1) at midline domain anterior to the KV and not overlapping with KV cells, for *lefty1*; 2) at dorsal domain straight above the KV and not overlapping with KV cells for *spaw*; and 3) at the KV cells and adjacent cell layers on the right side, for *dand5*. In conclusion, none of these domains are visibly overlapping with each other in terms of mRNA expression. These results further confirm the work of Hashimoto et al. (2004) that had already shown by 2D in situs that indeed these domains do not seem to overlap. Since *ncl1* and *nomo* expression domains seem to overlap in all these three domains, the resulting protein complex might be interacting with any of these Nodal players. Their level of expression in the KV-specific microarray is very similar to that of *dand5* (*ncl1*

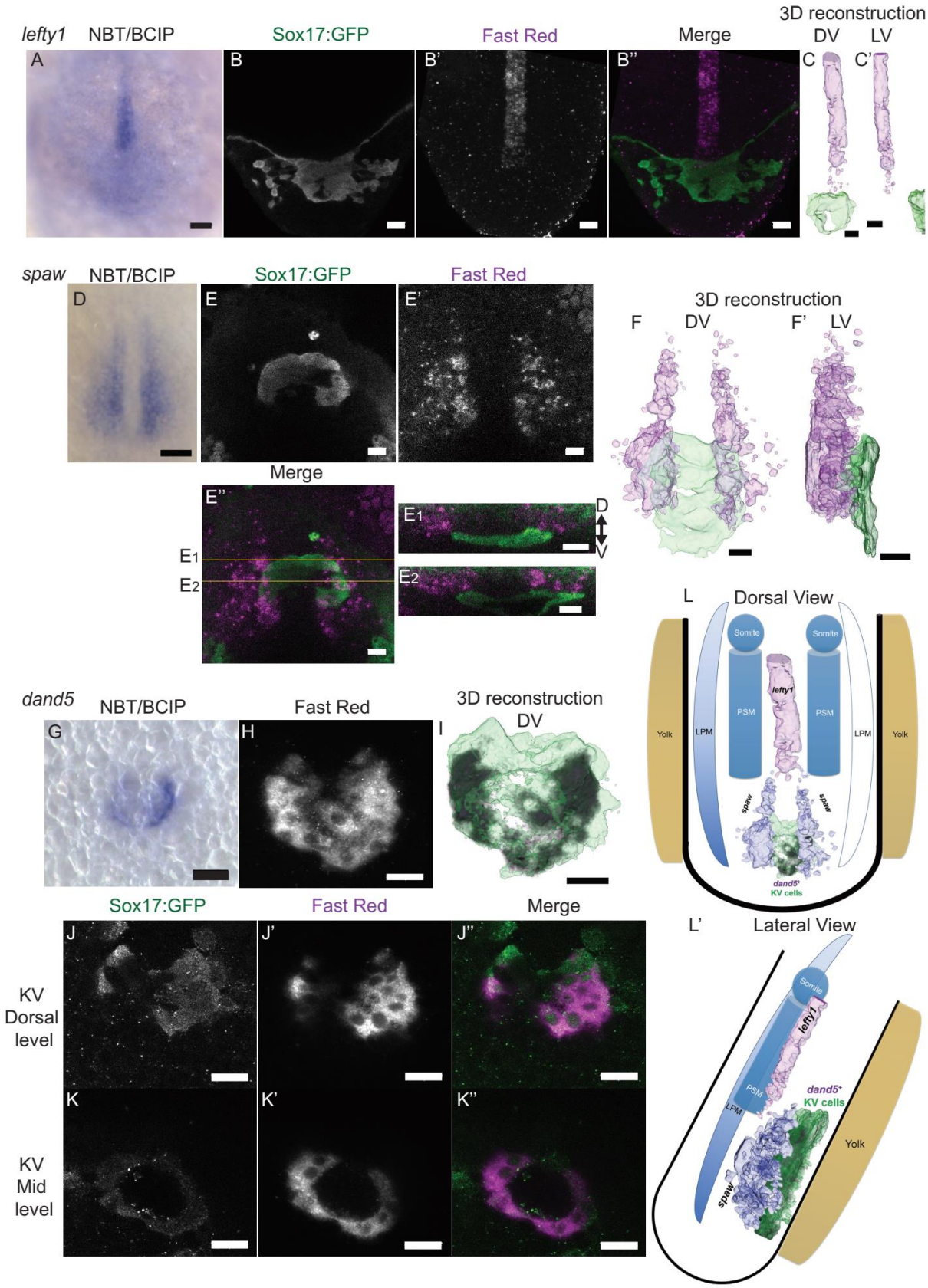

***Figure 1* - 3D Expression patterns of *lefty1*, *spaw* and *dand5* around the KV in 8-10ss embryos**

In situ hybridization using **(A, D and G)** NBT/BCIP staining of *lefty1, spaw* and *dand5*, respectively; Scale bars in black correspond to 50μm. *In situ* hybridization using **(B-B'', E-E'', H, J-J'' and K-K'')** Fast-red staining with immunostaining against GFP in sox17:GFP embryos for *lefty1* (B-B''), *spaw* (E-E'', E1 and E2 show different Z planes) and *dand5* (H shows maximum intensity projection, J-J'' shows KV dorsal level; K-K'' shows KV mid-level). Scale bars in white correspond to 20 μm. We used 5 embryos per gene and reconstructed 2 embryos for this 3D analysis **(C-C', F-F', I)** 3D reconstructions of *lefty1*, *spaw* and *dand5* in purple and the KV cells in green. DV – Dorsal view, LV – Lateral View, Scale bar corresponds to 20μm. **(L-L')** Schematics representing the dorsal view (L) and Lateral view (L') of the zebrafish embryo with the expression domains of the 3 genes in 3D. PSM – Pré-somitic Mesoderm, LPM – Lateral Plate Mesoderm.

expression level 6,1 and *dand5* expression level 8.4), so we trust and assume that these gene expression levels are going to be meaningful in terms of protein function.

Manipulating *ncl1* and *dand5* impacts differently on different players of left-right axis establishment

We first assessed the impact of *ncl1* manipulations and *dand5* absence on fluid flow speed pattern. Overexpression of *ncl1* or observation of *dand5*$^{-/-}$ mutants showed no defects on flow speed pattern, with stronger flows on the anterior part of the KV (Figure 2A, B and D). Also, flow speed was not different from WT situations (Figure A', B' and D'). This suggests an overall normal KV architecture, with the typical anterior dorsal cluster of cilia, and normal cilia in terms of beat frequency and length. In contrast, knockdown of *ncl1* led to a slower fluid flow, with no differences between the anterior and the posterior halves of the KV (Figure 2C and C'). This slower fluid flow could be due to inefficient ciliary beating, either due to cilia shorter length or slower cilia beat frequency. KV architecture could also be affected and therefore impact on the flow pattern. Further experiments should be done to understand the underlying causes for slower and homogeneous flow. At this point, further analysis of left-right markers for this treatment should have in consideration the fact that flow is not normal and thus could account for many of the defects observed.

Since flow impacts directly on *dand5* expression pattern (Nakamura et al., 2012; Sampaio et al., 2014; Schweickert et al., 2010), we proceeded to analyse the impact of these treatments in *dand5* expression patterns and expression levels. Manipulating *nicalin1* and *dand5* led to different phenotypes in *dand5* expression pattern. While overexpressing *ncl1* led to 50% of misdirection of

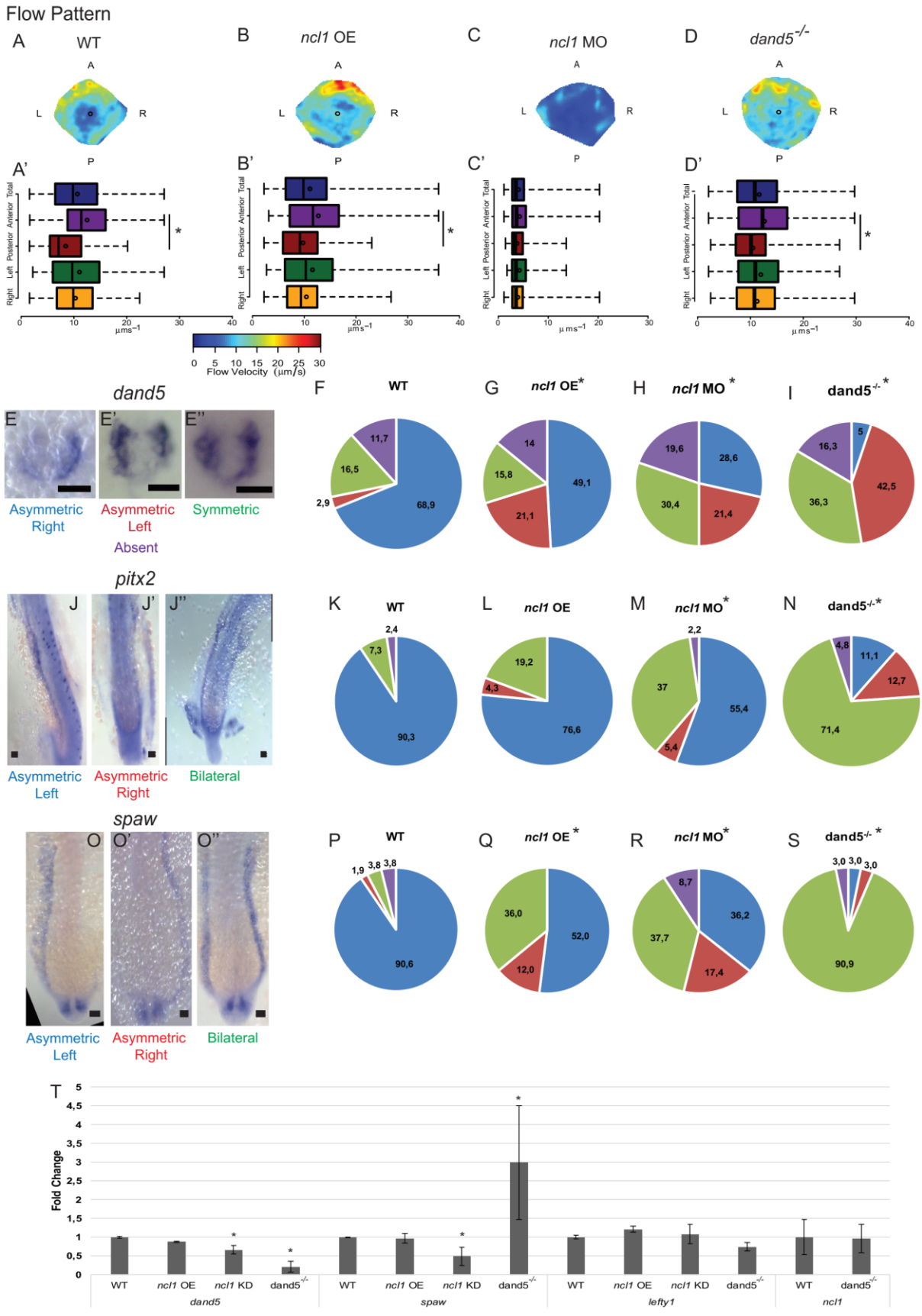
Flow Pattern
A WT
B ncl1 OE
C ncl1 MO
D dand5-/-
A' B' C' D'
Total Anterior Posterior Left Right
μms−1
Flow Velocity (μm/s)
dand5
E E' E''
Asymmetric Right
Asymmetric Left
Absent
Symmetric
F WT
G ncl1 OE*
H ncl1 MO*
I dand5-/-*
11,7 16,5 2,9 68,9
14 15,8 49,1 21,1
19,6 28,6 30,4 21,4
5 16,3 42,5 36,3
pitx2
J J' J''
Asymmetric Left
Asymmetric Right
Bilateral
K WT
L ncl1 OE
M ncl1 MO*
N dand5-/-*
2,4 7,3 90,3
19,2 4,3 76,6
2,2 37 55,4 5,4
4,8 11,1 12,7 71,4
spaw
O O' O''
Asymmetric Left
Asymmetric Right
Bilateral
P WT
Q ncl1 OE*
R ncl1 MO*
S dand5-/-*
1,9 3,8 3,8 90,6
36,0 52,0 12,0
8,7 36,2 37,7 17,4
3,0 3,0 3,0 90,9
T
Fold Change
WT ncl1 OE ncl1 KD dand5-/-
dand5
spaw
lefty1
ncl1

Figure 2* - Flow speed patterns and *dand5, pitx2* and *spaw* expression patterns when affecting *ncl1* and *dand5

(A-A', B-B', C-C' and D-D') Fluid flow heatmap and quantification of WT control embryos (n=9), *ncl1* OE (n=9), *ncl1* MO (n=4) and dand5$^{-/-}$ mutant embryos (n=8). Asterisks represent statistical significance (Wilcoxon Test, p-value<0.05). L left, R right, A anterior and P posterior. (E-E', J-J', O-O') Normal and altered expression patterns of *dand5*, *pitx2* and *spaw*, respectively. Scale bars in black correspond to 50μm. (F-I) Quantification of *dand5* expression pattern for WT (n=273), *ncl1* MO (n=56), *ncl1* OE (n=57) and dand5$^{-/-}$ (n=80) at 8-10 somite stage. (K-N) Quantification of *pitx2* expression pattern for WT (n=82), *ncl1* MO (n=92), *ncl1* OE (n=47) and dand5$^{-/-}$ (n=63) at 20 somite stage. (P-S) Quantification of *spaw* expression pattern for WT (n=53), *ncl1* MO (n=69), *ncl1* OE (n=50) and dand5$^{-/-}$ (n=66) at 20 somite stage. Asterisks represent statistical significance (Fisher test with Bonferroni correction for multiple comparisons, p-value<0.0125). Magenta in the graphs represent absent expression (T) qRT-PCR quantification for *dand5, spaw, lefty1* and *ncl1* in WT, *ncl1* OE, *ncl1* MO and dand5$^{-/-}$. Asterisks represent statistical significance (t-test, p-value<0.05).

dand5 asymmetry (either symmetric or asymmetric on the left; Figure 2G), knocking-down *ncl1* led to a randomization of pattern (*ncl1* MO not different from random; Figure 2H, Fisher test with Bonferroni correction, p-value>0.01). Also, *ncl1* MO affected the *dand5* expression level, as observed by qRT-PCR (Figure 2T, t-test p-value<0.05). Still, more interesting was that *dand5*$^{-/-}$ mutants had mainly *dand5* asymmetric on the left or symmetric, with embryos with asymmetric on the right only appearing in 5% of the cases. Also, we saw a strong downregulation of *dand5* levels by qRT-PCR (Figure 2T; t-test p-value<0.05). Interestingly, we did not observe any significant changes in the number of absent expression cases in all our manipulations.

We then investigated genes in the lateral plate mesoderm, the tissue that will later give rise to the heart and that will influence the endoderm derived organs such as the liver and pancreas through signalling pathways (Chung et al., 2008; Ober et al., 2006) and extracellular matrix deposition (Yin et al., 2010). *pitx2* and *spaw* are both typically expressed in the left lateral plate mesoderm in WT embryos. For *pitx2*, we found that knocking down *ncl1* led to 50% of laterality defects, most of the embryos presenting bilateral *pitx2* expression (*ncl1* MO different from control; Figure 2M, Fisher test with Bonferroni correction, p-value<0.0125). On the other hand, *dand5*$^{-/-}$ mutants had a great majority (over 70%) of bilateral *pitx2* expression (*dand5*$^{-/-}$ different from control; Figure 2N, Fisher test with Bonferroni correction, p-value<0.0125).

As for *spaw*, all three manipulations caused defects in its expression pattern. Overexpression of *ncl1* still had 50% of normal cases (Figure 2Q, Fisher test with Bonferroni correction, p-value<0.0125), while knocking down *ncl1* led a more severe phenotype, with more bilateral and more absent cases (Figure 2R, Fisher test with Bonferroni correction, p-value<0.0125). Interestingly, *spaw* was found downregulated by qRT-PCR when *ncl1* was knockdown (Figure 2T; t-test p-value<0.05), which might be either a direct effect of Ncl1 manipulation or downstream of the flow abnormalities. As Spaw indirectly influences its own transcription it may be interesting to explore if Spaw protein and activity is being affected by *ncl1* knockdown using a phospho-Smad antibody. Conversely, *dand5*$^{-/-}$ mutants presented a majority of bilateral *spaw* expression in the LPM (Figure 2S, Fisher test with Bonferroni correction, p-value<0.0125), as previously reported for the *dand5* knockdown (Hashimoto et al. 2004) and by qRT-PCR we showed a strong upregulation of *spaw* mRNA (Figure 2T; t-test p-value<0.05). In the same line as before, this data supports that more *spaw* is being transcribed in the absence of the Spaw inhibitor Dand5.

Finally, we checked by qRT-PCR the impact of these 3 treatments in *lefty1* expression and found no significant differences (Figure 2T; t-test p-value>0.05). We also checked if *ncl1* was differently expressed in *dand5*$^{-/-}$ mutants and found no significant differences either (Figure 2T; t-test p-value>0.05). In sum, manipulating *ncl1* had no impact on *lefty1* expression level and having no Dand5 protein had no impact on *lefty1* expression levels. It will be interesting in the future work to see if the *lefty1* expression patterns are affected despite the levels were not.

Nicalin1 knockdown causes organ *situs* defects in a dose-dependent manner and can be rescued by its overexpression

To test if the knockdown of *ncl1* has impact on organ *situs*, embryos were injected at one cell stage with increasing doses of morpholino against the 5'UTR of *ncl1* mRNA. Increasing doses of morpholino led to increasing organ *situs* defects, with a preponderance of heterotaxy (Figure 3A), without increasing mortality rate above 40%. *Situs inversus* did not increase substantially with decreasing amounts of *ncl1*. An important control for morpholino validation was a rescue experiment. We tried to rescue 0.26mM of *ncl1* morpholino with 1000pg of *ncl1* mRNA, but it proved to be too damaging, with

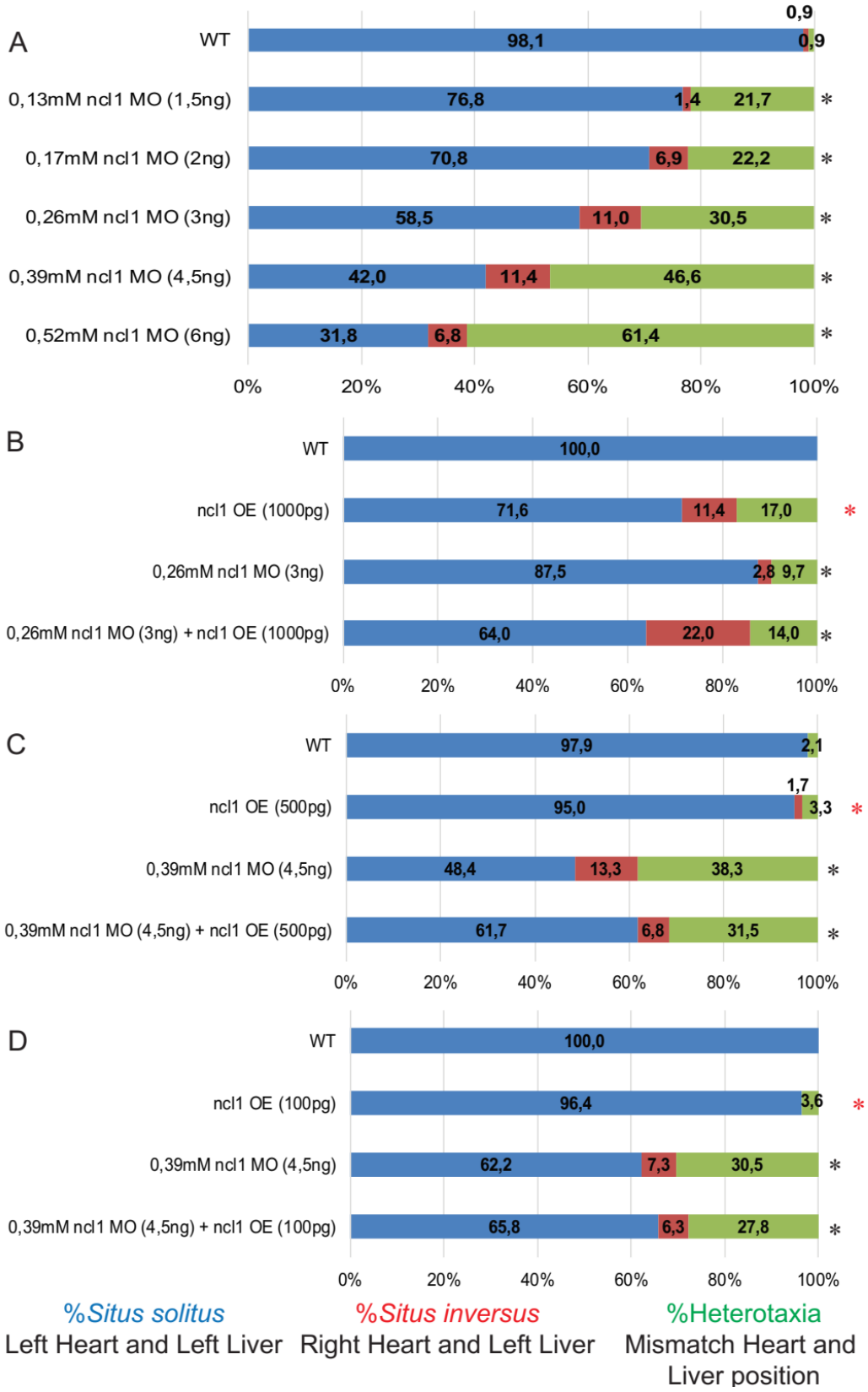
A
WT
0,13mM ncl1 MO (1,5ng)
0,17mM ncl1 MO (2ng)
0,26mM ncl1 MO (3ng)
0,39mM ncl1 MO (4,5ng)
0,52mM ncl1 MO (6ng)
98,1
0,9
76,8
1,4
21,7
70,8
6,9
22,2
58,5
11,0
30,5
42,0
11,4
46,6
31,8
6,8
61,4
0%
20%
40%
60%
80%
100%
B
WT
ncl1 OE (1000pg)
0,26mM ncl1 MO (3ng)
0,26mM ncl1 MO (3ng) + ncl1 OE (1000pg)
100,0
71,6
11,4
17,0
87,5
2,8
9,7
64,0
22,0
14,0
C
WT
ncl1 OE (500pg)
0,39mM ncl1 MO (4,5ng)
0,39mM ncl1 MO (4,5ng) + ncl1 OE (500pg)
97,9
2,1
1,7
95,0
3,3
48,4
13,3
38,3
61,7
6,8
31,5
D
WT
ncl1 OE (100pg)
0,39mM ncl1 MO (4,5ng)
0,39mM ncl1 MO (4,5ng) + ncl1 OE (100pg)
100,0
96,4
3,6
62,2
7,3
30,5
65,8
6,3
27,8
%Situs solitus
Left Heart and Left Liver
%Situs inversus
Right Heart and Left Liver
%Heterotaxia
Mismatch Heart and Liver position

***Figure 3 – ncl1* MO affects organ *situs* in a dose-dependent manner and can be partially rescued by *ncl1* mRNA**

(A) Organ *situs* for different doses of *ncl1* MO; WT control embryos (n=107), 0,13mM *ncl1* MO (1,5ng) (n=69), 0,17mM *ncl1* MO (2ng) (n=72), 0,26mM *ncl1* MO (3ng) (n=82), 0,39mM *ncl1* MO (4,5ng) (n=88), 0,52mM *ncl1* MO (6ng) (n=44). Asterisks represent statistical significance (Fisher test with Bonferroni correction for multiple comparisons, p-value<0.008). **(B-D)** Rescue experiments. (B) Rescue of 0,26mM *ncl1* MO (3ng) with 1000pg *ncl1* OE (n=50), *ncl1* MO (n=88), *ncl1* OE (n=72) and WT control embryos (n=48). (C) Rescue of 0,39mM *ncl1* MO (4.5ng) with 500pg *ncl1* OE (n=162), *ncl1* MO (n=128), *ncl1* OE (n=60) and WT control embryos (n=48). (D) Rescue of 0,39mM *ncl1* MO (4.5ng) with 100pg *ncl1* OE (n=79), *ncl1* MO (n=82), *ncl1* OE (n=83) and WT control embryos (n=51). Black asterisks represent statistical significance of WT vs the other treatments (Fisher test with Bonferroni correction for multiple comparisons, p-value<0.0125). Red asterisks represent statistical significance of rescue vs other treatments (Fisher test with Bonferroni correction for multiple comparisons, p-value<0.0167).

more organ *situs* defects than any of the conditions alone (Figure 3B). We thus decided to increase the concentration of morpholino to 0.39mM and decrease the amount of *ncl1* mRNA to half (500pg). This condition showed a mild rescue, with the cases of *situs solitus* increasing from 48% in the knockdown to 62% in the double injection (Figure 3C). We also tried to rescue 0.39mM of *ncl1* MO with 100pg of *ncl1* mRNA, but it proved to be insufficient to rescue (Figure 3D). This further confirmed that *ncl1* seems to work in a dose-dependent manner, typical of a nodal signalling player (Chen and Schier, 2001). With this rescue, we validated this morpholino and were able to proceed to the next set of experiments.

Overexpressing both *ncl1*/*nomo* and *dand5* in 1 cell-stage leads to embryo ventralization

Nicalin1 is described to work in a protein complex in the endoplasmic reticulum (ER) membrane with at least two other proteins: Nomo and TMEM174 (Figure 4A). TMEM147 has been identified as a potent negative regulator of M3R muscarinic acetylcholine receptor by interacting with it on the ER and impairing its trafficking towards the membrane (Rosemond et al., 2011). Ncl1 was also described as inhibiting Lefty secretion through its interaction with Nomo (Haffner et al., 2004, 2007). Although Ncl1 has been presented as the limiting reagent, only when both *ncl1* and *nomo* were overexpressed did the defects of mesendoderm patterning arise (Haffner et al., 2004). So, we further confirmed this by cloning and overexpressing different doses of *nomo* mRNA. Injecting *nomo* alone up to 1000pg did not

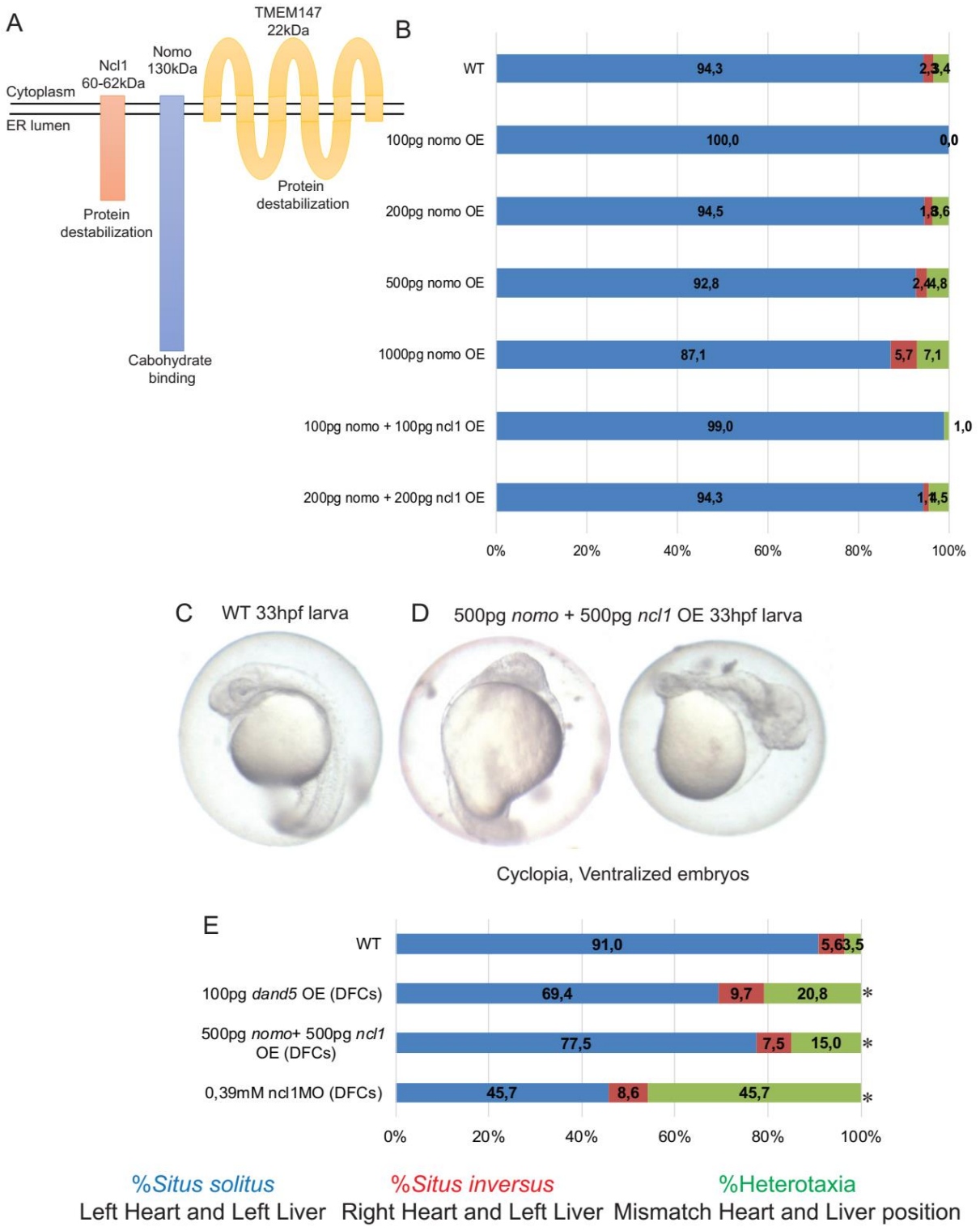

***Figure 4* – Overexpression of *ncl1* with its partner *nomo* leads to embryo ventralization**

(A) Schematics of Ncl1 complex with Nomo and TMEM147 in the endoplasmic reticulum membrane. **(B)** Impact on organ *situs* of overexpression of different doses of *nomo* mRNA, *nomo+ncl1* mRNA and *dand5* mRNA at 1-cell stage embryos. WT control embryos (n=176), 100pg *nomo* mRNA (n=51), 200pg *nomo* mRNA (n=55), 500pg

nomo mRNA (n=83), 1000pg *nomo* mRNA (n=70), 100pg *nomo*+100pg *ncl1* mRNA (n=97), 200pg *nomo*+200pg *ncl1* mRNA (n=88). **(C)** Normal WT larva with 33 hours post fertilization (hpf). **(D)** Ventralized larva upon injection of 500pg *nomo* + 500pg *ncl1* mRNA. **(E)** Organ *situs* of DFCs-targeted injection with *dand5* mRNA (n=72), *nomo*+*ncl1* mRNA (n=80) and *ncl1* MO (n=35) compared with WT control embryos (n=144). Asterisks represent statistical significance (Fisher test with Bonferroni correction for multiple comparisons, p-value<0.0125).

affect organ *situs* (Figure 4B). Co-overexpression of *nomo* and *ncl1* up to 200pg did not give any left-right defects either. Only when we tried to increase these amounts to 500 and 1000pg, we started to see defects in embryo dorsal-ventral patterning, with increasing amount of cyclopic and ventralized embryos (Figure 4D compared with Figure 4C). Injecting 100pg of *dand5* mRNA at 1-cell stage gave the same phenotypes as injecting *ncl1*+*nomo*. This result had already been described for both genes (Haffner et al., 2004; Hashimoto et al., 2004). Due to these severe defects, organ *situs* could not be properly determined.

To circumvent this situation, we injected *ncl1* and *nomo* mRNA, *dand5* mRNA and *ncl1* morpholino in 500-1000 cell stage WT embryos in order to target specifically the KV precursors, the dorsal forerunner cells (DFCs). By doing this, we manipulated the levels of these three genes only on the KV and not in the whole embryo, allowing to score for LR defects in normal looking embryos. As expected, overexpressing *dand5* and *ncl1*+*nomo* mRNAs in DFCs did not give rise to cyclopia or ventralized embryos, but still had an impact on left-right (Figure 4E). Between 20 and 30% of defects in organ *situs* were found in both treatments. On the other hand, injecting 0,39mM of *ncl1* morpholino in the same conditions gave rise to the same level of laterality defects as the injection of *ncl1* morpholino in the whole embryo at 1 cell stage. This strongly indicates that the role of *ncl1* in left-right is likely to be KV specific.

ncl1 cannot rescue dand5$^{-/-}$ mutant embryos and vice-versa

Since we have seen by qRT-PCR that in *dand5* homozygous mutants *ncl1* is not differentially expressed (Figure 2T), we decided to manipulate *ncl1* levels in both directions on these mutants. The rationale was to see if there was a crosstalk between these two inhibitors in left-right axis establishment and see if *ncl1* could somehow rescue *dand5* mutant defects in terms of organ *situs*.

dand5$^{-/-}$ mutants have very severe left-right organ *situs* defects, with almost 70% of embryos showing heterotaxy (Figure 5A). By overexpressing 100pg of dand5 mRNA specifically on DFCs, we could rescue the phenotypes, by reducing heterotaxy in ~20% and increasing both *situs solitus* and *situs inversus*. Since the mRNA we injected did not have the 3'UTR region, it might explain why we did not see a more substantial increase on *situs solitus* – mice data showed that, without the 3'UTR, mRNA should not be properly regulated (Nakamura et al., 2012). Knocking down *ncl1* on dand5$^{-/-}$ mutants made the organ *situs* defects even worse, increasing the heterotaxia from 70 to 90% (Figure 5A) and suggesting a synergistic epistasis. Since *ncl1* knockdown led to weaker flow (Figure 2C-C'), dand5 mutants without *ncl1* might accumulate flow problems that further impact on organ *situs* beside the loss of *dand5* asymmetric expression. Overexpressing *ncl1* and *nomo* on DFCs (500pg of each construct) cannot rescue any organ *situs* defects and higher amounts of *nomo* and *ncl1* mRNAs (750pg) led to increasing amounts of defects.

We also decided to try to do the inverse experiment, where we rescued *ncl1* knockdown with *dand5* overexpression (Figure 5A). Since *dand5* is downregulated when *ncl1* is knockdown, this might indicate that *dand5* is somehow downstream of *ncl1*. However, injection of *dand5* mRNA into DFCs of *ncl1* knockdown embryos did not showed any noticeable rescue. A potential explanation for this is the fact that our *dand5* mRNA does not have a 3'UTR to proper respond to flow (Nakamura et al., 2012). To further test this, it would be interesting to clone *dand5* with its 3'UTR. Still, due to the flow problems detected in the *ncl1* knockdown, having the 3'UTR alone might not be enough for proper rescue, since slow flow strongly impacts on *dand5* expression pattern (Sampaio et al., 2014).

ncl1$^{-/-}$ have stronger heart *situs* phenotype than ncl1 knockdown by morpholino

By using CRISPR technology, we produced a *ncl1* mutant fish line. The mutation was an insertion of 6 nucleotides, which changed the nature of one amino acid (from a Leucine into a Histidine) and inserted two new amino acids (both Methionine), leaving the rest of the protein intact. This mutation is situated in the signal sequence, an N-terminal extension which helps nascent or completed proteins from the cytosol to the membrane of the endoplasmic reticulum in eukaryotic cells, which is typically cleaved from the protein after membrane insertion (as reviewed in Martoglio and Dobberstein, 1998).

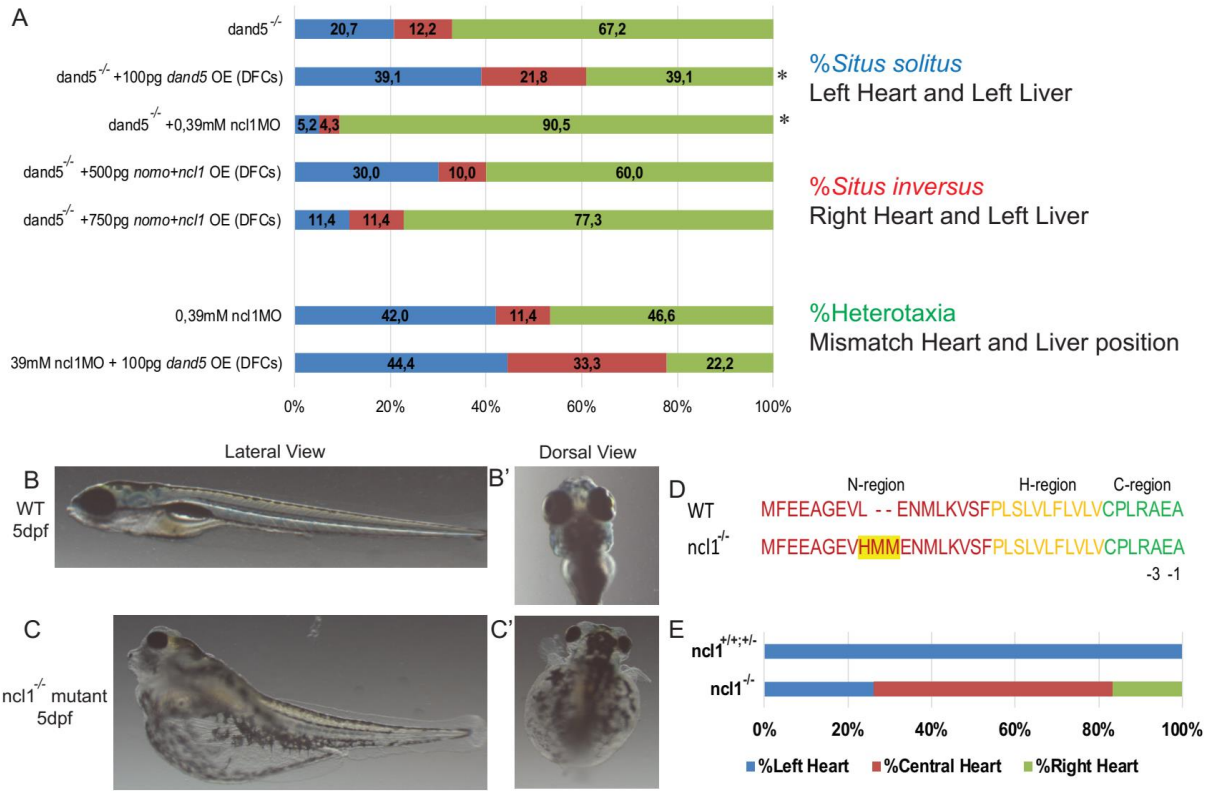

F

	Flow pattern	%Left Heart	%Central Heart	%Right Heart	spaw expression pattern	spaw expression level	
ncl1 OE	WT	88	6	6	50% Normal, 36% Bilateral	not altered	present work
ncl1 KD MO	weaker/homogeneous	60	28	11	37% Left, 37% Bilateral, 10% Absent	downregulated	
ncl1 -/-	?	26	57	17		?	
dand5 OE DFCs	?	76	16	8		?	present work
dand5 -/-	WT	20	57	23	Bilateral	upregulated	
dand5 KD MO	?	57	20	24	Bilateral	upregulated?	Hashimoto 2004/Wang and Yost 2008
spaw KD	?	52	30	18	Absent (80%), Left (20%)	downregulated?	Long et al 2003
spaw OE	?	34	33	33	Bilateral	upregulated?	
lefty1 KD	?	?	?	?	Bilateral	?	Wang and Yost 2008

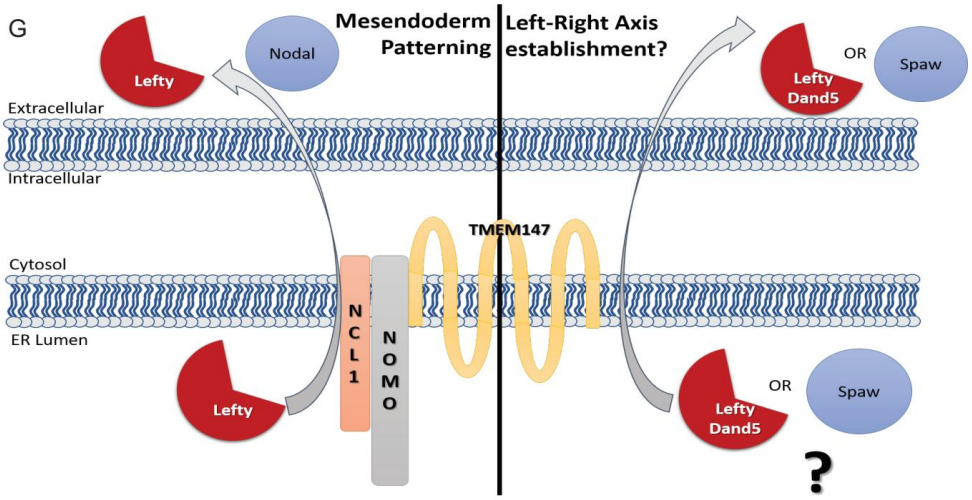

***Figure 5 – dand5 and ncl1/nomo* DFC injection prevent embryo ventralization, but only *dand5* OE is effective in rescuing *dand5*$^{-/-}$ mutant embryos**

(A) Organ *situs* of dand5$^{-/-}$ mutant embryos (n=329) or injected with 100pg *dand5* mRNA into DFCs (n=87), 0.36mM *ncl1* MO 1 cell-stage injection (n=116), 500pg *ncl1+nomo* mRNA DFCs injection (n=80) and 750 pg *ncl1+nomo* mRNA DFCs injection (n=44). Also, organ *situs* of 0.39mM *ncl1* MO (n=88) and morphants DFCs-injected with 100pg *dand5* mRNA (n=18). Asterisks represent statistical significance (Fisher test with Bonferroni correction for multiple comparisons, p-value<0.008) **(B-B')** WT and **(C-C')** ncl1-/- mutant larvae with 5 days post fertilization in (B,C) lateral view and (B',C') dorsal view. **(D)** Schematics of the signal peptide sequence of WT and ncl1$^{-/-}$ mutation (labelled at yellow). Red marks the N-region, yellow marks the H-region and green marks the C-region. -3 and -1 mark the last and third to last amino acids before the cleavage site **(E)** Heart situs of ncl1$^{+/+;+/-}$ (n=100) and ncl1$^{-/-}$ (n=84) embryos scored at 30 hours post fertilization. **(F)** Table summarizing flow defects, heart *situs*, *spaw* expression pattern and level from this work and other in several conditions from literature: *ncl1* overexpression, *ncl1* knockdown by morpholino, ncl1$^{-/-}$ mutant, *dand5* overexpression in the DFCs, dand5$^{-/-}$ mutant, *dand5* knockdown by morpholino, *spaw* knockdown by morpholino, *spaw* overexpression and *lefty1* knockdown. **(G)** Schematics of Ncl1 interaction with NOMO and TMEM147 in the ER membrane and how is impacting on Lefty secretion towards the extracellular space in mesendoderm patterning and might be influencing LR axis establishment by impacting on Nodal signalling inhibitors (Dand5 and Lefty) or agonists (Spaw or others).

Signal sequences have characteristic features like hydrophobic core region (H-region), a C-terminal side and a N-terminal side. The hydrophobic core comprises six to fifteen amino acid residues and is important for membrane insertion. The C-terminal side is a polar region that determine the site of signal peptide cleavage and the N-terminal is a polar region, typically with a net positive charge and is the most variable region (reviewed in Martoglio and Dobberstein, 1998). Analysis of the WT Ncl1 sequence with the SignalP 4.1 prediction website (http://www.cbs.dtu.dk/services/SignalP/) (Petersen et al., 2011) indicated the presence of a signal peptide that is cleaved between amino acid 35 and 36. It has an N-region with 17 amino acids, most of them hydrophobic and negatively charged, an h-region with 10 hydrophobic amino acids, and a C-region with 7 amino acids, having two Alanines in the -3 and -1 position which is typical of this region (Figure 5D). The mutated version inserted the two Methionines in the N-region, making it even more hydrophobic than what is typically found. According the website predictions, this mutation does not affect the cutting site of the signal peptide in the C-region.

The first observable phenotype in the mutants is the shape of the eyes, which are very different compared with the WT version. A much more striking phenotype can be observed in 5dpf larvae, with

very small eyes and strong oedema around the heart (Figure 5C and C' compared with B and B'). Having a phenotype in the eyes is concordant with the fact that *ncl1* is strongly expressed there (Haffner et al., 2004). Very preliminary data of heart scoring showed a majority of central hearts (>50%), supporting our data with the morpholino when using the highest concentration (Figure 5E). More experiments should be done to understand what is this mutation doing to the protein: it might be impacting the proper localization of Ncl1 in the cell.

DISCUSSION

This work allowed us to compare two inhibitors of LR axis establishment, Dand5, which was already known, and a new one not previously described as associated with LR – Nicalin1. According to the literature, Ncl1 works as a Nodal signalling antagonist due to the fact that helps secrete Lefty, the Nodal antagonist and impacting on mesendoderm patterning (Figure 5G) (Haffner et al., 2004). It is possible that, in LR, Ncl1 is doing something similar (Figure 5G). However, our *in situ* hybridizations showed that *lefty1* is not expressed strongly in the same domains than *ncl1*: while *lefty1* is strongly expressed in the midline but not in the KV region (Figure 1A-C'), *ncl1* is present in the KV and our DFCs injection point to the fact that Ncl1 impact in LR comes mainly from the KV (Figure 4E). Since *dand5* is strongly expressed in the KV cells (Figure 1H-I), Ncl1 could be helping secrete Dand5 instead of Lefty1 (Figure 5G). *dand5* absence does not affect flow pattern or strength (Figure 2D-D'), but strongly affects *pitx2* and *spaw* expression patterns, making the majority of embryos become bilateral for these LPM markers (Figure 2N and S). *ncl1* knockdown strikingly slows down the fluid flow (Figure 2C-C') and seems to randomize *dand5* and *spaw* expression patterns (Figure 2H and R). In terms of mRNA quantification, *dand5*$^{-/-}$ mutants show strong downregulation of *dand5* and strong upregulation of *spaw*, without significant differences detected for *lefty1* and *ncl1* (Figure 2T). This makes sense, since *dand5* is a strong antagonist of *spaw*, making it become asymmetric towards the left. Without *dand5*, *spaw* can activate on both sides of the LPM (Hashimoto et al., 2004; Wang and Yost, 2008) due to its ability to activate its own transcription and become strongly upregulated (Saijoh et al., 2000). Inversely, *ncl1* knockdown led to mild downregulation of *dand5* and, curiously, to a mild downregulation of *spaw* (Figure 2T). This highlights a difference between Ncl1 and Dand5: absence of

each protein affects *spaw* differently. If they were in the same pathway, i.e., if Ncl1 was responsible for Dand5 secretion, absence of Ncl1 should have the same impact as lack of Dand5. Therefore, it might have another role on other tissues and impact on *spaw* as well. It will be important to check how is *spaw* expression pattern and level in a *ncl1* DFCs-specific knockdown. Also, more experiments should be done on the *ncl1* mutant in terms of flow speed pattern and how *spaw* expression is affected in the mutant. Preliminary data in the mutant are pointing to stronger heart *situs* defects, similar to what is found in *dand5*$^{-/-}$ mutants. Checking the literature, the only situation that is similar to *ncl1* knockdown via morpholino injection in 1 cell stage is *spaw* knockdown: downregulation of spaw, with many absent cases, and mild heart problems, with a majority of left heart positioning (compare in Figure 5F ncl1 KD MO with spaw KD) (Long et al., 2003). So, another potential element that Ncl1 might be helping secrete is Nodal/Spaw itself (Figure 5G). In this case, Ncl1 would be working as an agonist in LR axis establishment while working as an antagonist in mesendoderm patterning.

An interesting result that we observed in the *dand5* mutants was the expression pattern and quantity of *dand5* itself. By qRT-PCR we saw that this gene was highly downregulated (Figure 2T) and the *in situ* hybridization took much longer to develop visible mRNA. The *dand5* mutant we analysed here has a four nucleotide deletion, leading to a premature stop codon at the nucleotide 166. This mRNA would be a good candidate for nonsense mediated mRNA decay, where mRNAs with premature stop codons 50-55 nucleotides upstream an exon-exon junction are degraded (Hwang et al., 2010 but further reviewed in Schoenberg and Maquat, 2012). Also, almost half of the cases were asymmetric left and not asymmetric right or symmetric (Figure 2I). This is a striking result and hard to explain since the flow was shown to be normal and normally *dand5* mRNA gets degraded where the flow is stronger (Sampaio et al., 2014). One possible explanation is that might be possible that the mutation somehow affects the 3'UTR and therefore affects its degradation downstream of flow (Nakamura et al., 2012), but more experiments should be done to address this question, like checking for 3'UTR integrity by PCR and sequencing in the mutants. Another interesting result was the fact that, in zebrafish, lack of Dand5 led to a great majority of bilateral *spaw* and heterotaxia, while in the mouse absence of Cerl2 led to randomization of *spaw* expression pattern and organ *situs* (Marques et al., 2004). This might be an indication that Dand5 has a stronger role in zebrafish than Cerl2 in the mouse. By injecting *dand5*

mRNA into DFCs of dand5$^{-/-}$ mutant embryos, we were able to partially rescue the organ *situs*, reducing heterotaxia into equally more *situs solitus* and *situs inversus* (Figure 4A). This might be happening because our *dand5* cloning did not contain the 3'UTR, which has been identified as important for flow mediated degradation on the left side *dand5* domain of mice's node (Nakamura et al., 2012). Therefore, even in the presence of normal flow, *dand5* mRNA may not respond to it and could be accumulating either more on the left or more on the right, producing more *situs solitus* or *situs inversus* correspondingly (Figure 4A). It will be interesting to re-clone this gene with the 3'UTR and see if there is any difference in these results. Interestingly, injection of *ncl1* MO into the *dand5* mutant background made almost all embryos become heterotaxic. This suggests a cumulative function of these two elements, since both treatments decrease the amount of *dand5* mRNA (Figure 2T). It might also be because of the weaker flow observed. It would be interesting to analyse the flow on these *dand5/ncl1* KD embryos. On the other hand, overexpressing *ncl1+nomo* into *dand5* mutant DFCs did not rescue the *dand5* mutant organ *situs* phenotype (Figure 5A). Actually, injecting 750pg also caused more defects, similar to *ncl1* KD although weaker. Doing the reverse experiment, injecting *dand5* into *ncl1* MO DFCs also did not rescue the *ncl1* morphant (Figure 4A). This would reinforce the idea that Ncl1 and Dand5 are not in the same pathway.

In sum, *dand5* is still currently the stronger nodal pathway inhibitor in the KV for LR axis establishment, with the mutant showing stronger heart *situs* phenotypes than the morphant (compare in Figure 4F the *dand5*$^{-/-}$ with *dand5* KD MO) (Hashimoto et al., 2004). Nicalin1 seems to occupy the second place, showing the same trend as Dand5: knockdown by morpholino seem to lead to milder heart *situs* phenotypes than *ncl1*$^{-/-}$ mutant (compare in Figure 5F ncl1 KD MO with ncl1$^{-/-}$). At the moment, it is unclear if it is acting in the trafficking of Dand5, Nodal/Spaw or other Nodal pathway components towards the outside of the cell, as it has been suggested for Lefty in mesendoderm patterning (Haffner et al., 2004). We are currently not considering Lefty1 since it is only strongly expressed in the midline (Bisgrove et al., 1999), or Lefty2 which is expressed in the left heart field and left habenula nucleus many hours later (Thisse and Thisse, 1999).

Acknowledgements

We would like to thank Dr Alex Schier for kindly giving the dand5$^{+/-}$ mutant line for these experiments.

REFERENCES

Bell, E., Munoz-Sanjuán, I., Altmann, C.R., Vonica, A., and Brivanlou, A.H. (2003). Cell fate specification and competence by Coco, a maternal BMP, TGFbeta and Wnt inhibitor. Development *130*, 1381–1389.

Belo, J.A., Bachiller, D., Agius, E., Kemp, C., Borges, A.C., Marques, C.L., Piccolo, S., and De Robertis, E.M. (2000). Cerberus-like is a secreted BMP and nodal antagonist not essential for mouse development. Genesis *26*, 265–270.

Bisgrove, B.W., Essner, J.J., and Yost, J.H. (1999). Regulation of midline development by antagonism of lefty and nodal signaling. Development *126*, 3253–3262.

Brennan, J., Norris, D.P., and Robertson, E.J. (2002). Nodal activity in the node governs left-right asymmetry. Genes Dev. *16*, 2339–2344.

Caron, A., Xu, X., and Lin, X. (2012). Wnt/beta-catenin signaling directly regulates Foxj1 expression and ciliogenesis in zebrafish Kupffer's vesicle. Development *139*, 514–524.

Chen, Y., and Schier, A.F. (2001). The zebrafish Nodal signal Squint functions as a morphogen. Nature *411*, 607.

Chung, W.-S., Shin, C.H., and Stainier, D.Y.R. (2008). Bmp2 signaling regulates the hepatic vs pancreatic fate decision. Dev Cell *49*, 1841–1850.

Collignon, J., Varlet, I., and Robertson, E.J. (1996). Relationship between asymmetric nodal expression and the direction of embryonic turning. Nat. Lett. *381*, 155–158.

Dettmer, U., Kuhn, P.H., Abou-Ajram, C., Lichtenthaler, S.F., Krüger, M., Kremmer, E., Haass, C., and Haffner, C. (2010). Transmembrane protein 147 (TMEM147) is a novel component of the Nicalin-NOMO protein complex. J. Biol. Chem. *285*, 26174–26181.

Haffner, C., Frauli, M., Topp, S., Irmler, M., Hofmann, K., Regula, J.T., Bally-Cuif, L., and Haass, C. (2004). Nicalin and its binding partner Nomo are novel Nodal signaling antagonists. EMBO J. *23*, 3041–3050.

Haffner, C., Dettmer, U., Weiler, T., and Haass, C. (2007). The nicastrin-like protein nicalin regulates assembly and stability of the Nicalin-Nodal modulator (NOMO) membrane protein complex. J. Biol. Chem. *282*, 10632–10638.

Hashimoto, H., Rebagliati, M., Ahmad, N., Muraoka, O., Kurokawa, T., Hibi, M., and Suzuki, T. (2004). The Cerberus/Dan-family protein Charon is a negative regulator of Nodal signaling during left-right patterning in zebrafish. Development *131*, 1741–1753.

Hojo, M., Takashima, S., Kobayashi, D., Sumeragi, A., Shimada, A., Tsukahara, T., Yokoi, H., Narita, T., Jindo, T., Kage, T., et al. (2007). Right-elevated expression of charon is regulated by fluid flow in medaka Kupffer's vesicle. Dev. Growth Differ. *49*, 395–405.

Hwang, J., Sato, H., Tang, Y., Matsuda, D., and Maquat, L.E. (2010). UPF1 Association with the Cap-Binding Protein, CBP80, Promotes Nonsense-Mediated mRNA Decay at Two Distinct Steps. Mol. Cell *39*, 396–409.

Inácio, J.M., Marques, S., Nakamura, T., Shinohara, K., Meno, C., Hamada, H., and Belo, J.A. (2013). The dynamic right-to-left translocation of Cerl2 is involved in the regulation and termination of Nodal activity in the mouse node. PLoS One *8*.

Kawasumi, A., Nakamura, T., Iwai, N., Yashiro, K., Saijoh, Y., Belo, J.A., Shiratori, H., and Hamada, H. (2011). Left-right asymmetry in the level of active Nodal protein produced in the node is translated into left-right asymmetry in the lateral plate of mouse embryos. Dev. Biol. *353*, 321–330.

Kimmel, C.B., Ballard, W.W., Kimmel, S.R., Ullmann, B., and Schilling, T.F. (1995). Stages of embryonic development of the zebrafish. Dev. Dyn. *203*, 253–310.

Lenhart, K.F., Lin, S.-Y., Titus, T.A., Postlethwait, J.H., and Burdine, R.D. (2011). Two additional midline barriers function with midline lefty1 expression to maintain asymmetric Nodal signaling during left-right axis specification in zebrafish. Development *138*, 4405–4410.

Levin, M., Johnson, R.L., Sterna, C.D., Kuehn, M., and Tabin, C. (1995). A molecular pathway determining left-right asymmetry in chick embryogenesis. Cell *82*, 803–814.

Long, S., Ahmad, N., and Rebagliati, M. (2003). The zebrafish nodal-related gene southpaw is required for visceral and diencephalic left-right asymmetry. Development *130*, 2303–2316.

Lowe, L.A., Supp, D.M., Sampath, K., Yokoyama, T., Wright, C.V.E., Potter, S.S., Overbeek, P., and Kuehn, M.R. (1996). Conserved left-right asymmetry of nodal expression and alterations in murine situs inversus. Lett. to Nat. *381*, 158–161.

Marques, S., Borges, A.C., Silva, A.C., Freitas, S., Cordenonsi, M., and Belo, J.A. (2004). The activity of the Nodal antagonist Cerl-2 in the mouse node is required for correct L/R body axis. Genes Dev. *18*, 2342–2347.

Martoglio, B., and Dobberstein, B. (1998). Signal sequences: More than just greasy peptides. Trends Cell Biol. *8*, 410–415.

Nakamura, T., Mine, N., Nakaguchi, E., Mochizuki, A., Yamamoto, M., Yashiro, K., Meno, C., and Hamada, H. (2006). Generation of Robust Left-Right Asymmetry in the Mouse Embryo Requires a Self-Enhancement and Lateral-Inhibition System. Dev. Cell *11*, 495–504.

Nakamura, T., Saito, D., Kawasumi, A., Shinohara, K., Asai, Y., Takaoka, K., Dong, F., Takamatsu, A., Belo, J.A., Mochizuki, A., et al. (2012). Fluid flow and interlinked feedback loops establish left-right asymmetric decay of Cerl2 mRNA. Nat. Commun. *3*, 1322.

Ober, E.A., Verkade, H., Field, H.A., and Stainier, D.Y.R. (2006). Mesodermal Wnt2b signalling positively regulates liver specification. Nature *442*, 688.

Pearce, J.J.H., Penny, G., and Rossant, J. (1999). A Mouse Cerberus / Dan-Related Gene Family. Dev. Biol. *110*, 98–110.

Petersen, T.N., Brunak, S., von Heijne, G., and Nielsen, H. (2011). SignalP 4.0: discriminating signal peptides from transmembrane regions. Nat. Methods *8*, 785.

Rosemond, E., Rossi, M., Mcmillin, S.M., Scarselli, M., and Donaldson, J.G. (2011). Regulation of M3 Muscarinic Receptor Expression and Function by Transmembrane Protein 147. Mol. Pharmacol. *79*, 251–261.

Saijoh, Y., Adachi, H., Mochida, K., Ohishi, S., Hirao, A., and Hamada, H. (1999). Distinct transcriptional regulatory mechanisms underlie left – right asymmetric expression of lefty-1 and lefty-2. Genes Dev. 259–269.

Saijoh, Y., Adachi, H., Sakuma, R., Yeo, C.Y., Yashiro, K., Watanabe, M., Hashiguchi, H., Mochida, K., Ohishi, S., Kawabata, M., et al. (2000). Left-right asymmetric expression of lefty2 and nodal is induced by a signaling pathway that includes the transcription factor FAST2. Mol. Cell *5*, 35–47.

Sampaio, P., Ferreira, R.R., Guerrero, A., Pintado, P., Tavares, B., Amaro, J., Smith, A.A., Montenegro-Johnson, T., Smith, D.J., and Lopes, S.S. (2014). Left-right organizer flow dynamics: how much cilia activity reliably yields laterality? Dev. Cell *29*, 716–728.

Schoenberg, D.R., and Maquat, L.E. (2012). Regulation of cytoplasmic mRNA decay. Nat. Rev. Genet. *13*.

Schweickert, A., Vick, P., Getwan, M., Weber, T., Schneider, I., Eberhardt, M., Beyer, T., Pachur, A., and Blum, M. (2010). The nodal inhibitor Coco is a critical target of leftward flow in Xenopus. Curr. Biol. *20*, 738–743.

Tavares, B., Jacinto, R., Sampaio, P., Pestana, S., Gardner, R., Lopes, T., Lopes, S.S., Schilling, B., Henry, I., and Sau, L. (2017). Notch / Her12 signalling modulates , motile / immotile cilia ratio downstream of Foxj1a in zebrafish left-right organizer. Elife *6:e25165*, 1–26.

Thisse, C., and Thisse, B. (1999). Antivin, a novel and divergent member of the TGFbeta superfamily, negatively regulates mesoderm induction. Development *126*, 229–240.

Wang, X., and Yost, H.J. (2008). Initiation and propagation of posterior to anterior (PA) waves in zebrafish left-right development. Dev. Dyn. *237*, 3640–3647.

Westerfield, M. (2000). The Zebrafish Book. A Guide for the Laboratory Use of Zebrafish (Danio rerio) (University of Oregon Press, Eugene).

Yin, C., Kikuchi, K., Poss, K.D., and Stainier, D.Y.R. (2010). Hand2 regulates extracellular matrix remodeling essential for gut-looping morphogenesis in zebrafish. Dev Cell *27*, 339–351.

CHAPTER 6

Usefulness of zebrafish larvae to evaluate drug-induced functional and morphological renal tubular alterations

"Yesterday is history, tomorrow is a mystery but today is a gift… That is why they call it present"

Bill Keane

Usefulness of zebrafish larvae to evaluate drug-induced functional and morphological renal tubular alterations

Rita Gorgulho M.Sc (1)*, Raquel Jacinto M.Sc (1)*, Susana S. Lopes PhD (1), Sofia A. Pereira PhD (1), Erin M. Tranfield PhD (2), Gabriel G. Martins PhD (2,3), Emilio J. Gualda PhD, (2), Rico J.E. Derks PhD (4), Ana C. Correia B.Sc (2), Evelyne Steenvoorden B.Sc (4), Petra Pintado PhD (1), Oleg A. Mayboroda PhD (4), Emilia C. Monteiro PhD (1) and Judit Morello PhD (1)
* These authors contributed equally to the study

(1) Chronic Diseases Research Center, NOVA Medical School, Rua Câmara Pestana 6, 1150-082 Lisbon, Portugal; (2) Unit of Imaging and Cytometry, Gulbenkian Institute of Science, Lisbon, Portugal Rua Quinta Grande 6, 2780-156 Lisbon, Portugal; (3) Centre for Ecology, Evolution and Environmental Changes, Faculty of Sciences, Campo Grande 1749-016, Lisbon, Portugal; (4) Center for Proteomics and Metabolomics, Leiden University Medical Centre, Albinusdreef 2, 2333 ZA, Leiden, The Netherlands;

Abstract

Prediction and management of drug-induced renal injury (DIRI) rely on the knowledge of the mechanisms of drug insult and on the availability of appropriate animal models to explore it. Zebrafish (*Danio rerio*) offers unique advantages for assessing DIRI because the larval pronephric kidney has a high homology with its human counterpart and it is fully mature at 3.5 days post-fertilization. Herein, we aimed to evaluate the usefulness of zebrafish larvae as a model of renal tubular toxicity through a comprehensive analysis of the renal alterations induced by the lethal concentrations for 10% of the larvae for gentamicin, paracetamol and tenofovir. We evaluated drug metabolic profile by mass spectrometry, renal function with the inulin clearance assay, the 3D morphology of the proximal convoluted tubule by 2 photon microscopy and the ultrastructure of proximal convoluted tubule mitochondria by transmission electron microscopy. Paracetamol was metabolized by conjugation and oxidation with further detoxification with glutathione. Renal clearance was reduced with gentamicin and paracetamol. Proximal tubules were enlarged with paracetamol and tenofovir. All drugs induced mitochondrial alterations including dismorphic shapes (“donuts”, “pancakes” and “rods”), mitochondrial swelling, cristae disruption and/or loss of matrix granules. These results are in agreement with the tubular effects of gentamicin, paracetamol and tenofovir in man and demonstrate that zebrafish larvae might be a good model to assess functional and structural damage associated with DIRI.

Keywords: nephrotoxicity, proximal tubule, mitochondria, renal clearance, zebrafish

Introduction

The kidney is a vulnerable organ to xenobiotic toxicity due to its rich blood supply and its important role in drug metabolism and excretion. Proximal tubular cells are the primary sensor of either ischemic or oxidative renal injury as a consequence of their high metabolic rate and strong dependence on oxidative phosphorylation. Thus, it is consensual that mitochondrial damage plays a key pathogenic role in drug-induced renal injury, (Basile et al. 2012; Chevalier 2016) which is partially explained by this dependence.

Animal experiments remain essential for understanding the mechanisms of drug toxicity and testing the safety of new compounds. However, rodent species, the most widely used animal model, predict only 41% of human toxicities (Olson et al. 2000) and are not useful for high throughput screenings. Thus, it is urgent to find better predictive animal models that capture all the complexities of human physiology while enabling for testing large libraries of compounds. Zebrafish larvae up to 5 days of development have unique features that make them potentially excellent models in toxicology: transparency, rapid development, small size that allows them to fit in 96 well-plates, easy and fast drug administration in small amounts, no need for feeding, transgenic capabilities and high homology with mammals in terms of genetics, metabolism and physiology (McGrath and Li 2008; Peterson and MacRae 2012). Regarding the zebrafish kidney, the larval pronephros is fully mature at 4 days post-fertilization (dpf) and consists of two nephrons with the glomeruli fused at the embryo midline. Although simple in form, the glomerulus is composed of cell types that are typical of higher vertebrate kidneys, including fenestrated capillary endothelial cells and podocytes; the tubules are composed of polarized epithelial cells that exhibit primary cilia and possess a segmental organization where each segment is specialized for the secretion and reabsorption of particular molecules in a similar fashion as mammal nephron tubules (Kramer-Zucker et al. 2005; Wingert et al. 2007; Drummond and Davidson 2010). These features make zebrafish a potential model for nephrotoxicity assessment. Indeed, paracetamol and gentamicin, two drugs associated with renal tubular damage in man, (Mazer and Perrone 2008; Lopez-Novoa et al. 2011) have been proved to cause morphological and/or functional alterations in the

zebrafish pronephros (Hentschel et al. 2005; Peng et al. 2010; Rider et al. 2012; Cianciolo Cosentino et al. 2013; Westhoff et al. 2013).

Herein, we aimed to evaluate the usefulness of zebrafish larvae as a model of tubular toxicity through a comprehensive analysis of the functional and morphological tubular alterations induced by three drugs known to cause tubulopathy in man: gentamicin, paracetamol and tenofovir in the form of tenofovir (TFV) and its prodrug tenofovir disoproxil fumarate (TDF) (Mazer and Perrone 2008; Smith et al. 2009; Lopez-Novoa et al. 2011).

Material and Methods

Zebrafish larvae

The transgenic and mutant zebrafish line Tg(wt1b:EGFP,cdh17:EGFP);mitfa$^{-/-}$;roy$^{-/+ \text{ or } +/+}$ was chosen for this study due to the expression of GFP at the renal tubules and transparency of the *nacre* mutant throughout the embryonic and larvae stages. Adult zebrafish were grown and mated at the Fish Facility of Gulbenkian Institute of Science, Lisbon, Portugal. Embryos were grown at 28 °C in embryo media of standard E3 solution (NaCl 5mM, KCl 0.17 mM, $CaCl_2$ 0.33 mM, $MgSO_4$ 0.33 mM) plus HEPES buffer 10 mM till 4 dpf, time when zebrafish pronephros is completely mature (Kramer-Zucker et al. 2005).

Drug exposure

Gentamicin and paracetamol were purchased from Sigma-Aldrich. Tenofovir was administered in two forms: a) the prodrug TDF, b) TFV (Sequoia Research Products, UK). Stock solutions were prepared for all drugs at solubility concentrations: gentamicin 5000 µg/mL, paracetamol 12000 µg/mL, TDF 6000 µg/mL and TFV 5000 µg/mL. All drugs except TFV were dissolved in sterile distilled water. TFV was prepared in embryo media. All stock solutions were aliquoted and stored at -20 ºC till further use.

Zebrafish larvae of 4 dpf were transferred to 96-well plates, 2 larvae per well. Embryo media was completely removed from each well and immediately after that, a specific volume of embryo media plus a specific volume of drug stock solution or drug vehicle (negative controls)

were added into each well to achieve the desired drug concentration (total volume per well = 350 µL). Zebrafish larvae were incubated for 24 hours at 28 ºC.

Lethality curves

Lethality curves were defined with five or six different concentrations for each drug. Drug concentrations were empirically chosen to cover all lethality percentages: gentamicin 200, 600, 1000, 1400, 1800, 2200 µg/mL; paracetamol 2000, 2500, 3000, 3500, 4000, 4500 µg/mL; TDF 1000, 1500, 2000, 2500, 3000 µg/mL; TFV 2500, 3000, 3500, 4000, 4500, 5000 µg/mL. 10 larvae of 4 dpf were tested per each concentration in triplicate or quadruplicate. After drug exposure, all larvae were observed under a stereoscope (Nikon SMZ 745) to evaluate body curvature, tail-flip response, swimming pattern, heart oedema, heartbeat and necrosis. Lethality was defined as the absence of heartbeat and/or the presence of body necrosis. Percentages of lethality were calculated and plotted against the logarithm of drug concentration in µM. Lethal concentrations for 10% of the larvae (LC10) and curve slopes were manually obtained after probit transformation (Randhawa 2009). LC10 concentrations were used for the rest of the experiments.

Mass Spectrometry for drug and metabolite identification

Pools of 50 zebrafish larvae of 4 dpf were exposed to the LC10 of paracetamol (n=10), gentamicin (n=10), TDF (n=10), TFV (n=5) or water (n=6). After drug exposure, dead larvae were discarded and 40 larvae were transferred from each well to a clean eppendorf. Larvae were immediately washed 4 times with cold water to remove drugs and/or drug metabolites from the embryo media. After that, larvae were euthanized by rapid chilling to remove all remaining embryo media before snap freezing in liquid nitrogen to quench any enzymatic activity.

Metabolite extraction was performed with methanol:water 2:1 (Huang et al. 2013). The extracted supernatant was dried under vacuum and reconstituted in half volume of water for further injection into the RPLC-Q-TOF (UPLC Ultimate 3000 RS tandem LC system, Dionex, Amsterdam, The Netherlands; ESI-UHR-QqToF impact HD, Bruker Daltonics, Bremen,

Germany). The details of the RPLC-Q-TOF method have already been reported (Nevedomskaya et al. 2011; Pacchiarotta et al. 2012).

Drugs and metabolites were identified by extracting the chromatograms of the expected *m/z* of the protonated drugs and/or metabolites of gentamicin (Clarot et al. 2004) paracetamol (Pacchiarotta et al. 2012) or TDF (Kurmi et al. 2016). To confirm those identifications, rational chemical formulas were generated based on the internally calibrated monoisotopic masses within 5 mDa mass error using the SmartFormula tool (version 4.2, build 395, Bruker Daltonics). Two parameters were registered for each ion-drug or metabolite assignment: mass error and mSigma. Only those *m/z* with an intensity > 10,000 units in at least half of the samples were registered. MZmine version 2.3 was used to build the chromatograms for each drug and metabolite (Pluskal et al. 2010).

Assessment of renal function

Renal function was assessed with a modified clearance assay from Rider *et al* (Rider et al. 2012). The casper zebrafish line (mitfa$^{-/-}$;roy$^{-/-}$) was used for these experiments due to its transparency and absence of fluorescence. After LC10 exposure, live larvae were anesthetized with tricaine and injected with 1.4 nL of fluoerescein isothiocyanate (FITC)-inulin 2.5% w/v in the duct of cuvier. FITC intensity was imaged over the caudal region 10-15 minutes (baseline) and 2 hours after injection (Zeiss Lumar V12). FITC intensity was quantified using the image-J software (Schindelin et al. 2015) selecting the area on the caudal artery between somites 16 and 18. Clearance of inulin was calculated as the percentage of decrease of FITC intensity on the caudal artery using the formula (FITC intensity at baseline - FITC intensity at 2 hours)*100 / FITC intensity at baseline. A minimum of 15 larvae were injected per group.

Two photon microscopy for evaluation of tubular morhology

After LC10 exposure, Tg(wt1b:EGFP,cdh17:EGFP);mitfa$^{-/-}$;roy$^{-/+ \text{ or } +/+}$ zebrafish larvae were fixed overnight with PFA 4% and washed with PBS 1X. Due to the central localization of the pronephros, zebrafish larvae were further processed for imaging by removing the head, yolk and gut with a sharp needle and bistoury. This procedure was easily performed under a fluorescent stereoscope because our transgenic zebrafish expressed GFP in the pronephros

and the gut. In a petri dish with a base of 2% agarose, the remaining tissue was mounted in a drop of low melting agarose 1% and oriented with the ventral side up. The petri dish was filled with PBS 1X. Embryos were then imaged on a Praire Multi-Photon microscope equipped with an Olympus 20x XLUMPLAN FL N (NA 1) water immersion lens and laser tuned to 890 nm. Stacks were obtained with 0.7 µm sectioning and further pre-processed with the FIJI software (Schindelin et al. 2012). 4 or 5 larvae were imaged for each condition. 3D reconstructions of the proximal convoluted tubule were performed using the Amira software (version 5.3.3). For the lumen caliber measurement, two orthogonal diameters were measured in transverse planes of the lumen at regular intervals along all the reconstructed proximal convoluted tubule (PCT). Both diameters were divided by two to obtain the radius and the formula π*radius1*radius2 was applied to calculate the transverse section area of the lumen. An average of 15 measurements was done per larvae across one PCT.

Transmission Electron Microscopy for evaluation of tubular mitochondria

After LC10 exposure, Tg(wt1b:EGFP,cdh17:EGFP);mitfa$^{-/-}$;roy$^{-/+ \text{ or } +/+}$ zebrafish larvae were euthanized by rapid chilling. Larvae were fixed following a modified protocol from Schieber *et al* (Schieber et al. 2010). In brief, larvae were fixed overnight with 2.5% glutaraldehyde and 2% PFA in 0.1M PHEM buffer. In a Pelco BioWave Microwave Processor (Ted Pella, Redding USA) larvae were post-fixed in 1% osmium tetroxide (EMS, Hatfield, PA, USA) in 0.1M PHEM Buffer on ice, and en-block stained with 1% aqueous uranyl acetate (EMS, Hatfield, PA, USA) before being dehydrated in a graduated ethanol series and embedded in EPON resin (EMS, Hatfield, PA, USA. Larvae were left in 100% EPON resin overnight before orientation, embedding and resin polymerization in a 60 ^{o}C oven. All larvae were processed simultaneously except gentamicin treated larvae.

Transverse portions of the proximal convoluted tubule were serial sectioned at 70 nm (for micrographs), 100 nm (for serial section TEM (ssTEM)) or 120 nm (for tomography) with a diamond knife (Diatome, Biel Switzerland) on a Reichert Ultracut S (Leica, Vienna, Austria). 10 nm Protein A Gold was added (UMC, Utrecht, The Netherlands) to the grids for tomography analysis. All grids were post-stained with uranyl acetate and lead citrate.

Data was collected on a Hitachi H-7650 Transmission Electron Microscope (Tokyo, Japan) at 100 kV using 3 approaches: (1) micrographs at a magnification of 1k, 3k, and 10k (a minimum of 50 tubular cells were screened from 10-20 micrographs per condition); (2) ssTEM to build coarse cellular 3D models with 24 or 36 micrographs covering an area of ~10 x 11 x 2.4µm or 3.6µm; (3) tomograms to build 3D mitochondrial models for an area of 3.8 x 4.4 x 0.36 µm and with an angle range from -55^{o} to 55^{o}, with a 1^{o} tilt increment. Data was aligned and modeled with the IMOD software (Kremer J.R. 1996; Mastronarde 1997). Due to the complexity of the 3D modelling, only one cellular model and one mitochondrial model were built for each condition. However, those models were carefully chosen to be the best in describing the changes observed from each condition (supplementary videos).

Mitochondrial swelling was assessed by measuring mitochondria grey intensities from 14 to 24 mitochondria from a total of 3 micrographs using the FIJI software. Mitochondrial granules were counted from 11 to 18 mitochondria from a total of 3 micrographs using the FIJI software. The volumes of the mitochondria, cristae and granules were measured with the IMOD software and expressed as percentage of the cellular or mitochondrial volume captured by the 3D model. All analyses were performed at the same time for the five different conditions of the study

Statistical analysis

Statistical analyses were performed with SPSS (IBM SPSS Statistics for Windows, version 22.0. Armonk, NY: IBM Corp). Differences in quantitative variables among treatment groups were analyzed with one-way ANOVA test followed by Games-Howell post-hoc test. All parameters were expressed as means and standard deviation. *P* values < 0.05 were considered statistically significant.

Results

Lethality curves

After 24 hours of exposure to each drug concentration, zebrafish larvae were observed under a stereoscope for macroscopic alterations. Swimming behaviour was reduced and the escape response to tail stimuli was retarded or absent in living larvae exposed to any drug

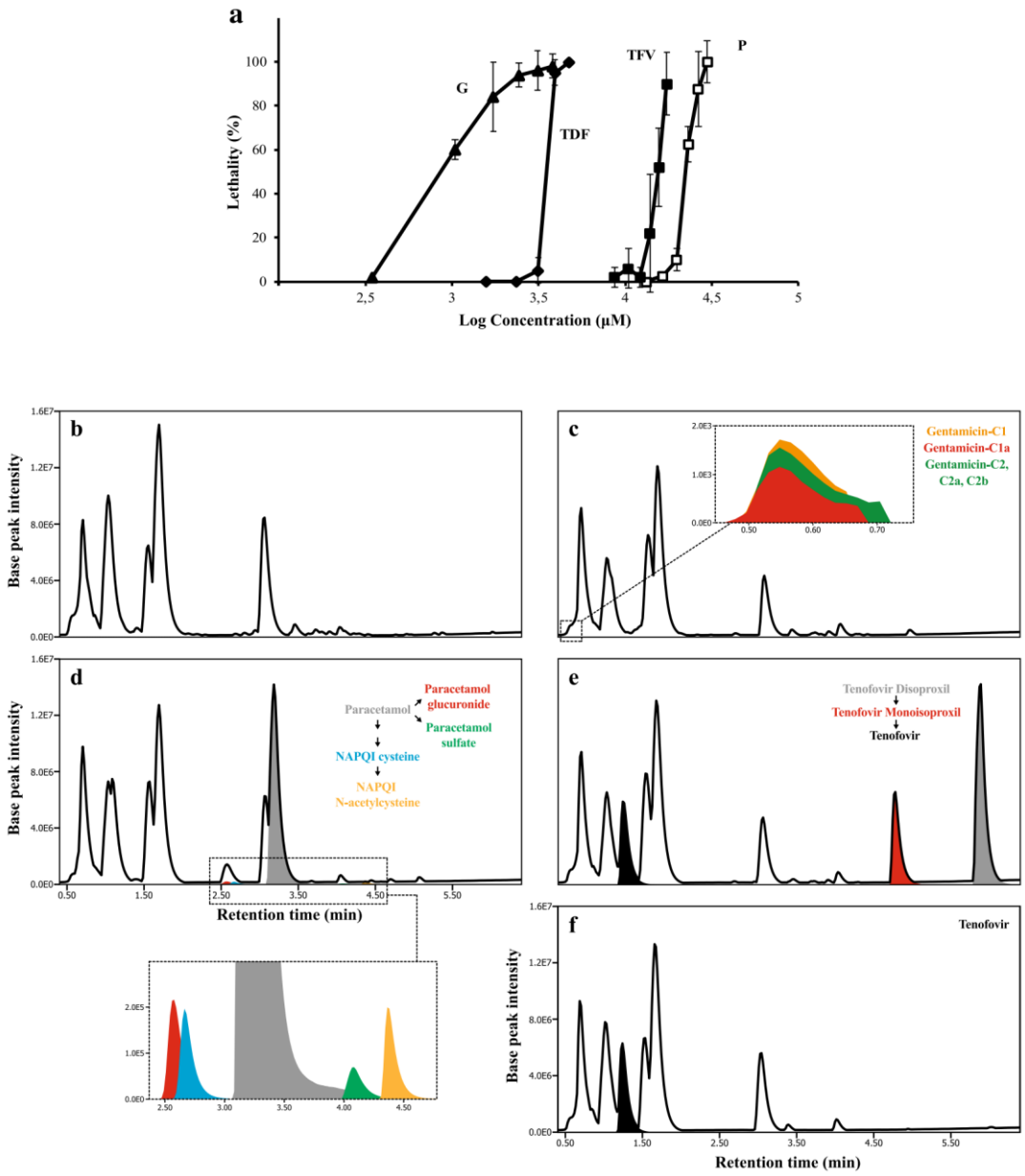

Fig. 1 Zebrafish exposure to LC10
(a) Lethality curves that were obtained to calculate the LC10 of gentamicin (G), tenofovir disoproxil fumarate (TDF), tenofovir (TFV) and paracetamol (P) **(b)** Chromatogram of untreated zebrafish larvae **(c)** Chromatogram of zebrafish exposed to gentamicin; a zoom of the chromatogram shows the extracted ion chromatograms (EICs) for [gentamicin 1 + H]$^+$ (*m/z* 478.3231), [gentamicin C2 C2a and C2b + H]$^+$ (*m/z* 464.3076) and [gentamicin C1a + H]$^+$ (*m/z* 450.2920) **(d)** Chromatogram of zebrafish exposed to paracetamol showing the EIC of [paracetamol + H]$^+$ (*m/z* 152.0706), [paracetamol glucuronide + H]$^+$ (*m/z* 328.1029), [paracetamol sulfate + H]$^+$ (*m/z* 232.0275), [paracetamol cysteine + H]$^+$ (m/z 271.0748) and [paracetamol N-acetylcysteine + H]$^+$ (*m/z* 313.0858); a zoom of the chromatogram shows in more detail the four paracetamol metabolites **(e)** Chromatogram of zebrafish exposed to TDF showing the EIC of [tenofovir disoproxil + H]$^+$ (*m/z* 520.1808), [tenofovir monoisoproxil + H]$^+$ (*m/z* 404.1336) and [tenofovir + H]$^+$ (*m/z* 288.0857) **(f)** Chromatogram of zebrafish exposed to TFV showing the EIC of [tenofovir + H]$^+$ (*m/z* 288.0859).

concentration when compared with control larvae. Albeit rarely, some larvae exposed to the second-fourth drug concentrations (in ascendant order) experienced upwards body curvature and/or heart oedema with visible heart haemorrhage. Dead larvae presented i) no heartbeat with no necrosis at the lowest lethal concentrations or ii) necrosis and body decomposition at the highest lethal concentrations (data not shown).

The percentages of lethality were calculated for each drug concentration and plotted against the logarithm of the drug concentration (Fig. 1a). Regarding the left-right position of the curves, the order of the drugs was gentamicin, TDF, TFV and paracetamol. LC10 (µM) calculated from the lethality curves after probit transformation were: 491 for gentamicin, 2338 for TDF, 11542 for TFV, and 17179 for paracetamol. All drugs exhibited sigmoidal lethality curves but with different slopes. Paracetamol, TDF and TFV curves were steeper than gentamicin curve as reflected by the values of the slopes (% of lethality/µM): 12 for paracetamol, 10 for TDF, 9 for TFV and 4 for gentamicin.

Identification of drugs and metabolites in zebrafish larvae

To test if drugs were absorbed and followed similar biotransformation patters as in man, extracts of whole zebrafish larvae exposed to the LC10 of each drug were analyzed by mass spectrometry.

Chromatograms of zebrafish exposed to paracetamol showed all known paracetamol metabolites found in man. We detected phase II metabolites derived from conjugation with glucuronic acid and sulfonic acid and paracetamol metabolites derived from the unstable and toxic phase I metabolite N-acetyl-p-benzoquinone imine (NAPQI) after conjugation with glutathione (Fig. 1d).

Chromatograms of zebrafish exposed to TFV showed only the peak corresponding to TFV (Fig. 1f). No traces were found for the intracellular phosphorylated metabolites of tenofovir. Regarding the prodrug of TFV, the chromatograms of zebrafish larvae exposed to TDF included the diester tenofovir disoproxil, the monoester tenofovir monoisoproxil and its non esterified metabolite TFV (Fig. 1e). The retention time and mass spectrum of TFV were similar to the ones described for zebrafish exposed to TFV (Fig. 1f, Supplementary Tables 2 and 3).

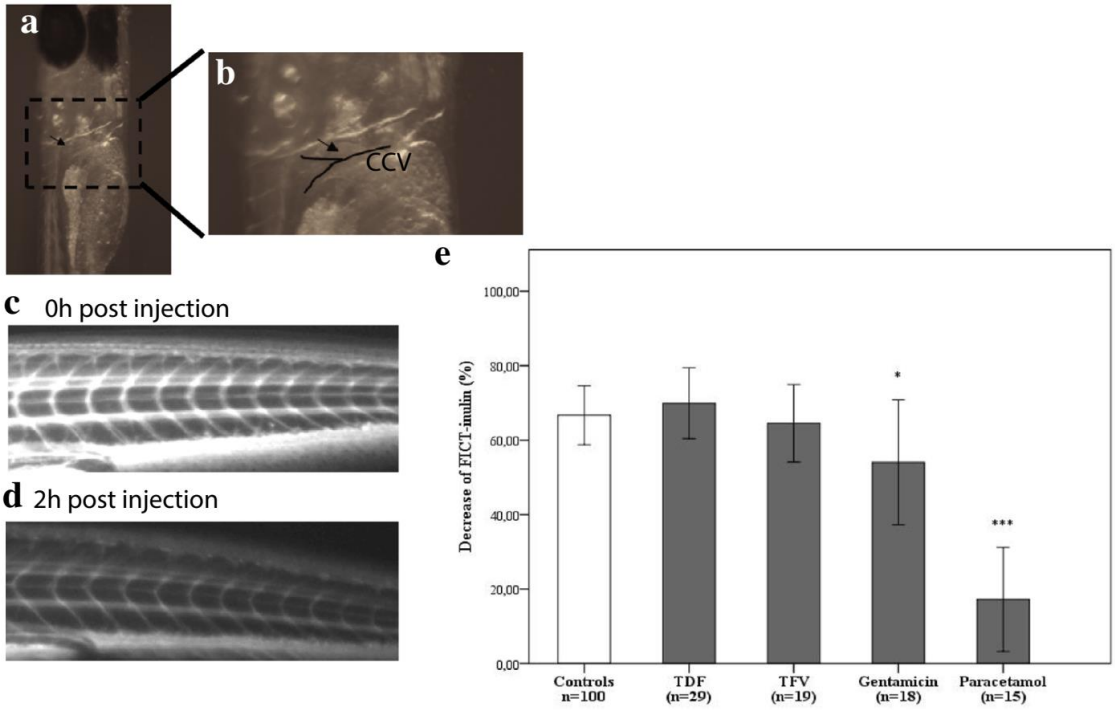

Fig. 2 Renal clearance is decreased in zebrafish larvae exposed to the LC10 of gentamicin and paracetamol
(a, b) Detail of the common cardinal vein (CCV) where inulin-FITC was injected to evaluate the renal clearance **(c, d)** Lateral posterior view of the FITC-intensity in blood 10-15 minutes **(c)** and 2 hours **(d)** after FICT-inulin injection **(e)** Clearance of inulin, expressed as the percentage of decrease of FITC-intensity in blood 2 hours after FICT-inulin injection, is decreased with gentamicin and paracetamol.
* for p-value < 0.05; *** for p-value < 0.001

In-source fragmentation occurred for paracetamol, TFV, TDF and their respective metabolites, which confirmed their identifications (Supplementary Tables 1-3).

Finally, zebrafish larvae exposed to gentamicin sulfate produced chromatograms that were unexpectedly identical to the chromatograms of untreated larvae (Fig. 1, b and c). The *m/z* of the five major components of gentamicin (C1, C1a, C2, C2a and C2b gentamicin) were found in the spectra from zebrafish larvae exposed to gentamicin but the intensities were < 2,000 units in all samples (Fig. 1c). In-source fragmentation (to *m/z* 322.1963 and 160.0966) was detected but with intensities between 2,000 and 10,000 units.

Renal function

Renal function was evaluated with the inulin clearance assay after exposure to the LC10 of each drug. Two hours after FITC-inulin injection, FITC intensity decreased by 67 ± 8% in untreated larvae (n=100) due to glomerular filtration of most of the FITC-inulin present in the blood (Fig. 2e). Larvae exposed to gentamicin (n=18) or paracetamol (n=15) had significantly

lower clearances with 54 ± 17% and 17 ± 14% of decrease of FITC intensity, respectively. TDF (n=29) or TFV (n=19) treatments did not affect inulin clearance (69 ± 9% and 64 ± 10%, respectively).

Microscopic alterations

General tubular morphology, epithelium organization and luminal area of the proximal convoluted tubule (PCT) were carefully compared between controls and treated larvae using 3D reconstructions.

Untreated zebrafish larvae showed PCT as coiled and intricate structures with a typical curvature. At the exit of the glomeruli, each of the PCT came dorsally and distally before curving ventrally and to the middle. Then, it continued posteriorly with several undulations or convolutions until the proximal straight tubule (PST) (Fig. 3). The two tubules were symmetric and diverged from each other at the exit of the glomerulus and then were brought closer from the beginning of the PST (Fig. 3). The fluorescent transgenic line cdh17:EGFP and wt1b:EGFP revealed a single layer of tightly packed epithelial cells surrounding the lumen of each tubule. Apical membranes were enriched with cadherin 17 (here seen by fusion with EGFP) and showed cells with a regular shape. The fluorescence from wt1b:EGFP reporter showed big nuclei, usually in the basal portion of the cell (Fig. 3a'' and a'''). The lumen caliber of the PCT had a mean area of 57 ± 43 μm^2, with some variations throughout the length of the PCT (Fig. 3f).

In general, there were no apparent differences regarding the curvature of the tubules between treated and untreated larvae, except for the terminal section of the PCT, which presented a simplified structure with less curves upon drug exposure (Fig. 3a', b', c', d' and e'). Tubular enlargements were observed with all drugs except gentamicin (53 ± 29 μm^2, Fig. 3f). Paracetamol showed irregular lumens and the most severe dilations with an average area of 136 ± 92 μm^2 (white asterisks in Fig. 3f, e'' and e''') followed by TFV with 114 ± 73 μm^2 (Fig. 3d'' and d'''). TDF treated larvae showed milder defects with more regular lumens. The lumen was also dilated compared to controls but the increase was not statistically significant (81 ± 71 μm^2, Fig. 3f).

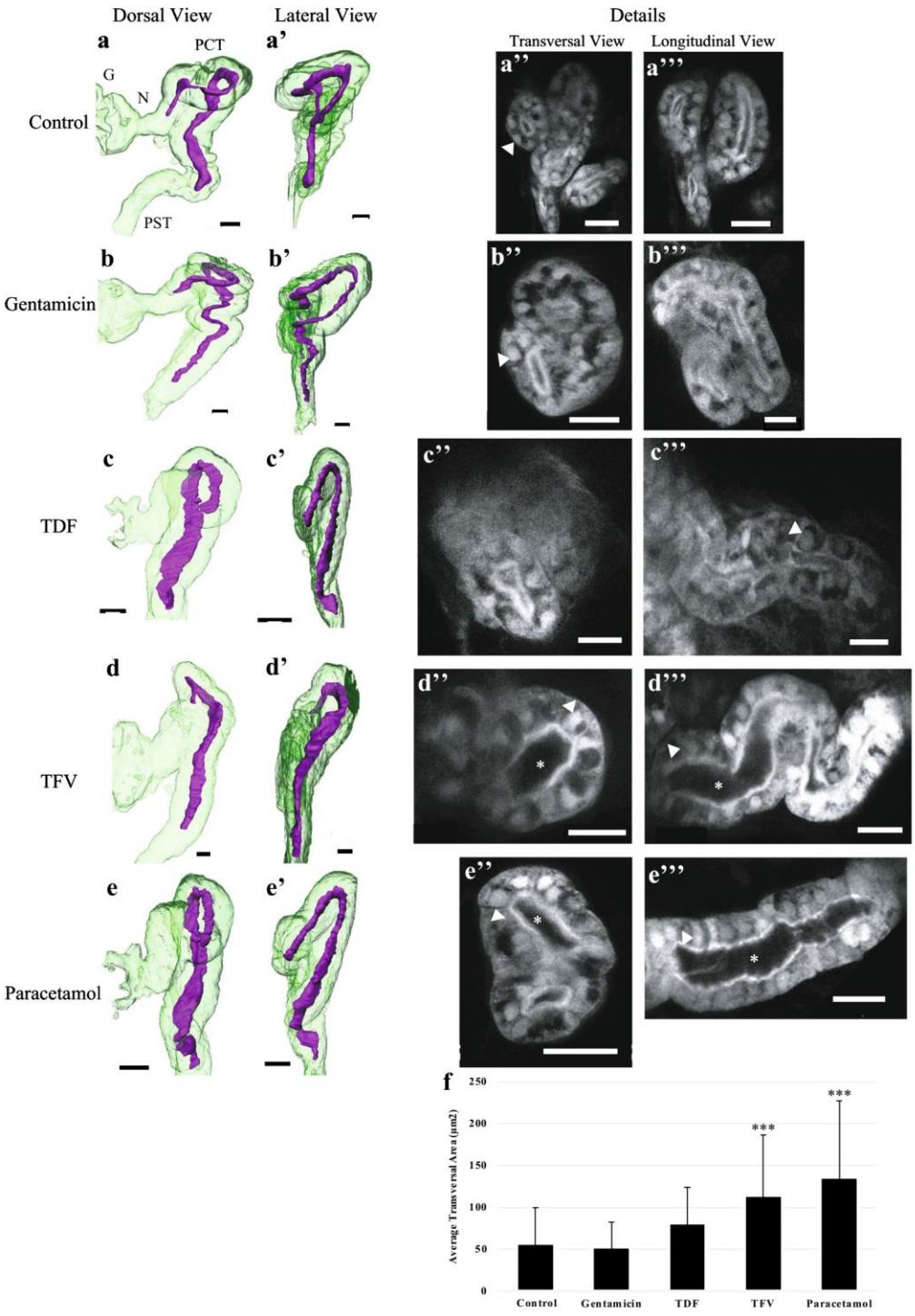

Fig. 3 The lumen of the proximal convoluted tubules is enlarged in zebrafish larvae exposed to the LC10 of TFV and paracetamol (a, a', b, b', c, c', d, d', e, e') Dorsal and lateral views of the proximal convoluted tubule of untreated larvae and larvae exposed to the LC10 of gentamicin, TDF, TFV or paracetamol. Compared to controls, the complexity of the coiled structure of the proximal convoluted tubules is reduced in the treated zebrafish larvae **(a'', a''', b'', b''', c'', c''', d'', d''', e'', e''')** Transversal and longitudinal amplifications of the proximal convoluted tubule of untreated larvae and treated larvae exposed to LC10 of gentamicin, TDF, TFV or paracetamol. GFP labels the nuclei and the membrane of the tubular cells **(d'', d''', e'', e''')** The lumen of the tubule is enlarged in zebrafish exposed to TFV and paracetamol **(f)** Transversal area of the proximal convoluted tubules.
Scale: 20 µm
G: glomeruli; N: nuclei; PCT: proximal convoluted tubule; PST: proximal straight tubule.

White asterisks mark tubule enlargements; white arrowheads show misplaced nuclei.
*** for p-value < 0.001

Paracetamol, TDF and TFV lead to epithelium disorganization with displaced nuclei towards the middle portion of the cell (Fig. 3e'' and e''', Fig. 3d'' and d''', Fig. 3c'' and c'').

Tubular mitochondrial alterations

Mitochondria morphology was evaluated using three different approaches: micrographs, serial section transmission electron microscopy 3D reconstructions of proximal tubular cells, and tomographic 3D reconstructions of mitochondria.

Micrographs from control larvae showed mitochondria as tubular organelles with smooth contours and regular shapes differing in size (Fig. 4b-b''). 3D cellular models enabled us to notice that they were interconnected, forming a vast mitochondria network (Fig. 5b'). Cristae were thin and long cylindrical structures distributed throughout the mitochondrion in different orientations. They branched from several places creating bridges that interconnected with each other (Fig. 5m'). Matrix granules occurred outside the cristae as tiny electron dense puncta.

3D cellular models revealed changes in mitochondria shape and size from drug exposed larvae. Gentamicin and TFV caused "donut"-like shapes (Fig. 5g). Paracetamol caused "pancakes" (Fig. 4d'', Fig. 5h) and "rods"-like shapes (Fig. 5i). TDF and TFV produced mitochondria with irregular contours (Fig. 5j) and huge mitochondria (Fig. 5k). There were no differences in the volume occupied by mitochondria (Supplementary Table 4). However, mitochondrial electron densities were significantly lower in gentamicin, TDF and TFV than in controls (141 ± 6 in controls, gentamicin 172 ± 5, TDF 161 ± 6, TFV 163 ± 6) (Fig. 4g). These results are in agreement with the enlarged mitochondria that were seen in the micrographs and 3D cellular models of gentamicin, TDF and TFV (Fig. 4c'', e'', f'' and 5k).

3D mitochondrial models showed no differences in the volume occupied by cristae (Supplementary Table 4). However, cristae from treated larvae, were clearly fragmented and/or degraded when compared with control larvae (Fig. 4c'', e'' and f'', 5n', o', p' and q').

The number of mitochondrial granules was reduced in all treated larvae, although it was only statistically significant for gentamicin, TDF and TFV (5 ± 2 granules/mitochondrion in controls, 0.7 ± 0.4 in gentamicin, 3 ± 1 in paracetamol, 2 ± 0.9 in TDF p = 0.031, 2 ± 1 in TFV) (Fig. 4h).

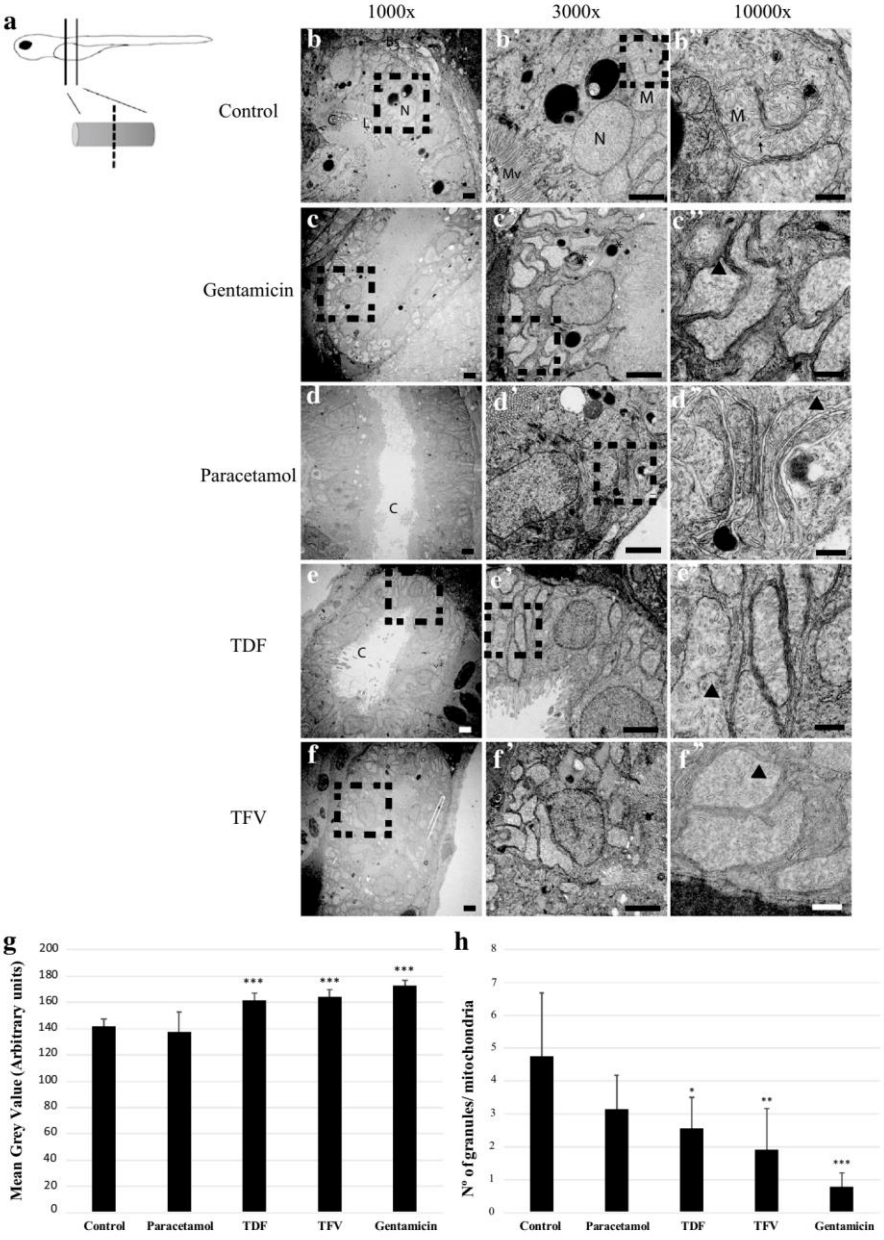

Fig. 4 Mitochondrial morphological alterations in electron micrographs after exposure to the LC10 of gentamicin, paracetamol, TDF and TFV

(a) Scheme of the sectioning of the proximal convoluted tubule for single micrographs; each section had a z of 70 nm **(b, c, d, e, f)** Micrographs at 1000x showing the proximal tubular epithelium as one cell layer with the basal membrane leading to blood and the apical membrane ending in microvilli that gave in to the lumen of the tubule **(b', c', d', e', f')** Micrographs at 3000x showing one proximal tubular cell with the nucleus in the center and the mitochondria in the basal and lateral sides for all condition **(b'', c'', d'', e'', f'')** Micrographs at 10000x showing some mitochondria. Thin and long mitochondria like "pancakes" are seen in larvae exposed to paracetamol. Swollen mitochondria are observed in larvae exposed to gentamicin, TDF and TFV. Mitochondria cristae are fragmented and mitochondria granules are missing in all treated larvae **(g)** The mean gray intensity reveals mitochondrial swelling in larvae exposed to gentamicin, TDF and TFV **(h)** Mitochondrial granules are decreased by all drugs and significantly for gentamicin, TDF and TFV.

Scale: 1000x – 2 µm; 3000x – 2 µm; 10000x – 500nm.

Bs: basolateral membrane; C: cilia; L: lumen; Mv: microvilli; M: mitochondria; N: nucleus.

Arrows mark granules; arrow heads mark fragmented cristae; asterisks mark phospholipidosis; square boxes, when present, indicate the area that was zoomed in and presented in the next image.
* for p-value < 0.05, ** for p-value < 0.01, *** for p-value < 0.001

The volume occupied by granules from each representative mitochondrion 3D model was also reduced in all treated larvae (Supplementary Table 4).

Discussion

In the present study, acute toxicity was induced in zebrafish by three drugs associated with tubular damage in man. For all tested drugs, morphological and/or functional tubular alterations were found, which supports the usefulness of the zebrafish model to evaluate tubular toxicity.

Physiological and biochemical characterization of zebrafish is of utmost importance to support its use in toxicology studies. Vertebrate kidneys play essential roles in the excretion of metabolic waste products and in the maintenance of the internal electrolyte and acid–base balances. Similarly to man, the nephron of zebrafish larvae consists of a glomerulus, responsible for blood filtration, followed by a renal tubule and duct, which are responsible for solute reabsorption and secretion (Drummond and Davidson 2010). Likewise, the zebrafish tubular epithelium expresses ion channels, transporters and claudins in a segment-specific manner that confer unique absorptive and secretory properties to each nephron segment. Among other examples, the PCT expresses the Na^+/ bicarbonate cotransporter Slc4a4a and the endocytic receptors megalin and cubilin; the distal early tubule (equivalent to the human thick ascending limb) expresses the $Na^+/Cl^-/K^+$ cotransporter Nkcc2; the distal late tubule (equivalent to the human distal convoluted tubule) expresses the Na^+/Cl^- cotransporter Ncc (Kersten and Arjona 2017). Information about regulation of renal ion transport in zebrafish is limited, but the renin-angiotensin system plays a very important role in the control of Na^+ reabsorption (Kumai et al. 2014; Rider et al. 2015). Despite these similarities, functional differences exist between zebrafish and human nephrons: i) absence of water-absorptive segments such as the human thin descending limb because freshwater fish do not need to concentrate urine; ii) absence of aldosterone (although zebrafish have mineralocorticoid receptors); iii) presence of unique structures with no clear human counterpart like the

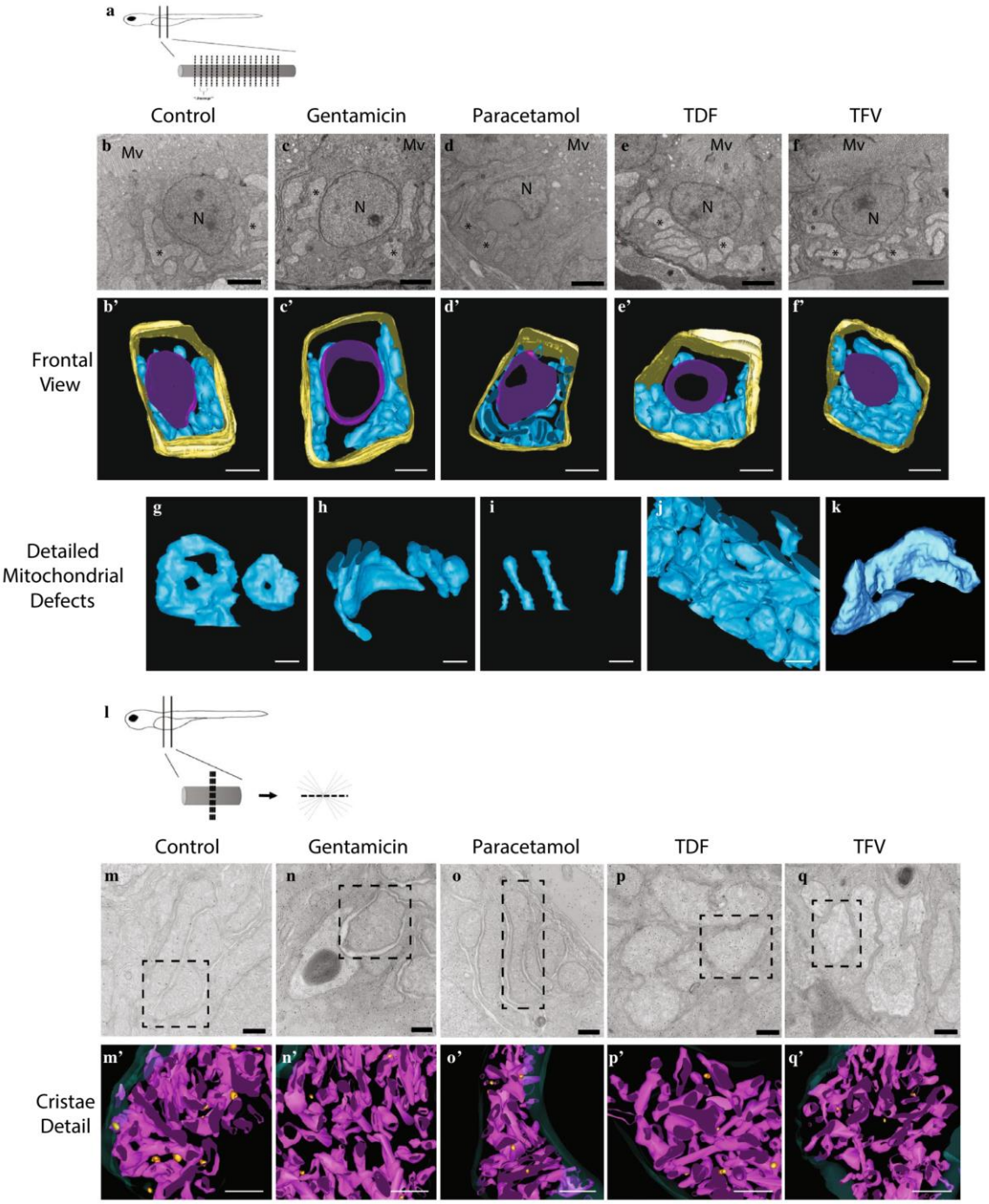

Fig. 5 Mitochondrial morphological alterations in ssTEM and tomograms after exposure to the LC10 of gentamicin, paracetamol, TDF and TFV
(a) Scheme of the serial sectioning of the proximal tubule for ssTEM to build 3D cellular models; 24-36 sections were cut for each ssTEM with a z of 100 nm per section **(b, c, d, e, f)** Micrographs at 3000x showing the cell that was chosen to build the cellular 3D representative model for each condition **(b', c', d', e', f')** Frontal section of the cellular 3D model for each condition **(g, h, i, j, k)** Weird mitochondrial shapes caused by the drugs: **(g)** "donuts" with gentamicin, **(h)** "pancakes" with paracetamol, **(i)** "rods" with paracetamol, **(j)** fragmented mitochondria with irregular shapes with TDF and TFV, **(k)** huge mitochondria occupying a big part of the cytosol with TDF and TFV.
(l) Scheme of the serial sectioning of the proximal tubule for tomograms to build 3D mitochondrial models; 3 sections were cut for each tomogram with a z of 120 nm per section **(m, n, o, p, q)** Micrographs at 8000x with Protein A Gold showing the mitochondrion that was

chosen to build the representative mitochondrial 3D model for each condition **(m', n', o', p', q')** Frontal section of the mitochondrial 3D model for each condition; cristae are fragmented in drug treated larvae.
Scale: b, c, d, e, f – 2 µm; b', c', d', e', f' – 2.5 µm; g, h, i, j, k – 1 µm; m, n, o, p, q – 500 nm; m', n', o', p', q' – 95 nm.

Corpuscle of Stannius, a renal gland involved in the regulation of calcium and phosphate levels potentially linked with the human macula densa (Wingert and Davidson 2008; Kersten and Arjona 2017).

ADME processes have been insufficiently characterized in zebrafish and are restricted to some metabolizing enzymes and membrane transport proteins. Phase I (CYPs) and phase II (UGT1A1, SULTs) enzymes have been identified (Hill et al. 2012), but most of functional information is only known for CYPs. The genetic homology of the most relevant CYPs between zebrafish and man is diverse. While there are orthologous relationships for most of CYP1s and CYP3s, only 26 from the 46 zebrafish CYP2s genes have human CYP orthologs (Goldstone et al. 2010). In line to what is well known in man, the expression of most of CYPs throughout zebrafish development is variable. With regards to CYP activity, zebrafish and human CYPs share some substrates, inhibitors and inducers. Moreover, some of those inducers proved to be agonists of the zebrafish pregnane X receptor (PXR) or aryl hydrocarbon receptor, which suggests common regulatory pathways of CYPs expression. However, there are important differences in the response to many substrates, inducers and inhibitors as reviewed by Saad and collaborators (Saad et al. 2016). Membrane transport proteins involved in the uptake and excretion of drugs and/or metabolites (i.e. SLC, ABC proteins) are also present in zebrafish. The most relevant ABC drug efflux pumps in man, namely ABCB1, ABCC1-5 and ABCG2, are expressed in zebrafish tissues that are involved in absorption, excretion or serving as a barrier function (intestine, liver, kidney, gills, brain blood barrier). Interestingly, despite the lack of data about transcriptional regulation of ABC transporters, an association was found between PXR, CYP3A and ABCB1 in zebrafish (Luckenbach et al. 2014). This example supports a similar regulation of detoxification enzymes and transporters between zebrafish and man.

Due to the limited information about pharmacokinetics in zebrafish, we assessed the drug metabolic profile of 5-day zebrafish larvae. In the case of paracetamol, all metabolites were

detected except NAPQI and paracetamol glutathione probably due to their high instability (Cook et al. 2015). Upon these results, we can conclude that zebrafish and man share the same pathways for paracetamol metabolism: glucuronidation, sulfonation and oxidation with posterior detoxification to paracetamol N-acetylcysteine. In the case of TDF, MS experiments identified tenofovir monoisoproxil and TFV in zebrafish extracts. TDF follows enzymatic hydrolysis through intestinal and blood esterases but also non enzymatic hydrolysis in water (Kurmi et al. 2016). Although we cannot exclude the possibility of some TDF hydrolysis in the embryo media, zebrafish expresses esterases (Levi et al. 2012), which supports TDF metabolism in zebrafish. TFV phosphorylated metabolites were not detected in zebrafish exposed to either TFV or TDF. Zebrafish expresses both organic anion transporters, necessary for intracellular TFV uptake, and nucleotide kinases, necessary TFV phosphorylation (Pannicke et al. 2009; Mihaljevic et al. 2016). So, a plausible explanation for the absence of TFV metabolites might be related with technical limitations of our extraction or LC-MS methods. Finally, gentamicin, which is not metabolized, was present in the zebrafish extracts but at very low concentrations probably due to its low bioavailability (Gemer et al. 1983).

Renal clearance was decreased by 19% and 74% by gentamicin and paracetamol, respectively. Drugs can decrease renal clearance by different mechanisms that do not necessarily involve damage to the renal parenchyma. For instance, drugs that inhibit renal prostaglandin-mediated vasodilation such as paracetamol (Graham and Scott) and gentamicin (Lopez-Novoa et al. 2011) and hepatotoxic drugs such as paracetamol (Mazer and Perrone 2008) can decrease renal clearance. Neither the liver nor the renal blood flow were evaluated in this work but previous studies found that gentamicin decreases the venous erythrocyte velocity and the heart rate in zebrafish larvae (Hentschel et al. 2005; Rider et al. 2012). Besides these indirect mechanisms, drugs that directly damage the glomeruli and/or the renal tubule can also decrease the renal clearance via several mechanisms (Basile et al. 2012). In this study all tested drugs caused morphological tubular alterations but only gentamicin and paracetamol reduced inulin clearance. Interestingly, similar results are seen in men: HIV patients on TDF can develop proteinuria, a specific marker of tubular injury, with normal values

of glomerular filtration rate (Tourret et al. 2013). Thus, tubular morphological alterations associated with TFV seem to precede the decline in the renal clearance. In the case of gentamicin and paracetamol, a combination of their intrinsic tubular effects and their potential pre-renal effects could explain the observed decrease in renal clearance. Besides, gentamicin can cause intraglomerular mesangial cell contraction (Lopez-Novoa et al. 2011), which can also decrease the renal clearance.

The intrinsic complexity of the PCT represented a big challenge for imaging. Previous works applied confocal or conventional optical microscopy to image the pronephros but with poor quality results (Peng et al. 2010; Westhoff et al. 2013). We provide for the first time exhaustive imaging of the PCT that allowed building 3D images to objectively measure the caliber of the tubular lumen. Paracetamol, TDF and TFV induced tubular dilatations and epithelium disorganization with nuclei delocalization. Tubular dilatations are one of the earliest morphological alterations of acute tubular injury followed by loss of cytoskeletal integrity and cell polarity (Bonventre and Yang 2011; Basile et al. 2012). We didn't perform any immunostaining for apical or basal markers but epithelium and nuclei disorganization found in our study could be associated with the loss of cell polarity.

The loss of the structure of the tubular epithelium is associated with ATP depletion and thus mitochondrial damage (Price 2002; Basile et al. 2012). Mitochondrial morphology is highly variable and dynamic due to the ability of mitochondria to undergo the highly coordinated processes of fusion and fission. Mitochondrial fusion allows the exchange and complementation of partially damaged mitochondria contents when the stress is below a critical threshold while mitochondrial fission is required to remove damaged mitochondria during high levels of stress (Youle and van der Bliek 2012; Rafelski 2013). Thus, quantification of mitochondria volume and number can be regarded as a measure of the insult intensity. We provide for the first time 3D models of PCT cells and mitochondria. These models were very useful to understand the complexity of mitochondria networks, to get accurate measurements of mitochondria volume and number and to identify alterations in mitochondria shape and cristae fragmentation. However, because 3D modeling at the ultrastructural level is a laborious

task, only one model was made for each condition. Although each model was carefully chosen to represent each condition, there was a substantial number of mitochondria that were not fully captured by the models. Thus, we cannot conclude about drug-induced changes in the volume or number of mitochondria.

Drug-induced mitochondrial defects were manifested as: mitochondrial shape alterations including “donuts” with gentamicin and TFV in comparison to “pancakes” and “rods” with paracetamol; mitochondrial size alterations in the form of mitochondrial swelling with gentamicin, TDF and TFV; mitochondrial cristae fragmentation and reduction in the number of mitochondrial granules with all drugs. Mitochondrial morphological alterations have a direct impact on mitochondrial functions, which are vital for cellular functioning, from ATP generation to regulation of apoptosis (Galloway and Yoon 2012). For example, mitochondrial swelling, considered to be an early sign of functional deterioration of the organelle, is an indicator of the opening of the mitochondrial permeability transition pore (Arpagaus et al. 2002; Herlitz et al. 2010). Thus, mitochondrial swelling together with cristae damage can result in a disruption of the electron transport chain, leading to a decrease in the ATP production.

In conclusion, this work demonstrates the high homology between zebrafish and mammals for drug metabolism and drug-induced morphological and functional tubular alterations. Together, these results support the use of zebrafish in toxicological studies.

Corresponding author
Judit Morello Bullón
orcid.org/0000-0002-1148-9329
Chronic Diseases Research Centre, NOVA Medical School, NOVA University of Lisbon
Rua Câmara Pestana, 6, 1150-082
Lisbon, Portugal
judit.morello@nms.unl.pt

Acknowledgments
We would like to thank Maysa Franco and Ana Cristina Borges from the Fish Facility of the Gulbenkian Institute of Science.

Funding

This work was supported by the Calouste Gulbenkian Foundation, Gulbenkian Professorship 121986/2012; the Foundation for Science and Technology through the grant ANR/BEX-BID/0153/2012, contract IF/00951/2012 (to SSL), fellowship PD/BD/52420/2013 (to RJ) and travel ship SFRH/BSAB/114291/2016 (to JM); iNOVA4Health Research Unit, LISBOA-01-0145-FEDER-007344.

Ethical statement

All procedures performed in studies involving animals were in accordance with the ethical standards of the institution or practice at which the studies were conducted.

Conflict of interests

None.

References

Arpagaus S, Rawyler A, Braendle R (2002) Occurrence and characteristics of the mitochondrial permeability transition in plants. J Biol Chem 277:1780–1787.

Basile D, Anderson M, Sutton T (2012) Pathophysiology of Acute Kidney Injury. Compr Physiol 2:1303–1353.

Bonventre J, Yang L (2011) Cellular pathophysiology of ischemic acute kidney injury. J Clin Invest 121:4210–4221.

Chevalier RL (2016) The proximal tubule is the primary target of injury and progression of kidney disease: role of the glomerulotubular junction. Am J Physiol Renal Physiol 311:F145-61.

Cianciolo Cosentino C, Skrypnyk NI, Brilli LL, et al (2013) Histone deacetylase inhibitor enhances recovery after AKI. J Am Soc Nephrol 24:943–53.

Clarot I, Chaimbault P, Hasdenteufel F, et al (2004) Determination of gentamicin sulfate and related compounds by high-performance liquid chromatography with evaporative light scattering detection. J Chromatogr A 1031:281–7.

Cook SF, King AD, van den Anker JN, Wilkins DG (2015) Simultaneous quantification of acetaminophen and five acetaminophen metabolites in human plasma and urine by high-performance liquid chromatography-electrospray ionization-tandem mass spectrometry: Method validation and application to a neonatal pharmacok. J Chromatogr B Analyt Technol Biomed Life Sci 1007:30–42.

Drummond IA, Davidson AJ (2010) Zebrafish kidney development. In: Detrich HW, Westerfiled M, Zon LI (eds) Methods in cell biology, Third Edit. Elsevier Inc., pp 233–60

Galloway CA, Yoon Y (2012) Perspectives on: SGP symposium on mitochondrial physiology and medicine: what comes first, misshape or dysfunction? The view from metabolic

excess. J Gen Physiol 139:455–63.

Gemer O, Zaltztein E, Gorodischer R (1983) Absorption of orally administered gentamicin in infants with diarrhea. Pediatr Pharmacol (New York) 3:119–23.

Goldstone J V, McArthur AG, Kubota A, et al (2010) Identification and developmental expression of the full complement of Cytochrome P450 genes in Zebrafish. BMC Genomics 11:643.

Graham GG, Scott KF Mechanism of action of paracetamol. Am J Ther 12:46–55.

Hentschel DM, Park KM, Cilenti L, et al (2005) Acute renal failure in zebrafish: a novel system to study a complex disease. Am J Physiol Ren Physiol 288:F923-929.

Herlitz LC, Mohan S, Stokes MB, et al (2010) Tenofovir nephrotoxicity: acute tubular necrosis with distinctive clinical, pathological, and mitochondrial abnormalities. Kidney Int 78:1171–1177.

Hill A, Mesens N, Steemans M, et al (2012) Comparisons between in vitro whole cell imaging and in vivo zebrafish-based approaches for identifying potential human hepatotoxicants earlier in pharmaceutical development. Drug Metab Rev 44:127–140.

Huang SM, Xu F, Lam SH, et al (2013) Metabolomics of developing zebrafish embryos using gas chromatography- and liquid chromatography-mass spectrometry. Mol Biosyst 9:1372–1380.

Kersten S, Arjona FJ (2017) Ion transport in the zebrafish kidney from a human disease angle: possibilities, considerations, and future perspectives. Am J Physiol Renal Physiol 312:F172–F189.

Kramer-Zucker AG, Wiessner S, Jensen AM, Drummond IA (2005) Organization of the pronephric filtration apparatus in zebrafish requires Nephrin, Podocin and the FERM domain protein Mosaic eyes. Dev Biol 285:316–329.

Kremer J.R. DNM and JRM (1996) Computer visualization of three-dimensional image data using IMOD. J Struc Biol 116:71–76.

Kumai Y, Bernier NJ, Perry SF (2014) Angiotensin-II promotes Na+ uptake in larval zebrafish, Danio rerio, in acidic and ion-poor water. J Endocrinol 220:195–205.

Kurmi M, Golla VM, Kumar S, et al (2016) Stability behaviour of antiretroviral drugs and their combinations. 4: Characterization of degradation products of tenofovir alafenamide fumarate and comparison of its degradation and stability behaviour with tenofovir disoproxil fumarate. J Pharm Biomed Anal 131:146–155.

Levi L, Ziv T, Admon A, et al (2012) Insight into molecular pathways of retinal metabolism, associated with vitellogenesis in zebrafish. AJP Endocrinol Metab 302:E626–E644.

Lopez-Novoa JM, Quiros Y, Vicente L, et al (2011) New insights into the mechanism of aminoglycoside nephrotoxicity: an integrative point of view. Kidney Int 79:33–45.

Luckenbach T, Fischer S, Sturm A (2014) Current advances on ABC drug transporters in fish. Comp Biochem Physiol Part - C Toxicol Pharmacol 165:28–52.

Mastronarde DN (1997) Dual-axis tomography: an approach with alignment methods that preserve resolution. J Struc Biol 120:343–352.

Mazer M, Perrone J (2008) Acetaminophen-induced nephrotoxicity: pathophysiology, clinical manifestations, and management. J Med Toxicol 4:2–6.

McGrath P, Li C-Q (2008) Zebrafish: a predictive model for assessing drug-induced toxicity. Drug Discov Today 13:394–401.

Mihaljevic I, Popovic M, Zaja R, Smital T (2016) Phylogenetic, syntenic, and tissue expression analysis of slc22 genes in zebrafish (Danio rerio). BMC Genomics 17:626.

Nevedomskaya E, Mayboroda OA, Deelder AM (2011) Cross-platform analysis of longitudinal data in metabolomics. Mol Biosyst 7:3214–22.

Olson H, Betton G, Robinson D, et al (2000) Concordance of the toxicity of pharmaceuticals in humans and in animals. Regul Toxicol Pharmacol 32:56–67.

Pacchiarotta T, Hensbergen PJ, Wuhrer M, et al (2012) Fibrinogen alpha chain O-glycopeptides as possible markers of urinary tract infection. J Proteomics 75:1067–1073.

Pannicke U, Hönig M, Hess I, et al (2009) Reticular dysgenesis (aleukocytosis) is caused by mutations in the gene encoding mitochondrial adenylate kinase 2. Nat Genet 41:101–105.

Peng H-C, Wang Y-H, Wen C-C, et al (2010) Nephrotoxicity assessments of acetaminophen during zebrafish embryogenesis. Comp Biochem Physiol C Toxicol Pharmacol 151:480–6.

Peterson RT, MacRae CA (2012) Systematic Approaches to Toxicology in the Zebrafish. Annu Rev Pharmacol Toxicol 52:433–453.

Pluskal T, Castillo S, Villar-Briones A, Oresic M (2010) MZmine 2: modular framework for processing, visualizing, and analyzing mass spectrometry-based molecular profile data. BMC Bioinformatics 11:395.

Price VR (2002) ATP Depletion Of Tubular Cells Causes Dissociation of the Zonula Adherens and Nuclear Translocation of -Catenin and LEF-1. J Am Soc Nephrol 13:1152–1161.

Rafelski SM (2013) Mitochondrial network morphology: building an integrative, geometrical view. BMC Biol 11:71.

Randhawa MA (2009) Calculation of LD50 values from the method of Miller and Tainter, 1944. J Ayub Med Coll Abbottabad 21:184–185.

Rider SA, Mullins LJ, Verdon RF, et al (2015) Renin expression in developing zebrafish is associated with angiogenesis and requires the notch pathway and endothelium. Am J Physiol - Ren Physiol 309:F531–F539.

Rider SA, Tucker CS, Del-Pozo J, et al (2012) Techniques for the in vivo assessment of cardio-renal function in zebrafish (Danio rerio) larvae. J Physiol 590:1803–9.

Saad M, Cavanaugh K, Verbueken E, et al (2016) Xenobiotic metabolism in the zebrafish: a review of the spatiotemporal distribution, modulation and activity of Cytochrome P450 families 1 to 3. J Toxicol Sci 41:1–11.

Schieber NL, Nixon SJ, Webb RI, et al (2010) Modern Approaches for Ultrastructural Analysis of the Zebrafish Embryo. In: Methods Cell Biol. pp 425–442

Schindelin J, Arganda-Carreras I, Frise E, et al (2012) Fiji: an open-source platform for

biological-image analysis. Nat Methods 9:676–682.

Schindelin J, Rueden CT, Hiner MC, Eliceiri KW (2015) The ImageJ ecosystem: An open platform for biomedical image analysis. Mol Reprod Dev 82:518–529.

Smith KY, Patel P, Fine D, et al (2009) Randomized, double-blind, placebo-matched, multicenter trial of abacavir/lamivudine or tenofovir/emtricitabine with lopinavir/ritonavir for initial HIV treatment. AIDS 23:1547–1556.

Tourret J, Deray G, Isnard-Bagnis C (2013) Tenofovir effect on the kidneys of HIV-infected patients: a double-edged sword? J Am Soc Nephrol 24:1519–27.

Westhoff JH, Giselbrecht S, Schmidts M, et al (2013) Development of an automated imaging pipeline for the analysis of the zebrafish larval kidney. PLoS One 8:1–13.

Wingert R a, Davidson a J (2008) The zebrafish pronephros: a model to study nephron segmentation. Kidney Int 73:1120–1127.

Wingert RA, Selleck R, Yu J, et al (2007) The cdx genes and retinoic acid control the positioning and segmentation of the zebrafish pronephros. PLoS Genet 3:1922–1938.

Youle RJ, van der Bliek AM (2012) Mitochondrial fission, fusion, and stress. Science 337:1062–5.

CHAPTER 7

Discussion

"What if it's not everything I dreamed it would be?"

"It will be."

"And what if it is? What do I do then?"

"Well, that's the good part I guess. You get to go find a new dream."

Tangled, Disney

GENERAL DISCUSSION

Establishing a correct body plan in terms of LR is very important for the correct function of the internal organs and overall wellbeing. Understanding the several mechanisms that lead to correct organ positioning has clinical relevance since, for example in humans, defects in heart positioning can lead to severe congenital chronic heart problems. Besides, in the LR field we assist to the coordination between the physical properties of a fluid flow, potential morphogens, several signalling pathways and overall cell and tissue biology. All together makes LR field an interesting and lively one, with still many questions to tackle.

With this Thesis, we tried to provide new insights into different steps of left-right axis establishment. First, we delved into the motility nature of cilia that constitute the zebrafish LRO (Kupffer's Vesicle, KV) and further understood what is the importance of the ratio between motile and immotile cilia in order to generate a functional fluid-flow in the LRO. We focused on what determines being an immotile vs being a motile cilium. We have demonstrated via unprecedented transmitted electron microscopy thorough sampling that all KV cilia seem to have a motile ultrastructure. However, we found out that Notch signalling, through its effector Her12, is instructing around 20% of these cells to switch off ciliary motility. This finding was new and opened a new research line regarding what are the target genes for Her12, previously known to be a transcription inhibitor involved in somitogenesis (Shankaran et al., 2007).

We next investigated events that are responding to the flow mediated signalling. We tried to evaluate the difference between having no flow and having no Pkd2-mediated way of sensing that flow. Evidence for mechanosensation are strongly supported by mutants without this calcium channel or its sensing partner, Pkd1l1 (Field et al., 2011; Kamura et al., 2011), which suggests that having no Pkd2-mediated flow sensing is the same as having no flow.

The experimental difficulties faced on this work made impossible this comparison but gave us the surprising suggestion that manipulating Pkd2, even by mildly reducing its levels, had a huge impact on LR organ *situs*.

We proceeded with further investigating how the lack of Pkd2 was impacting on KV cells transcriptome. By doing a KV specific transcriptome profiling, we were able to identify four genes: *parvalbumin6*, *frizzled related protein, calcycling binding protein* and *nicalin1*, that are differentially expressed in the KV cells between Pkd2 knockdown embryos and controls, although none of them was expressed in an asymmetric fashion like *dand5*. Unfortunately, none of these 4 genes had a huge impact on LR when manipulated independently mimicking the trends present in the array. Actually, even when the genes were manipulated at the same time the resulting organ *situs* phenotypes showed only around 30% of abnormal laterality, which was still not as strong as the phenotype found in the knockdown of Pkd2 (around 60% laterality defects). This might indicate that Pkd2 affects left-right in a very broad manner, affecting many players downstream. It might also be the case that we are still missing the central players affected downstream of Pkd2.

Among the gene profiling study, we identified a new nodal player in the LR pathway – *nicalin1 (ncl1)*. While overexpressing this gene did not produce many defects in terms of LR, knocking it down gene by morpholino antisense technology showed a dose-dependent phenotype in terms of organ *situs* defects that increased to as high as 70%. It also affected the expression levels and pattern of *dand5*, the first known right sided asymmetric gene expressed in the KV, and left sided lateral plate mesoderm genes like *spaw* and *pitx2*. Since Ncl1 was identified as a Nodal signalling antagonist acting at the ER to regulate secretion of TGF beta proteins, we compared it with another known LR nodal antagonist, *dand5*. By using a null mutant for *dand5*$^{-/-}$ we were able to assess the role of these two inhibitors and infer on how they cooperate to establish a correct LR. We understand now that they are most likely

working independently, and both converge on the regulation of the available Nodal/Spaw protein levels or other element of the TGF-β signalling pathway.

To move or not to move

Cilia motility has been formally demonstrated to be connected to LR axis establishment in 1998 by Hirokawa's lab (Nonaka et al., 1998) followed by work done by Supp et al. (1999) where they demonstrated that the ATP binding domain of dynein motors was fundamental for cilia motility. Subsequently, the mechanosensation hypothesis (McGrath et al., 2003) gained popularity that states the need for motile cilia to generate the flow and immotile cilia to sense the flow and transmit this asymmetric information into the cells and tissues. Finding motile and immotile cilia and the players of a sensing mechanism in mice, frog and zebrafish LRO gave strength to this hypothesis (Bisgrove et al., 2005; McGrath et al., 2003; Sampaio et al., 2014; Schottenfeld et al., 2007; Schweickert et al., 2007). Yet, some questions remain to be answered. How strong does the flow need to be for reliable LR? Reports in mice show that slow flow is very effective in establishing LR. Flow starts very slow in the beginning of the process in mice LRO (Shinohara et al., 2012), and our flow analysis in Chapter 2 confirmed the same progression for zebrafish, showing a strong correlation between increasing cilia motility and increasing flow strength (Tavares et al., 2017). Interestingly, in mutant mice for *dpcd*$^{-/-}$, a ciliary gene that when mutated makes most motile cilia immotile and reduces the number of immotile cilia in the crown cells) embryos with flow generated by only two motile cilia or reducing the flow with low concentration methylcellulose in WT mice embryos still generated embryos with normal expression of LR genetic markers like *cerl2* and *pitx2*. Also, it has been shown in mice that asymmetric gene expression happens hours before the flow becomes strong (Shinohara et al., 2012). In fish, intraciliary calcium oscillations are already observed with a very slow flow (Yuan et al., 2015) but whether these are meaningful for LR was not addressed in a time specific manner. The differences between the two models might

be solely explained by the differences in the topography of the two LROs. While mice LRO is a concave, tear-drop-shaped epithelial field of cells located distally on the ventral surface of the embryo (Sulik et al., 1994) where all cilia are useful for flow production, the zebrafish LRO is a ciliated vesicle that has to have motile cilia in the equatorial line and dorsal anterior region for flow direction and strength, respectively (Pintado et al., 2017).

If immotile cilia are indeed the sensors, a second question we can ask is what is the minimum number of immotile cilia needed for sensing flow reliably. For this the evidence is even scarcer and mostly relies on mathematical modelling. In mice it is known that immotile cilia in the crown cells, present in the periphery of the node, are crucial for LR (Yoshiba et al., 2012). Mice mutants for *dpcd* (a ciliary gene) also have a significant reduction of immotile cilia in the crown cells accompanying the shortage of motile cilia and still have normal expression of LR genetic markers (providing the existence of at least two motile cilia) (Shinohara et al., 2012). Mathematical simulations for the zebrafish LRO predict that the number of immotile cilia present in zebrafish are not sufficient to reliably sense the flow due to its variability and high noise level (Ferreira et al., 2017). However, by using a slower scanning speed our own work contradicted Ferreira et al. (2017) observations: while they only see around 5% of immotile cilia, we see around 20%. This value, according to their mathematical modelling, would be enough for mechanosensation to occur (Tavares et al., 2017). Although recent work by Clapham lab by Delling et al. (2016) has disputed the role of node primary cilium as a mechanosensor in mice, many labs are still working to build on this hypothesis. One of the reasons being the fact that in Delling et al. (2016) study, the calcium probe used had a very high dissociation constant, which means that it is good for time-resolution, but it has less affinity for calcium when in low, resting, concentrations (Delling et al., 2016). This might indicate that small calcium oscillations occurring in the cilium, like the ones observed in Yuan et al. (2015), might have been missed by Delling et al. (2016).

Another pertinent unanswered question is if the Pkd2-mediated sensing mechanism is the only one necessary for reliable LR. Pkd2 and its partner Pkd1l1 are present in mice (Field et al., 2011) and medaka (Kamura et al., 2011) and are both needed for correct LR. Field et al. (2011) showed that Pkd2 and Pkd1l1 physically interact and are co-localized in the cilium. Also, Pkd1l1 mutant phenocopies the Pkd2 mice mutant, leading to no *nodal* or *pitx2* expression on the LPM, indicating a failure to activate Nodal signalling in the LPM, while *nodal* and *cerl2* are still expressed around the node in a symmetric fashion (Field et al., 2011; Pennekamp et al., 2002). Since the node architecture and cilia motility are not affected, this evidence strongly supports that Pkd2-Pkd1l1 are mechanically sensing the flow and without it, *cerl2* remains symmetric and blocks further Nodal signalling from occurring. In zebrafish, *pkd2* mutant leads to a majority of bilateral *spaw* in the LPM while *pkd2* morphant shows near randomization (Bisgrove et al., 2005; Schottenfeld et al., 2007). As for *dand5*, it is reported normal in the mutants (Schottenfeld et al., 2007) and mainly symmetric in the morphants (present in this Thesis, Chapter 3). When compared with mice model, Pkd2 in zebrafish does not seem to have such a strong impact on Nodal signalling, i.e., Nodal signalling still occurs but the asymmetries are strongly affected, resulting in randomization of organ *situs*. However, *dand5* showed the same phenotype as *cerl2* in mice in the absence of Pkd2. Therefore, in this Thesis Chapter 3, we aimed to compare absence of flow in the LRO, that we know causes severe organ *situs* defects in zebrafish (Sampaio et al., 2014), and reduced levels of Pkd2-leading to a defective calcium mediated signalling situation. We wanted to see if there were any differences between these two situations in terms of outcomes: *dand5* and organ *situs*. This revealed to be hard to execute, since lowering the levels of Pkd2 led to defects in the KV cell shape and overall architecture, impacting severely on the flow. Since Pkd2 is expressed in many tissues and regulates extracellular matrix in the notochord (Mangos et al., 2010), which has been shown to influence KV architecture (Compagnon et al., 2014), we decided to use a very well-established technique to

knockdown Pkd2 only on the LRO cells (Amack and Yost, 2004). Although it has been published that lack of Pkd2 in the LRO alone produced mild results (around 13% of reversed heart or gut) (Bisgrove et al., 2005), in our hands and with a lower *pkd2* MO concentration, we observed organ *situs* defects similar to what was found in embryos injected at 1-cell stage with the same *pkd2* MO. Curiously, we still observed the presence of Pkd2 by immunostaining along the cilia and in the LRO cells in the *pkd2* MO^{DFCs}, but so did we find Pkd2 protein in the Pkd2 null mutant *cup*$^{-/-}$ at later stages (Roxo-Rosa et al., 2015). This is likely to be due to maternal contribution and long protein half-life, which makes it impossible to completely knockdown Pkd2 in the DFC type of morphants. Nevertheless, all these treatments still showed severe organ *situs* defects. All this together suggested that slightly reducing the levels of Pkd2 has a huge impact on LR, reinforcing the importance of this protein and pointing to the existence of a threshold type of activity for this channel in terms of impact in LR. Finally, we still decided to proceed and compare this *pkd2* MO DFC injection with the absence of flow situation. Our results showed that there were no significant differences between reducing Pkd2 (even partially) or eliminating flow.

Putting it all together, we still cannot rule out the compatible hypothesis that, travelling with the flow, there might be morphogens (likely inside vesicles) that will elicit asymmetric responses between the left and right sides of the LRO. For example a feasible explanation is that it is still possible that Pkd1l1 is not only sensing flow by mechanosensory mechanisms but it may be binding to proteins, like Wnts, and mediating calcium responses as reported by Kim et al., (2016). Pkd1 has a G-protein-coupled receptor that, when cleaved, produces a C-terminal fragment that can enter the nucleus and bind to β-catenin (reviewed in Dalagiorgou et al., 2010). This interaction reduced the affinity between β-catenin and T-cell factor transcription factor, inhibiting gene transcription and attenuating Wnt signalling (Lal et al.,

2008). More work can and should be done to identify potential morphogens and further testing the potential sensing alternatives of the LR relevant complex Pkd1l1- Pkd2.

Downstream of calcium

Calcium is an important signalling pathway in the cell and impacts on cell survival (Yano et al., 1998). In LR, calcium is important for the asymmetric oscillations, being present in the LRO's cilia and cells (McGrath et al., 2003; Tanaka et al., 2005; Yuan et al., 2015). A leftward calcium wave is the first asymmetric event found, that precedes asymmetric gene expression (McGrath et al., 2003). The nodal antagonist *cerl2*, mouse homologue of *dand5*, is thought to be the first asymmetric gene (Marques et al., 2004), after an asymmetric calcium wave on the left also happens (McGrath et al., 2003). In fact, *cerl2* mRNA is expressed first symmetrically around the mice LRO and then, downstream of flow and upon the calcium wave, a Wnt3-dependent *cerl2* mRNA degradation starts on the left side, establishing an asymmetry towards the right (Marques et al., 2004; Nakamura et al., 2012). Only then, *nodal* asymmetric expression around the node is also established in the mouse, being stronger on the left. One interpretation was that such bias was a direct consequence of the presence of less Nodal inhibitor Cerl2, predicted by the degradation of *cerl2* mRNA on the left side and not directly because of left calcium waves or flow (Kawasumi et al., 2011). In zebrafish, the way that this animal achieves the same result is slightly different, *dand5* also starts by being symmetrically expressed and, as the flow grows stronger, a right-sided asymmetry is observed (likely due to a left sided degradation). This asymmetry seems to be completely dependent on flow, since lack of flow renders *dand5* mostly symmetric (Sampaio et al., 2014). This raised the question: is *dand5* the only asymmetric gene downstream of calcium and flow in the LRO? To answer this, our lab decided to do a transcriptomic profile for the LRO cells of WT and Pkd2 knockdown embryos, which we detailed in Chapter 4. This strictly designed microarray gave us an interesting list of differently expressed genes between these

two situations and an even more interesting list of all genes expressed at this time (13-14 hpf). We therefore looked for obvious candidates such as Wnts, as these had already been involved in studies with the mouse model (Nakamura et al., 2012). We looked for Wnt3 and Wnt8, genes that have expression domains in the KV region (Lin and Xu, 2009). However, although they are expressed at the zebrafish LRO, they are not strongly expressed nor asymmetrically expressed, and they were not differently expressed in our microarray. Besides, if these genes were responsible for *dand5* degradation, overexpressing them would lead to less *dand5* and knocking them down would lead to more *dand5*. The authors observed exactly the opposite (Lin and Xu, 2009). Other Wnt signalling related gene observed was the wnt signalling inhibitor *frizzled-related protein*. Overexpressing this gene led to a significant decrease of *dand5* expression level without affecting its pattern. It is known that Wnt signalling downregulation leads to cilia length decrease and *lefty1* expression problems in the midline (Lin and Xu, 2009). Our *frzb* overexpression is concordant with this data and might be affecting the LRO in a similar fashion. This is strongly contrasting with what is found in mice, suggesting that these two animal models might be regulating *cerl2/dand5* expression pattern/level differently.

On the other hand, another interesting candidate was the gene coding for Calcyclin binding protein, since its mRNA manipulations led to randomization of *dand5* expression pattern. Cacybp is known as a central protein that can connect to calcium via calcium binding proteins and E3 ubiquitin ligases that degrade β-catenin. β-catenin might be stabilizing *dand5* mRNA, a role that has been described for other mRNAs (Briata et al., 2003), and therefore could be mediating a *dand5* targeted degradation on the left side dependent on Cacybp. We will in the future manipulate β-catenin and assess the impact on *dand5* expression pattern.

We also investigated calcium effectors and found *parvalbumin6* to be differently expressed between WT and Pkd2 morphants. Knocking down *parvalbumin6* did not affect organ *situs*,

while overexpressing it had an impact, suggesting that other *parvalbumin* genes might compensate for its absence while its overexpression might affect calcium normal homeostasis. Interestingly, manipulating *parvalbumin6* did not have any impact on *dand5* pattern or level, which is against the idea that calcium impacts on *dand5* regulation. A way to confirm this is to ensure by calcium imaging that manipulating *parvalbumin6* levels leads to changes in calcium dynamics in the zebrafish LRO.

Although we found new and interesting and also minor players in LR axis establishment, our search did not find any new asymmetrically expressed gene between left and right sides of the LRO, as *dand5*. This raises the question: is *dand5* the only asymmetrically expressed gene in the LRO or were we looking in the wrong list? In fact, *dand5* itself does not appear in our differently expressed list, since *pkd2* knockdown does not alter *dand5* expression level, only pattern. To find other asymmetrically expressed genes, we might need to focus on the list of all expressed LRO genes and screen for asymmetric candidates with similar expression levels as *dand5*.

Two inhibitors, One pathway (or maybe two?)

Cerl2/Dand5 protein is thought to be important on the right side of the mouse LRO to inhibit Nodal protein by binding directly to it (Inácio et al., 2013; Marques et al., 2004). More recently, Inácio et al. (2013) suggested a new later role of Cerl2/Dand5 on the left side where, in a flow dependent manner, Cerl2/Dand5 is needed to terminate Nodal signalling (Inácio et al., 2013). This is an interesting observation that suggests new ways of thinking about Cerl2/Dand5. So, first, Cerl2/Dand5 protein is secreted locally from the right sided cells of the LRO and bind secreted Nodal in the peri-node region. Concordantly, an asymmetry in Nodal activity towards the left is detected by phosphorylated Smad2/3 antibody in the peri-node region at a time when *nodal* expression is still symmetric. Therefore, this first role of Cerl2/Dand5 would occur in the extracellular space on the right side, blocking the Nodal

activity there and therefore enforcing the downregulation of *nodal* on the peri-node region that is later observed (Kawasumi et al., 2011). At the same time, flow-triggered *cerl2*/*dand5* degradation would occur on the left side, allowing Nodal activity there (Nakamura et al., 2012). Secondly, Cerl2/Dand5 would be secreted into the node lumen from the right side and would travel with the flow towards the left side in a time where flow is much stronger (Inácio et al., 2013). This is a different concept altogether. The authors show that Cerl2 only disappears from the right side of the node in the presence of flow because, when using mutants with compromised flow, Cerl2 stays symmetric (Inácio et al., 2013). To assess if this termination of Nodal signalling is indeed relevant and necessary, a conditional *cerl2*$^{-/-}$ mutant activated at different timings would be needed.

When we look to the zebrafish model, the major difference is that the LRO cells do not express both *dand5* and *spaw*. Our 3D reconstruction of these expression domains in Chapter 5 confirmed what has already been published by Hashimoto et al. (2004): *dand5* expression domain is restricted to the LRO cells and to one extra cell layer laterally, very strong in the dorsal cells, while *spaw* domains are dorsally located and do not overlap with those of *dand5*. Therefore, if Dand5 was being released into the KV lumen on the right side and travelling towards the left side, it would have to be incorporated into the KV cells by endocytosis and then exocytosed towards the Spaw domain dorsally in order to terminate the Nodal signalling there, as it is suggested in mice. Although possible, it is more likely that Dand5 protein is being released to the extracellular domain and impacting on Spaw being released by this *spaw* domain on both sides, stronger on the right than on the left. If this has an impact on *spaw* expression domain, it remains to be further validated, but it certainly seems it should be affecting Spaw travelling towards the LPM. Experiments using a phosphorylated SMAD antibody would be useful to clarify this question in zebrafish. Also, to ensure if Dand5 is being secreted into the lumen or not, it would be interesting to collect the

LRO liquid and analyse it through mass spectrometry. Unfortunately, due to the minute liquid amounts (60 picoliters per KV) these experiments are still technically very challenging.

Our microarray also identified a novel Nodal antagonist that has not been associated with LR before. Nicalin1, expressed on the endoplasmic reticulum and thought to be responsible for the correct trafficking of Lefty in mesendoderm patterning (Haffner et al., 2004, 2007). Knocking down *ncl1* in the whole embryo or just in the LRO cells leads to the same organ *situs* defects, meaning that it has an important role in the LRO. When we compare Nicalin1 knockdown to *dand5*$^{-/-}$ mutants, we can appreciate that lack of *dand5* is more severe for LR than that of *ncl1*, since the first leads to 70% of heterotaxia and the second to less than 50%. However, when both Nodal inhibitors are downregulated, 90% of embryos end up showing heterotaxia, pointing to a potential synergistic epistasis. Due to its ER function, and since we do not detect any Lefty1 expression in the zebrafish LRO by *in situ* hybridization, we can hypothesize that Ncl1 could have a role in Dand5 or for Nodal secretion. In the *dand5*$^{-/-}$ mutant, *ncl1* overexpression cannot rescue LR because Dand5 protein is probably not being produced. This is further confirmed with the very high and bilateral *spaw* expression pattern in the LPM. Dand5 mutants have a majority of bilateral *spaw* due to the absence of Dand5 secretion by the LRO cells. On the other hand, *ncl1* morphants show less *spaw* mRNA levels which is incompatible with the idea as Ncl1 being regulating Dand5 secretion. In a situation where Ncl1 would be needed for Dand5 secretion more *spaw* mRNA levels should be expected because Spaw regulates its own expression positively (Saijoh et al., 2000). Also, overexpressing *dand5* in *ncl1* morphants cannot rescue the organ *situs* defects. All this together indicates that these two proteins might work independently and Ncl1 might be responsible for the trafficking of other TGF-β signalling elements.

To further address the role of Ncl1, we decided to mutate *ncl1* with CRISPR-Cas9 technique. Although it has been described that mutants can sometimes develop compensatory

mechanisms to overcome the impact of the mutations (Rossi et al., 2015), morpholinos have been looked upon with mistrust by the scientific community due to high toxicity and off-targets. Also, an approach with morpholinos in early stage of development blocks even mRNAs maternally provided, leading to stronger phenotypes compared with mutations that do not affect the maternal contribution. Although our *ncl1* morpholino was partially rescued by *ncl1* mRNA, we still intend on ordering a mismatch morpholino in order to control for developmental delay (Stainier et al., 2017). Another important control is indeed producing a mutant that can phenocopy the morphant (Stainier et al., 2017). So, by using CRISPR-Cas9 technology, we produced a mutant for *ncl1* that has a six base pair insertion, altering one amino acid (a Leucine into an Histidine) and inserting 2 new ones (both Methionine). This detected mutation happens in the signal peptide sequence that impacts on protein localization to the endoplasmic reticulum. Very preliminary data show that embryos homozygous mutant had smaller eyes, which can be explained by the strong expression of *ncl1* found in the eyes during development. Also, these embryos showed strong heart *situs* phenotypes, with a majority of central hearts. In the future, we will be analysing these mutants with all the LR markers and we will study flow and *dand5* patterns. In addition, crossing these new mutants with *dand5* mutants will enable for epistatic tests and for potential rescue experiments by *spaw* and *dand5* overexpression in a much cleaner approach.

Zebrafish as a good model for Human Diseases

Despite many differences between animal models and humans, animal models are still unparalleled to study many human related diseases. Zebrafish has been continuously growing as disease model, mainly due to their physical characteristics like transparency and giving numerous progeny, all of which allow cutting costs at many levels, but also due to incredible similarities with the human species in terms of genetics and metabolism. Work

from our lab has shown how zebrafish LRO can be used as a model to study cyst inflation mechanisms and assess the impact of compounds that would ameliorate patients with Polycystic Kidney Disease (Roxo-Rosa et al., 2015). The similarities between zebrafish pronephros and human kidney in terms of compound metabolism and acute response were described in chapter 6 (Gorgulho et al., 2017). In sum, zebrafish is attractive and less expensive alternative to the mouse model, and a more complete system than cell cultures.

Final remarks

Science progression is nowadays, and more than ever, done by small incremental steps. I hope that, with this Thesis, we shed new light in some aspects of zebrafish LR axis establishment, like the role of Notch signalling in cilia motility and new potential targets working downstream of the calcium signalling. The addition of a new Nodal signalling inhibitor to the already complex network of genes working on LR is a new important piece that was until now unknown and will be further validated in the future. LR is a very interesting field that brings together scientists from very different grounds of expertise. It also needs more people working in the same direction: analysing the same readouts with fairly similar methods and presenting the results in a way that can be comparable between different labs. It is an area with still many interesting unanswered questions that will keep bringing people together in the future.

REFERENCES

Amack, J.D., and Yost, H.J. (2004). The T box transcription factor no tail in ciliated cells controls zebrafish left-right asymmetry. Curr. Biol. *14*, 685–690.

Bisgrove, B.W., Snarr, B.S., Emrazian, A., and Yost, H.J. (2005). Polaris and Polycystin-2 in dorsal forerunner cells and Kupffer's vesicle are required for specification of the zebrafish left-right axis. Dev. Biol. *287*, 274–288.

Briata, P., Ilengo, C., Corte, G., Moroni, C., Rosenfeld, M.G., Chen, C.Y., and Gherzi, R. (2003). The Wnt/β-catenin→Pitx2 pathway controls the turnover of Pitx2 and other unstable mRNAs. Mol. Cell *12*, 1201–1211.

Compagnon, J., Barone, V., Rajshekar, S., Kottmeier, R., Pranjic-Ferscha, K., Behrndt, M., and Heisenberg, C.-P. (2014). The notochord breaks bilateral symmetry by controlling cell shapes in the zebrafish laterality organ. Dev. Cell *31*, 774–783.

Dalagiorgou, G., Basdra, E.K., and Papavassiliou, A.G. (2010). Polycystin-1: function as a mechanosensor. Int. J. Biochem. Cell Biol. *42*, 1610–1613.

Delling, M., Indzhykulian, A.A., Liu, X., Li, Y., Xie, T., Corey, D.P., and Clapham, D.E. (2016). Primary cilia are not calcium-responsive mechanosensors. Nature *531*, 656–660.

Ferreira, R.R., Vilfan, A., Jülicher, F., and Supatto, W. (2017). Physical limits of flow sensing in the left-right organizer. Elife *6:e25078*, 1–27.

Field, S., Riley, K.-L., Grimes, D.T., Hilton, H., Simon, M., Powles-Glover, N., Siggers, P., Bogani, D., Greenfield, A., and Norris, D.P. (2011). Pkd1l1 establishes left-right asymmetry and physically interacts with Pkd2. Development *138*, 1131–1142.

Gorgulho, R., Jacinto, R., Lopes, S.S., Pereira, S.A., Tranfield, E.M., Martins, G.G., Gualda, E.J., Derks, R.J.E., Correia, A.C., Steenvoorden, E., et al. (2017). Usefulness of zebrafish larvae to evaluate drug-induced functional and morphological renal tubular alterations. Arch. Toxicol. 1–13.

Haffner, C., Frauli, M., Topp, S., Irmler, M., Hofmann, K., Regula, J.T., Bally-Cuif, L., and Haass, C. (2004). Nicalin and its binding partner Nomo are novel Nodal signaling antagonists. EMBO J. *23*, 3041–3050.

Haffner, C., Dettmer, U., Weiler, T., and Haass, C. (2007). The nicastrin-like protein nicalin regulates assembly and stability of the Nicalin-Nodal modulator (NOMO) membrane protein complex. J. Biol. Chem. *282*, 10632–10638.

Hashimoto, H., Rebagliati, M., Ahmad, N., Muraoka, O., Kurokawa, T., Hibi, M., and Suzuki, T. (2004).

The Cerberus/Dan-family protein Charon is a negative regulator of Nodal signaling during left-right patterning in zebrafish. Development *131*, 1741–1753.

Inácio, J.M., Marques, S., Nakamura, T., Shinohara, K., Meno, C., Hamada, H., and Belo, J.A. (2013). The dynamic right-to-left translocation of Cerl2 is involved in the regulation and termination of Nodal activity in the mouse node. PLoS One *8*.

Kamura, K., Kobayashi, D., Uehara, Y., Koshida, S., Iijima, N., Kudo, A., Yokoyama, T., and Takeda, H. (2011). Pkd1l1 complexes with Pkd2 on motile cilia and functions to establish the left-right axis. Development *138*, 1121–1129.

Kawasumi, A., Nakamura, T., Iwai, N., Yashiro, K., Saijoh, Y., Belo, J.A., Shiratori, H., and Hamada, H. (2011). Left-right asymmetry in the level of active Nodal protein produced in the node is translated into left-right asymmetry in the lateral plate of mouse embryos. Dev. Biol. *353*, 321–330.

Kim, S., Nie, H., Nesin, V., Tran, U., Outeda, P., Bai, C.-X., Keeling, J., Maskey, D., Watnick, T., Wessely, O., et al. (2016). The polycystin complex mediates Wnt/Ca2+ signalling. Nat. Cell Biol. *18*.

Lal, M., Song, X., Pluznick, J.L., Di Giovanni, V., Merrick, D.M., Rosenblum, N.D., Chauvet, V., Gottardi, C.J., Pei, Y., and Caplan, M.J. (2008). Polycystin-1 C-terminal tail associates with β-catenin and inhibits canonical Wnt signaling. Hum. Mol. Genet. *17*, 3105–3117.

Lin, X., and Xu, X. (2009). Distinct functions of Wnt/beta-catenin signaling in KV development and cardiac asymmetry. Development *136*, 207–217.

Mangos, S., Lam, P., Zhao, A., Liu, Y., Mudumana, S., Vasilyev, A., Liu, A., and Drummond, I.A. (2010). The ADPKD genes pkd1a/b and pkd2 regulate extracellular matrix formation. Dis. Model. Mech. *3*, 354–365.

Marques, S., Borges, A.C., Silva, A.C., Freitas, S., Cordenonsi, M., and Belo, J.A. (2004). The activity of the Nodal antagonist Cerl-2 in the mouse node is required for correct L/R body axis. Genes Dev. *18*, 2342–2347.

McGrath, J., Somlo, S., Makova, S., Tian, X., and Brueckner, M. (2003). Two populations of node

monocilia initiate left-right asymmetry in the mouse. Cell *114*, 61–73.

Nakamura, T., Saito, D., Kawasumi, A., Shinohara, K., Asai, Y., Takaoka, K., Dong, F., Takamatsu, A., Belo, J.A., Mochizuki, A., et al. (2012). Fluid flow and interlinked feedback loops establish left-right asymmetric decay of Cerl2 mRNA. Nat. Commun. *3*, 1322.

Nonaka, S., Tanaka, Y., Okada, Y., Takeda, S., Harada, A., Kanai, Y., Kido, M., and Hirokawa, N. (1998). Randomization of left-right asymmetry due to loss of nodal cilia generating leftward flow of extraembryonic fluid in mice lacking KIF3B motor protein. Cell *95*, 829–837.

Pennekamp, P., Karcher, C., Fischer, A., Schweickert, A., Skryabin, B., Horst, J., Blum, M., and Dworniczak, B. (2002). The ion channel polycystin-2 is required for left-right axis determination in mice. Curr. Biol. *12*, 938–943.

Pintado, P., Sampaio, P., Tavares, B., Montenegro-Johnson, T.D., Smith, D.J., and Lopes, S.S. (2017). Dynamics of cilia length in left-right development. R. Soc. Open Sci. *4*, 161102.

Rossi, A., Kontarakis, Z., Gerri, C., Nolte, H., Hölper, S., Krüger, M., and Stainier, D.Y.R. (2015). Genetic compensation induced by deleterious mutations but not gene knockdowns. Nature.

Roxo-Rosa, M., Jacinto, R., Sampaio, P., and Lopes, S.S. (2015). The zebrafish Kupffer's vesicle as a model system for the molecular mechanisms by which the lack of Polycystin-2 leads to stimulation of CFTR. Biol. Open *4*, 1356–1366.

Saijoh, Y., Adachi, H., Sakuma, R., Yeo, C.Y., Yashiro, K., Watanabe, M., Hashiguchi, H., Mochida, K., Ohishi, S., Kawabata, M., et al. (2000). Left-right asymmetric expression of lefty2 and nodal is induced by a signaling pathway that includes the transcription factor FAST2. Mol. Cell *5*, 35–47.

Sampaio, P., Ferreira, R.R., Guerrero, A., Pintado, P., Tavares, B., Amaro, J., Smith, A.A., Montenegro-Johnson, T., Smith, D.J., and Lopes, S.S. (2014). Left-right organizer flow dynamics: how much cilia activity reliably yields laterality? Dev. Cell *29*, 716–728.

Schottenfeld, J., Sullivan-Brown, J., and Burdine, R.D. (2007). Zebrafish curly up encodes a Pkd2 ortholog that restricts left-side-specific expression of southpaw. Development *134*, 1605–1615.

Schweickert, A., Weber, T., Beyer, T., Vick, P., Bogusch, S., Feistel, K., and Blum, M. (2007). Cilia-driven leftward flow determines laterality in Xenopus. Curr. Biol. *17*, 60–66.

Shankaran, S.S., Sieger, D., Schröter, C., Czepe, C., Pauly, M.-C., Laplante, M.A., Becker, T.S., Oates, A.C., and Gajewski, M. (2007). Completing the set of h/E(spl) cyclic genes in zebrafish: her12 and her15 reveal novel modes of expression and contribute to the segmentation clock. Dev. Biol. *304*, 615–632.

Shinohara, K., Kawasumi, A., Takamatsu, A., Yoshiba, S., Botilde, Y., Motoyama, N., Reith, W., Durand, B., Shiratori, H., and Hamada, H. (2012). Two rotating cilia in the node cavity are sufficient to break left–right symmetry in the mouse embryo. Nat. Commun. *3*.

Stainier, D.Y.R., Raz, E., Lawson, N.D., Ekker, S.C., Burdine, R.D., Eisen, J.S., Ingham, P.W., Schulte-Merker, S., Yelon, D., Weinstein, B.M., et al. (2017). Guidelines for morpholino use in zebrafish. PLoS Genet. *13*, 6–10.

Sulik, K., Dehart, D.B., Inagaki, T., Carson, J.L., Vrablic, T., Gesteland, K., and Schoenwolf, G.C. (1994). Morphogenesis of the murine node and notochordal plate. Dev. Dyn. *201*, 260–278.

Supp, D.M., Brueckner, M., Kuehn, M.R., Witte, D.P., Lowe, L.A., McGrath, J., Corrales, J., and Potter, S.S. (1999). Targeted deletion of the ATP binding domain of left-right dynein confirms its role in specifying development of left-right asymmetries. Development *126*, 5495–5504.

Tanaka, Y., Okada, Y., and Hirokawa, N. (2005). FGF-induced vesicular release of Sonic hedgehog and retinoic acid in leftward nodal flow is critical for left – right determination. Nature *435*, 172–177.

Tavares, B., Jacinto, R., Sampaio, P., Pestana, S., Gardner, R., Lopes, T., Lopes, S.S., Schilling, B., Henry, I., and Sau, L. (2017). Notch / Her12 signalling modulates , motile / immotile cilia ratio downstream of Foxj1a in zebrafish left-right organizer. Elife *6:e25165*, 1–26.

Yano, S., Tokumitsu, H., and Soderling, T.R. (1998). Calcium promotes cell survival through CaM-K kinase activation of the protein-kinase-B pathway. Nature *396*, 584.

Yoshiba, S., Shiratori, H., Kuo, I.Y., Kawasumi, A., Shinohara, K., Nonaka, S., Asai, Y., Sasaki, G.,

Belo, J.A., Sasaki, H., et al. (2012). Cilia at the Node of Mouse Embryos Sense Fluid Flow for Left-Right Determination via Pkd2. Science (80-.). *338*, 226–231.

Yuan, S., Zhao, L., Brueckner, M., and Sun, Z. (2015). Intraciliary Calcium Oscillations Initiate Vertebrate Left-Right Asymmetry. Curr. Biol. *25*, 1–12.